Galactic Winds in Nearby Starburst Galaxies: Observations of M82 and NGC 1808

Dragan Salak

February 2014

Galactic Winds in Nearby Starburst Galaxies:

Observations of M82 and NGC 1808

Dragan Salak
Doctoral Program in Physics

Submitted to the Graduate School of
Pure and Applied Sciences
in Partial Fulfillment of the Requirements
for the Degree of Doctor of Philosophy in
Science

at the
University of Tsukuba

Abstract

In galaxies, formation of stars is observed to occur in clouds of molecular gas. Massive-star formation inflicts strong feedback to the interstellar medium (ISM) mainly through ionizing radiation, stellar winds (SWs), and supernova (SN) explosions. Stellar evolution in ordinary, star-forming galaxies partially returns the gas and dust to the ISM and thus supplies further star formation. In some galaxies, called starbursts, extremely high star formation rate may lead to the phenomenon known as "galactic wind" (GW): various phases of the ISM are expelled from the host galaxy by radiation force from young star clusters in synergy with expansion of high-pressure gas heated by SN explosions and SWs. Radiation pressure, SN explosions, and SWs drive large-scale outflows of gas and dust into the galactic halo and intergalactic medium (IGM). GWs are therefore effective mechanisms that remove molecular gas from the central regions and disks of galaxies. As a consequence, star formation is significantly reduced and heavy elements forged inside stars are transported to the IGM.

Galactic winds have been detected both at low and high redshift. Classical examples in the nearby universe are the starburst galaxies M82, NGC 253, NGC 1808, and NGC 3079. In the distant universe, spectroscopic measurements have revealed that large outflows are present in starburst galaxies and active galactic nuclei, and that the IGM is enriched in heavy elements that were formed in stellar interiors. In M82, the exemplar of starburst-driven winds, all major phases of the ISM (ionized, atomic, and molecular gases, dust grains, and polycyclic aromatic hydrocarbon molecules) have been detected in the wind. Outflow energetics shows that the momentum of the outflow is comparable in the ionized and neutral phases. In particular, observations of the rotational transitions of CO, as a reliable tracer of molecular gas, have shown that the molecular gas outflow in M82 is dynamically significant.

Detailed studies of the GW feedback require sensitive observations that can probe various phases of the ISM in high angular resolution. In this work, we report radio-astronomical observations and analysis of M82 and NGC 1808 - nearby starburst galaxies with GWs. The main body of the research is centered on observations of the molecular gas, as summarized below.

M82 was imaged on a large scale in ^{12}CO ($J = 1 \rightarrow 0$) at the frequency of 115 GHz with the Nobeyama Radio Observatory (NRO) 45-m telescope in 2009 and 2010. The 45-m single dish data were combined with interferometer data acquired with the Combined Array for Research in mm-wave Astronomy (CARMA) in 2012 in collaboration with the CANON team (CARMA-Nobeyama Nearby Galaxies Survey). The product of combining is a sensitive image in high angular resolution (4.0 and 3.3 arcsec corresponding to 68 and 56 pc) with a wide range of spatial frequencies. In addition, 3-mm survey observations were conducted with the 45-m telescope in 2013 toward selected regions in the galactic disk and outflow in M82 to probe the physical conditions of molecular gas. The survey included the following molecular lines: ^{12}CO ($J = 1 \rightarrow 0$), ^{13}CO ($J = 1 \rightarrow 0$), C^{18}O ($J = 1 \rightarrow 0$), CN ($N = 1 \rightarrow 0$), and CS ($J = 2 \rightarrow 1$).

The combined CARMA-NRO 45m image of M82 reveals the morphology and kinematics of molecular gas: the CO gas is concentrated in a 500-pc edge-on nuclear ring, polar outflow, and dusty streamers. Two prominent nascent outflows were found to extend 300 pc perpendicular to the nuclear ring with average expansion velocities of 50 km s^{-1}. We have calculated dynamical timescales, kinetic energies, and mass outflow rates. The outflows were triggered 5 Myr ago during the second

starburst episode that had been going on in the nuclear ring. The large-scale ($\gtrsim 2$ kpc) outflow detected with the 45-m telescope was formed after the onset of the first starburst episode in the central 500 pc $\sim 10-50$ Myr ago. The galactic center is now depleted of molecular gas and outflows are generated in the nuclear ring. It can be shown that the 300-pc outflows can be powered by radiation pressure (governed by the star formation rate) and momentum carried by the material ejected in SN explosions. We propose that the outflow is initially driven by radiation pressure from star clusters embedded in dusty gas, and then re-accelerated by momentum deposition and thermal energy deposition in subsequent SN explosions.

The line-survey observations of M82 yielded significant detections of ^{12}CO ($J = 1 \rightarrow 0$) in the halo at distances 2 and 4 kpc from the center confirming that molecular gas is present at least 3.5 kpc above the galactic plane. We have detected ^{13}CO ($J = 1 \rightarrow 0$), C^{18}O ($J = 1 \rightarrow 0$), CN ($N = 1 \rightarrow 0$), and CS ($J = 2 \rightarrow 1$) in the inner outflow (500 pc above the galactic plane) and found a difference in line intensity ratios in the inner outflow and the nuclear ring. The ratios of ^{12}CO/^{13}CO $J = 1 \rightarrow 0$ and ^{13}CO/C^{18}O $J = 1 \rightarrow 0$ line intensities are higher in the outflow compared to the ring. Similarly, ^{12}CO($J = 1 \rightarrow 0$)/CN($N = 1 \rightarrow 0$) and ^{12}CO($J = 1 \rightarrow 0$)/CS($J = 2 \rightarrow 1$) are higher in the outflow. We have found that the line intensity ratio of CN($N = 1 \rightarrow 0$)/CS($J = 2 \rightarrow 1$) is increased too, suggesting a depletion of dense gas and the presence of large photo-dissociation regions (PDRs) in the outflow.

Observations of the molecular gas in NGC 1808 were carried out with the Atacama Submillimeter Telescope Experiment (ASTE) 10-m telescope in 2013. We observed the ^{12}CO ($J = 3 \rightarrow 2$) line at the frequency of 346 GHz over a $100'' \times 80''$ (5×4 kpc^2) field and measured the intensity of ^{13}CO ($J = 3 \rightarrow 2$) at the central position (~ 550 pc radius of the projected telescope beam of $22''$). NGC 1808 was also observed with the Very Large Array (VLA) in 2012 in high angular resolution ($0.2'' - 0.4''$) to measure the flux density of the radio continuum at 21 and 32 GHz in the galactic nucleus and determine its position and size.

We present the first fully sampled map of ^{12}CO ($J = 3 \rightarrow 2$) and the first detection of ^{13}CO ($J = 3 \rightarrow 2$) in NGC 1808. The molecular gas is clearly concentrated in the inner 2-kpc region of the galaxy with prominent extended structure along the galactic bar (major axis) but also along the minor axis. The minor-axis structure can be explained as molecular gas entrained in the GW observed as a dust outflow at optical wavelengths. We have carried out a radiative transfer analysis of the excitation conditions of CO in the starburst region (radius ≈ 550 pc) with the RADEX program. The results suggest that the beam-averaged density and kinetic temperature of the molecular gas can be fitted at $n(\mathrm{H_2}) \approx 10^{3.5}$ cm^{-3} and $T_\mathrm{k} \approx 32$ K, close to the estimated dust temperature of $T_\mathrm{d} \sim 34$ K, with uncertainty ranging within $3.0 \lesssim \log[n(\mathrm{H_2})/\mathrm{cm^{-3}}] \lesssim 4.0$ and $20 \lesssim T_\mathrm{k} \lesssim 100$ K. RADEX calculations show that, for the adopted physical parameters, $J = 2 \rightarrow 1$ and $J = 3 \rightarrow 2$ of ^{12}CO are optically thick, ^{12}CO $J = 1 \rightarrow 0$ is only moderately optically thick, and all transitions of ^{13}CO are optically thin.

We have compared the properties of M82 and NGC 1808. The results are summarized as follows: (1) both galaxies have increased concentration of molecular gas within 500 pc from the center; (2) molecular gas masses are comparable in this region: 2.3×10^8 $M_\odot$ in M82 and 1.6×10^8 $M_\odot$ in NGC 1808, derived by using the same CO-to-H$_2$ conversion factor of $X_\mathrm{CO} = 0.5 \times 10^{20}$ cm^{-2} (K km s^{-1})$^{-1}$; (3) star formation rate is higher in M82, but both galaxies have experienced bursts of star formation in the past 50 Myr; (4) we find low line intensity ratios of 3.7 ± 0.3 and 58.3 ± 4.0 for ^{13}CO/C^{18}O $J = 1 \rightarrow 0$ and ^{12}CO/C^{18}O $J = 1 \rightarrow 0$ in M82, respectively. This is very similar to the values reported previously for NGC 1808 and suggests that C^{18}O is enhanced in both starburst galaxies as a consequence of massive-star formation and nuclear processing in stars.

Preface

Figure 1: Clockwise from top left: Nobeyama Radio Observatory 45-m telescope, Combined Array for Research in mm-wave Astronomy (image credit: http://bima.astro.umd.edu), Atacama Submillimeter Telescope Experiment, and the Very Large Array (image credit: Britannica).

Contents

Chapter 1

Introduction

1.1 Starburst galaxies and galactic winds

During the last fifty years, evidence has accumulated showing that many galaxies at low and high redshifts host large-scale outflows called galactic winds (hereafter GWs; also called superwinds) (figure 1.1). Since the pioneering discovery of an "explosion" in the galaxy M82 by Lynds & Sandage (1963), observations at various wavelengths have implied that the origin of the GW phenomenon must be in the central regions of host galaxies where either vigorous star formation (starburst), or gaseous jets perpendicular to accretion disks around supermassive black holes in active galactic nuclei (AGN, in Seyfert galaxies), or both, power the winds with large diversity in morphology and scale (e.g., review in Veilleux et al. 2005). The region where the energy is released (starburst region or AGN jet) is called the energy injection zone (EIZ). In starbursts, frequent supernova (SN) explosions several million years after the onset of star formation, input kinetic energy that heats the ambient gas and increase its pressure in the interstellar medium (ISM), as discussed in the classic papers of Chevalier & Clegg (1985) and Schiano (1985), and recently by numerical simulations (e.g., Creasey et al. 2013; von Glasow et al. 2013). Consequently, the gaseous medium expands and develops a large-scale wind associated with outflows of gas and dust (Strickland et al. 2004). A semi-analytical approach studying the evolution of superbubbles into galactic winds was recently written by Roy et al. (2013).

In recent years, however, it has become evident that SN explosions fail to account for some observations. The main problem is that thermal heating from SNe tends to destroy molecular clouds by vaporization and ram pressure. In order to circumvent this problem, several authors have proposed that radiation pressure and stellar winds could contribute energy and momentum deposition at least comparably to that of SN explosions (Murray et al. 2005; Murray et al. 2011; Shetty et al. 2011; Zhang & Thompson 2012). Murray et al. (2005) suggest that radiation pressure has been an essential feedback, not only in nearby, present-day galaxies, but even more strikingly in the early universe when elliptical galaxies and stellar bulges of spiral galaxies were forming. It has been well known that these spheroidal objects obey the Faber-Jackson relation between the luminosity and stellar velocity dispersion, $L \propto \sigma^4$ (Faber & Jackson, 1976). Another similar relation was discovered at the turn of the century, when the mass of the supermassive black hole in the centers of some galaxies was discovered to be proportional to the stellar velocity dispersion as $M_{\rm BH} \propto \sigma^4$ (Ferrarese & Merritt 2000; Gebhardt et al. 2000; Tremaine et al. 2002; di Mateo et al. 2005). Murray et al. (2005) interpret this similarity as coming from a common origin. The idea is that in the past, when these galaxies had active star formation, the stellar luminosity reached a galactic Eddington luminosity, $L_M \simeq (4 f_{\rm g} c/G)\sigma^4$ (where $f_{\rm g}$ is the gas fraction and σ is the stellar velocity dispersion), that was the turning point when the molecular gas was gradually expelled from the entire galaxies in large-scale outflows. As a consequence, star formation and supermassive-black-hole growth was quenched, and the black hole's mass was locked in the relation with stellar luminosity. Today, we observe these objects as elliptical galaxies, which

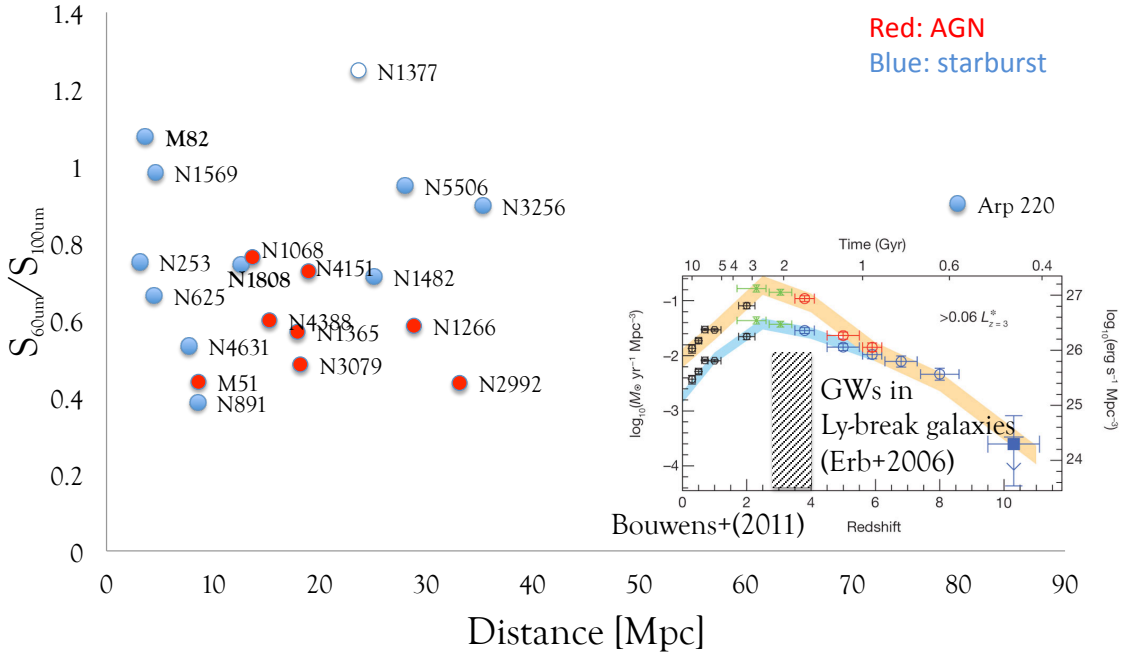

Figure 1.1: Galactic winds in the local and distant Universe. The ratio of fluxes at 60 μm and 100 μm as star formation indicator is plotted against distance from the Milky Way. A plot of SFR density against redshift (cosmic age) is shown in the bottom right corner; GWs have been detected in Ly-break galaxies. The compilation of galaxies is not complete.

have low star formation rate (SFR), although they are not entirely devoid of cool gas and dust, as found in recent surveys of nearby early type galaxies (such as ATLAS^{3D}; Cappellari et al. 2013).

Similarly, Shetty et al. (2011) have proposed a dust-driven wind model, which shows that radiation pressure on dust grains, which are hydrodynamically coupled with gas, can account for observations. On the other hand, Nath & Silk (2009) have developed a hybrid model which accounts for both SN explosions (= thermal pressure) and radiation pressure. Dust-driven outflows have been studied in numerical simulations too, for example, by Krumholz & Thompson (2013).

The connection between galaxy formation and stellar feedback in GWs is supported by observations. Recent studies show that cool gas outflows were present at different epochs of the cosmic history (Heckman et al. 1990; Shapley et al. 2003; Martin 2005; Veilleux et al. 2013). Compared to the present day, we expect that GWs were even more common in the past, at redshifts $z = 2-5$ when SFR density was by more than an order of magnitude higher than today; the latest estimate for the historical peak of SFR density is near $z \approx 3$ (Bouwens et al. 2011). Likewise, observations (SDSS and 2dF surveys) show that the density of luminous quasars peaks at $z \approx 3$ (Fan 2012). By this time many galaxies have assembled their supermassive black holes and luminosity has approached the critical Eddington luminosity of Murray et al. (2005). What followed is the formation and growth of early type systems such as elliptical galaxies. The connection between the galactic wind feedback and galaxy evolution is shown in figure 1.2.

In order to study galactic winds, observations of all components of the ISM and at all scales are essential. In the case of M82, the most thoroughly studied starburst galaxy, it has been found that the molecular gas is dynamically a significant component (Walter et al. 2002; Salak et al. 2013). Considering the enrichment of heavy elements in the intergalactic medium (IGM) as a major feedback to galaxy evolution, the importance of observing molecular-gas outflows is clear. Observations on kpc-scale unveil large-scale kinematics, whereas resolving the sub-kpc scale reveals the structure and kinematics of giant molecular clouds (GMCs). However, the details of the entrainment of GMCs and

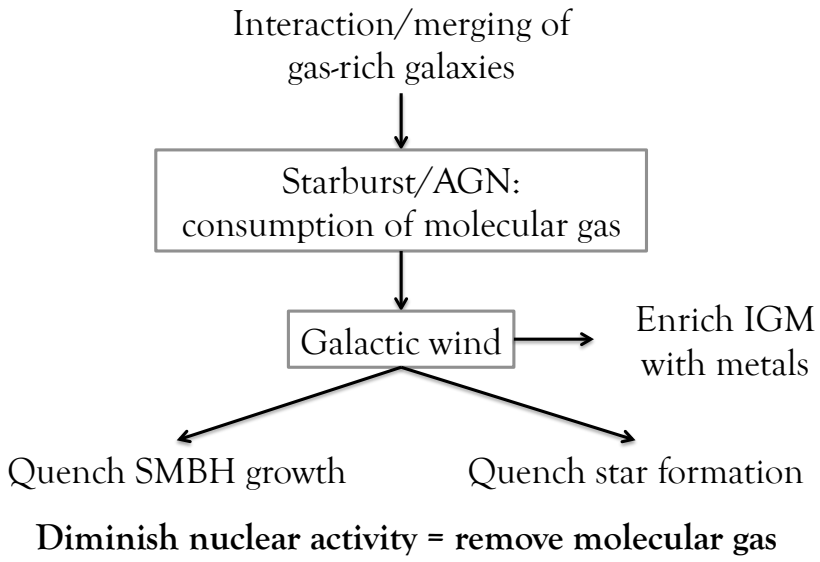

Figure 1.2: Galactic wind feedback and galaxy evolution.

dust into outflows in the EIZ lacks high-resolution observational data.

In this work, we present multi-wavelength and multi-scale observations of two nearby starburst galaxies, M82 (NGC 3034) and NGC 1808. The observations comprise molecular lines of ^{12}CO, ^{13}CO, C^{18}O, CN, and CS, as well as radio continuum at 22 and 33 GHz. The molecular lines, especially those of CO, are used to probe the molecular gas in the outflows driven by GWs. In the following subsections, we summarize basic properties of M82 and NGC 1808.

Throughout this work, CO ($J = 1 \rightarrow 0$) and other transitions are denoted by CO (1-0), etc., and CO stands for ^{12}C^{16}O.

1.1.1 M82

M82 is one of the nearest (3.53 Mpc, Karachentsev et al. 2002) and brightest starburst galaxies with a prominent superwind (figure 1.3), classified as I0 (de Vaucouleurs et al. 1991) and S0 (Ichikawa et al. 1995). Despite being a small galaxy, M82 contains so much molecular gas that it is the brightest galaxy on the sky in the CO (1-0) emission. Strong CO (1-0) in the nuclear region implies that other molecular emission lines too may well be strong, hence many studies have been focused on studying the molecular gas phase by analyzing the physical state and astrochemistry. In addition to the starburst nucleus, the galaxy is a particularly good observational target for studying the extra-planar ISM because of the high inclination of its galactic plane ($i = 80^0$, de Vaucouleurs et al. 1991) - this allows us to examine the tenuous outflow material but involves larger uncertainties in outflow energetics.

Followed by the discovery of an "explosion" in M82 by Lynds & Sandage (1963), one of the first observational summaries and interpretations of the activity in the galactic nucleus was given in Rieke et al. (1980). Nakai et al. (1987) were the first to suggest that the molecular gas in the nuclear region is driven in an outflow that takes the shape of an expanding cylinder, and encloses the Hα-emitting gas, because of the ring-like nuclear distribution of the molecular gas that surrounds the galactic center region. Other observations of CO (e.g., Shen & Lo 1995; Seaquist & Clark 2001; Taylor et al. 2001; Walter et al. 2002; Salak et al. 2013) have confirmed the presence of a molecular gas outflow, and studied its morphology and kinematics.

The halo of M82 contains atomic gas (H I) that occupies the intergalactic medium around the galaxies of the M81-M82 group (e.g., Cottrell 1977; Appleton et al. 1981; Yun et al. 1994), Hα filaments of ionized gas perpendicular to the major optical axis (Lynds & Sandage 1963; Shopbell & Bland-Hawthorn 1998; figure 1.3), UV and X-ray emission as far as 11 kpc above the galactic plane in the so-called Cap region (Hoopes et al. 2005; Tsuru et al. 2007, respectively), and a large PAH and dust halo recently imaged with the AKARI and Herschel satellites (Kaneda et al. 2010; Yamagishi et al. 2012; Roussel et al. 2010, respectively).

In recent years, we have carried out extensive observations of M82. First, in 2009 and 2010, on-the-fly (OTF) mapping on a large scale with the Nobeyama 45-m telescope was made to unveil the extent of detectable CO emission in the galactic halo (Salak et al. 2013). Next, in 2012, M82 was observed with the Combined Array for Research in Millimeter-wave Astronomy (CARMA) and combined with our OTF map to correct the interferometer map for short-baseline spacing. The combining is part of the "CARMA-Nobeyama nearby galaxies survey" (CANON), in which the main goal is to resolve and study molecular clouds in nearby galaxies. Finally, in 2013, based on previous results, I led a project to observe several molecular lines (CO, CN and CS) toward selected positions in the galaxy: the nucleus, inner outflow, and outer outflow. The results of these observations and data analysis constitute the first part of my thesis.

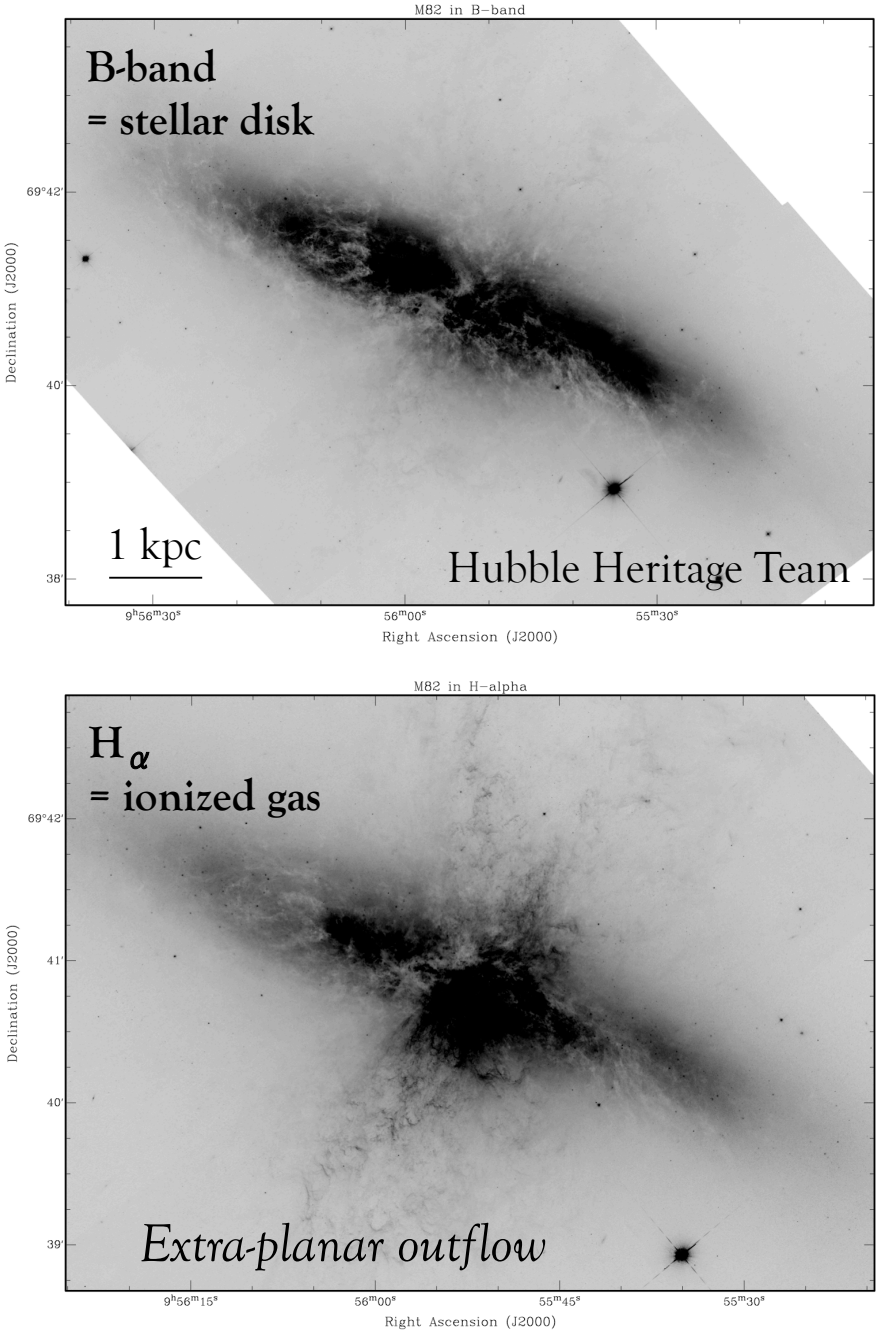

Figure 1.3: Optical image of M82 in a) B-band and b) Hα emission at 656.5 nm. Credit: Hubble Heritage Team.

1.1.2 NGC 1808

NGC 1808 is a nearby (10.8 Mpc, Tully 1988) peculiar spiral galaxy (figure 1.4) with clear signatures of a starburst (IR flux $S_{60\mu m}/S_{100\mu m} \simeq 0.7$, where $\gtrsim 0.4$ indicates starburst, Sanders et al. 2003). Observations of the nuclear region have revealed hot spots and knots at optical and near-IR wavelengths (Morgan 1958; Sérsic & Pastoriza 1965) and compact ($\sim 1''$) radio-continuum sources, which trace H II regions and SN remnants (Saikia et al. 1990), young globular clusters at mid-IR (Galliano et al. 2005), as well as a candidate for a low-luminosity AGN (Veron-Cetty & Veron 1985; Awaki et al. 1996; Kotilainen et al. 1996; Jiménez-Bailón et al. 2005), suggesting that the galaxy may be a type 2 Seyfert.

Although unresolved due to low angular resolution, the molecular gas traced with the CO (1-0) line was found to be concentrated in the central region (Dahlem et al. 1990; Aalto et al. 1994), while the atomic gas (H I 21-cm line) shows a large-scale warp, unusually high abundance in the bar, a torus around the galactic center, and a possible outflow from the central region (Koribalski et al. 1993; Koribalski et al. 1996).

Further attention was drawn to this galaxy when observations of Hα unveiled a large-scale outflow of ionized gas perpendicular to the plane of the galaxy (Phillips 1993). The existence of the outflow had previously been suspected from the presence of unusual polar dust filaments on photographic plates (Burbidge & Burbidge 1968; Sandage & Bedke 1994; figure 1.4). Clearly, there is evidence for ionized and neutral gas in polar motion outward from the central region of NGC 1808, similarly to M82.

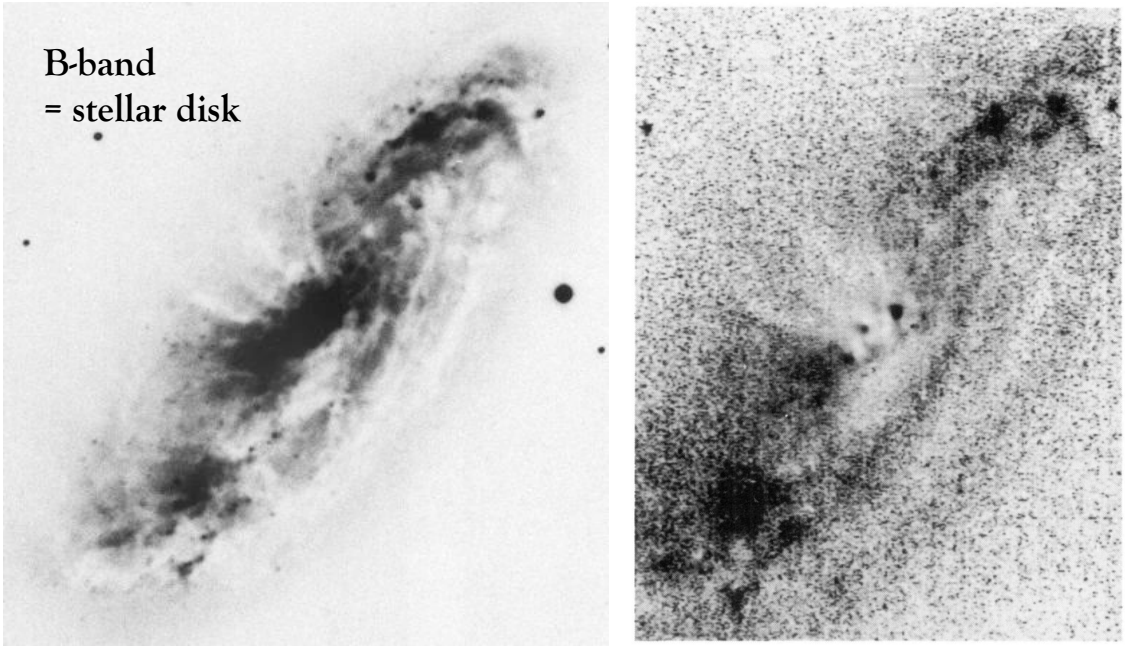

Figure 1.4: Images and maps of NGC 1808. From top left: (a) Optical (B-band) (Sandage & Bedke 1994); (b) optical(B)/IR(z) color index (Veron-Cetty & Veron 1985).

1.2 Molecular lines in the 3-mm band

Observation of the molecular gas in galaxies is ordinarily performed with radio telescopes. The most abundant molecule in the universe, H_2, has no permanent dipole moment and therefore direct observations are difficult. On the contrary, the CO molecule, which is second in abundance after H_2, has observable pure rotational transitions in a wide range from 115 GHz (fundamental frequency), hence provides a useful tool to reveal the distribution of molecular gas in galaxies. Although CO does not necessarily trace all of H_2 in the ISM, it is the best known probe that we have today. For a review on molecular gas in our and other galaxies, see Young & Scoville (1991), Snow & McCall (2006) and Fukui & Kawamura (2010).

In addition to CO, which traces both diffuse ($n \sim 10^3$ cm^{-3}) and dense ($n \gtrsim 10^4$ cm^{-3}) molecular gas, molecules such as CN and CS lie in the same frequency range and can be observed simultaneously. These species are less abundant than CO and have at least one order of magnitude higher critical densities[1], which make them good tracers of dense molecular clouds ($n \sim 10^5$ cm^{-3}). The frequencies of rotational transitions of CO, CN and CS are shown in figure 1.5.

Unlike CO and CS, which have simple rotational spectra, CN contains one nitrogen atom that has even number (seven) of protons and neutrons, and therefore non-zero nuclear spin. This complicates the energy levels as explained in the following subsection, where we choose CN as an example to illustrate molecular spectroscopy related to astrophysics.

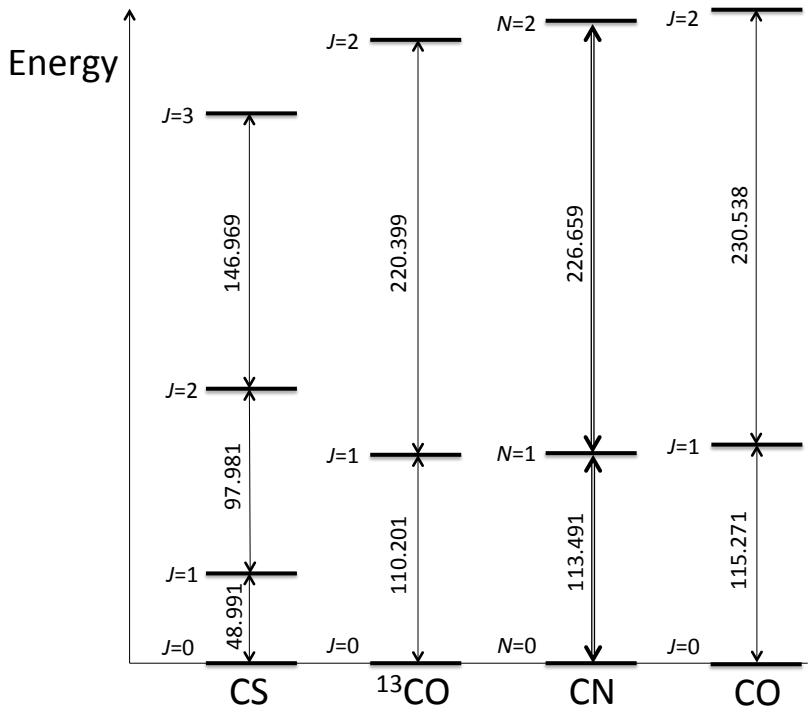

Figure 1.5: Several lowest rotational transitions of the ground vibrational state $v = 0$ of CS, CN, ^{13}CO and ^{12}CO. Note that C refers to ^{12}C unless otherwise indicated. Only $\Delta J = \pm 1$ rotational transitions are allowed. Frequencies in GHz are given next to each line.

[1]Critical density, n_c, is the density at which collisional deexcitation is equal to radiative deexcitation. Line emission in the ISM is typically strongest at densities near n_c.

1.2.1 Example: the CN molecule

The cyanide radical (CN) is one of the first molecules discovered in the interstellar medium (McKellar 1940). As a heteronuclear diatomic molecule, it has a permanent dipole moment, and hence allowed rotational and vibrational transitions. With a relatively large permanent moment of 1.45 D, the Einstein coefficient is high, $A_{21} \sim 10^{-5}$ s^{-1}, which makes spontaneous deexcitation rapid. Interestingly, it was found that the excitation temperature of CN (1-0) at 2.64 mm in the Galactic ISM is $T_{\rm ex} = 2.74 \pm 0.02$ K (Roth & Meyer 1995), which is very close to the temperature of the cosmic microwave background radiation (CMB), $T_{\rm CMB} = 2.73$ K. Consequently, it was realized that the populations of rotational levels of CN are in radiative equilibrium with CMB (Thaddeus & Clauser 1966). In diffuse molecular clouds (see below), excitation of CN molecules is influenced both by CMB photons and collisions with molecules, atoms, and electrons, where typical electron densities are $(0.01 - 0.06)$ cm^{-3}, more than three orders of magnitude lower than that of molecules (Harrison et al. 2013, see also figure 1.8).

The CN molecule contains a nitrogen atom with 7 protons and 7 neutrons. Two unpaired nucleons (1 proton and 1 neutron) contribute to a non-zero total spin of the N nucleus. The molecular angular momentum can be written as

$$\mathbf{J} = \mathbf{N} + \mathbf{S}. \tag{1.1}$$

Here, $\mathbf{N}$ is the orbital angular momentum of the two nuclei, $\mathbf{S}$ is the total electronic spin, and $\mathbf{J}$ is the total angular momentum where the nuclear spin of N, namely $\mathbf{I}_{\rm N}$ is neglected. If included,

$$\mathbf{F} = \mathbf{J} + \mathbf{I}_{\rm N}. \tag{1.2}$$

The energy levels of the combinations of adding the angular momenta are shown in figure 1.6. Note that the hyperfine structure leads to 9 distinct transitions. Their properties for the lowest rotational transitions $N = 1 \rightarrow 0$ are given in table 1.1 along with relative intensities. The hyperfine structure results from the interaction between the electric quadrupole moment (spin) of the N nucleus and molecular rotation.

The ground state of CN is X $^2\Sigma^+$. This means that the total spin is a half-integer, $S = 1/2$, since the multiplicity is $2S + 1 = 2$. Unlike other molecules whose lines were observed in this work (^{12}C^{16}O, ^{13}C^{16}O and ^{12}C^{32}S), CN has half-integer values of the total angular momentum $\mathbf{J}$ (because the nuclear rotational angular momentum $\mathbf{N}$ is always an integer number).

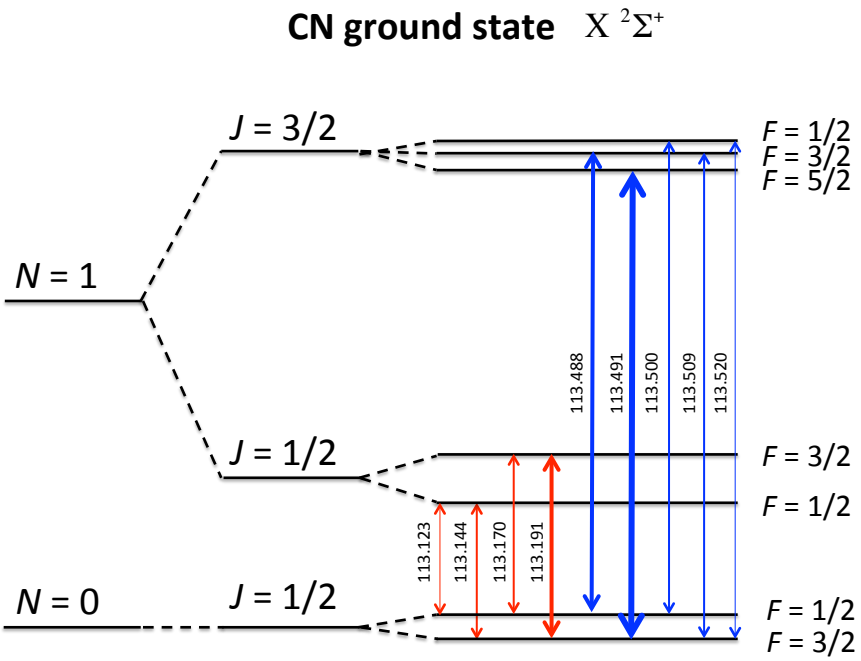

Figure 1.6: Two lowest rotational levels of the CN molecule in the lowest vibrational state $v = 0$. Thickness of the lines indicates relative intensities of the transitions. Frequencies in GHz are given next to each line.

Table 1.1: Rotational transitions $N = 1 \rightarrow 0$ of the CN molecule in the lowest vibrational state $v = 0$.

Rest frequency [GHz]	$J \rightarrow J'$	$F \rightarrow F'$	Relative intensity
113.123	1/2-1/2	1/2-1/2	1.23
113.144	1/2-1/2	1/2-3/2	9.88
113.170	1/2-1/2	3/2-1/2	9.88
113.191	1/2-1/2	3/2-3/2	12.35
113.488	3/2-1/2	3/2-1/2	12.35
113.491	3/2-1/2	5/2-3/2	33.33
113.500	3/2-1/2	1/2-1/2	9.88
113.509	3/2-1/2	3/2-3/2	9.88
113.520	3/2-1/2	1/2-3/2	1.23

Note. The intensity of all the $J = 3/2 \rightarrow 1/2$ transitions together comprises 66.7%, while that of the $J = 1/2 \rightarrow 1/2$ transitions comprises 33.3%. See Skatrud et al. (1983).

1.3 Molecules in photodissociation regions

1.3.1 Photodissociation regions

Photodissociation regions (PDRs) are boundary regions in the ISM between relatively dense molecular clouds and ionized (H II) regions. The structure is rather complex from physico-chemical perspective, because the local radiation field, abundances and chemistry of ions, atoms and molecules play a key role. One of the first comprehensive PDR models for diffuse gas was developed by van Dishoeck & Black (1986). For recent numerical calculations of PDRs and X-ray-dominated regions (XDRs, in which the radiation field is not far-UV but X-rays) in dense gas, see Meijerink & Spaans (2005), Meijerink et al. (2006) and Meijerink et al. (2007). The outer edge of a PDR is the *ionization front*. Outside this limit, chemistry is nearly non-existent, because most of the gas phase is composed of ionized nuclei of hydrogen (protons), electrons, and helium. Depending on the temperature, He is often only once ionized (He^+), but near very hot stars, e.g., in planetary nebulae, He III regions exist too. Other atoms, most notably oxygen, carbon and nitrogen, are singly ionized because of low ionization potentials, lower than that of H. The ionization potentials of the most relevant species are: $I(\mathrm{H}) = 13.6$ eV, $I(\mathrm{He}) = 24.6$ eV, $I(\mathrm{C}) = 11.3$ eV, $I(\mathrm{N}) = 14.5$ eV, $I(\mathrm{O}) = 13.6$ eV, $I(\mathrm{Na}) = 5.1$. Obviously, even if H is not ionized, it is possible to have C II regions. Oxygen is ionized at similar energies as hydrogen; nitrogen needs little more. Note that He requires much higher energy. For this reason, He II regions are usually smaller than H II regions.

At the neutral side of the ionization front, chemistry thrives because various species begin to recombine. Most of hydrogen is in the form of H^0, as well as O and N. This is the realm of atomic hydrogen (H I region), which is easily observed via the 21-cm line of neutral hydrogen arising from the flip of the electron spin relative to that of the proton.

Molecular gas

In regions of higher density of hydrogen nuclei, $n(\mathrm{H})$, the optical depth is high enough to allow molecules to exist (figure 1.7). This is the *diffuse molecular gas* that is within the *photodissociation front*. The most abundant species is H_2, followed by CO. Self-shielding, which protects H_2 from photodissociation, makes H_2 abundant already at lower densities and opacities, compared to CO, which is shielded by H_2 and by CO itself at $A_V \gtrsim 0.2$. This is crucial, because it implies that regions of CO are inside those of H_2.

Snow & McCall (2006) define another low-density molecular gas phase that is farther inside the molecular medium, as *translucent clouds* (see figure 1.8). This component is within the boundary where the abundance curves of neutral and once-ionized carbon intersect at the column density of $N(\mathrm{H}) \simeq 2 \times 10^{21}$ cm^{-2}. Inside translucent clouds, the neutral fraction of carbon increases, while the fraction of C^+ and the abundance of free electrons decreases. It is the region where CO, CN, OH and other molecules are observed (see below). Apparently, translucent clouds are hosts to different and more complex chemistry compared to diffuse clouds. As an example, consider one channel of the reactions that lead to the formation of CO:

$$\begin{aligned} \mathrm{C}^+ + \mathrm{OH} &\rightarrow \mathrm{CO}^+ + \mathrm{H} \\ \mathrm{CO}^+ + \mathrm{H}_2 &\rightarrow \mathrm{HCO}^+ + \mathrm{H} \\ \mathrm{HCO}^+ + e^- &\rightarrow \mathrm{CO} + \mathrm{H} \end{aligned} \tag{1.3}$$

The main players are C^+, OH, but also H_2. Therefore, CO is much more likely to be created in already molecular gas abundant in H_2.

In diffuse and translucent molecular clouds, the fractional abundance of H_2, $f(H_2)$, is governed by the balance between the formation of H_2 on dust grains and its destruction by UV photons. Direct photodissociation of H_2 requires a high energy of 14.7 eV, and is *not* the main process that destroys the molecule. Instead, H_2 absorbs UV photons of energies able to excite the molecule into vibrational states within a higher electronic state. In spectroscopic notation, this occurs within Lyman bands X-B, and Werner bands X-C, where X is the ground state, while B and C are the lowest excited states. As a result, there is certain probability that deexcitation will lead to dissociation of the molecule. The probability is higher for X-B than for X-C.

Van Dishoeck & Black (1988) studied the photodissociation and chemistry of H_2 and CO in the ISM. Their results are illustrated in figure 1.8, especially the part which concerns H, H_2 and CO. Note that there is a zone in diffuse and translucent clouds where the abundances of H and CO significantly change, whereas H_2 remains nearly constant. In diffuse clouds, even at column densities of $\sim 1 \times 10^{21}$ cm^{-2}, the fraction of H is relatively high (> 10 %). However, in translucent clouds, where densities rise to 10^3 cm^{-3} and above, the fraction drops to about 1%. Here, CO abundance rapidly increases with $N(H)$, and reaches its peak in the innermost regions of the dense molecular clouds where $N(H) \gtrsim 7 \times 10^{21}$ cm^{-2}. The CO molecule is destroyed by discrete absorption to excited predissociation states. Therefore, similarly to H_2, direct photodissociation is not efficient. At sufficient densities, self-shielding and shielding by coincident *lines* of H_2 and H protect CO molecules. The transition between C^+, C and CO was estimated so that $n(C^+) \sim n(CO)$ at $N(H) \sim 10^{21}$ cm^{-2} and $n(H) \sim 700$ cm^{-3}.

Finally, deep inside the protected (shielded) molecular medium, molecules become increasingly abundant. Depending on the environment, these *dense molecular clouds* are rich in "dense-gas tracers" such as HCN and CS, but also H_2 and CO. The abundance of free electrons is very low, and the dominant sources of heating and ionization are cosmic rays. Carbon is almost entirely locked in CO and other C-bearing molecules. Note, however, that higher density does not necessarily mean increase in abundance of all molecular species, since, for instance, CN is found to be *less* abundant in the cores of dense clouds compared to their outer envelopes (Jansen et al. 1995b). Therefore, details in chemical and physical processes are important and sophisticated models are required to disentangle observations.

1.3.2 Diffuse and translucent molecular clouds

Diffuse interstellar medium is abundant in molecules. The first detected interstellar molecules in space were CN, CH and CH^+. In diffuse media, CO, C_2, C_3, H_3^+, HCO^+, OH, SO, CS, SiO, C_2H, etc. have been observed, OH being the first to be detected at radio wavelengths (for a comprehensive review, see Snow & McCall 2006).

Emission and absorption of CO rotational transitions at mm-waves have been observed in diffuse molecular gas in our Galaxy since 1970's. Here are some examples. Knapp & Jura (1976) observed and detected radio lines of CO in diffuse clouds where the molecule was previously detected in UV by the Copernicus satellite. Koribalski et al. (1996) made observations towards the bright star ζ Ophiuchi where ^{13}CO data indicated low density; in the region, it was found that the ^{12}CO/^{13}CO line intensity ratio was very large (30-60) and the density rather low ($n(H_2) \sim 10^3$ cm^{-3}). Liszt (1997) observed the same region and detected lines of OH and CH. Here, CH and CO were found to be distributed similarly, unlike OH. Recently, Pan et al. (2005) studied the physical conditions in star-forming regions of our Galaxy. Their findings suggest that the column densities of CO and CN are strongly correlated in diffuse clouds.

These and similar measurements made comparison of the CO line emission with H_2 absorption in the far-UV possible along the same sight lines. This method, although dangerous because of pathlength differences, brought estimates of a very law abundance ratio $[CO]/[H_2] \sim 10^{-6}$ in diffuse

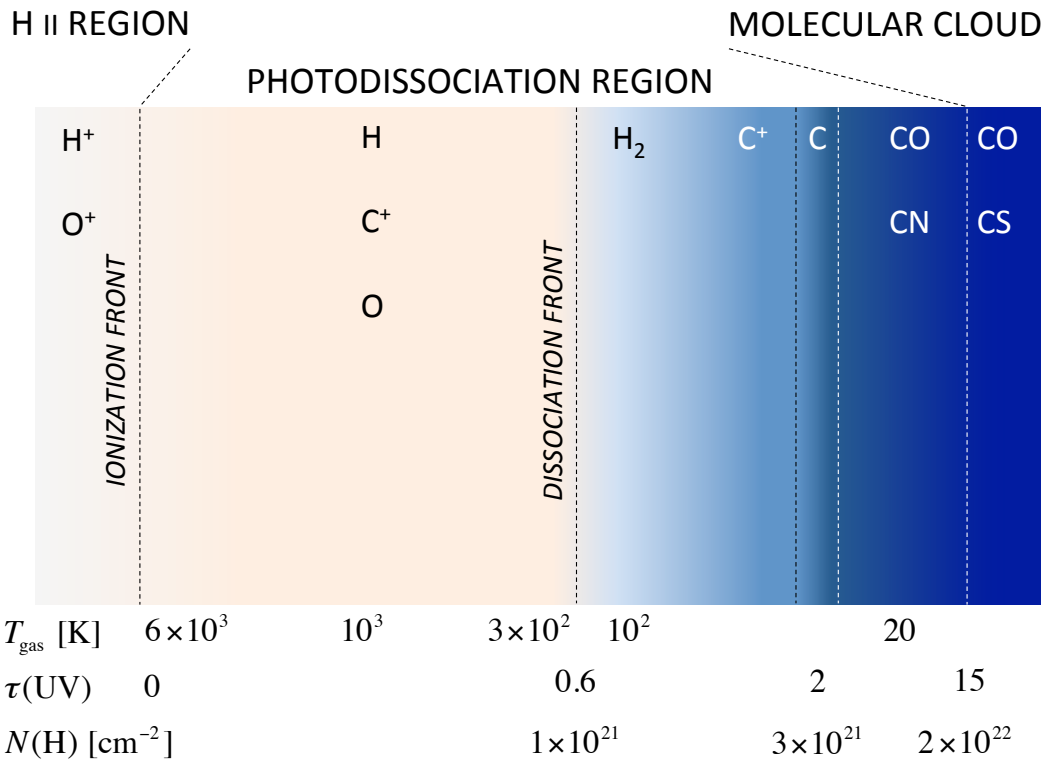

Figure 1.7: Structure of a photodissociation region (PDR) in between H II regions and dense molecular clouds. The illustration is based on Draine & Bertoldi (1996).

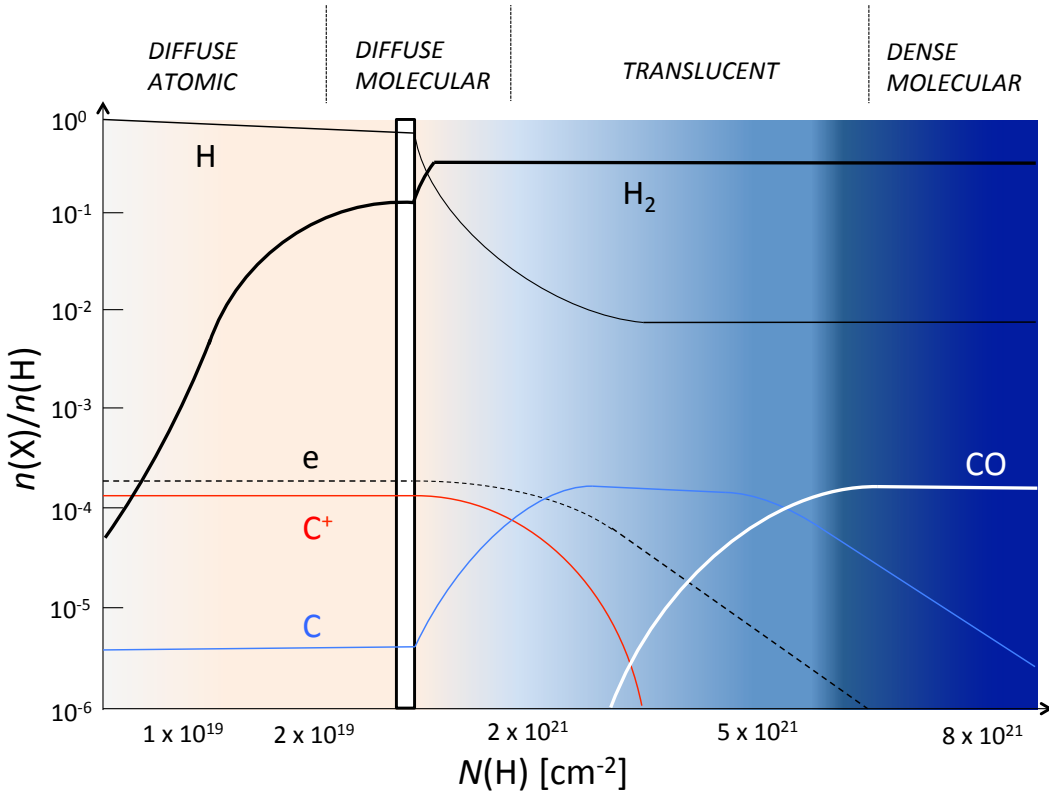

Figure 1.8: Structure of a PDR within the ionization front. The horizontal axis is the total column density of hydrogen nuclei, $N(\mathrm{H}) = N(\mathrm{H\,I}) + 2N(\mathrm{H_2})$. This is related to the visual extinction by $N(\mathrm{H}) \sim A_V \times 1.7 \times 10^{21}$ cm^{-2} mag^{-1}. The illustration is based on the classification of molecular clouds in Snow & McCall (2006).

clouds (Snow & McCall 2006). Apparently, there is ample evidence that diffuse molecular clouds hide much H_2 which is not traced with CO.

Photoionization and photodissociation rates of CO and CN are given for a variety of optical depths in table 1.2.

^{12}CO, ^{13}CO and C^{18}O

Emission lines of the three isotopic varieties of carbon monoxide, ^{12}CO, ^{13}CO, and C^{18}O are useful for studying the molecular clouds. Their intensity ratios can provide information about the physical conditions of the gas, especially if data of several rotational transitions are available. However, the intensities in diffuse molecular gas can be strongly affected by two main effects:

1. The transitions of rarer isotopic species ^{13}CO and C^{18}O have lower optical depths than ^{12}CO. This is because the ^{12}CO molecules are much more abundant ($[^{12}\mathrm{CO}]/[^{13}\mathrm{CO}] > 50$ in the solar neighborhood and lower in the inner parts of the Galaxy; in some regions, such as Ophiucus, UV observations indicate that the ratio is as high as 120; see Federman et al. 2003), and high number density implies higher values of the optical depth τ. In local thermodynamic equilibrium (LTE), the dependence on the temperature is weak, and $\tau_{12}/\tau_{13} \approx [^{12}\mathrm{CO}]/[^{13}\mathrm{CO}]$. On the other hand, low-τ transitions of C^{18}O are naturally the best probe of the densest regions, which are usually opaque in ^{12}CO and even in ^{13}CO lines sometimes.

2. Photodissociation is more severe for rare isotopic species because of their lower number density. ^{12}CO is readily self-shielded at extinctions of $A_V \gtrsim 0.2$, whereas this is not the case for ^{13}CO and C^{18}O. Therefore, in observations of distant sources (e.g., external galaxies) the beam filling factors for radio telescopes can be different between the three species.

Table 1.2: Photodissociation and photoionization rates (in s^{-1}) for CO and CN at different cloud depths.

Reaction	$A_V = 0$	0.5	1	3
$\mathrm{CO} + h\nu \rightarrow \mathrm{C} + \mathrm{O}$	2.6×10^{-10}			
$\mathrm{CN} + h\nu \rightarrow \mathrm{C} + \mathrm{N}$	1.1×10^{-9}	9.7×10^{-11}	7.0×10^{-12}	7.5×10^{-18}
$\mathrm{CO} + h\nu \rightarrow \mathrm{CO}^+ + e^-$	$I = 14.01$ eV			
$\mathrm{CN} + h\nu \rightarrow \mathrm{CN}^+ + e^-$	$I = 14.1$ eV			

Note. The column with $A_V = 0.5$ is given at the center of a slab of $A_V = 1.0$; columns with $A_V = 1$ and 3 are given at 10% and 30% through a slab with $A_V = 10$. At $A_V \gtrsim 0.2$, CO is efficiently shielded by H_2 and by itself (self-shielding). See Draine (2011).

1.3.3 Optical depth and critical density of CO (1-0)

In radiative transfer, the absorption coefficient for the CO (1-0) transition can be expressed as (see appendix C)

$$\alpha_{10} = \frac{c^2 n_0}{8\pi\nu^2}\frac{g_1}{g_0}A_{10}\left(1 - \frac{g_0 n_1}{g_1 n_0}\right)\phi_{10}, \tag{1.4}$$

where subscripts indicate $J = 0$ and $J = 1$ rotational quantum numbers and the frequency is $\nu = 115$ GHz. Assuming a Gaussian line profile ϕ, the absorption coefficient is

$$\alpha_{10} = \frac{n_0 \lambda^2}{8\pi} \frac{g_1}{g_0} A_{10} \left(1 - \frac{g_0 n_1}{g_1 n_0}\right) \frac{1}{\sqrt{2\pi}} \frac{\lambda}{\sigma} \mathrm{e}^{-(\Delta v)^2/2\sigma^2}. \tag{1.5}$$

The line-center optical depth ($\Delta v = 0$) for a cloud of radius R from the center to the edge is

$$\tau_{10} = \alpha_{10} R = \frac{n_0 \lambda^3}{8\pi^{3/2} b} \frac{g_1}{g_0} A_{10} \left(1 - \frac{g_0 n_1}{g_1 n_0}\right) R, \tag{1.6}$$

where $b = \sigma\sqrt{2}$. Following Draine (2011), this can be rewritten as

$$\tau_{10} = 281 \frac{n}{10^3} \frac{R}{10^{19}} \left(\frac{n_{\mathrm{CO}}/n_{\mathrm{H}}}{7 \times 10^{-5}}\right) \left(\frac{n_0}{n_{\mathrm{CO}}}\right) \left(\frac{2 \text{ km s}^{-1}}{b}\right) \left(1 - \frac{n_1 g_0}{n_0 g_1}\right). \tag{1.7}$$

Here, R is the size of a diffuse molecular cloud. Introducing an appropriate partition function Z, the optical depth can be derived from [see section 19.3 of Draine (2011)]

$$\frac{n_{\mathrm{CO},J}}{n_{\mathrm{CO}}} = \frac{1}{Z}(2J+1)\mathrm{e}^{-B_0 J(J+1)/kT_{\mathrm{ex}}} = \frac{(2J+1)\mathrm{e}^{-B_0 J(J+1)/kT_{\mathrm{ex}}}}{\sum_J (2J+1)\mathrm{e}^{-B_0 J(J+1)/kT_{\mathrm{ex}}}}, \tag{1.8}$$

where the summation is over all J-levels, and B_0 is the rotational constant for CO. The optical depth becomes

$$\tau_{10} \approx 281 \frac{n}{10^3} \frac{R}{10^{19}} \left(\frac{n_{\mathrm{CO}}/n_{\mathrm{H}}}{7 \times 10^{-5}}\right) \left[\frac{1 - \mathrm{e}^{-5.53 \text{ K}/T_{\mathrm{ex}}}}{[1 + (T_{\mathrm{ex}}/2.77 \text{ K})^2]^{1/2}}\right] \left(\frac{2 \text{ km s}^{-1}}{b}\right) \tag{1.9}$$

for $Z \approx \sqrt{1 + (kT_{\mathrm{ex}}/B_0)^2}$. Then,

$$\tau_{10} \approx 46 \frac{n}{10^3} \frac{R}{10^{19}} \left(\frac{n_{\mathrm{CO}}/n_{\mathrm{H}}}{7 \times 10^{-5}}\right) \left(\frac{2 \text{ km s}^{-1}}{b}\right), \tag{1.10}$$

where the excitation (rotation) temperature $T_{\mathrm{ex}} \approx 8$ K was assumed. Inserting typical values in this equation, CO emission appears to be optically thick in ordinary Galactic molecular clouds. Note that accurate estimates of density, cloud size, CO/H abundance and line width are necessary to calculate τ.

The critical density for CO ($J = 1$) is defined as the density at which collisional deexcitation of the level $J = 1$ is equal to its radiative deexcitation. Ignoring stimulated emission, this can be expressed as

$$n_{\mathrm{cr}}(1) \equiv \frac{\langle \beta_{10} \rangle A_{10}}{k_{10}}, \tag{1.11}$$

where $\langle \beta_{10} \rangle$ is the photon escape probability, and k_{10} is the collisional rate coefficient. Inserting the same parameters from above, with $\langle \beta_{10} \rangle \approx 1(1 + 0.5\tau_{10}) \approx 0.04$, and $k_{10} \approx 6 \times 10^{-11} (T/10^2)^{-0.2}$ cm^3 s^{-1} from Draine (2011), we get

$$n_{\mathrm{cr}}(1) \approx 50 \left(\frac{T}{10^2}\right)^{-0.2} [\mathrm{cm}^{-3}]. \tag{1.12}$$

Apparently, $J = 1$ level of CO is thermalized already at densities of $\gtrsim 10^2$ cm^{-3}. Molecular clouds in general have densities $n \sim 10^3 - 10^5$ cm^{-3}, hence this level is expected to be thermalized in most astrophysical situations.

Chapter 2

Fundamentals of radio interferometry

2.1 Interferometer response and visibility

Groundbreaking advances in radio interferometry were made in 1950's when Martin Ryle developed aperture synthesis (Ryle shared the Nobel prize in physics with Antony Hewish in 1974, which was the first in astronomical research!) In this section we derive the most fundamental observable in radio interferometry - the complex visibility and its relation to the source intensity.

Geometric representation of a two-element interferometer is shown in figure 2.1. Here, two antennas (antenna 1 and 2) are pointed toward a reference point which is defined by the unit vector $\mathbf{s}_0$, with magnitude $|\mathbf{s}_0| = 1$. The direction to an arbitrary position is $\mathbf{s}$, and the position is defined with respect to the reference as $\sigma = \mathbf{s} - \mathbf{s}_0$. Assuming that the source is at a distance much farther than the distance between the antennas (far-field approximation), electromagnetic waves approach antenna 2 after a time delay

$$\tau = D \sin\theta / c, \tag{2.1}$$

where D is the distance between the antennas. The signals at antennas 1 and 2 induce voltages ($V_1 = V \sin(\omega t)$ and $V_2 = V \sin[\omega(t-\tau)]$), which are multiplied and averaged in the correlator to give the following cosine response:

$$\langle V_1 V_2 \rangle \propto F = \cos(\omega\tau) = \cos\left(\frac{\omega}{\nu}\mathbf{D}_\lambda \cdot \mathbf{s}\right) = \cos\left(2\pi \mathbf{D}_\lambda \cdot \mathbf{s}\right). \tag{2.2}$$

Here, F is the *fringe function*, and $\mathbf{D}_\lambda$ is called the *baseline*, which is the vector pointing from one antenna to another. If the number of antennas is larger than two, or they change positions, then more than one baseline can be defined. The subscript λ means that the baseline is expressed in wavelength units $|\mathbf{D}_\lambda| = D/\lambda$. Thus,

$$\mathbf{D}_\lambda \cdot \mathbf{s} = \frac{D}{\lambda}\cos(90^0 - \theta) = \tau c \frac{1}{\lambda} = \tau\nu. \tag{2.3}$$

The total power received from the source within the solid angle $\mathrm{d}\Omega$ at $\mathbf{s}$ is

$$\mathrm{d}P = \frac{1}{2} A(\sigma)\, I(\sigma)\, \mathrm{d}\nu\, \mathrm{d}\Omega \ [\mathrm{W}]. \tag{2.4}$$

Here, 1/2 is included because the antenna responds to one half of the power in the randomly polarized wave, $A(\sigma)$ is the effective collecting area of a single-dish telescope (reception pattern of a single element), $I(\sigma)$ the specific intensity (brightness) [W m^{-2} Hz^{-1} sr^{-1}], $\mathrm{d}\nu$ the bandwidth of the receiving system. The response of the system is

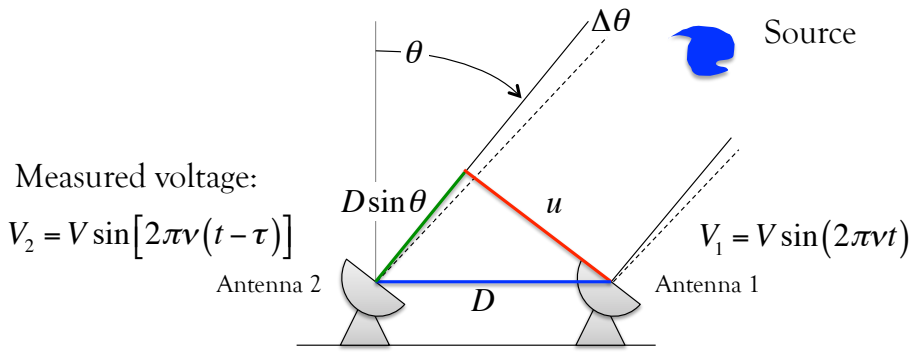

Instrumental response:

$$\left\langle V_1 V_2 \right\rangle \propto F = \cos\left(2\pi\nu\tau\right) = \cos\left(\frac{2\pi D\sin\theta}{\lambda}\right)$$

Fringe function

$$F = \cos\left(2\pi u l\right)$$

$$u = \frac{D\cos\theta}{\lambda}$$ *Spatial frequency*

$$l = \sin\left(\Delta\theta\right)$$ *Sky coordinate*

Figure 2.1: Basic geometry of a two-element interferometer in one dimension. The antennas are pointed toward $\mathbf{s_0}$ (phase reference position) defined as the nominal source position. Any other direction relative to the center is given by $\mathbf{s}$.

$$r(\mathbf{D}_\lambda, \mathbf{s}_0) = \Delta\nu \int_{4\pi} A(\sigma) I(\sigma) \cos[2\pi \mathbf{D}_\lambda \cdot (\mathbf{s}_0 + \sigma)] \, \mathrm{d}\Omega, \tag{2.5}$$

where the cosine term inside the integral is the fringe function. Let us rewrite the above equation as

$$r(\mathbf{D}_\lambda, \mathbf{s}_0) = \Delta\nu \int_{4\pi} A(\sigma) I(\sigma) \cos(2\pi \mathbf{D}_\lambda \cdot \mathbf{s}_0 + 2\pi \mathbf{D}_\lambda \cdot \sigma) \, \mathrm{d}\Omega. \tag{2.6}$$

By using

$$\cos(\alpha + \beta) = \cos\alpha\cos\beta - \sin\alpha\sin\beta, \tag{2.7}$$

the equation can be expressed as

$$r(\mathbf{D}_\lambda, \mathbf{s}_0) = \Delta\nu \int_{4\pi} A(\sigma) I(\sigma) \left[\cos(2\pi \mathbf{D}_\lambda \cdot \mathbf{s}_0)\cos(2\pi \mathbf{D}_\lambda \cdot \sigma) - \sin(2\pi \mathbf{D}_\lambda \cdot \mathbf{s}_0)\sin(2\pi \mathbf{D}_\lambda \cdot \mathbf{s}_0)\right] \mathrm{d}\Omega \tag{2.8}$$

and

$$r(\mathbf{D}_\lambda, \mathbf{s}_0) = \Delta\nu \cos(2\pi \mathbf{D}_\lambda \cdot \mathbf{s}_0) \int_{4\pi} A(\sigma) I(\sigma) \cos(2\pi \mathbf{D}_\lambda \cdot \sigma) \mathrm{d}\Omega \tag{2.9}$$

$$-\Delta\nu \sin(2\pi \mathbf{D}_\lambda \cdot \mathbf{s}_0) \int_{4\pi} A(\sigma) I(\sigma) \sin(2\pi \mathbf{D}_\lambda \cdot \sigma) \mathrm{d}\Omega.$$

This leads us to the concept of *complex visibility*, which was introduced in 1958 by Ronald Bracewell and others. The complex visibility is defined as

$$\mathscr{V} = r_c - ir_s = |\mathscr{V}|\mathrm{e}^{i\phi_v}, \tag{2.10}$$

where r_c and r_s are the cosine and sine responses from the equation above. The observed quantity is $\mathscr{V}$, which is the Fourier transform of the specific intensity I. Note that the visibility is expressed as a complex function because its amplitude and phase vary with the source intensity, structure, and antenna spacing. This is because the source intensity is in general neither symmetrical nor point-like. From Euler's formula, $\mathrm{e}^{\pm i\phi} = \cos\phi \pm i\sin\phi$, the visibility becomes

$$\mathscr{V} = |\mathscr{V}|e^{i\phi_v} = \int_{4\pi} A_n(\sigma)\, I(\sigma)\, \mathrm{e}^{-i2\pi\mathbf{D}_\lambda\cdot\sigma}\mathrm{d}\Omega, \tag{2.11}$$

where $A_n(\sigma) \equiv A(\sigma)/A_0$ is the normalized reception pattern (A_0 is the collective area normal to the source - antenna surface area). Let us now separate the real and imaginary parts of $\mathscr{V}$:

$$\mathscr{V} = \int A_n(\sigma)\, I(\sigma)\, [\cos(2\pi\mathbf{D}_\lambda\cdot\sigma) - i\sin(2\pi\mathbf{D}_\lambda\cdot\sigma)]\mathrm{d}\Omega. \tag{2.12}$$

The real and imaginary parts are, respectively,

$$\{\mathrm{Re}\} = \int A_n(\sigma)\, I(\sigma)\, \cos(2\pi\mathbf{D}_\lambda\cdot\sigma)\mathrm{d}\Omega = |\mathscr{V}|\cos\phi_v \tag{2.13}$$

and

$$\{\mathrm{Im}\} = \int A_n(\sigma)\, I(\sigma)\, \sin(2\pi\mathbf{D}_\lambda\cdot\sigma)\mathrm{d}\Omega = -|\mathscr{V}|\sin\phi_v. \tag{2.14}$$

The response is now

$$\begin{aligned} r(\mathbf{D}_\lambda,\mathbf{s}_0) = {} & \Delta\nu\cos(2\pi\mathbf{D}_\lambda\cdot\mathbf{s}_0)A_0\int A_n(\sigma)\, I(\sigma)\cos(2\pi\mathbf{D}_\lambda\cdot\sigma)\mathrm{d}\Omega \\ & -\Delta\nu\sin(2\pi\mathbf{D}_\lambda\cdot\mathbf{s}_0)A_0\int A_n(\sigma)\, I(\sigma)\sin(2\pi\mathbf{D}_\lambda\cdot\sigma)\mathrm{d}\Omega, \end{aligned} \tag{2.15}$$

or

$$\begin{aligned} r(\mathbf{D}_\lambda,\mathbf{s}_0) &= \Delta\nu\cos(2\pi\mathbf{D}_\lambda\cdot\mathbf{s}_0)A_0|\mathscr{V}|\cos\phi_v - \Delta\nu\sin(2\pi\mathbf{D}_\lambda\cdot\mathbf{s}_0)A_0(-|\mathscr{V}|\sin\phi_v) \\ &= \Delta\nu|\mathscr{V}|A_0[\sin(2\pi\mathbf{D}_\lambda\cdot\mathbf{s}_0)\sin\phi_v + \cos(2\pi\mathbf{D}_\lambda\cdot\mathbf{s}_0)\cos\phi_v]. \end{aligned} \tag{2.16}$$

By using

$$\begin{aligned} \sin\alpha\cos\beta + \cos\alpha\cos\beta &= \frac{1}{2}[\cos(\alpha-\beta) - \cos(\alpha+\beta)] + \frac{1}{2}[\cos(\alpha+\beta) + \cos(\alpha-\beta)] \\ &= \cos(\alpha-\beta), \end{aligned} \tag{2.17}$$

we can write

$$r(\mathbf{D}_\lambda,\mathbf{s}_0) = A_0\Delta\nu|\mathscr{V}|\cos(2\pi\mathbf{D}_\lambda\cdot\mathbf{s}_0 - \phi_v). \tag{2.18}$$

Note that the dimensions of visibility are the same as that of flux density: W m^{-2} Hz^{-1} equivalent to Jy = 10^{26} W m^{-2} Hz^{-1}. The flux density and brightness are related by

$$S_\nu \equiv \int_{\text{source}} I_\nu(\theta,\phi)\cos\alpha\, d\Omega, \tag{2.19}$$

where α is the angle of inclination between the intercepting area and the direction to the source.

Below are some properties of the complex visibility:

1. $\mathscr{V}$ is a function of the source structure and the interferometer baseline.
2. Observation of the source with known $\mathbf{D}_\lambda$ gives $\mathscr{V}$.
3. Modulus $|\mathscr{V}|$ and phase ϕ_v of the complex visibility are related to the amplitude and phase of the fringes. These, in turn, are related to the intensity and structure of the source, respectively.
4. $\mathscr{V}$ is a complex function and Hermitian: $\mathscr{V}(x,y) = \mathscr{V}^*(-x,-y)$.
5. Dimensions of $\mathscr{V}$ are the same as of the flux density S_ν [Jy].

We have seen that the response of an interferometer is proportional to $\cos(2\pi\mathbf{D}_\lambda \cdot \mathbf{s})$, i.e., to the baseline $\mathbf{D}_\lambda$. The cosine term is a *Fourier component*, hence interferometer imaging is *de facto* a process of collecting Fourier components of the visibility. As the Earth rotates, the collected components change because of the change in the angle θ and the sampling coverage draws arcs in the Fourier plane. Raw visibility data are further processed by deconvolving with a point spread function ("dirty beam") to restore the brightness (specific intensity) distribution. The relations between visibility, geometry, and brightness are discussed in the next section.

In this simple picture, it is obvious that the angular resolution and image fidelity of an interferometric map will depend on the number of antenna pairs, $N(N-1)/2$, because an interferometer consists of at least two elements whose data are cross-correlated, and the range of baselines $\mathbf{D}_\lambda$ (see figure 2.2). Arrays with a high dynamic range (difference between the shortest and longest baselines) sample the sky brightness in greater detail than those with a low range. However, all interferometers suffer from one intrinsic limitation: since the shortest baseline is larger than the diameter of a single antenna (and usually at least several times larger to avoid shadowing), there are no sampled Fourier components that correspond to short spacing. This results in a central hole in the Fourier plane, and the total flux cannot be recovered. This problem is illustrated in figure 2.3. We will see below that the missing-flux problem was solved in this work by combining interferometer and single-dish data.

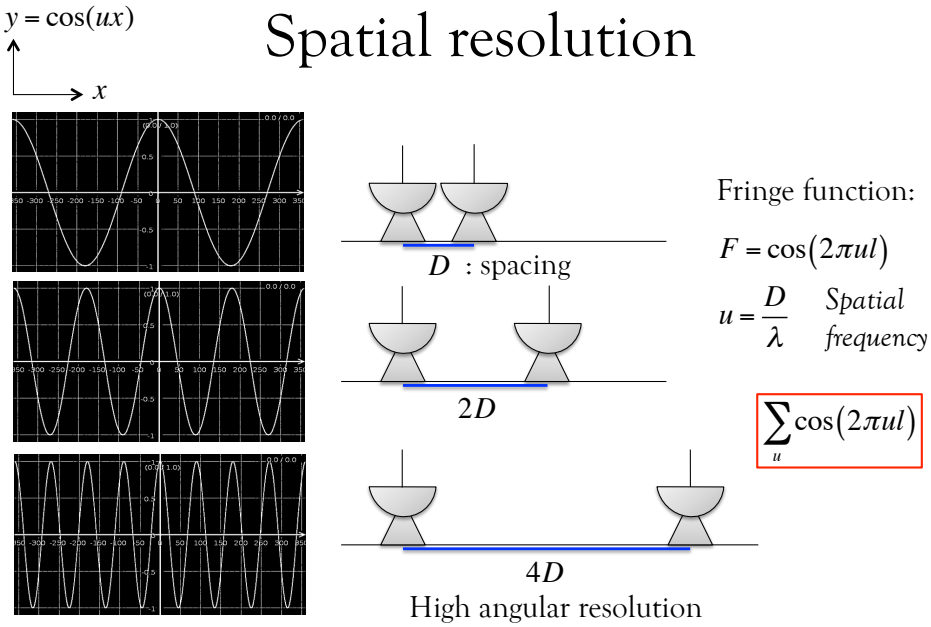

Figure 2.2: Angular resolution of an interferometer as a function of antenna spacing. For simplicity, the fringe function is defined as $F = \cos(2\pi ul)$, where $u = D/\lambda$ and $l = \sin\theta$, and the plotted functions are simply $y = \cos(ux)$. Larger antenna spacing increases the angular resolution. In the example, the primary beam attenuation which originates from the response of a single element is ignored.

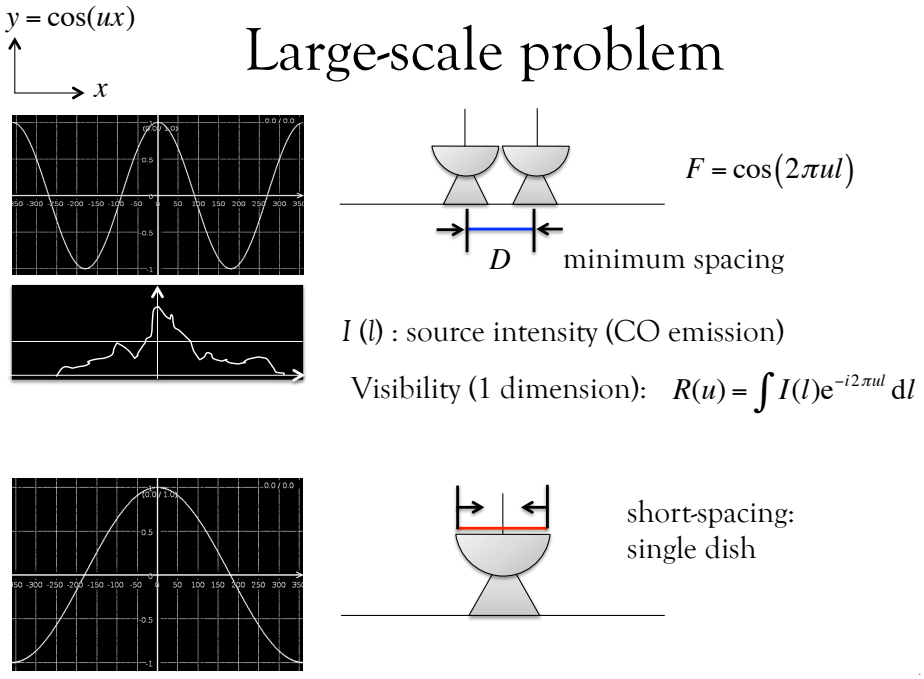

Figure 2.3: Antenna spacing and the largest angular scale visible to the interferometer. The instrument response is the convolution of the fringe function and the source intensity: $\cos(2\pi ul) * I(l)$. Bottom illustration shows that a single dish telescope has baselines which are not available in the interferometer, and hence can "see" the whole source $I(l)$.

2.1.1 Geometry and intensity

Geometry in interferometer observations can be specified by three spatial coordinates and three direction cosines (figure 2.4). The baseline $\mathbf{D}_\lambda$ is specified by (u,v,ω), and is generally not in the (u,v) plane except when $\omega = 0$ as illustrated in figure 2.4. The direction cosines are:

$$l = \cos\alpha \tag{2.20}$$
$$m = \cos\beta \tag{2.21}$$
$$n = \cos\gamma \tag{2.22}$$

Vector $\mathbf{s}$ is a unit vector, hence

$$l^2 + m^2 + n^2 = 1, \tag{2.23}$$

or

$$n = \sqrt{1 - l^2 - m^2}. \tag{2.24}$$

Also,

$$\mathbf{D}_\lambda \cdot \mathbf{s}_0 = (u,v,\omega)\cdot(0,0,1) = \omega \tag{2.25}$$

and

$$\mathbf{D}_\lambda \cdot \mathbf{s} = (u,v,\omega)\cdot(l,m,n) = ul + vm + \omega n = ul + vm + \omega\sqrt{1 - l^2 - m^2}. \tag{2.26}$$

In spherical coordinates, we can express l and m as

$$\sin^2\theta = l^2 + m^2 \tag{2.27}$$
$$\tan\phi = \frac{m}{l},$$

or

$$\theta = \arcsin\sqrt{l^2 + m^2} \tag{2.28}$$
$$\phi = \arctan\left(\frac{m}{l}\right).$$

Our task is to obtain the transformation $\Omega(\theta,\phi) \to \Omega(l,m)$. Firstly,

$$\mathrm{d}\Omega = \sin\theta\,\mathrm{d}\theta\,\mathrm{d}\phi \tag{2.29}$$
$$\sin\theta = \sqrt{l^2 + m^2}.$$

The appropriate Jacobian determinant for coordinate transformation is

$$\mathscr{J} \equiv \left|\frac{\partial(\theta,\phi)}{\partial l,m}\right| = \begin{pmatrix} \frac{\partial\theta}{\partial l} & \frac{\partial\theta}{\partial m} \\ \frac{\partial\phi}{\partial l} & \frac{\partial\phi}{\partial m}. \end{pmatrix} \tag{2.30}$$

Calculating

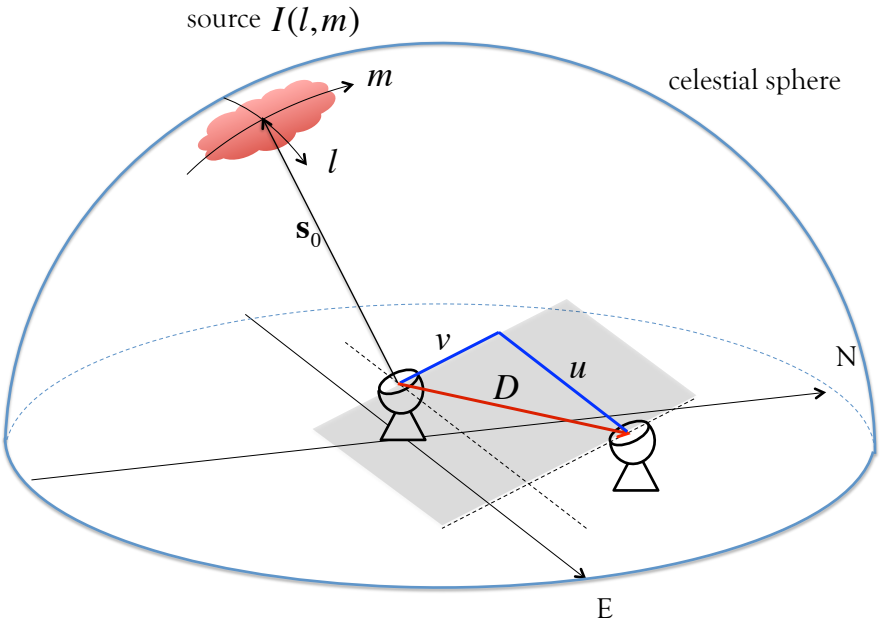

Figure 2.4: Geometry of the (u,v) plane of a 2-element interferometer. The u and v are equivalent to west-east and south-north, respectively, but they are in the plane normal to the reference direction $\mathbf{s_0}$. The baseline D points from one antenna to the other.

$$\frac{\mathrm{d}}{\mathrm{d}x}(\arcsin x) = \frac{1}{\sqrt{1-x^2}} \tag{2.31}$$
$$\frac{\mathrm{d}}{\mathrm{d}x}(\arctan x) = \frac{1}{1+x^2},$$

we obtain

$$\frac{\partial\theta}{\partial l} = \frac{1}{\sqrt{1-l^2-m^2}}\frac{1}{2}(l^2+m^2)^{-1/2}2l = \frac{l}{\sqrt{1-l^2-m^2}\sqrt{l^2+m^2}} \tag{2.32}$$
$$\frac{\partial\theta}{\partial m} = \frac{m}{\sqrt{1-l^2-m^2}\sqrt{l^2+m^2}}$$
$$\frac{\partial\phi}{\partial l} = \frac{1}{1+m^2/l^2}(-1)l^{-2}m = -\frac{m}{l^2+m^2}$$
$$\frac{\partial\phi}{\partial m} = \frac{l}{l(1+m^2/l^2)}.$$

Calculation of the Jacobian $\mathscr{J}$ leads to

$$\mathscr{J} = \frac{1}{\sqrt{(l^2+m^2)(1-l^2-m-2)}} \tag{2.33}$$

and

$$\mathrm{d}\Omega = \sqrt{l^2+m^2}\,\mathscr{J}\,\mathrm{d}l\,\mathrm{d}m = \frac{\mathrm{d}l\,\mathrm{d}m}{\sqrt{1-l^2-m^2}}. \tag{2.34}$$

Thus dΩ can be expressed

$$\mathrm{d}\Omega = \frac{\mathrm{d}l\,\mathrm{d}m}{n}. \tag{2.35}$$

2.1.2 Visibility-intensity relation

Let us rewrite the baseline vector as

$$\begin{gathered}\mathbf{D}_\lambda \cdot \mathbf{s} = \mathbf{D}_\lambda \cdot (\mathbf{s}_0 + \sigma) = \mathbf{D}_\lambda \cdot \mathbf{s}_0 + \mathbf{D}_\lambda \cdot \sigma \\ \mathbf{D}_\lambda \cdot \sigma = \mathbf{D}_\lambda \cdot \mathbf{s} - \mathbf{D}_\lambda \cdot \mathbf{s}_0.\end{gathered} \tag{2.36}$$

The complex visibility can now be written as

$$\begin{aligned}\mathscr{V}(u,v,\omega) &= \iint A_n(l,m)\, I(l,m)\, \mathrm{e}^{-i2\pi(\mathbf{D}_\lambda\cdot\mathbf{s}-\mathbf{D}_\lambda\cdot\mathbf{s}_0)} \frac{\mathrm{d}l\,\mathrm{d}m}{\sqrt{1-l^2-m^2}} \\ &= \iint A_n(l,m)\, I(l,m)\, \mathrm{e}^{-i2\pi[ul+vm+\omega(\sqrt{1-l^2-m^2}-1)]} \frac{\mathrm{d}l\,\mathrm{d}m}{\sqrt{1-l^2-m^2}}.\end{aligned} \tag{2.37}$$

Apparently, this is *not* a 3-dimensional Fourier transform because of the square-root term in the exponential. If we could drop the dependence on ω, we would obtain a 2-dimensional Fourier transform. The solution can be obtained by considering two approximations:

a) The baseline vector $\mathbf{D}_\lambda$ lies in the uv-plane and $\mathbf{D}_\lambda = (u,v,0)$. Then,

$$\mathscr{V}(u,v) = \iint \frac{A_n(l,m)\, I(l,m)}{\sqrt{1-l^2-m^2}} \mathrm{e}^{-i2\pi(ul+vm)} \mathrm{d}l\,\mathrm{d}m. \tag{2.38}$$

However, because of the Earth's rotation, this is not possible.

b) Coordinate transformation in the "small-field". $\mathbf{D}_\lambda$ remains in $u'v'$-plane which is any plane parallel to the equator. In the small-field approximation, the source is small, and $l^2+m^2=0$. Then,

$$n = \cos\gamma = \sqrt{1-\sin^2\gamma} = \sqrt{1-\theta^2} \approx 1 - \frac{\theta^2}{2}. \tag{2.39}$$

The visibility becomes

$$\mathscr{V}(u,v,\omega) = \iint \frac{A_n(l,m)\, I(l,m)}{\sqrt{1-l^2-m^2}} \mathrm{e}^{-i2\pi\omega} \mathrm{e}^{-i2\pi(ul+vm-\omega\theta^2/2)} \mathrm{d}l\,\mathrm{d}m. \tag{2.40}$$

The equation further simplifies if we assume that

$$\omega\theta^2 << 1, \tag{2.41}$$

appropriate for extended interferometer configurations and low frequencies. Note that ω approaches $\mathbf{D}_\lambda$ when the source is near the horizon.

The visibility is now

$$\frac{\mathscr{V}(u,v,\omega)}{\mathrm{e}^{-i2\pi\omega}} = \mathscr{V}(u,v,\omega)\mathrm{e}^{i2\pi\omega} \equiv \mathscr{V}_0(u,v), \tag{2.42}$$

where $\mathscr{V}_0$ is a "modified visibility":

$$\mathscr{V}_0(u,v) = \iint \frac{A_n(l,m)\, I(l,m)}{\sqrt{1-l^2-m^2}} \mathrm{e}^{-i2\pi(ul+vm)} \mathrm{d}l\,\mathrm{d}m. \tag{2.43}$$

Finally, a 2-dimensional Fourier pair of $\mathscr{V}_0$ and I is obtained:

$$\frac{A_n(l,m)\,I(l,m)}{\sqrt{1-l^2-m^2}} = \iint \mathscr{V}_0(u,v)\mathrm{e}^{i2\pi(ul+vm)}\mathrm{d}u\,\mathrm{d}v. \tag{2.44}$$

This is a form of the van Cittert-Zernike theorem introduced in optics in 1930. Note, however, that this is only an approximation. In reality, visibilities are measured in three dimensions.

2.1.3 Visibility and the (u,v) plane

The following derivation is based on a more detailed text in Thompson, Moran, & Swenson (2004). In one dimension, the response of a single dish telescope can be expressed as

$$R(\theta) = \int \mathscr{A}(\theta'-\theta)I(\theta')\,\mathrm{d}\theta', \tag{2.45}$$

where $\mathscr{A}(\theta)$ is the effective collecting area (θ is measured from the peak), and $I(\theta')$ is the one-dimensional intensity (where θ' is measured from the nominal central position). By taking $A = \mathscr{A}(-\theta)$, this becomes a convolution

$$R(\theta) = \int A(\theta-\theta')I(\theta')\,\mathrm{d}\theta'. \tag{2.46}$$

In the case of an interferometer, the fringe component, $\cos(2\pi ul)$, and the bandwidth pattern F_{BW} must be added, and the response expressed in l defined above becomes

$$R(l) = \int \cos[2\pi u(l-l')]A(l')F_{\mathrm{BW}}(l')I(l')\mathrm{d}l', \tag{2.47}$$

or

$$R(l) = \cos(2\pi ul) * A(l)F_{\mathrm{BW}}(l)I(l). \tag{2.48}$$

This is a convolution of the fringe pattern and the modified intensity distribution. Using the convolution theorem of Fourier transform, which states that the convolution of two functions, f and g, and the product of their Fourier transforms, F and G, are a Fourier pair:

$$f * g \rightleftharpoons FG, \tag{2.49}$$

we can derive $r(u) \rightleftharpoons R(l)$. The fringe term becomes

$$\cos(2\pi u_0 l) \rightleftharpoons \frac{1}{2}\left[\delta(u+u_0)+\delta(u-u_0)\right], \tag{2.50}$$

and, because $I(l) \rightleftharpoons \mathscr{V}(u)$, the response in the u-direction is

$$r(u) = \frac{1}{2}\left[\delta(u+u_0)+\delta(u-u_0)\right]\mathscr{V}(u). \tag{2.51}$$

Thus, the instantaneous response of an interferometer consists of two delta functions at positions $+u_0$ and $-u_0$; in two dimensions, this corresponds to positive and negative values on the (u,v) plane (see figure 2.5). The negative values have no physical meaning, and appear only because we do not use cosine and sine, but exponential expressions in Fourier transforms.

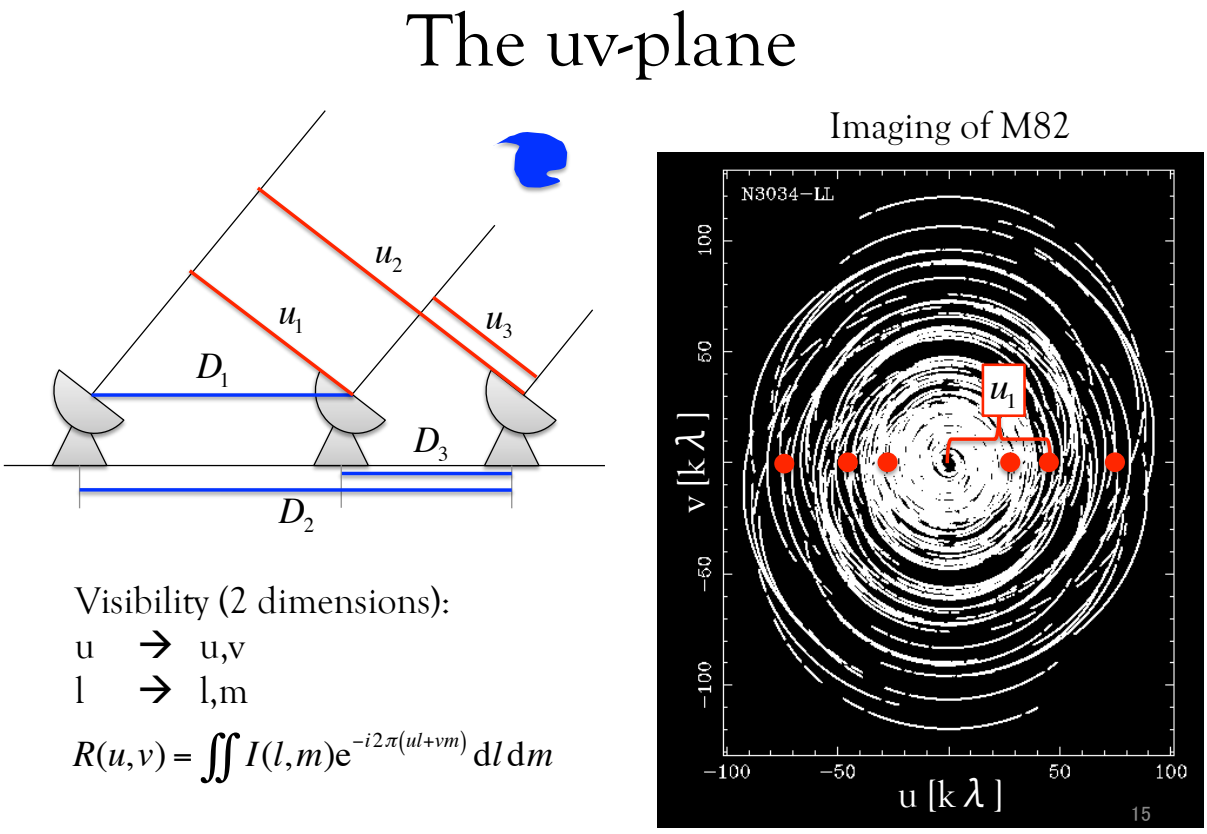

Figure 2.5: Two-dimensional imaging. The visibility is a 2-D Fourier transform of intensity. The amplitude of the visibility is related to the source intensity, and the phase is related to the source structure on the sky.

Chapter 3

Observations of M82 with NRO 45m

3.1 OTF mapping of CO (1-0)

First observations of M82 as part of this research were carried out in the on-the-fly (OTF) mapping mode with the 45-m telescope of the Nobeyama Radio Observatory (figure 3.1) in 2009 and 2010. These observations were first introduced in my master thesis in 2011, and more recently in Salak et al. (2013) with improvements in data reduction and analysis. In this section the observations are reviewed with emphasize on work done since 2011 that includes: 1) improvement of data reduction in 2012 by using a new method for the later publication; 2) the results from the newly created map related to the follow-up line-survey observations, as well as to a more detailed study of the molecular gas outflow; and 3) creating a new map of the CO (1-0) emission in M82 which was used to form a combined NRO-CARMA image of the central 2.5 kpc (section Combining NRO and CARMA data of M82).

3.1.1 Observations

The observations were carried out with the 25-Beam Array Receiver System (BEARS) in the OTF mode that allows large-scale mapping within reasonable telescope time. The total time allocated to our project was 60 hours, which spanned through 2009 and 2010. Differently from traditional position-switch radio-astronomical observations (e.g., see the next section), where observing is done toward fixed positions on the sky (from which a grid map would be created), OTF mapping is done by constantly driving the telescope across the observed object (on the fly, as its name suggests). The mapping area is scanned in two directions perpendicular to each other (X and Y) several times until the desirable sensitivity is achieved. In the final phase of data reduction, the X and Y maps are combined to correct for the "scanning effect". Basically, this effect is a consequence of unequal sensitivity in scan rows, and its correction as well as the process of combining FITS data of maps with perpendicular scans was developed by Emerson & Gräve (1988) as the "basket-weave method". For further reading: OTF mapping with radio telescopes of NAOJ (NRO 45 m and ASTE 10 m) was described in Sawada et al. (2008), whereas general information about OTF can be found, e.g., in Mangum et al. (2000) and Mangum et al. (2007). Details related to NRO can be found on the following web page: http://www.nro.nao.ac.jp/ nro45mrt/obs/otf/index-e.html.

3.1.2 Data reduction

The basic procedure of the data reduction of OTF data in NRO's reduction software NOSTAR was described in my master thesis. The main difference from the result published there and in Salak et al. (2013) is in the after-NOSTAR reduction. After carefully flagging the spectra to exclude bad

data, subtracting the baselines and combining the maps by applying the basket-weave method, the output product was a FITS data cube. In order to visualize the data, i.e., to create an image, we used several tasks of the Astronomical Image Processing System (AIPS) developed by the National Radio Astronomy Observatory (NRAO, USA). The tasks, in order of execution, were: FITLD (load the data), TRANS (create an image by arranging the data cube in the velocity - coordinates order of axes), XMOM (create moment maps) and KNTR (plot data images). Optionally, one may use the task XSUM to select a velocity (frequency) range in the step of creating an integrated intensity map.

The CO (1-0) spectra of M82 show a broad range of velocities from about 0 to 450 km s^{-1}. Being a nearly edge-on disk galaxy, the peak of the CO line drifts in velocity from one side of the map to the other. For that reason, setting a common velocity window to integrate the intensity over the entire map may lead to large uncertainties in the integrated intensity. This is especially the case in large OTF maps where, in addition to real varying of emission velocity, spatial baselines and baseline ripples produce artificial "bumps" that increase the uncertainty of integrated intensity.

To deal with the problem of noise, the integrated intensity was carefully measured in all pixels of the map. Each pixel was examined by measuring its r.m.s. noise, $T_{\rm mb}$ of the CO line peak (if present) and the integrated intensity $I_{\rm CO}$. This was done by using the software package Spectral Analysis Tool (SPLAT)[1], which can display the spectra of all the positions on the map directly from the image cube created in AIPS. Spectra where the signal was lower than 3σ in $T_{\rm mb}$ were not included in the map, i.e., the final map was masked at the low limit of 3σ. In the final phase of creating maps, the result was displayed by loading the measured data set into Interactive Data Language (IDL). Other analyses, such as measuring the intensity profiles and ratio maps were done in SAOImage DS9 developed by Smithsonian Astrophysical Observatory.

[1] http://star-www.dur.ac.uk/ pdraper/splat/splat-vo/.

3.2 The 3-mm line survey

3.2.1 Observations

The *3-mm line survey* refers to the follow-up observations of the molecular gas in M82 that took place between March 30 and April 13, 2013, at the Nobeyama Radio Observatory. We employed the 2SB receiver TZ1[2] onboard the 45-m telescope, in double polarization (TZ1H and TZ1V). The observing technique was position-switching between ON and OFF positions. The backend comprised the new digital spectrometer SAM45 with a maximum bandwidth of 32 GHz (16 arrays x 2) with the A/D converter PANDA. The broad band of the intermediate frequency (IF) from 4 to 8 GHz in combination with SAM45 capabilities allowed simultaneous observations of multiple frequencies using the spectrometer arrays, each observing a bandwidth of 2 GHz (effectively $\sim$ 1.6 GHz) with a spectral resolution of 488.281 kHz. The observing configuration is summarized in table 3.1. More on 2SB receivers designed primarily for ALMA can be found in Claude et al. (2000).

Figure 3.1: NRO 45-m telescope in March 2013.

TZ is a "heterodyne" receiver system, which means that the observed radio frequency is down-converted to a lower, intermediate frequency (IF) by using a superconductor-insulator-superconductor (SIS) tunnel junction device called mixer. This is convenient mainly because signal processing (e.g., amplifying, filtering, sampling and digitizing) is easier at lower frequencies, and because signal losses in transmission cables increase with frequency. The radio frequency (RF), $\nu_{\rm RF}$, is mixed with a frequency generated in the local oscillator (LO), $\nu_{\rm LO}$:

$$\nu_{\rm RF} = \nu_{\rm LO} \pm \nu_{\rm IF}. \tag{3.1}$$

[2]TZ1 refers to one beam of the two-beam receiver TZ, the other being TZ2, which were developed for ON-ON observations at NRO. In the season 2012/2013, the ON-ON technique was not yet implemented for open use, so we made standard ON-OFF observations with TZ1.

Table 3.1: Observing configuration of the spectrometer SAM45.

Spectral line	TZ1 H	TZ1 V	Sideband	ν [GHz]	$\nu_{\rm A}$ [GHz]
CS (2-1)	A7, A8	A3, A4	LSB	98.0	97.98097
^{13}CO (1-0)	A5, A6	A1, A2	USB	110.0	110.20135
C^{18}O (1-0)					
CN (1-0)	A9, A10	A1, A2	USB	114.231	113.341
CO (1-0)	A11, A12	A3, A4	USB	114.231	115.2712

Note. H and V denote horizontal and vertical polarizations to which TZ1 receiver is sensitive, A's denote arrays of the receiver, and USB and LSB denote upper sideband and lower sideband, respectively. The ν is the tracking frequency of the receiver system, while $\nu_{\rm A}$ is the central frequency of an array, set to the rest frequency of the spectral lines. The only exception is CN (1-0), for which $\nu_{\rm A}$ was set between two prominent hyperfine lines (see text).

Here, $\nu_{\rm IF}$ is the intermediate frequency. $\nu_{\rm LO}+\nu_{\rm IF}$ is the frequency of the upper sideband, and $\nu_{\rm LO}-\nu_{\rm IF}$ is the frequency of the lower sideband. Unwanted products are filtered out. For example, if the observed frequency is 115.271 GHz, in order to place it at $\nu_{\rm IF}=6$ GHz, one injects a LO frequency $\nu_{\rm LO}=109.271$ GHz. Observing systems usually contain more than one LO, subsequently at lower frequencies. The tuning range can be different for the receiver and for the LO; in the case of TZ, it is LSB: 78-104 GHz and USB: 90-120 GHz, but for the LO, it is 86-112 GHz. The IF in our observations was 6 GHz for CS (2-1) and ^{13}CO (1-0), ≈ 5 GHz for CN (1-0) and ≈ 7 GHz for CO (1-0). In the latter, the IF of the tracking frequency was 6 GHz, but the two lines were separated by ≈ 2 GHz.

3.2.2 Calibration

Chopper-wheel calibration of intensity

The intensity calibration was conducted by the standard chopper-wheel method (Ulich & Haas, 1976). The noise temperature that originates in the receiver itself ($T_{\rm rx}$) is usually measured by using hot and cold loads (absorbers), at the ambient temperature and at the temperature of liquid nitrogen (78 K). The output powers are, respectively,

$$P_{\rm hot}=kG(T_{\rm hot}+T_{\rm rx})\Delta\nu \tag{3.2}$$

and

$$P_{\rm cold}=kG(T_{\rm cold}+T_{\rm rx})\Delta\nu, \tag{3.3}$$

where k is the Boltzmann constant, G is gain, and $\Delta\nu$ is the frequency bandwidth. From here,

$$T_{\rm rx}=\frac{T_{\rm hot}-YT_{\rm cold}}{Y-1}, \tag{3.4}$$

where

$$Y\equiv\frac{P_{\rm hot}}{P_{\rm cold}}=\frac{T_{\rm hot}+T_{\rm rx}}{T_{\rm cold}+T_{\rm rx}} \tag{3.5}$$

is the Y-factor. Note that this measurement need not be done frequently.

In the first phase of the receiver tuning prior to observations, the chopper wheel was rotated rapidly to allow measurement of the output powers when the receiver was facing the sky and the absorber in turns with negligible influence of atmospheric fluctuations. Here, it is useful to define the system noise temperature.

The system noise temperature, $T_{\rm sys}$, is the sum of the receiver noise temperature, the antenna temperature (including the contribution from the antenna and its surroundings, the Earth's atmosphere and the source itself):

$$T_{\rm sys} = T_{\rm rx} + T_{\rm A}. \tag{3.6}$$

The system noise temperature was measured by comparing the output powers of the hot load and the sky. This is the so-called R-SKY calibration. When the hot load (absorber at ambient temperature) is in front of the receiver, the output power of the receiver is the relation for $P_{\rm hot} \equiv P_{\rm R}$. When the absorber is removed and the receiver is facing blank sky, the output power is

$$P_{\rm sky} = T_{\rm atm}\left(1-{\rm e}^{-\tau}\right)\eta + T_{\rm amb}\left(1-\eta\right) + T_{\rm rx}, \tag{3.7}$$

where τ is the optical depth of the atmosphere, $T_{\rm amb}$ is the ambient (room) temperature, and $\eta \equiv {\rm e}^{-\tau_{\rm ant}}$ is the ohmic loss of the antenna. In the following, it is assumed that $T_{\rm atm} = T_{\rm amb} = T_{\rm R}$. Then,

$$P_{\rm sky} = T_{\rm R}\left(1-{\rm e}^{-\tau}\right)\eta + T_{\rm R}\left(1-\eta\right) + T_{\rm rx} = T_{\rm R}\left(1-\eta{\rm e}^{-\tau}\right) + T_{\rm rx} \tag{3.8}$$

and

$$P_{\rm R} = T_{\rm R} + T_{\rm rx}. \tag{3.9}$$

The difference is

$$P_{\rm R} - P_{\rm sky} = T_{\rm R} - \left(1-\eta{\rm e}^{-\tau}\right)T_{\rm R} = \eta{\rm e}^{-\tau}T_{\rm R}. \tag{3.10}$$

If the system noise temperature is

$$T_{\rm sys} = \frac{P_{\rm sky}{\rm e}^{\tau}}{\eta}, \tag{3.11}$$

then

$$P_{\rm R} - P_{\rm sky} = \frac{P_{\rm sky}{\rm e}^{\tau}}{T_{\rm sys}}{\rm e}^{-\tau}T_{\rm R} = \frac{T_{\rm R}P_{\rm sky}}{T_{\rm sys}}, \tag{3.12}$$

and finally

$$T_{\rm sys} = \frac{P_{\rm sky}}{P_{\rm R}-P_{\rm sky}}T_{\rm R}. \tag{3.13}$$

After correcting for the atmospheric extinction and ohmic losses, the calibration yielded the antenna temperature $T_{\rm A}^{*} = T_{\rm A}{\rm e}^{\tau}/\eta$, which represents the signal from space. Note, however, that the results of the observations below will be expressed in the form of the main beam temperature, $T_{\rm mb}$, which was calculated from the available information of the main beam efficiency, as explained in the next chapter.

The R-SKY calibration was repeated after every 15 sequences of ON-OFF position-switching. The OFF position was chosen to be at $Az = +15'$ with respect to the ON position. One observing run repeated 60 sequences, which included calibrating 5 times (one before sequence 1, after sequences 15, 30, 45 and 60). The integration time at ON and OFF positions, as well as during R-SKY, was 15 s. In total, one observing run took about 55 minutes to complete.

Relative intensity of H and V

The absolute intensity of the receiver and the relative intensities of H and V were checked by observing a reference source in the center of M82. The source was the eastern peak of the nuclear ring, which showed bright emission in all lines: CO (1-0), ^{13}CO (1-0), CN (1-0), and CS (2-1). The absolute intensity was adopted as reference when the wind was weak, while pointing errors did not affect the relative intensity. The intensity difference between H and V during a single observing run, as well as day-to-day variation, was typically $\sim 10\%$. The absolute intensity uncertainty of the final spectra is estimated to be better than 20%.

Measurement of the image rejection ratio

TZ is a 2SB (sideband separating) receiver, which by definition, can observe upper and lower sidebands simultaneously with independent IF outputs. The separation of sidebands requires that the unwanted signal from the other sideband (the image) be suppressed. The performance of the receiver is dependent on the bias voltage of the SIS mixer chips, that can be tuned to achieve as low $T_{\rm sys}$ as possible with relatively high suppression of image signals. The ratio of the real and image signals is called the *image rejection ratio* (IRR), and the measurement of IRR was performed each day prior to observations. The measurement method for 2SB receivers on the 45-m telescope was explained in Nakajima et al. (2010).

The measured data were used to calculate the scaling factor (Kerr et al., 2001) by which the spectra were multiplied in order to calibrate the intensity. The integrated intensity in the signal band is

$$I_{\rm signal} = \frac{I_{\rm real}}{1+1/R}, \tag{3.14}$$

where $R = 10^{\rm IRR/10}$, i.e., IRR $= 10\log R$ [dB]. From here, the scaling factor is

$$f_{\rm IRR} \equiv \frac{I_{\rm real}}{I_{\rm signal}} = 1+\frac{1}{R} = 1+\frac{1}{10^{\rm IRR/10}}. \tag{3.15}$$

The factor was no larger than 1.1, hence the intensity loss was of the order $< 10\%$.

The achieved performance of the receiver was relatively good, with IRRs typically between 10 and 20 dB and negligible variation with time (see table 3.2). In USB & LSB observations of CS (2-1) and ^{13}CO (1-0), the tracking frequency was set to IF $= 6$ GHz, and the measurement was done for points 6.0 ± 0.5 GHz. In the case of USB observations of CN (1-0) and CO (1-0), data were taken for IFs from 5 to 7 GHz.

Reference pointing

The reference pointing was performed after each observing run, in regular intervals of about one hour. The reference source was R-UMa, a late-type star in the constellation of Ursa Major. The wind speed during observations was below 5 m s^{-1} with the pointing error typically $2''$ - $3''$. Observations of weak lines of ^{13}CO, CS and CN in the outflow were performed when the wind speed was < 3 m s^{-1}, and the pointing error was $\leq 1.5''$ which is $< 1/10$ of the telescope beam at these frequencies. The source intensity was typically $T_{\rm A}^* \approx 10$ K, observed in the 5-point cycle with an integration time of 7 s per position.

3.2.3 Data reduction

During the observations, data reduction was done in NRO's software NEWSTAR periodically to evaluate the so-far achieved results. The post-observation data reduction, whose results are presented

Table 3.2: Measurement of IRR [dB].

Date of obs.	CS (2-1)	^{13}CO (1-0)	CN (1-0)	CO (1-0)
2013/3/30				
3/31	18.7/9.8	13.1/11.6		
4/1	18.0/9.6	12.8/12.0		
4/2				
4/3			11/17	16/9
4/4	18.6/10.8	13.1/11.9		
4/5	14.5/16.6	15.8/13.0		
4/6				
4/7			12/18	17/9
4/8	18/10	13/12		
4/9				
4/10			12/17	17/9
4/11			12/17	17/9
4/12	18/10	12/12		
5/14	20/17	23/17		
5/15	19/19	23/19		
5/16	20/19	23/16		
5/17	20/20	23/17		

Note. Measurement data are expressed as H/V (polarization) in decibels. The decibel [dB] is a logarithmic unit defined as $10\log(P_2/P_1)$, where P_2/P_1 is the ratio of powers. IRR of 10 dB is equivalent to the power ratio of 10.

in this paper, was done in CASA (Common Astronomy Software Application) partially by using a python script which I had created for the purpose of these observations. Below, the adopted procedure to reduce the NRO 45-m telescope data in CASA is briefly explained.

Startup

CASA is initilized by executing the following command on the terminal:[3]

casa

or casapy

Note that in CASA version 4.0.1 which was used here, the startup automatically initilizes the tools necessary for single dish (hereafter SD) data called ASAP (ATNF Spectral Analysis Package, where ATNF stands for Australia Telescope National Facility). In older versions, one has to execute

asap_init

before starting single dish data reduction.

Preliminary data reduction: executing a python script

First step in every radio-astronomical data reduction is to exclude (or flag) unwanted data. Such data nearly always appear because of bad weather or some other cause of degrading data quality. In CASA, such action is taken on SD data by executing sdflag. The relevant options to set in the task are, e.g.,

```
infile='data1'
maskflag=[0,299],[3796,4095]
interactive=T
outfile='data1.f'
plotlevel=3
```

With this set of options the input data file is data1, all spectra will be flagged automatically from channel 0 to 299 and from 3795 to 4095 (the last one); the flagging will be done interactively with a number of spectra plotted at the same time. The user then clicks on spectra to flag them entirely, or can select a range of channels to make more specific target for flagging. The output file is named data1.f, where the extension .f is arbitrary.

The next step is to fit and subtract the baselines. In the flag step we have excluded bad-looking spectra, so the remaining spectra can be nicely fitted with a first-order polynomial function, i.e., a function of the form $y = ax + b$. (One can chose higher orders of polynomials too, but it usually need not be done.) The process is again interactive by making the following setup:

```
specunit='GHz'
masklist=[300,3795]
maskmode='interact'
blfunc='poly'
order=1
plotlevel=3
```

Here, we have selected that the fitting will be done only within channels no. 300 and 3795, in accordance with the selection during flagging. We can choose the x-axis to be expressed in units GHz, km/s or simply channel number.

In order to increase the speed of reducing large amount of data, I have prepared a simple Python script that contains several steps of the early processing the data. Those include: sdflag, sdbaseline, and automatic correction for IF numbers. The IF correction is necessary in order to combine the data from different polarization products in the averaging process. It can be done easily inside or outside

[3]CASA works on Linux and Mac machines. In this case I used Mac OS X 10.7.4 and nearly all operations were carried out on the terminal.

CASA in the application browsetable, where "IFNO" is the IF number. Note that, although a script was used, the process was basically interactive. The script only speeds up progress because there is no need to input the parameters from one data to another. Human action is reduced to interactive flagging and selecting regions to fit the baselines. And lastly, the IF correction is completely automatic.

Coadding, averaging and scaling

Various data from different observing dates can be gathered into one file by using the task sdcoadd. If there are three data sets with the same observing parameters, e.g., data1, data2, and data3, they can be marked for coadding:

infiles=['data1','data2','data3']
outfile='data123'

By doing this we create a single file data123 which contains the spectra from all three data sets. Next, we would like to average the data. It is done by using the task sdcal. Here, we must be careful to set the following options:

scanaverage=T
timeaverage=T
tweight='tsys'

Here, 'tsys' means that the averaging is weighted by $T_{\rm sys}^2$. Additionally, one may select specunit='km/s' in order to plot the data with velocity as the horizontal axis. By further specifying, e.g., restfreq='109.782176GHz', it is possible to choose the rest frequency for zero velocity (in this case the rest frequency of $C^{18}O$ (1-0) which was observed simultaneously with ^{13}CO (1-0)). If the data contain information about the LSR velocity, the final spectra will be given in rest radio velocity, i.e., zero velocity is set to the specified LSR velocity.

Finally, correcting for the loss due to image rejection in the 2SB receiver (IRRs) and for the main beam efficiency, we used the task sdscale to multiply the spectra with a scaling factor. The process is, e.g., simply

infile='data.ta'
factor=3.33
outfile='data.tmb'

Here, we have converted the data from $T_{\rm A}^*$ to $T_{\rm mb}$ by using a main beam efficiency of $\eta_{\rm mb} = 0.3$.

Output product

There is a number of ways to export the final data. The easiest way to do so is to make an ASCII table. We used the task sdsave and modified the options to become:

infile='data.tmb'
outfile='data.save'
outform='ASCII'

The output file is a text file which can be opened in any editor. The visualization and manipulation of the spectrum was done by using the software SPLAT-VO.

Chapter 4

Combining NRO 45-m and CARMA data of M82

Figure 4.1: Combined Array for Research in Millimeter-Wave Astronomy (CARMA). Image from: http://bima.astro.umd.edu.

4.1 CARMA observations of M82

The Combined Array for Research in Millimeter-Wave Astronomy (CARMA) is a world-class radio-astronomical interferometer for mm-wave observations, located in California, U.S.A. (figure 4.1). It is a heterogeneous array of 15 antennas, which were previously part of the Owens Valley Radio Observatory (OVRO) and Berkeley Illinois Maryland Association (BIMA) arrays. Out of 15 CARMA antennas, six belong to the 10-m array (10.4 m) while nine belong to the 6-m array (6.1 m). The total collecting area is 772 m^{-2}, with the highest angular resolution of $0.15''$ at 230 GHz in A-array (baselines 0.25-2 km). Larger number of antennas, N, compared to previous independent arrays has significantly improved the (u,v) coverage. The number of antenna pairs (baselines) is now

$$\frac{N(N-1)}{2} = 105. \tag{4.1}$$

The observations of M82 in configurations C and D took place in 2012 (see figure 4.2 for antenna positions). They were carried out by the "CANON" team (CARMA-Nobeyama Nearby Galaxies Survey; principal investigator: J. Koda). The final map is a mosaic of 19 pointings with three different baseline types involved: 6.1m-6.1m, 10.4m-10.4m, and 6.1m-10.4m. In the following subsection, I describe the data reduction of the combining and imaging part. The adopted symbols are similar to those in Koda et al. (2011).

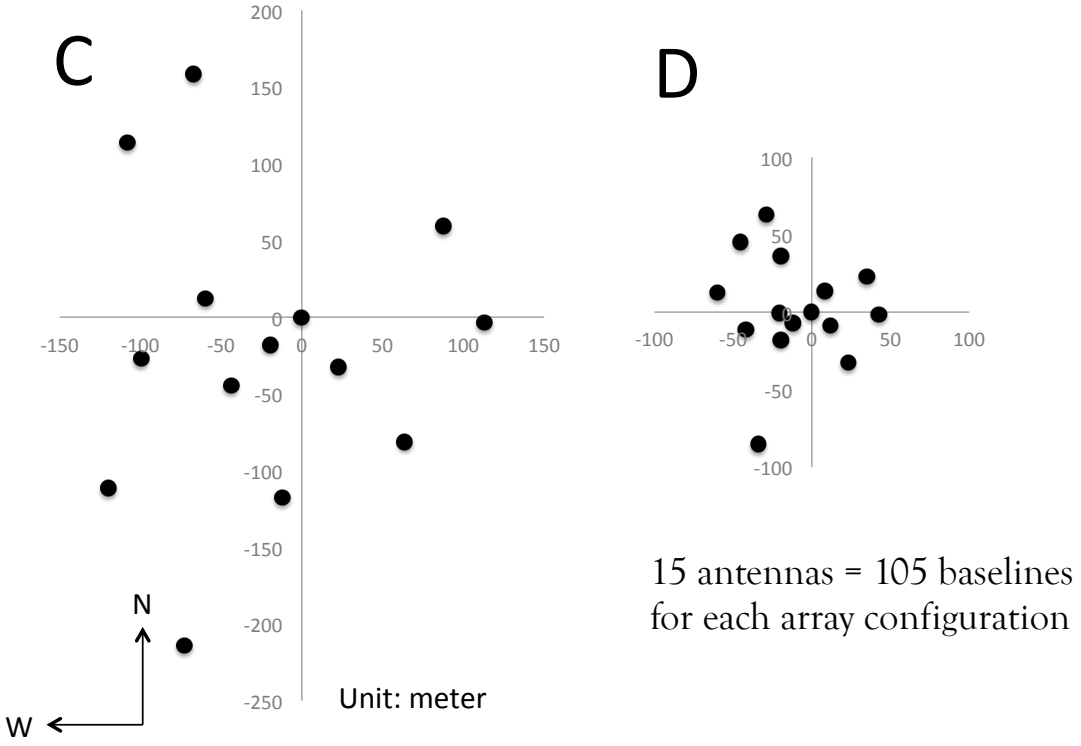

Figure 4.2: Antenna positions during CARMA observations of M82 in array configurations C and D.

4.1.1 Imaging with CARMA

Let us define an image obtained with an interferometer as

$$I(l,m) = \frac{\bar{I}(l,m)}{P(l,m)}. \tag{4.2}$$

Here, $\bar{I}(l,m)$ is the image uncorrected for the primary beam, and $P(l,m)$ is the primary beam. The coordinates are in the image domain (l,m). In the case of three types of baselines (e.g., in CARMA), this is

$$I(l,m) = \sum_{i=1}^{3} W_i \frac{\bar{I}_i}{P_i}, \tag{4.3}$$

where $i = 1,2,3$. W_i are the weights proportional to $[P_i(l,m)/\sigma]^2$, where σ is the noise level. The weights are normalized so that $W_1 + W_2 + W_3 = 1$.

Data processing of 19 pointings of M82, as illustrated in figure 4.3, leads to a joint image

$$I(l,m) = \sum_{i=1}^{3} \sum_{j=1}^{19} W_{i,j} I_{i,j}. \tag{4.4}$$

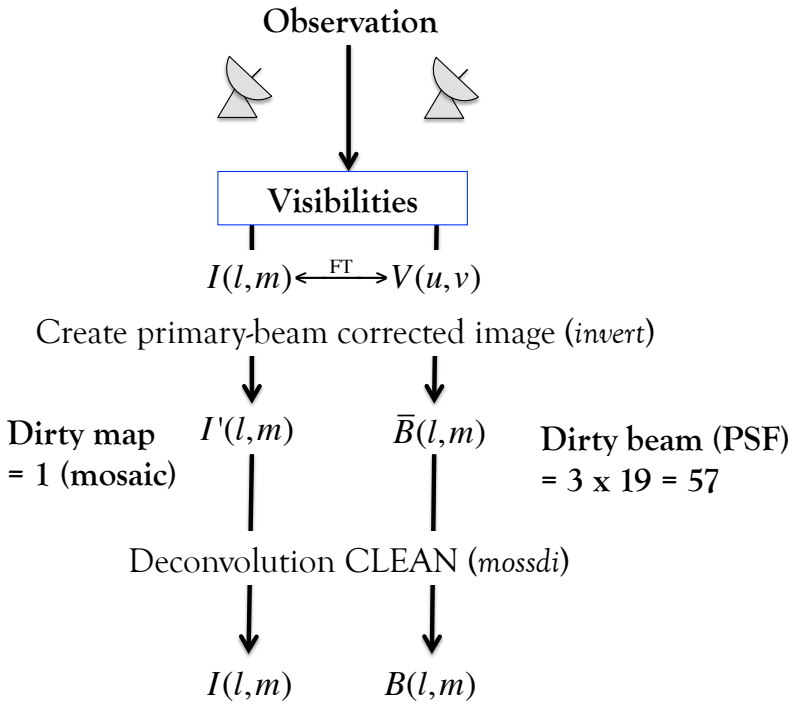

Figure 4.3: Imaging process with CARMA.

Note that the image is corrected for the primary beam already in the transformation process. There is only one dirty map, but 57 dirty beams corresponding to 3 baseline types multiplied by 19 pointings. The angular resolution is then determined by the weighted average:

$$B(l,m) = \sum_{i=1}^{3} W_i(l,m) \frac{\bar{B}_i(l-l_0, m-m_0)}{P_i(l,m)}. \tag{4.5}$$

In the case of a uniformly sampled (u,v) plane, a single synthesized beam can be adopted for the entire map. In general, the synthesized beam is different at each pointing because the (u,v) coverage is different.

4.2 Short-spacing visibilities

The (u,v) coverage of CARMA is much better than that of OVRO and BIMA, but, as with any other interferometer, zero-spacing information is not sampled with extended C and D configurations. In chapter 2 we saw that the visibility and intensity are related by the Fourier transform:

$$\mathscr{V}(u,v) = \iint I(l,m)\mathrm{e}^{-i2\pi(ul+vm)}\mathrm{d}l\,\mathrm{d}m. \tag{4.6}$$

However, the antennas are separated by a distance larger than their diameters, which means that the shortest spacing, where $(u,v) = (0,0)$ is missing. The zero-spacing data,

$$\mathscr{V}(0,0) = \iint I(l,m)\mathrm{d}l\,\mathrm{d}m, \tag{4.7}$$

contain information about the total flux, and therefore are essential to fully image extended sources.

In order to sample short-spacing baselines, CARMA can operate in a very compact configuration E (8-66 m), which is similar to the Atacama Compact Array of ALMA. But even then the *zero-spacing* information is incomplete because the antenna spacing is limited by the antenna diameter. The short-spacing correction can be made by combining interferometer and single-dish data, because sensitivity in the Fourier space is highest at the smallest values of (u,v). The size of the central hole in the (u,v) plane is $\propto D/\lambda$, where D is the antenna diameter and λ is the observed wavelength. In the case of CARMA, where $D \approx 10$ m, the hole is ~ 3800 which corresponds to $\sim 0.9'$. This sets a limit to imaging capabilities.

The sensitivity of the NRO 45-m telescope in the (u,v) plane is a function of the baseline coverage from 0 to 45 m. Since the beam of the telescope is a Gaussian, the response in the (u,v) plane is another Gaussian function. The sensitivity peaks at zero spacing and declines as a Gaussian toward the edge at 45 m. The standard deviation of this function is at 3.9 kλ, or 3.9×2.6 m $\simeq 10$ m for CO (1-0).

The OTF observations explained above were carried out at a fine sampling rate much higher than the Nyquist rate ($2v$) at every 0.1 s during observing runs. In order to avoid *aliasing*, the grid spacing in the final map must be carefully chosen. The final product of OTF data reduction is the sampled data distribution convolved with a spheroidal function. Although the telescope beam is $15''$, the final point spread function (PSF) depends on the grid spacing. This is determined by considering the spatial sampling rate. In the case of the 45-m telescope, the telescope resolution is proportional to λ/D. The Nyquist rate is achieved if the sampling is better or equal to $(1/2)\lambda/D$, i.e., $5.96''$ in the case of the 45-m telescope and CO (1-0). Hence, the grid spacing was set to this value, and the resulting angular resolution of the OTF map prior to combining was $19.7''$. These concepts are illustrated in figure 4.4.

In this work, observations were carried out in configurations C and D. In configuration C, the array baselines are between 30 and 350 m, and in configuration D, they are between 11 and 150 m. The projected baseline in our observations of M82 was of the order 10 m. As shown in figures 4.5 and 4.7, this is well matched to the visibility data of NRO 45m.

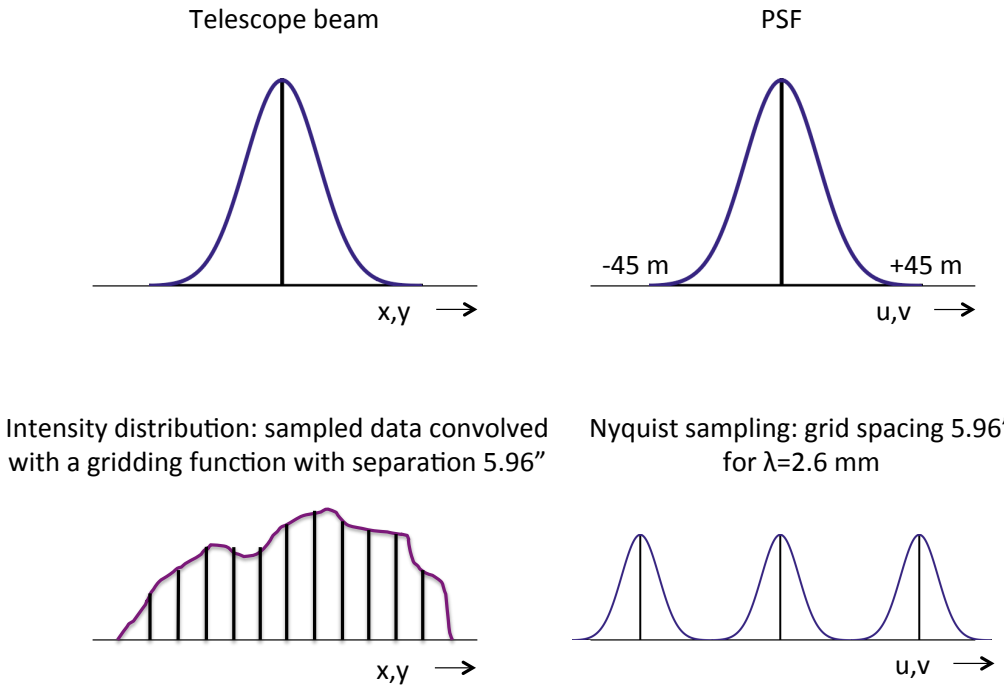

Figure 4.4: Nyquist sampling in OTF mapping with the 45-m telescope. See also Koda et al. (2011).

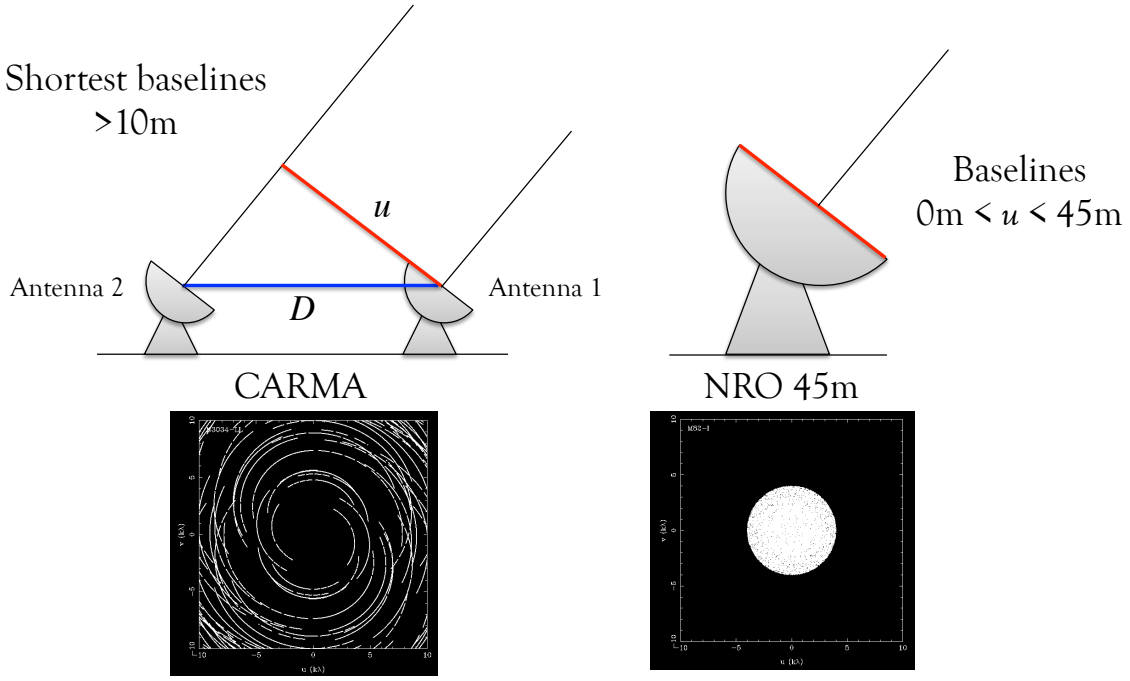

Figure 4.5: Comparison of CARMA and NRO 45m baselines. The NRO 45-m baselines were flagged at $(u,v) > 4$ kλ.

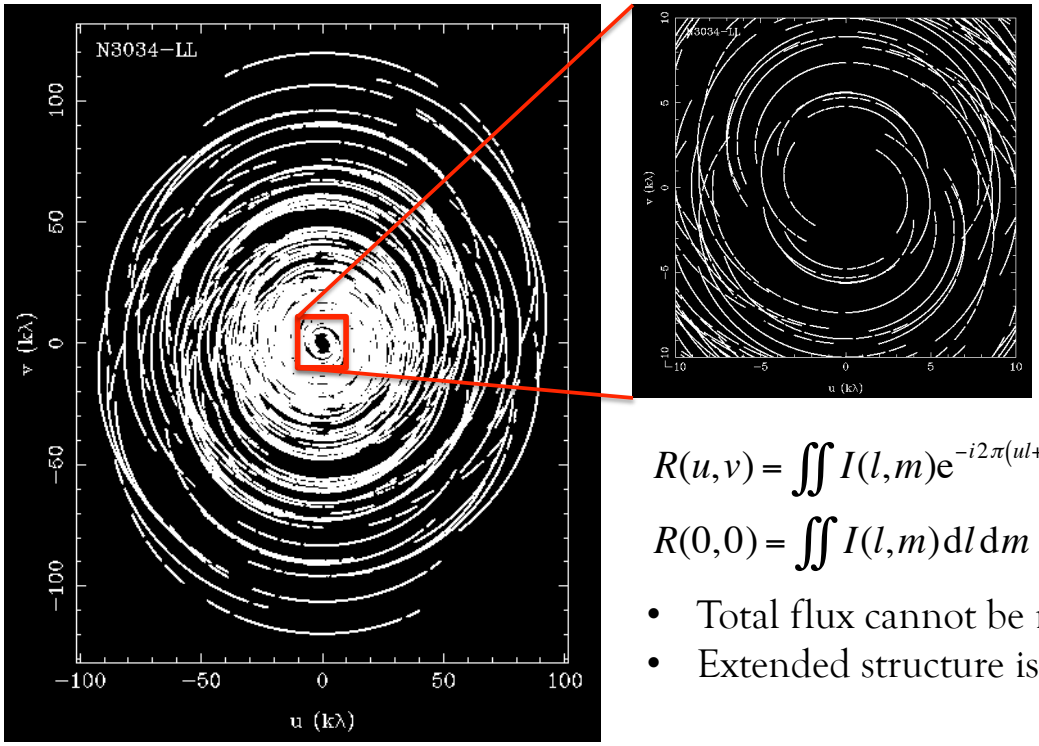

Figure 4.6: (u,v) coverage of the CARMA observations in configuration D and the problem of missing short-spacing information.

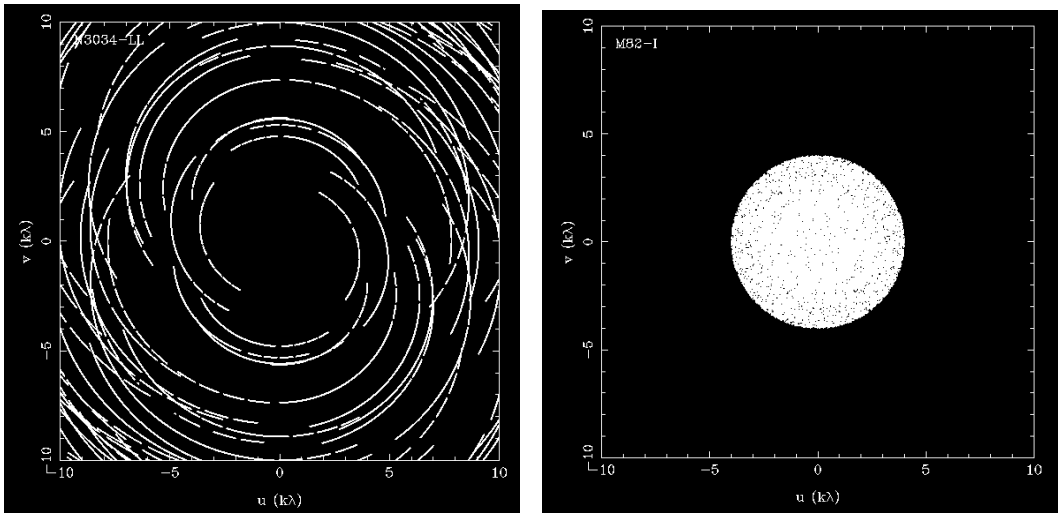

(a) (b)

Figure 4.7: a) Innermost region of the (u,v) coverage of the CARMA data. b) NRO (u,v) data after the baselines larger than 4 kλ were flagged.

4.3 CARMA and NRO 45m imaging

In this section, we explain the basic steps of combining CARMA and NRO data by using the reduction package MIRIAD. First, the CARMA and NRO data were calibrated and the output products are visibility data sets for both telescopes. Note that standard NRO 45m data reduction produces a data cube. The conversion to visibilities is based on the method described in Koda et al. (2011), and was carried out by the CANON team. The complete procedure of the reduction is shown in figure 4.8. The visibilities in CARMA observations were sampled uniformly as shown in figure 4.6.

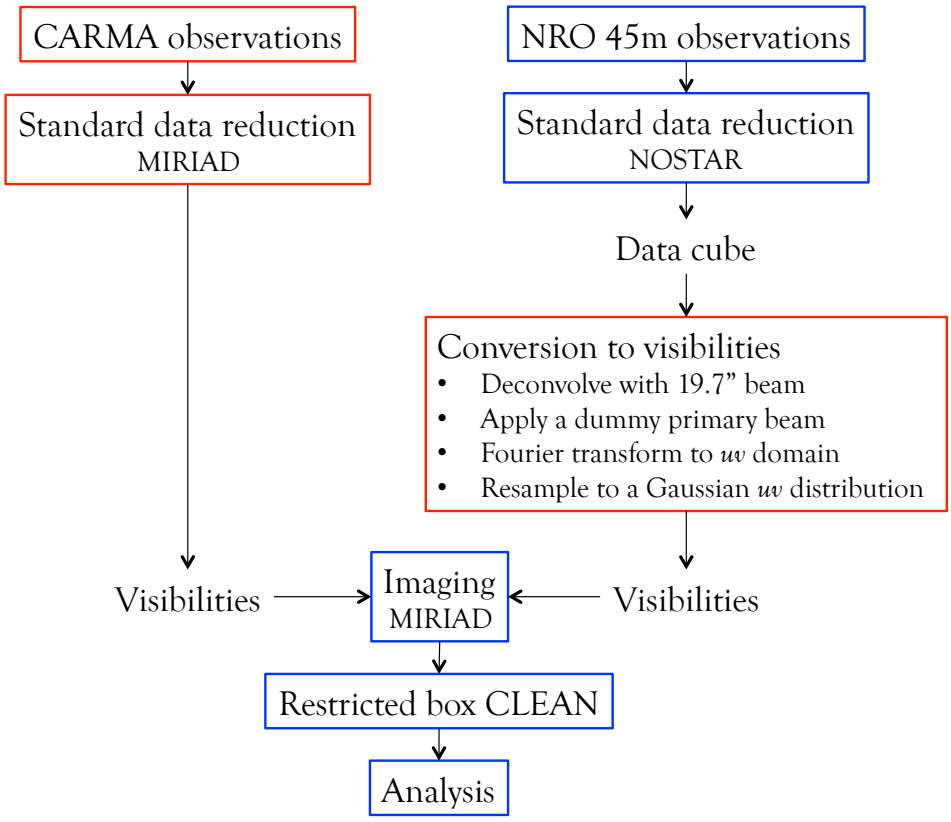

Figure 4.8: Data reduction flow. Blue and red rectangles indicate steps done by us and by the CANON team, respectively.

Invert, emission mask

Invert is a task used to create an image or map from multi-pointing visibility data, i.e., it transforms visibility data into one dirty map (combination of different baselines and antennas of CARMA) and a synthesized beam. In the present work, invert was executed with the following options:

invert vis=vis1,vis2,vis3,vis4,vis5,vis6,vis7nro map=dmap.dm beam=dbeam.bm imsize=513,513 cell=0.5,0.5 line=vel,45,-8.6,10.16,10.16 "select=source(N3034,M82)" slop=1 options=mosaic,systemp,double

Here, seven different visibility data sets were combined (six from CARMA mosaic observations and one from NRO 45m observations after converting to visibilities) by setting vis=vis1,...,vis7nro. A dirty map and 76 dirty beams[1] were created too, and the image size was set to $513'' \times 513''$ with

[1]The number of dirty beams = $3 \cdot 19 + 19 = 76$ because there were three baseline types for CARMA and one for NRO 45m.

a cell (pixel) size of 0.5″. In the line option, 45 velocity channels (45 planes of the data cube) were specified as starting from -8.6 km s^{-1} with a velocity bin of 10.16 km s^{-1}. The source taken into processing was M82 (labeled NGC 3034 in the CARMA data). slop=1 makes processing tolerant with poor-channel data (0 means rejecting spectra with at least one poor channel, while 1 means accepting spectra if at least one channel is good). Finally, we set mosaicking, weighting as inverse proportion to the noise variance, and the beam patterns to be twice the size of the output image. The output data sets are the dirty map (dmap.dm) and the dirty beam (dbeam.bm).

In the next step, we implemented the "restricted box CLEAN" method in order to suppress the sidelobes. The procedure is explained below. First, we make one sensitivity map and one gain map by executing

mossen in=dmap.dm sen=dmap.se gain=dmap.ga

Then, find the minimum value of the map intensity and cut the sensitivity map where the primary beam attenuation is only 1/3. To obtain the minimum value,

histo in=dmap.se region="image(1)"

The minimum value was 1.197937×10^{-2}. Next, make a mask map for emission that is defined as three times the minimum value:

maths exp=dmap.dm out=dmap.mk1 mask="((dmap.se/1.197937E-02/dmap.ga).lt.3.0)"

Note that lt is from "less than". After inspecting the emission-free channel maps by using DS9, it was judged that the flux density larger than 0.1 Jy beam^{-1} is strong detection ($\gtrsim 5\sigma$). We make a mask for emission:

maths exp=dmap.mk1 out=dmap.mk2 mask="dmap.mk1.gt.0.1"

Here, gt stands for "greater than". Finally, before applying CLEAN, we make a smoothed mask. First, replace blanked pixels in the image with arbitrary values (need to avoid unmasking; in this case from blanked to 0.0):

imblr in=dmap.mk2 out=dmap.mk3 value=0.0

and smooth:

smooth in=dmap.mk3 out=dmap.mk4 fwhm=10.0

After inspecting the results, we note a threshold and execute

maths exp=dmap.mk4 out=dmap.mk5 mask="dmap.mk4.gt.30"

where the threshold is set to count 30.

CLEAN

The task to run the CLEAN algorithm on our mosaic image is

mossdi2 map=dmap.dm beam=dbeam.bm out=map.cl "region=mask(dmap.mk5)" niters=20000 gain=0.1

To get the combined dirty beam,

mospsf beam=dbeam.bm out=beam.mb

Next, we fit the beam with a Gaussian:

imfit in=beam.mb object=gauss "region=relcen,boxes(-10,-10,10,10)"

and find that the beam size is major axis $= 4.000''$, minor axis $= 3.314''$, and the position angle P.A. $= -9.52^0$.

Finally, to restore the cleaned map:

restor model=map.cl map=dmap.dm beam=dbeam.bm out=map.mp fwhm=4.000,3.314 pa=-9.52

Before creating moment maps, we masked emission in each channel based on the channel maps of the NRO 45-m data cube (figure 5.3), thereby effectively removing the remaining artefacts that resembled the sidelobes. The masking procedure in MIRIAD is explained in Appendix H. The moment maps were created by executing

moment in=xmap.mp out=xmap.mom0 mom=0
Converting to FITS was done by executing
fits in=xmap.mom0 out=mapxM0.fits op=xyout
and likewise for moments 1 and 2.

4.3.1 The synthesized beam

Dirty beams of different baseline types

CARMA has three types of baselines because it is a heterogeneous array. The resulting dirty beams are displayed in figures 4.9 and 4.10. In principle, the beams are different at each pointing and in each array configuration (C or D). In the figures below, the total beam of each baseline type is shown (numbers 1, 2, 3 for CARMA baselines, and the first for NRO 45m, which is no. 58 because there are 57 combinations for CARMA) and the beams are the result of joint C+D output of the MIRIAD task INVERT. Inspection of all 76 beams (19×4) shows that they are nearly identical, which is supported by a symmetric appearance of the beams. Also, note that the NRO 45m beam is a Gaussian produced to represent the telescope beam of FWHM $= 19.7''$. Note that the Gaussian distribution of the 45-m visibilities and the PSF of the telescope beam are Fourier pairs (Fourier transform of a Gaussian is a Gaussian).

The combined synthesized beam

The synthesized beam in the resulting image is a combination of four baseline types as discussed above. During the deconvolution process in CLEAN, the true synthesized beam is replaced by a Gaussian convolution beam. In the combining procedure, the total fluxes were calculated for the 45-m data only and for the dirty image, with an unknown beam size. The beam size is determined by the condition that the fluxes are equal. The position angle is determined by fitting a Gaussian by using the MIRIAD task IMFIT. The synthesized beam of the combined image is shown in figure 4.11 (a). A smaller-scale image is shown in panel (b). The green line indicates the direction of the projection shown in panel (b) of figure 4.12. The combined synthesized beam has the size of $4.0'' \times 3.3''$ and P.A. $= -9.5^0$.

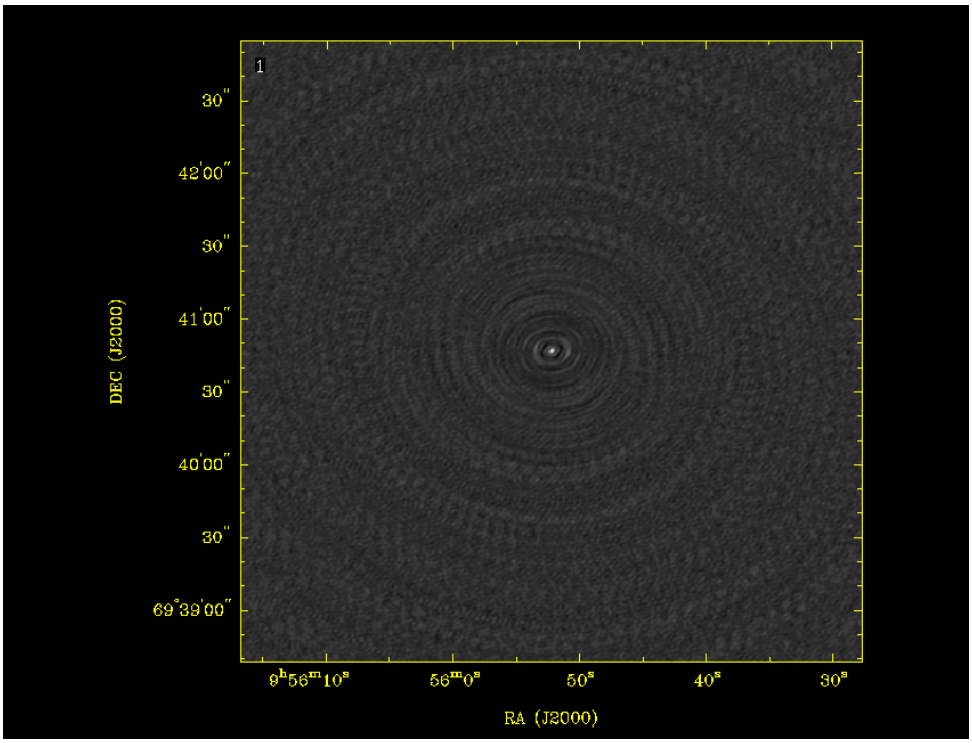

(a)

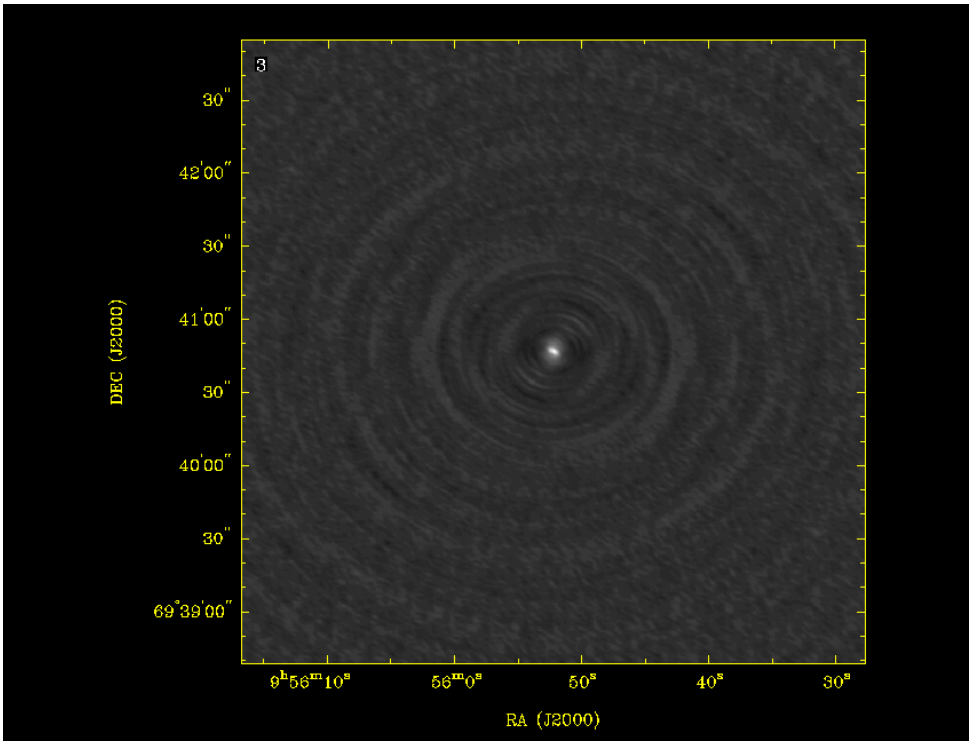

(b)

Figure 4.9: Synthesized beam of baseline types: a) 10-m antennas, b) 6-m antennas.

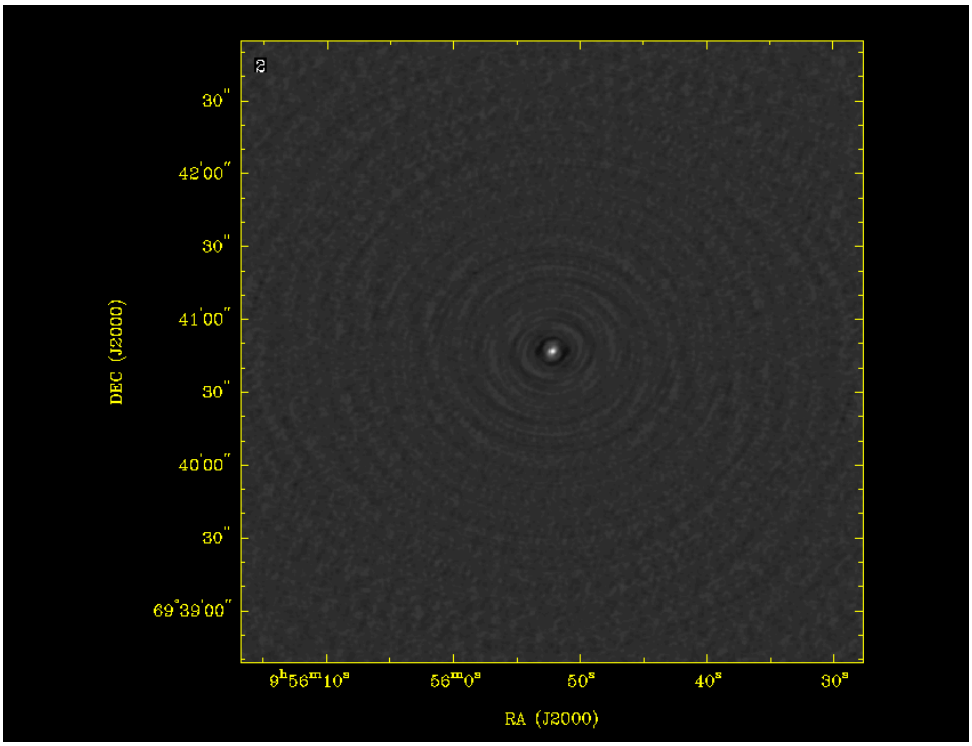

(a)

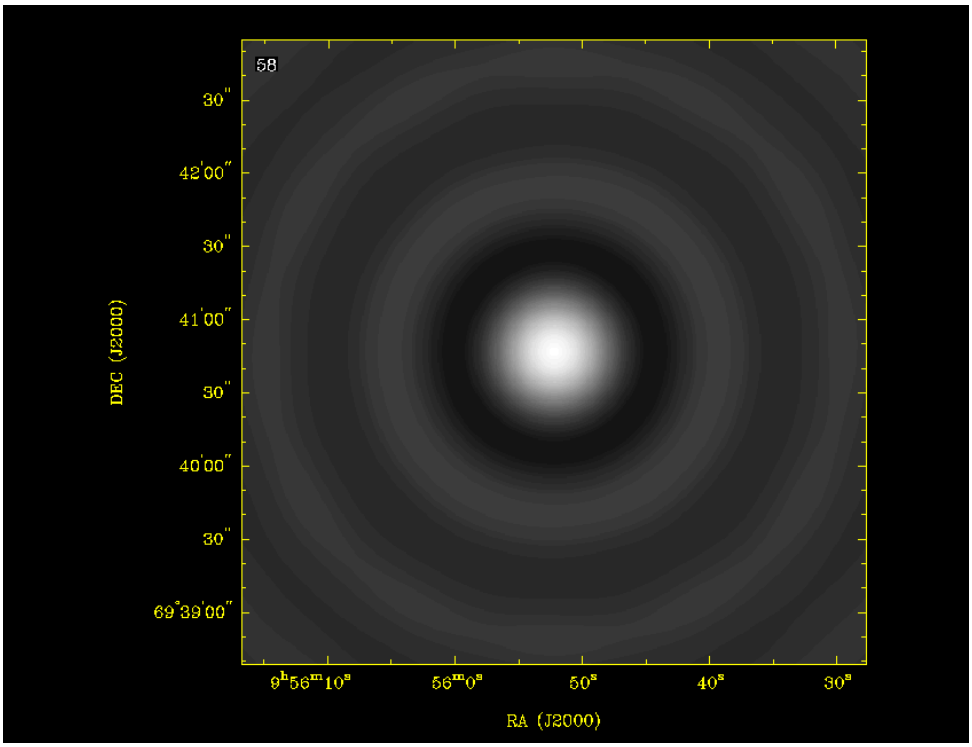

(b)

Figure 4.10: Synthesized beam of baseline types: a) 10-m-to-6-m antennas, b) NRO 45m.

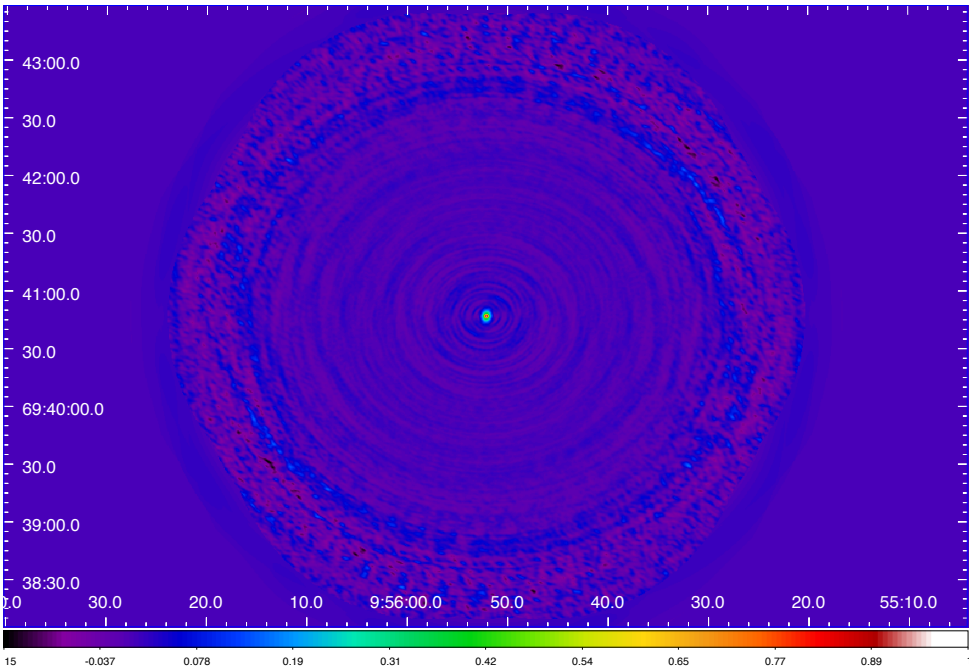

(a)

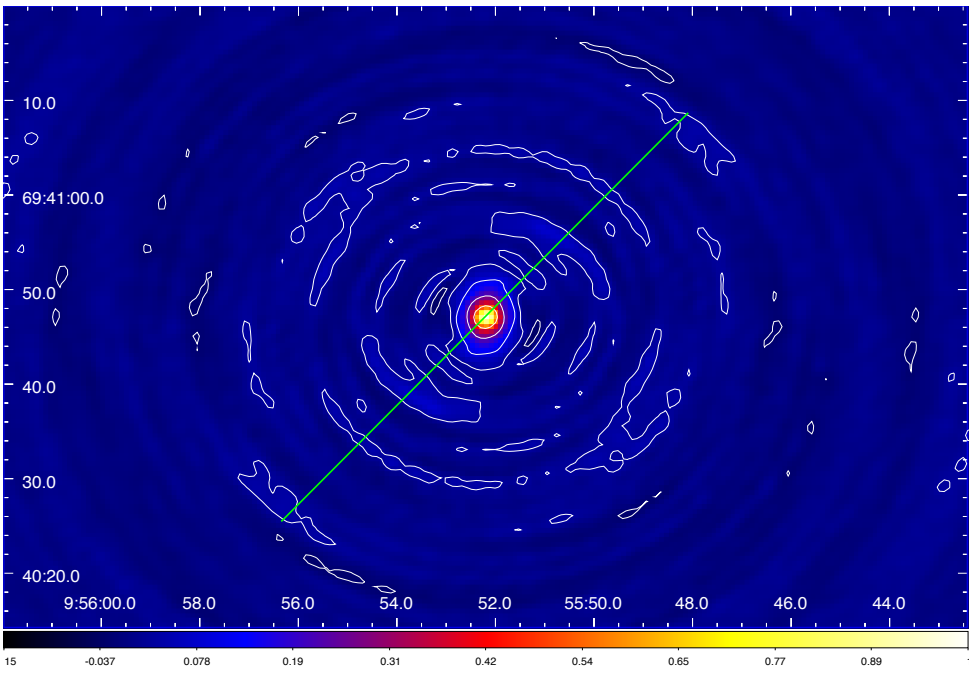

(b)

Figure 4.11: a) Synthesized beam of the combined CARMA-NRO 45m image (superposition of 19 pointings). b) The inner 1 arcmin of the image in (a). The green line marks the projection shown in figure 4.12 (b). The contours are -0.025, 0.025, 0.1, 0.25, and 0.5, where the peak is normalized to 1.

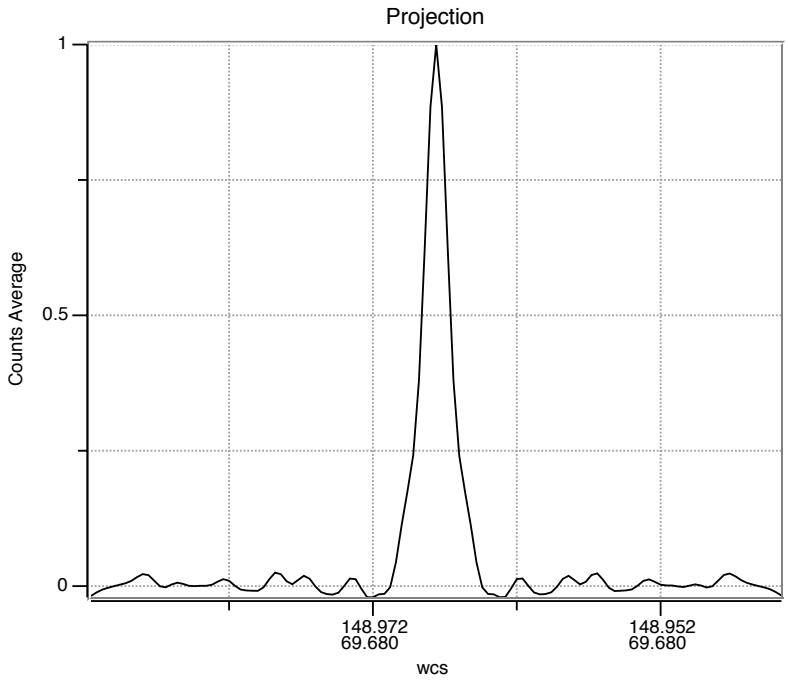

(a)

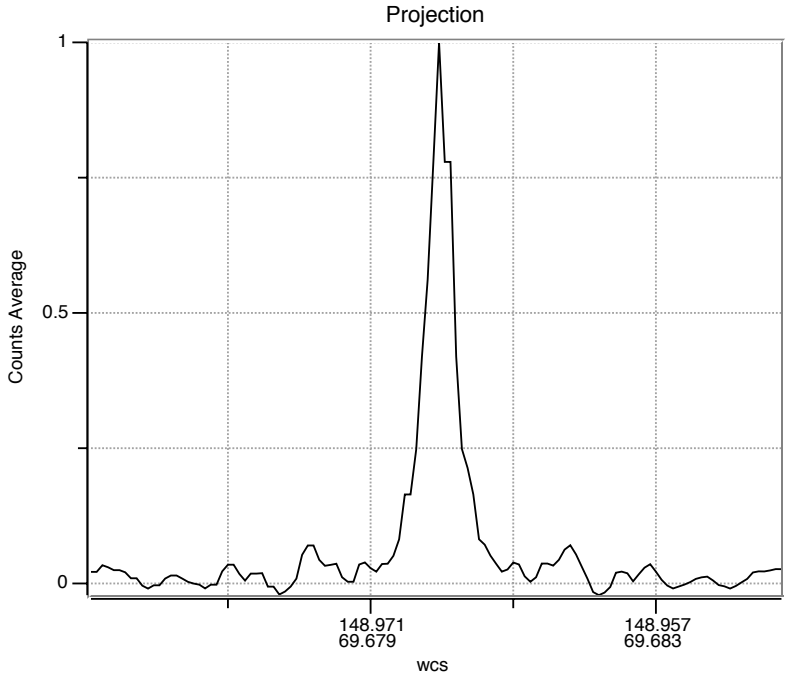

(b)

Figure 4.12: a) Projection of the synthesized beam of the combined CARMA+45m image from $(\Delta\alpha, \Delta\delta) = (+30'', 0'')$ to $(\Delta\alpha, \Delta\delta) = (-30'', 0'')$. The vertical axis is the normalized amplitude of the beam response. b) Projection along the green line shown in figure 4.11.

Chapter 5

Results and analysis of M82

Observations of M82 with the 45-m telescope in 2009 and 2010 resulted in a large-scale map of the CO (1-0) emission. Follow-up observations in 2011 and 2013 contributed further to our analysis by providing us with the intensities of the molecular lines of ^{12}CO (1-0), ^{13}CO (1-0), C^{18}O (1-0), CN (1-0) and CS (2-1) at selected positions. In this chapter, we present the data and discuss the results. First, let us introduce the uncertainty of the integrated intensity I [K km s^{-1}], which is used throughout the text as the radio-astronomical equivalent of surface brightness.

Uncertainty of the integrated intensity

The uncertainty of the integrated intensity (I) is calculated as follows. From the definition, $I = \sum_i T_i \Delta v_{\rm ch}$, the standard deviation is

$$(\Delta I)^2 = \left(\frac{\partial I}{\partial T}\right)^2 \sigma_T^2 + \left(\frac{\partial I}{\partial \Delta v_{\rm ch}}\right)^2 \sigma_{\Delta v_{\rm ch}}^2. \tag{5.1}$$

Here, $\sigma_T \equiv \Delta T$, and since the channel width is constant, i.e., $\sigma_{\Delta v_{\rm ch}} = 0$, the uncertainty per channel is simply

$$(\Delta I_i)^2 = \left(\frac{\partial I}{\partial T}\right)^2 (\Delta T)^2 = (\Delta v_{\rm ch})^2 (\Delta T)^2. \tag{5.2}$$

Assuming that ΔT is the same for all channels, the standard deviation can be expressed as a sum of uncorrelated random variables:

$$\sigma^2 \left(\sum_i X_i\right) = \sum_i \sigma^2(X_i) = n\sigma^2(X_i). \tag{5.3}$$

Thus, the uncertainty of the total integrated intensity is

$$(\Delta I)^2 = n(\Delta v_{\rm ch})^2 (\Delta T)^2 \tag{5.4}$$

and

$$\Delta I = \Delta T \sqrt{n(\Delta v_{\rm ch})^2} = \Delta T \sqrt{\Delta v_{\rm int} \Delta v_{\rm ch}}. \tag{5.5}$$

Here, $\Delta v_{\rm int} = n\Delta v_{\rm ch}$ is the integration range, and n is the number of channels in that range. Assuming $\Delta v_{\rm ch} = 20$ km s^{-1} and $\Delta v_{\rm int} \lesssim 100$ km s^{-1}, the uncertainty was typically $\Delta I_{\rm CO} \simeq 1.8$ K km s^{-1} in the case of our OTF observations. Note that this uncertainty does not include the error in baseline fitting. The baseline fitting error is proportional to $\propto \sqrt{\Delta v_{\rm ch}/\Delta v_{\rm bl}}$, where $\Delta v_{\rm bl}$ is the velocity range where the

baselines were fitted. Since $\Delta v_{\rm ch} = 20$ km s^{-1}, and $\Delta v_{\rm bl} \gtrsim 800$ km s^{-1}, the uncertainty was typically a few times smaller than the uncertainty calculated above.

5.1 Large-scale CO (1-0) emission

5.1.1 Distribution of the CO integrated intensity

The large-scale CO (1-0) emission is shown in figure 5.1. The map is 15.7×16.9 arcmin^2 wide (equivalent to 16.1 kpc $\times$ 17.4 kpc) with an angular resolution of $22.1''$, which corresponds to about 378 pc. The contours in the map show isophotes of the same integrated intensity defined as $I_{\rm CO} \equiv \int T_{\rm mb}\,{\rm d}v$, where $T_{\rm mb} = T_{\rm A}^*/\eta_{\rm mb}$ is the main beam brightness temperature, and $\eta_{\rm mb} = 0.32 \pm 0.02$ is the main beam efficiency obtained from NRO's status summary of the telescope. All data in this work are expressed in $T_{\rm mb}$ and $V_{\rm LSR}$ where the velocity is with respect to the local standard of rest (LSR) in the radio definition. The adopted systemic velocity is $V_{\rm sys} = 220$ km s^{-1} (Olofsson & Rydbeck 1984), and the adopted distance to M82 is 3.53 Mpc (Karachentsev et al. 2002), at which 1 arcmin corresponds to 1.03 kpc. The average r.m.s. in a channel is $\Delta T_{\rm mb} \simeq 40$ mK.

The CO gas is strongly peaked in the central 1-kpc region where the maximum integrated intensity is $I_{\rm CO} \simeq 507$ K km s^{-1}. Outside this region, the intensity decreases sharply, and most of the halo gas a few kpc farther out has intensities of $\lesssim 50$ K km s^{-1}. This indicates that the molecular gas is concentrated mainly in the nuclear region of the galaxy where vigorous star formation is taking place. Our OTF data do not have sufficient angular resolution to probe the galactic center in detail, and previous observations with the 45-m telescope have already revealed bright CO emission in the inner 1 kpc (Nakai et al. 1987). The aim of our project was to reveal the distribution of the molecular gas outside the nuclear region, to map the halo that was previously found to be highly abundant in atomic gas traced with the H I 21-cm line (Yun et al. 1994). In addition, figures 5.1 (a) and (b) confirm previous observations at higher resolution (e.g., Lo et al. 1987; Shen & Lo 1995; Walter et al. 2002) by revealing a double peak in the central region and a number of molecular gas streamers (labeled S1-S4 in Walter et al. 2002) emerging from the inner part of the galaxy.

From closer inspection of figures 5.1 (a) and (b), and comparison with an optical image (figure 5.4) we find that the CO gas comprises five distinct components, each briefly discussed below.

1. The galactic nucleus that coincides with star-forming regions is very bright. Figure 5.1 (b), in which $T_{\rm mb}$ is plotted vs. X and Y coordinates, reveals a double peak with a separation of $\simeq 400$ pc. This has been observed before (e.g., Nakai et al. 1987) and is understood to represent a nuclear ring (or torus) seen nearly edge-on. The ring is discussed in more detail in the next section where high-resolution data are presented.

2. Along the minor axis Y, figure 5.4 reveals a molecular gas outflow where the CO emission and Hα are prominent up to at least 2 kpc above the galactic plane. In this region, it appears that both molecular and ionized gases are being ejected from the starburst nucleus, where the molecular gas is expanding along the Y axis while diverging outwards. In some places, we note filamentary structure traced by elongated spurs and streams. The most prominent CO filament in the outflow is the structure labeled "F" in figure 5.1 (b).

3. Figures 5.1 and 5.4 reveal streams of molecular gas a few kpc long. Two of them are labeled WS ("western stream") and ES ("eastern stream") in figure 5.1 (b). As obvious from figure 5.4, the streams coincide well with dark stripes where optical light is absorbed by thick columns of dust. The nature of these streams is not well understood although they must be related to either central star-forming activity or tidal interaction with the nearby spiral galaxy M81. Since from

our vantage point M82 appears nearly edge-on, it is difficult to resolve the spatial distribution and velocity field of the streams.

4. The CO distribution and its spectral information indicate the presence of diffuse CO emission coincident with the galactic bulge (Ichikawa et al. 1995). Its most prominent feature is observed as the "western arm" (WA in figure 5.1 (b)), showing the only significant CO-emission peak outside the bright nuclear region.

5. In the deep halo, $\simeq 3.5$ kpc above the galactic plane, a region was discovered with integrated CO emission exceeding the statistical significance of 4σ. The region is referred to as the "NW clump", residing northwest from the galactic center. It is curious that it is only $\simeq 500$ pc wide and apparently isolated, although it correlates well with the atomic gas (see Comparison with other data). The NW clump is further discussed below.

Note that figures 5.1 (a) and (b) show a patchy distribution in the halo. Some of these features appear real, but some of them are most certainly instrumental artifacts. The most convincing is the NW clump, hence it is the only one discussed in this work.

In 2011, we observed one point in the Cap region located 11 kpc above the galactic plane. The Cap region was found to be bright in UV and X-rays, which has been interpreted as the consequence of interaction between the outflow plasma from M82 and cool neutral intergalactic clouds (e.g., Lallement 2004; Hoopes et al. 2005; Tsuru et al. 2007). At the position $(\alpha, \delta)_{\mathrm{J2000}} = (09^{\mathrm{h}}55^{\mathrm{m}}00^{\mathrm{s}}, +69^{0}50'15'')$, which is outside the OTF map, CO (1-0) was not detected at the noise level of $\Delta T_{\mathrm{mb}} \simeq 6$ mK.

5.1.2 Kinematics of the CO gas

Figures 5.2 and 5.3 show the velocity field of the CO (1-0) emission. The CO intensity was integrated between $V_{\mathrm{LSR}} \simeq 0$ and 450 km s^{-1} where emission was detected. The maximum rotation speed is $\simeq 200$ km s^{-1}, which is typical for disk galaxies. From figure 5.2, it is obvious that the western part of the disk is blueshifted with respect to the V_{sys}, while it is opposite for the eastern part. The main properties of the CO kinematics are summarized below.

1. In the central region, the double peak discussed above coincides with elevated line-of-sight velocities. This is because the central torus is rotating at a higher rate compared to low-intensity surrounding material.

2. Contrary to the western part of the disk, which seems to have regular rotation, the eastern part appears to be heavily disrupted. The white line in figure 5.2 shows that the systemic velocity runs parallel to the major galactic axis in the eastern part, suggesting that considerable portion of the gas is in motion perpendicular to the line of sight. This is most likely due to the tidal interaction with M81, which is the origin of an H I tidal arm coincident with the eastern CO arm.

3. The most blueshifted velocities with peaks around $\simeq 110$ km s^{-1} were found in the region of the western arm. On the other side, the most redshifted velocities are emerging from the eastern peak of the central torus toward NE, at a position angle of $\simeq 45^{0}$. These structures are interpreted as part of the underlying galactic disk, without firm relation to tidal and outflow components.

4. In the molecular gas outflow, we note a clear distinction between the northern side which is mainly redshifted, and the southern side that is blueshifted. Such pattern is expected from a nearly edge-on disk galaxy if the outflow is along the minor axis Y. In fact, it is possible to

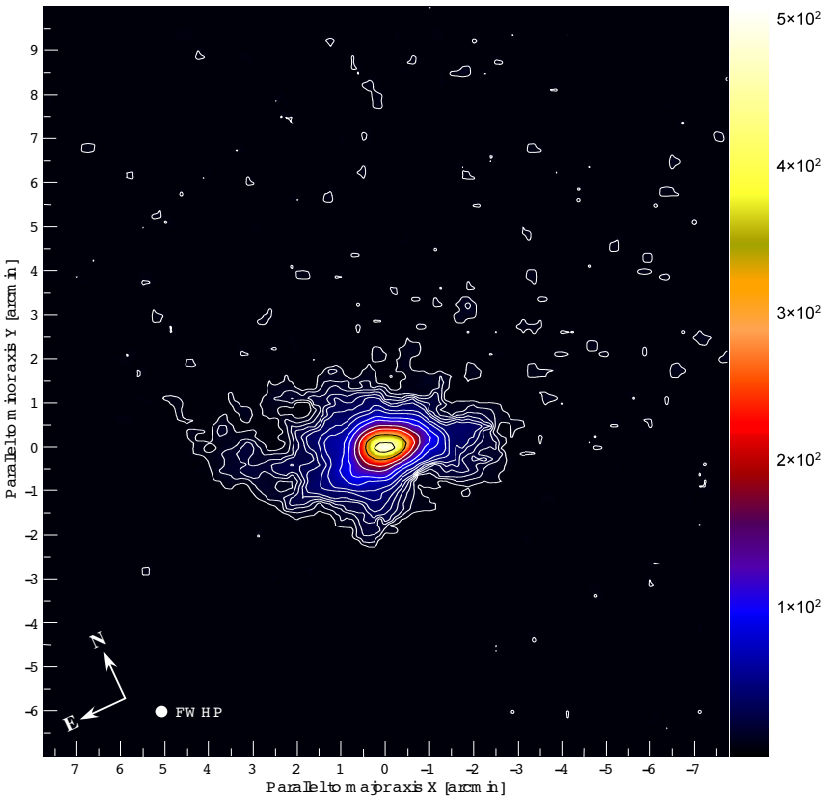

(a)

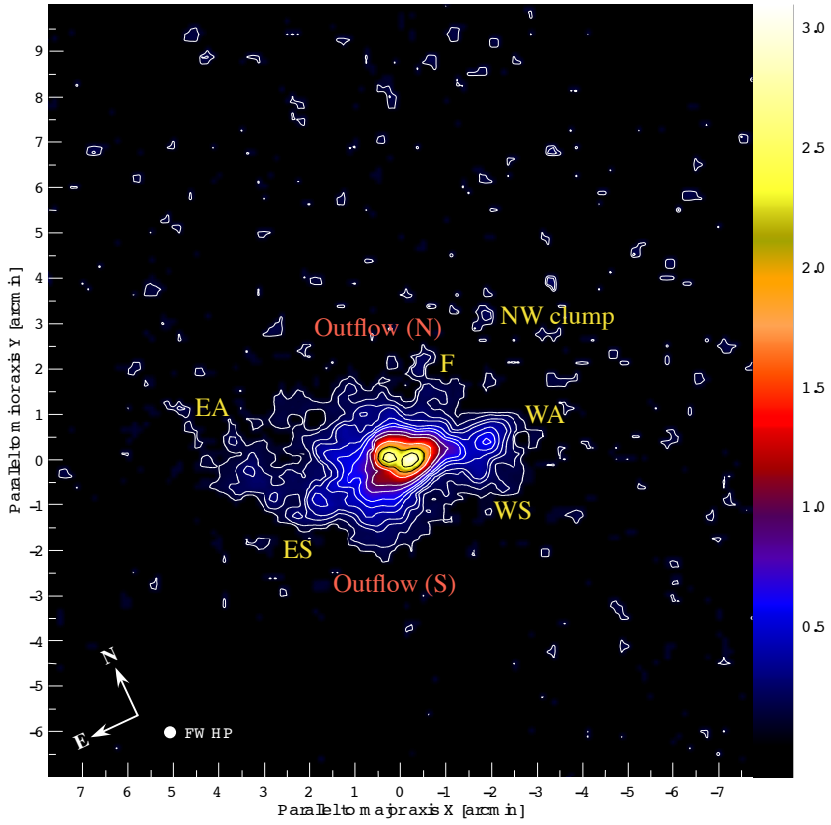

(b)

Figure 5.1: (a) CO (1-0) emission in M82 (Salak et al. 2013). Color bar = integrated intensity I_{CO} [K km s^{-1}]; FWHP = angular resolution of 22″. The galactic position angle is 65^0. (b) Main beam temperature of the CO (1-0) emission. Color bar = T_{mb} [K], and the contours are $T_{mb} = 0.12, 0.18, 0.25, 0.3, 0.4, 0.5, 0.6, 0.8, 1.0, 1.5, 2.0, 2.6$ K.

resolve the outflow component from the background disk emission, as explained in Salak et al. (2013).

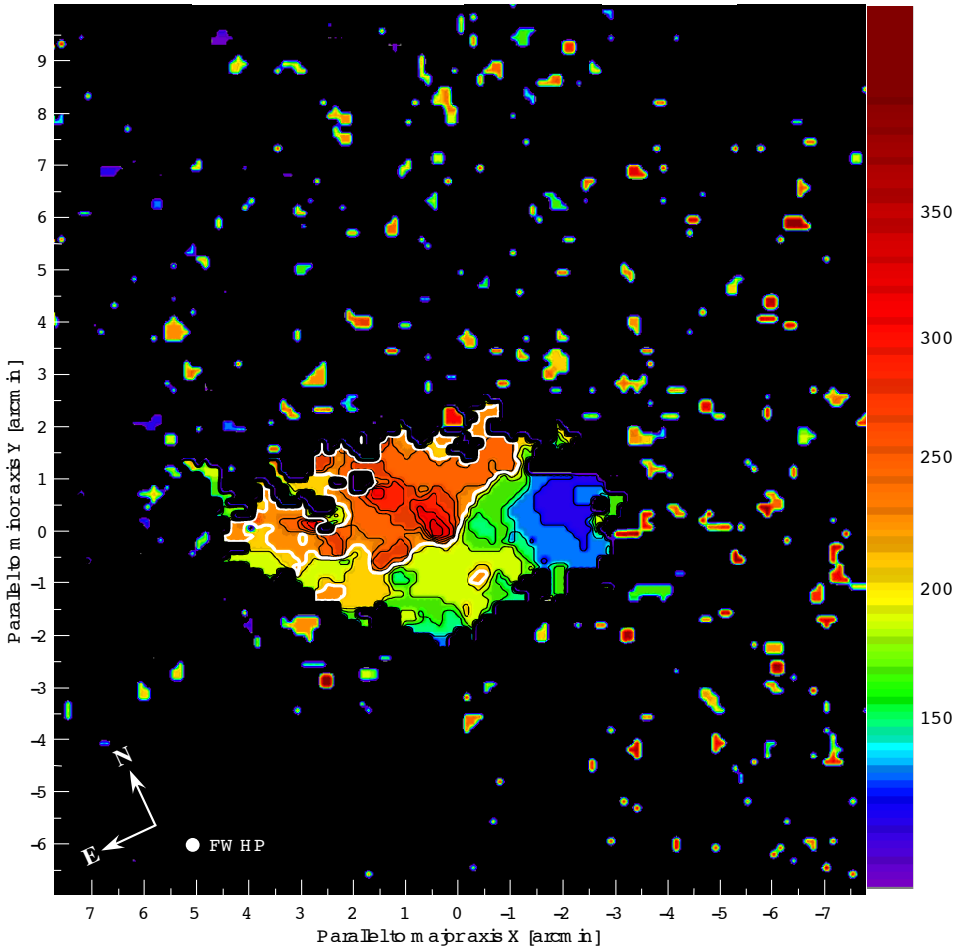

Figure 5.2: Velocity field of the CO emission (Salak et al. 2013). The color bar is in km s^{-1}; the white line marks the systemic velocity, $V_{\rm sys} = 220$ km s^{-1}.

Figure 5.3 shows channel maps from 50 to 390 km s^{-1} with intervals of 20 km s^{-1}. In addition to a rotational pattern, note the stream east from the nucleus corresponding to ES in figure 5.1 (b) that is persistant in all channels. This can be interpreted as a stream of molecular gas dispersed in a plane perpendicular to the observer with an average velocity near the galactic systemic velocity. Note that the stream appears to be physically connected to the nuclear region, although we cannot see clearly at this angular resolution.

Another feature, resolved in figure 5.3, is the eastern tidal arm (EA in figure 5.1 (b)). It appears in channels from 190 to 230 km s^{-1}, while most emission comes from gas in motion at near-systemic velocity in a stream perpendicular to the line of sight.

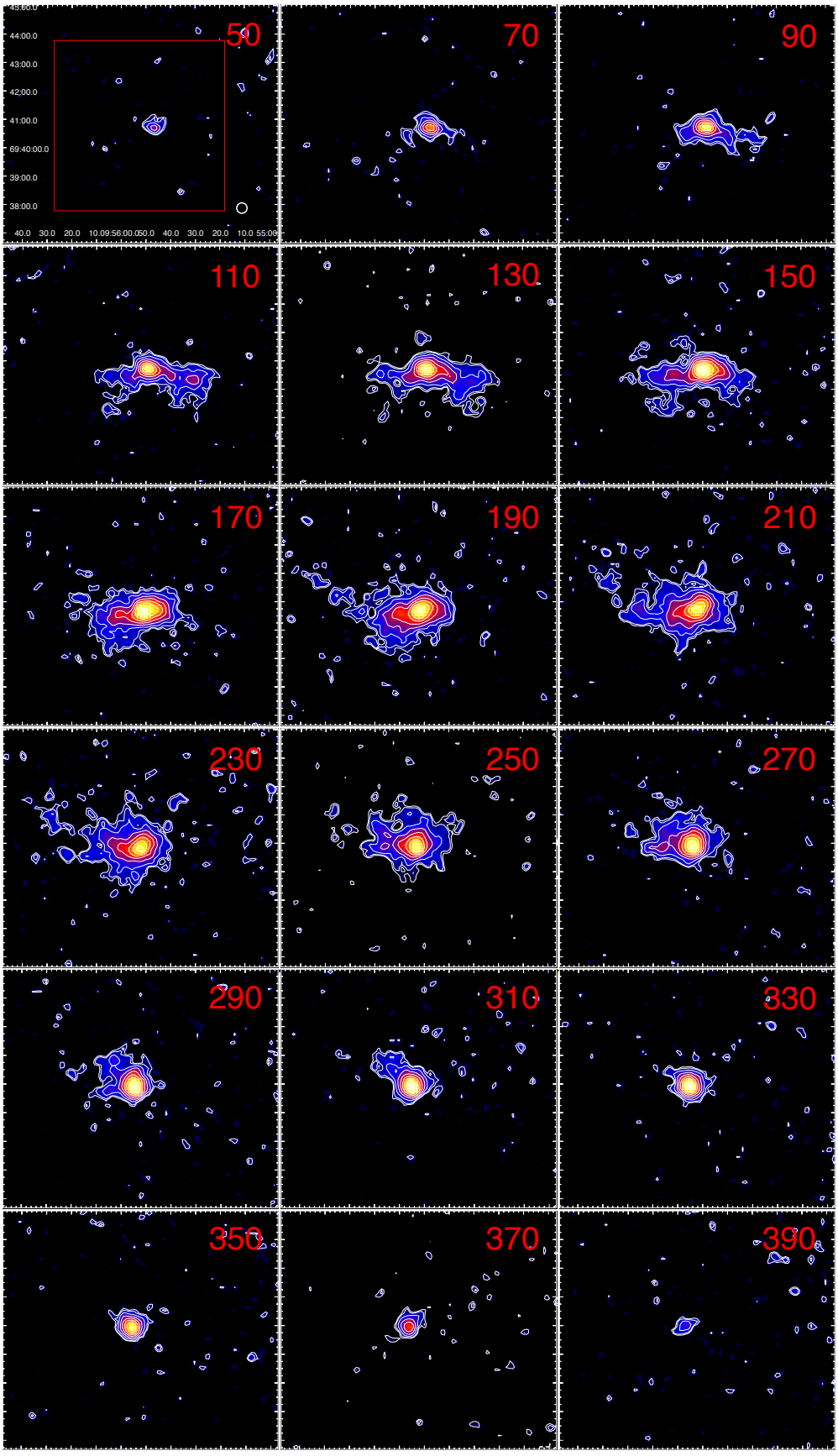

Figure 5.3: Channel maps of the CO (1-0) emission from 50 to 390 km s^{-1} with a separation of 20 km s^{-1}. The intensity is displayed on a square-root scale with the lowest contour at 50 mK in $T_{\rm A}^{*}$. Red rectangle: 6×6 arcmin^2; white circle in the upper left panel: angular resolution $22''$.

Comparison between CO and H-alpha

Figure 5.4 shows CO (1-0) contours superimposed on an Hα image taken with the Hubble Space Telescope (Mutchler et al. 2007). The outflow and streams of molecular gas are indicated. Note the spatial correlation between the dust lanes, visible as bright regions in the negative photograph, and CO streams. The molecular gas outflow was detected up to 2 kpc above the galactic plane.

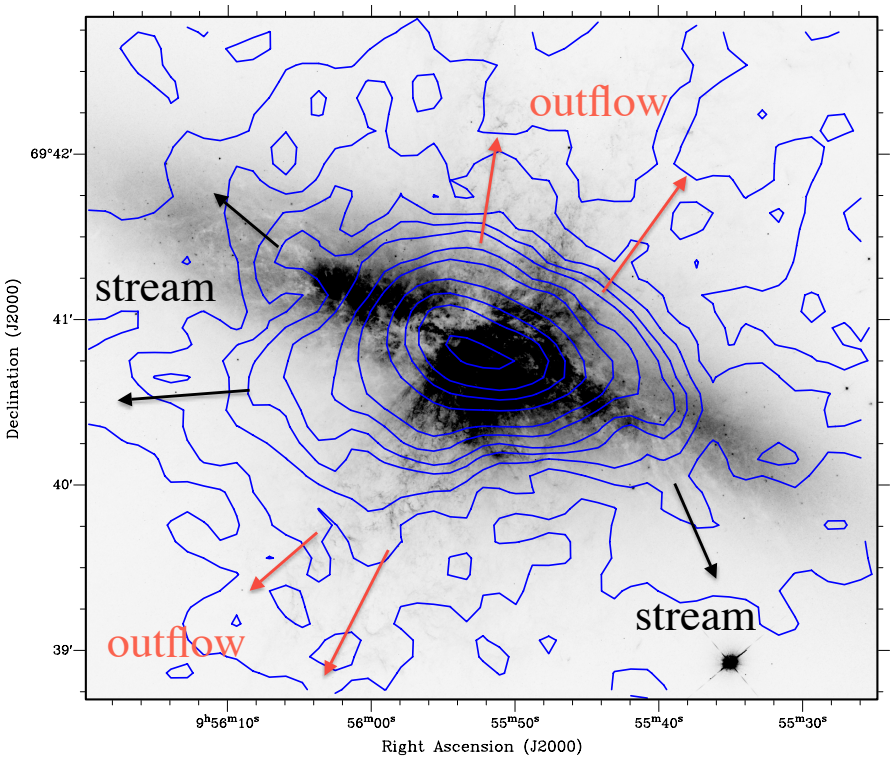

Figure 5.4: CO emission contours superimposed on an optical image obtained with the Hubble Space Telescope (image credit: The Hubble Heritage Team; Mutchler et al. 2007).

5.2 Combined CARMA-NRO 45m image of CO (1-0)

5.2.1 Distribution and kinematics of the CO gas

Result of CARMA observations

CARMA observations of CO (1-0) in M82 were conducted toward a 19-pointing mosaic with a maximum spatial coverage of 6 arcmin in diameter and the effective (high-sensitivity) area of ~ 3.5 arcmin. The resulting image is shown in figures 5.5 and 5.6. The angular resolution is $3.56'' \times 3.04''$ (position angle -10.35^0), or 60×52 pc^2 at the adopted distance of 3.53 Mpc. The r.m.s. noise in a channel of 10.16 km s^{-1} is ~ 0.02 Jy beam^{-1}. The (u,v) coverage was fairly uniform which resulted in uniform noise level throughout the image.

Figure 5.5 shows that CO emission is strongly detected in the central region. In addition to the bright nucleus, patchy structure is detected southeast and west from the center. As discussed before, interferometers cannot sample large-scale emission; even in mosaicking this problem persists, so the patchy structure in the CARMA image resulted from spatially biased sampling and the lack of zero-spacing data in the (u,v) plane. The outer $\sim$ 2-arcmin regions have lower sensitivity because those regions were not fully sampled; no CO emission was detected there. The FWHM of 6-m and 10-m antennas is shown on the right.

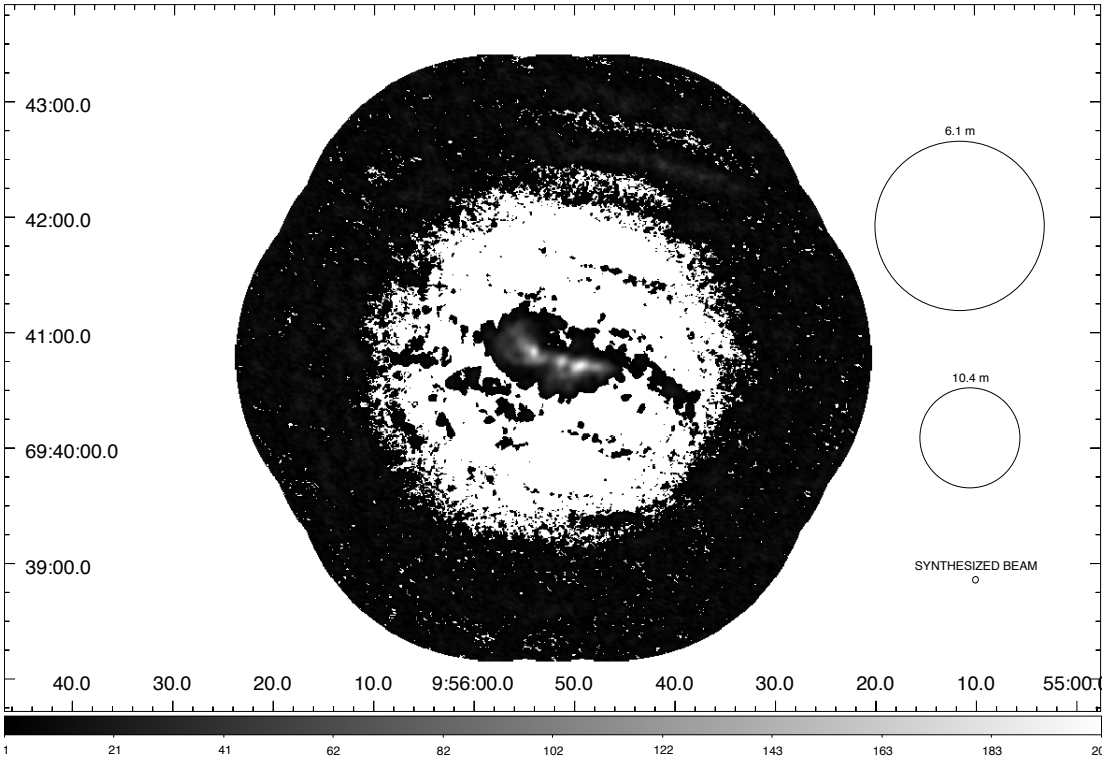

Figure 5.5: CO (1-0) integrated intensity mosaic image taken with CARMA. The FWHM ($\lambda_{\rm CO}/D$) of the antenna beams of CARMA are shown on the right; they should be multiplied by 1.22 to get the angular resolution (1/2 of the width between the first nulls). The mosaic consists of 19 pointings. The outer regions are of two times lower sensitivity because the pointings do not overlap there. The intensity bar is in Jy beam^{-1} km s^{-1}.

Result of CARMA-NRO 45m combining

The data were combined with the NRO 45-m data taken in 2009 and 2010, as explained in previous sections. The resulting integrated intensity map of the CO (1-0) emission is shown in figure 5.7. The

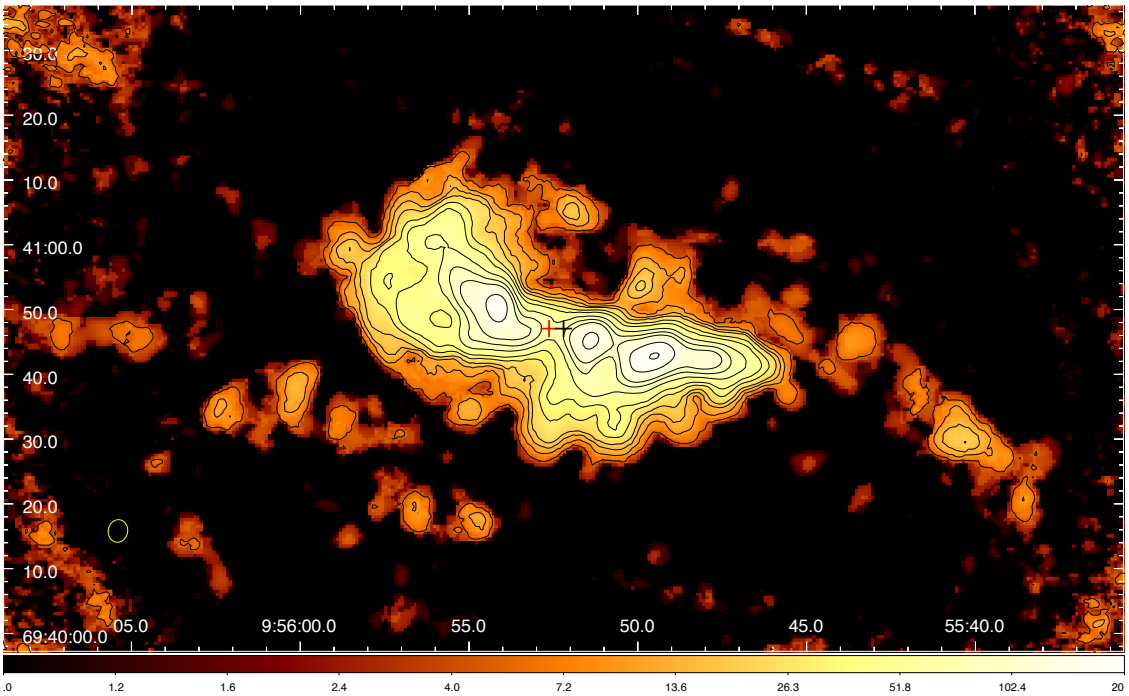

Figure 5.6: Central part of the image of the CO (1-0) integrated intensity from figure 5.5. Contours: 5, 10, 15, 20, 30, 40, 60, 80, 100, 150, 200 Jy beam^{-1} km s^{-1}. The angular resolution ($3.5'' \times 3.0''$ at P.A. $= -10.3^0$) is shown in the bottom left corner. The black cross marks the center of the map at $(\alpha, \delta)_{\rm J2000} = (9^{\rm h}55^{\rm m}52.2^{\rm s}, 69^0 40' 47.1'')$ (Walter et al. 2002); the red cross marks the 2.2 μm peak at $(\alpha, \delta)_{\rm J2000} = (9^{\rm h}55^{\rm m}52.63^{\rm s}, 69^0 40' 47.1'')$ (Olofsson & Rydbeck 1984).

r.m.s. noise in emission-free channels of the final data cube (velocity resolution 10.16 km s^{-1}) is 20 mJy beam^{-1}, and the lowest intensity level in the image is 1.0 Jy beam^{-1} km s^{-1}, which is $\approx 5\sigma$ in flux density. The synthesized beam is $4.0'' \times 3.3''$ (68 and 56 pc) at the position angle of -9.5^0. The beam is larger than in the CARMA image because the synthesized beam is a composite of all antennas involved, thereby includes the implemented "synthesized beam" of the 45-m antenna. The final angular resolution is determined by a weighted average of all synthesized beams (3 different baselines for CARMA and 1 for NRO 45m).

High-resolution observations of M82 have been made before with interferometers (Lo et al. 1987; Shen & Lo 1995; Weiß et al. 1999), and by combining interferometer and single dish data (Walter et al. 2002). The interferometer-only observations revealed only the nuclear ring, whereas the combined observation of Walter et al. (2002) revealed CO emission to a similar extent as in this work. However, the study of Walter et al. (2002) focused on larger scale - mainly the kpc-scale structure of the outflow and molecular gas streamers. Also, the previous observations were made with Owens Valley Radio Observatory (OVRO) interferometer which is now part of CARMA, meaning that the image fidelity of the CARMA data is better (105 simultaneous antenna cross-correlations compared to 36 in OVRO). Differently from their work, we focus on the *inner outflow*, the region ± 1 kpc within the midplane where most of the molecular-gas mass is located. Disk-outflow connection, which is observed at the inner base of the outflow, is important to understand the process of entrainment of the molecular gas into the outflow, i.e., the evolution of the cold phase of the ISM. The properties of molecular gas are investigated mainly from: (1) distribution of the integrated intensity, (2) velocity field, and (3) line intensity ratios. In this section, we present (1) and (2).

The CO (1-0) emission in the central region of M82 reveals the well-known ring of molecular gas that comprises three prominent peaks. The ring is rotating at a projected velocity of $\simeq 180$ km s^{-1}, as shown in the intensity-weighted velocity field map (moment 1) in figure 5.8. In figure 5.9 we note

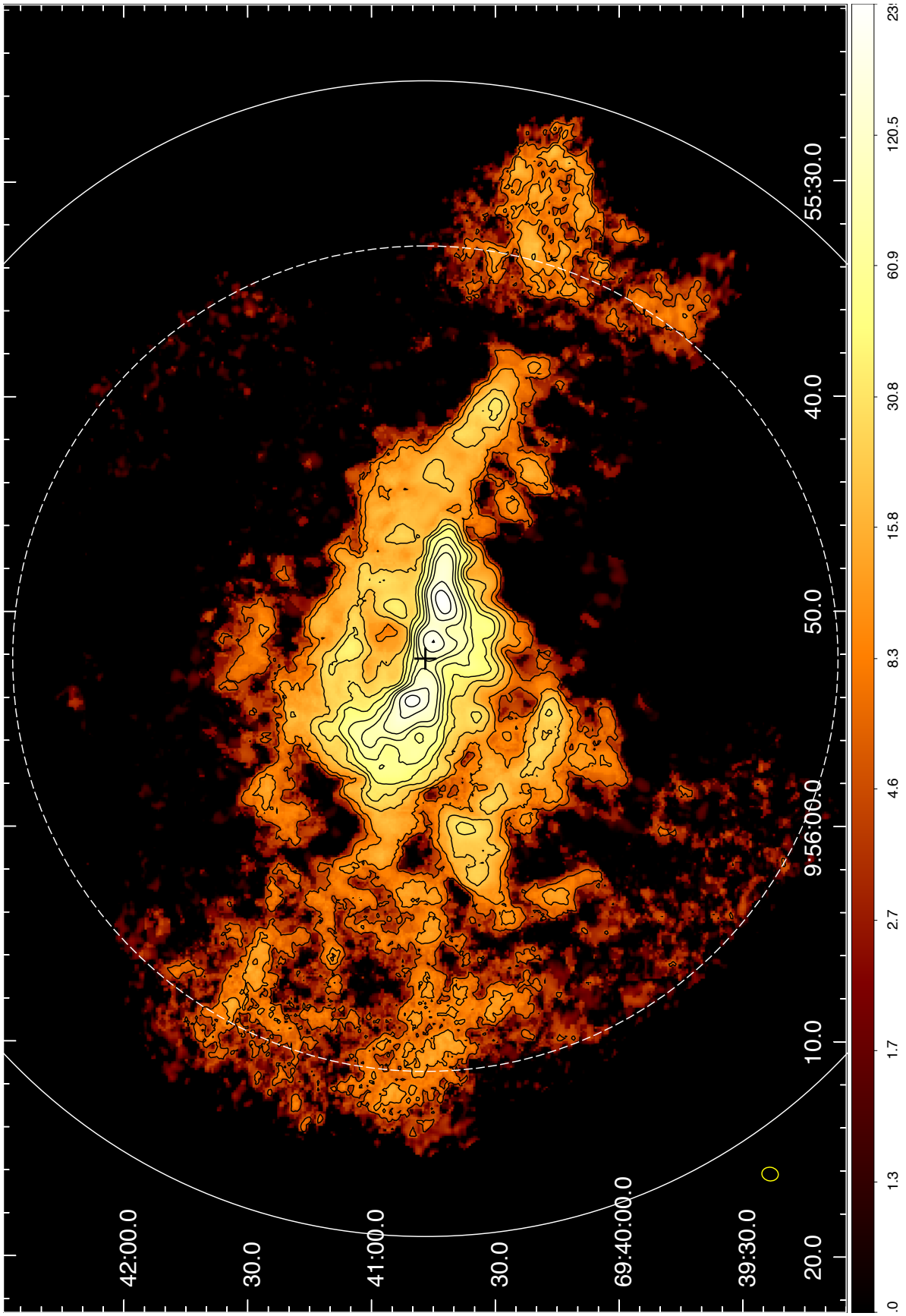

Figure 5.7: CO (1-0) integrated intensity map displayed on a logarithmic scale. Contours: 5, 10, 20, 30, 40, 60, 80, 100, 150, 200 Jy beam^{-1} km s^{-1}. The angular resolution ($4.0'' \times 3.3''$ at P.A. $= -9.5^0$) is shown in the bottom left corner. The black cross marks the center of the map near the 2.2 μm peak. Full line marks the combining region and dashed line marks where sensitivity decreases twofold. The physical scale is $1' \simeq 1$ kpc, where the coordinates are equatorial for J2000.

that the extremes of the velocity are not coincident with the emission peaks. This behavior is expected from the fact that the peaks reflect projections of the longest path that photons travel through the ring, whereas the radial velocity is highest farther outside, at the "outer boundary" of the projected ring.

The absolute position of the central peak is difficult to deduce from our edge-on vantage point. Rotational pattern in figure 5.9 suggests that the peak is likely part of the western side of the ring rather than being a structure near the center of the galaxy, as it appears when projected on the sky.

Most of the emission south and southeast of the ring is near the systemic velocity of the galaxy, $V_{\rm sys}$, or blueshifted with respect to it. North of the ring, we observe mostly redshifted velocities. This was noticed in our single dish data as well - the molecular gas outflow and the galactic disk are inclined with respect to the observer. Also, note that the streams of gas are redshifted in the east and blueshifted in the west with respect to the outflow gas.

CO filaments, shells and voids

It is clear from figure 5.7 that the distribution of the molecular gas is not uniform but consists of spurs or filaments (50 to 200-pc wide ensemble of ejected molecular clouds), shells, central "CO void", and molecular gas streams. Below is a short description of these features.

Filaments. Since the progenitor of the molecular gas outflow is the nuclear ring, the ejected gas is physically related to it. As seen edge-on, the walls of the outflow cones appear as spurs or filaments. Northwest from the ring, we clearly see two prominent walls which join each other at one point $40''$ from the galactic center. On the southeast side, the structure is less symmetric, with the bulk of the gas towards SE. This feature is kinematically not coupled with the rotation of the ring.

Supershells. Figure 5.7 shows resolved outflows within $\pm 20''$ from the ring, ~ 300 pc in size. One is seen on the western side (WS), and one on the eastern side (ES) of the ring. The western outflow was discussed by Neininger et al. (1998), Wills et al. (1999), Weiß et al. (1999) and Matsushita et al. (2000) as a "superbubble", while the eastern outflow is a new discovery. The outflows are discussed below.

The central void. In the region between the walls of the northern part of the outflow, CO emission is relatively weak. This region is just "above" the nucleus of the galaxy, which appears to be devoid of molecular gas. The central region of M82 is ejecting hot ionized gas, bright in X-rays, and such environment is too harsh for molecular clouds to survive. The central void is the origin of the bubble filled with hot plasma (wind fluid) that broke away and reached distances as far as 11 kpc from the galactic center thereby enriching the halo with heavy elements (e.g., Hoopes et al. 2005; Tsuru et al. 2007).

Streams. Walter et al. (2002) discovered four molecular-gas streams ~ 1 kpc from the nuclear ring. They were labeled S1-S4 and correspond spatially to some of the streams in figure 5.7. Our map is in good agreement with their map, and figure 5.9 confirms that the streams are kinematically independent. The structure of the large streams can also be traced in our single dish (OTF) map (figures 5.1 (a) and (b). In figure 5.1 (b), S1 was labeled WS and S3 was ES. The streams extend up to at least 3 kpc from the galactic center as revealed with our OTF map, which has lower resolution but higher sensitivity than the interferometer map.

Velocity dispersion

The velocity dispersion of CO gas (σ), i.e. the second moment of integrated intensity, is shown in figure 5.10. In figure 5.11, integrated intensity contours are superimposed on the velocity dispersion image.

Most of the gas in the nuclear ring has $\sigma \simeq (30-40)$ km s^{-1}. This is high compared to typical nearby galaxies (e.g., see Fukui & Kawamura 2010 for the basic properties of molecular clouds in nearby galaxies), but expected from a rotating system observed edge-on because of cloud crowding

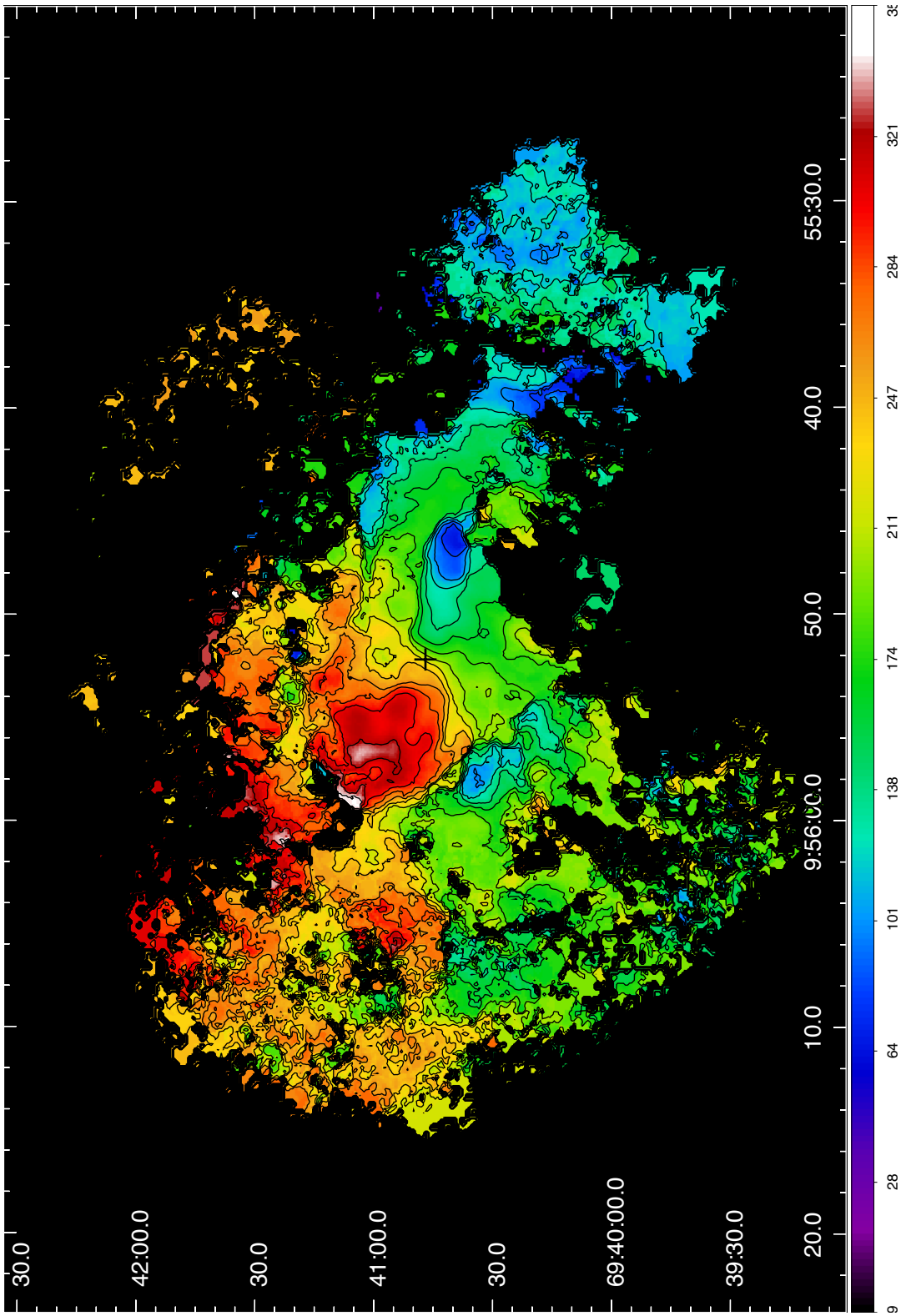

Figure 5.8: Intensity-weighted velocity field map of the CO emission (moment 1). Contours: from 80 to 340 km s^{-1} separated by 20 km s^{-1}.

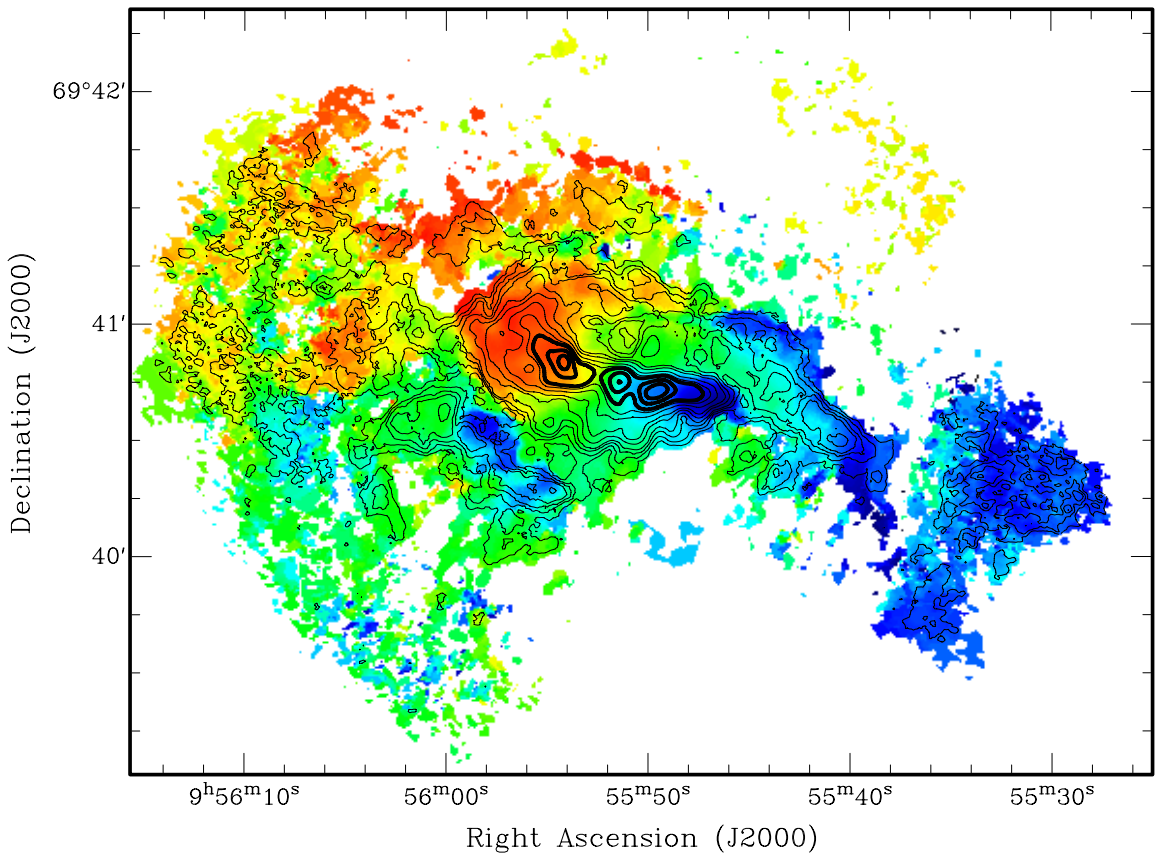

Figure 5.9: Integrated intensity of the CO emission (contours) overlaid on a velocity field image.

and turbulence. In the inner outflow, beyond the ring, we observe two distinct environments. In the molecular stream west of the nuclear ring, in the outflow $\gtrsim 30''$ south of the galactic center, as well as in some places northwest of it, $\sigma \simeq (5-20)$ km s^{-1}. The molecular gas here is quiescent, in a steady outflow/stream. On the contrary, in other parts, e.g., southeast of the center, σ is as high as $(50-60)$ km s^{-1}. These high-σ regions are where shocked clouds and cloud collisions are present. We can infer the kinematic properties of the outflow gas from CO data alone (channel maps and position-velocity maps), and by comparing with other data. As will be shown below, emission from the SiO (2-1) molecular line was detected in these regions, presumably shocked, and radio continuum in SN remnants, sources that heat the ISM in the nuclear ring.

In figure 5.11 we show that σ sharply increases in regions where molecular clouds are either in collision with each other, subject to external shocks, or overlap in the line of sight. For now, we only emphasize the spatial correlation between the general structure described above and σ, although the detailed structure will be discussed later. It is interesting that σ is not necessarily large where the ring peaks are located. For instance, between the two western peaks and southeast of the eastern peak we find increased velocity dispersion. These regions are candidates for expanding structures, as will be shown when we examine position-velocity diagrams.

North of the nuclear ring, the walls of the conical outflow seem to overlap and/or collide. The molecular gas walls are expanding in a broad opening angle. A clumpy ring would produce clumpy features in the outflow cone that would overlap and likely collide in extra-planar regions.

Dust lanes

The CO emission, as a tracer of molecular gas, is likely to be spatially correlated with the continuum emission from dust grains. Figure 5.12 shows a comparison of the B-band image (negative) taken

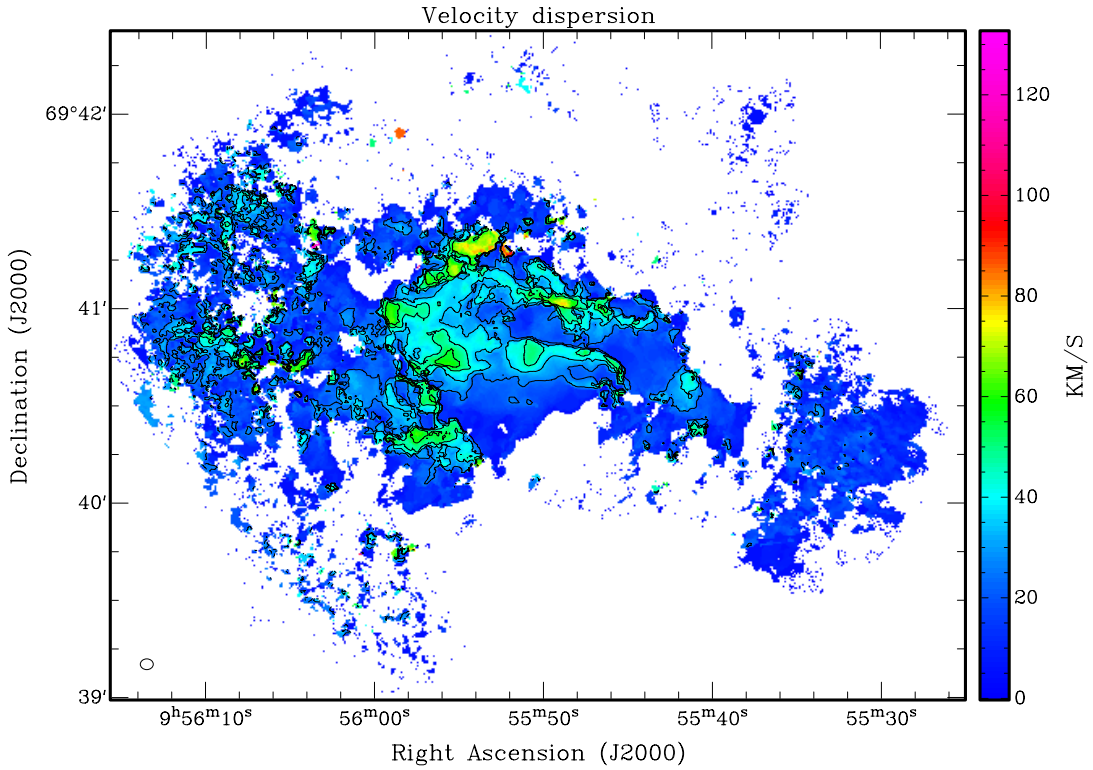

Figure 5.10: Velocity dispersion map of the CO emission (moment 2). Contours: 25, 35, 45 km s^{-1}.

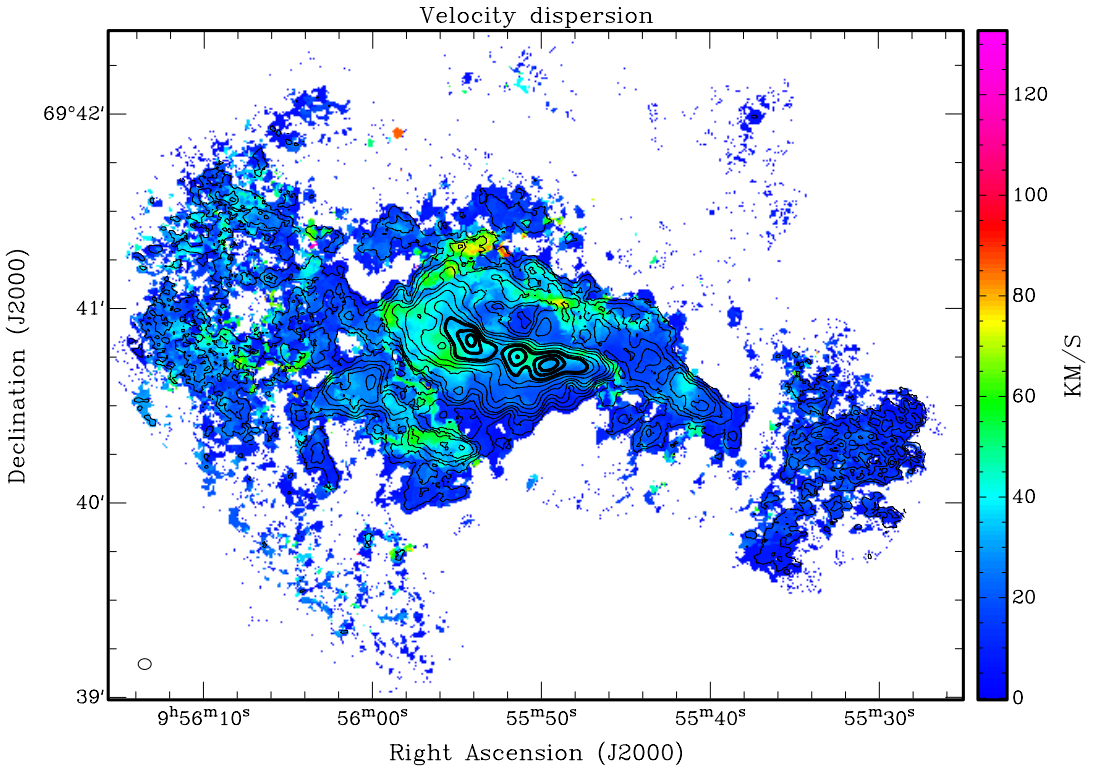

Figure 5.11: Integrated intensity of the CO emission (contours) overlaid on a velocity dispersion image.

with the Hubble Space Telescope and the CO (1-0) contours from our combined image. For clarity, a region that exhibits large contrast between starlight and dust absorption was selected for comparison. The CO contours trace the dust absorption very well.

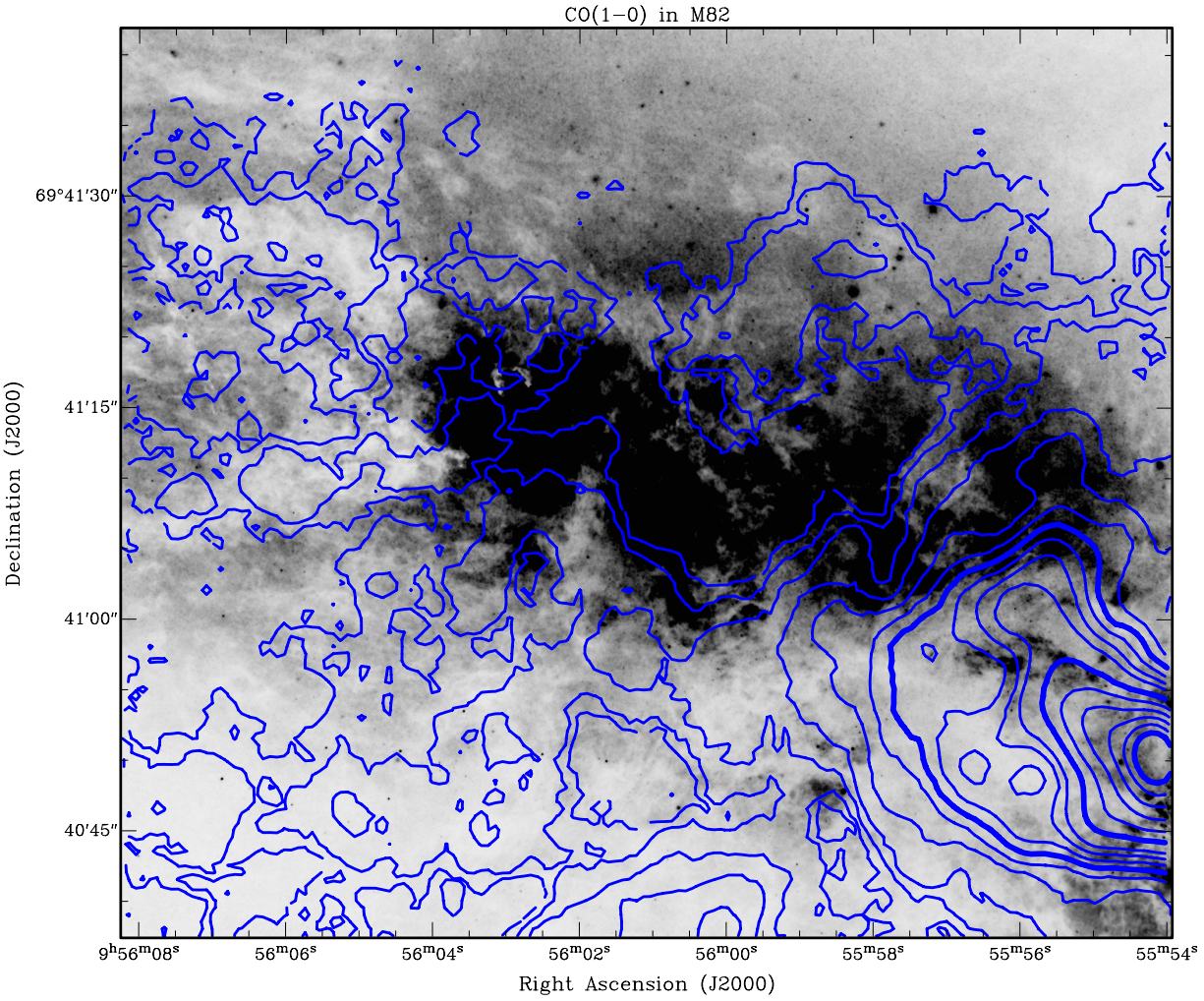

Figure 5.12: CO (1-0) contours overlaid on a B-band optical image (negative) taken with the Hubble Space Telescope (Image credit: Hubble Heritage Team).

5.2.2 Comparison of single-dish and combined data

In order to evaluate the image fidelity in the measurements, single-dish data were compared to the combined interferometer + single-dish data. A direct comparison with different (original) angular resolutions is shown in figure 5.13. The combined image was then smoothed by using the MIRIAD command SMOOTH to the common angular resolution of 19.7″. The FWHM of the beams in the smoothing process is $\theta_{\rm in}^2 + \theta_{\rm sm}^2 = \theta_{\rm out}^2$, where $\theta_{\rm in} = 3.6''$ and $\theta_{\rm out} = 19.7''$. These results are shown in figure 5.14. In figure 5.15 we present a detailed comparison of the integrated intensity and the velocity field in the two data sets.

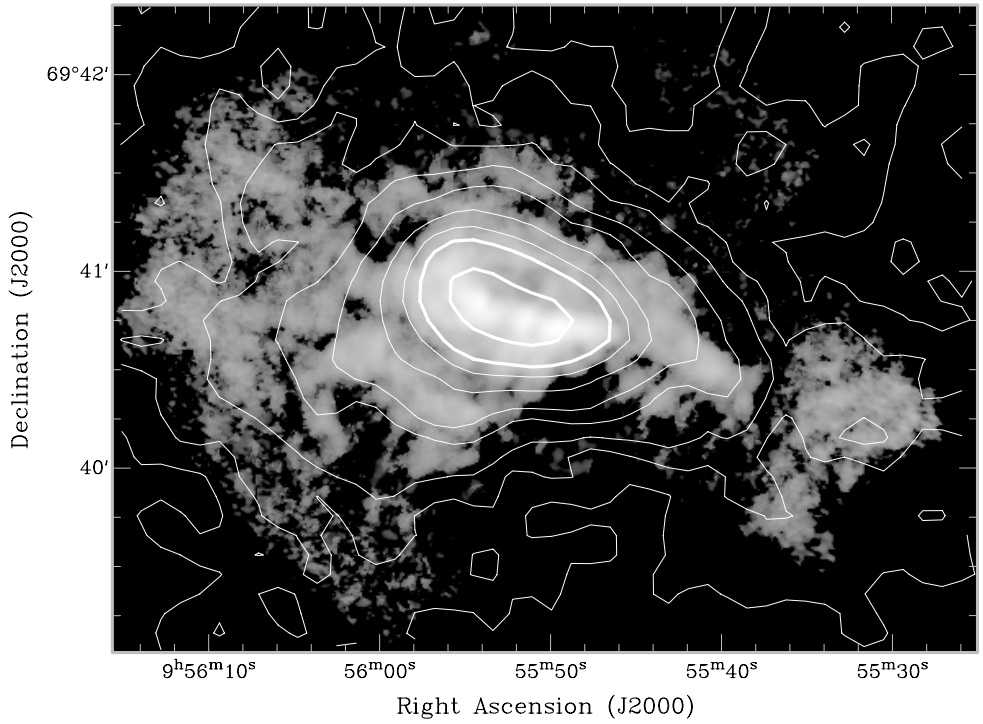

Figure 5.13: CO (1-0) integrated intensity map contours (10, 15, 20, 30, 40, 50, 75, 100, 150 K km s^{-1}) from the 45-m data superimposed on the CARMA+NRO 45m combined image.

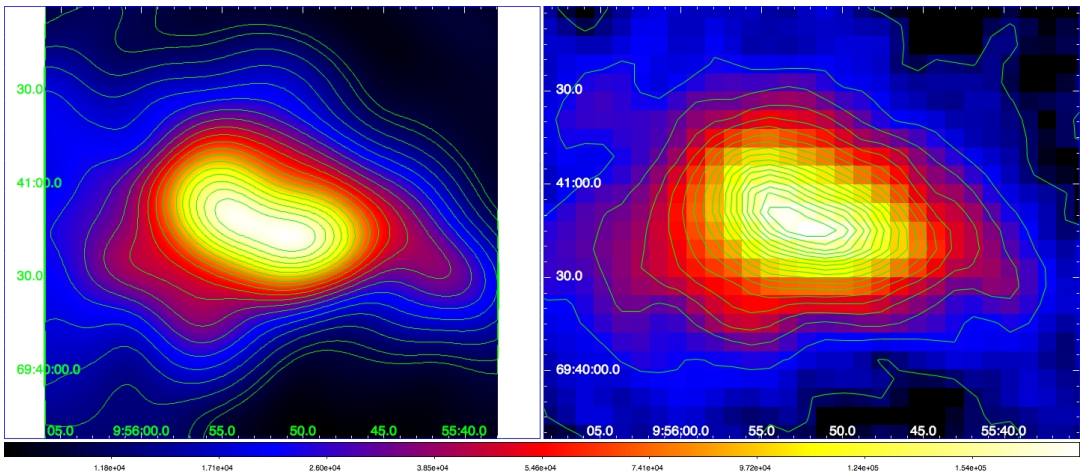

Figure 5.14: *Left.* Combined CARMA-NRO 45m image smoothed to the angular resolution of 19.7″. *Right.* OTF map.

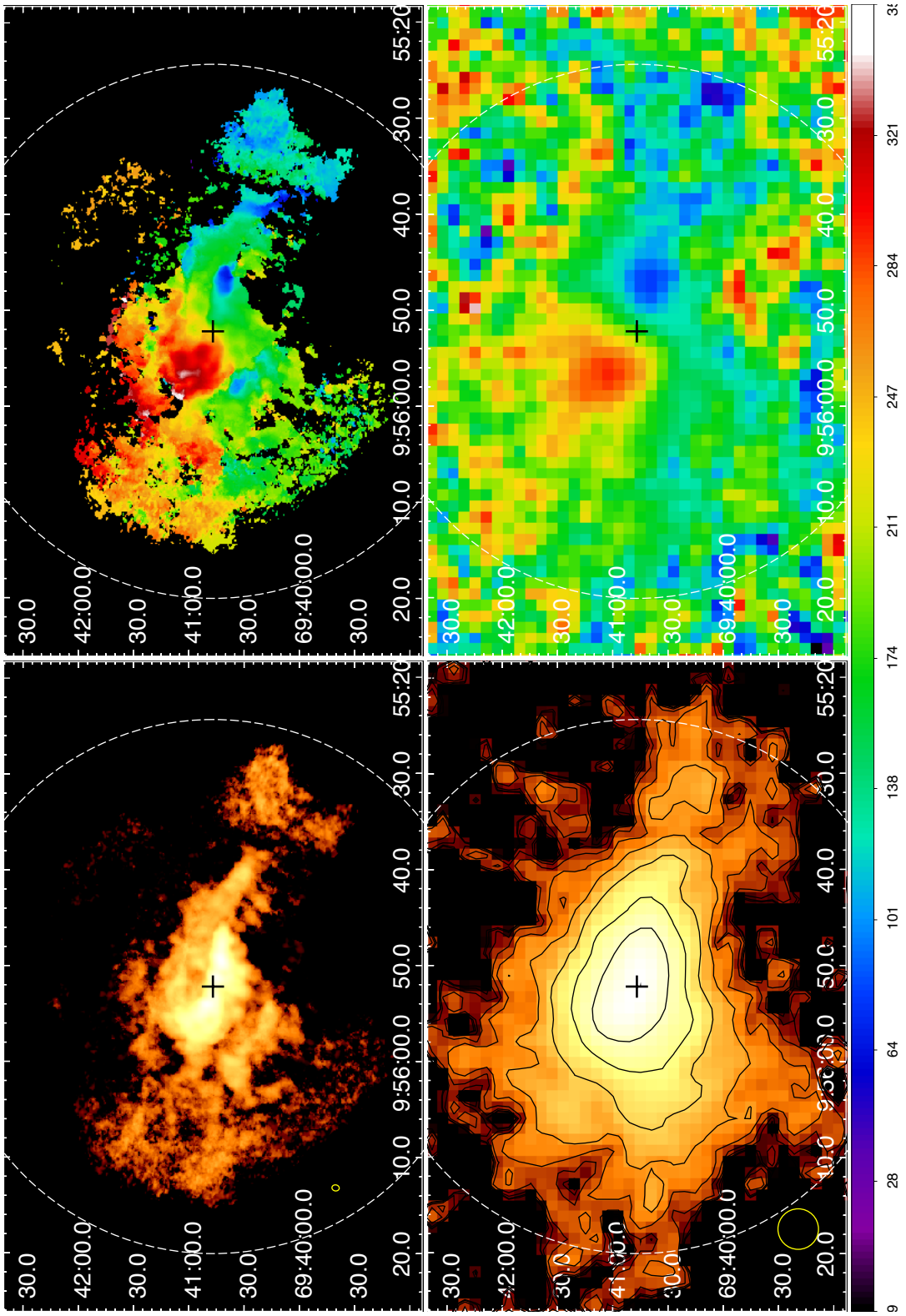

Figure 5.15: Comparison of moment 0 and moment 1 for the combined (upper panels) and NRO 45-m data from Salak et al. (2013) (lower panels) without adjusting to the same angular and spectral resolution. Dashed white circle (radius 150″) marks the combined region.

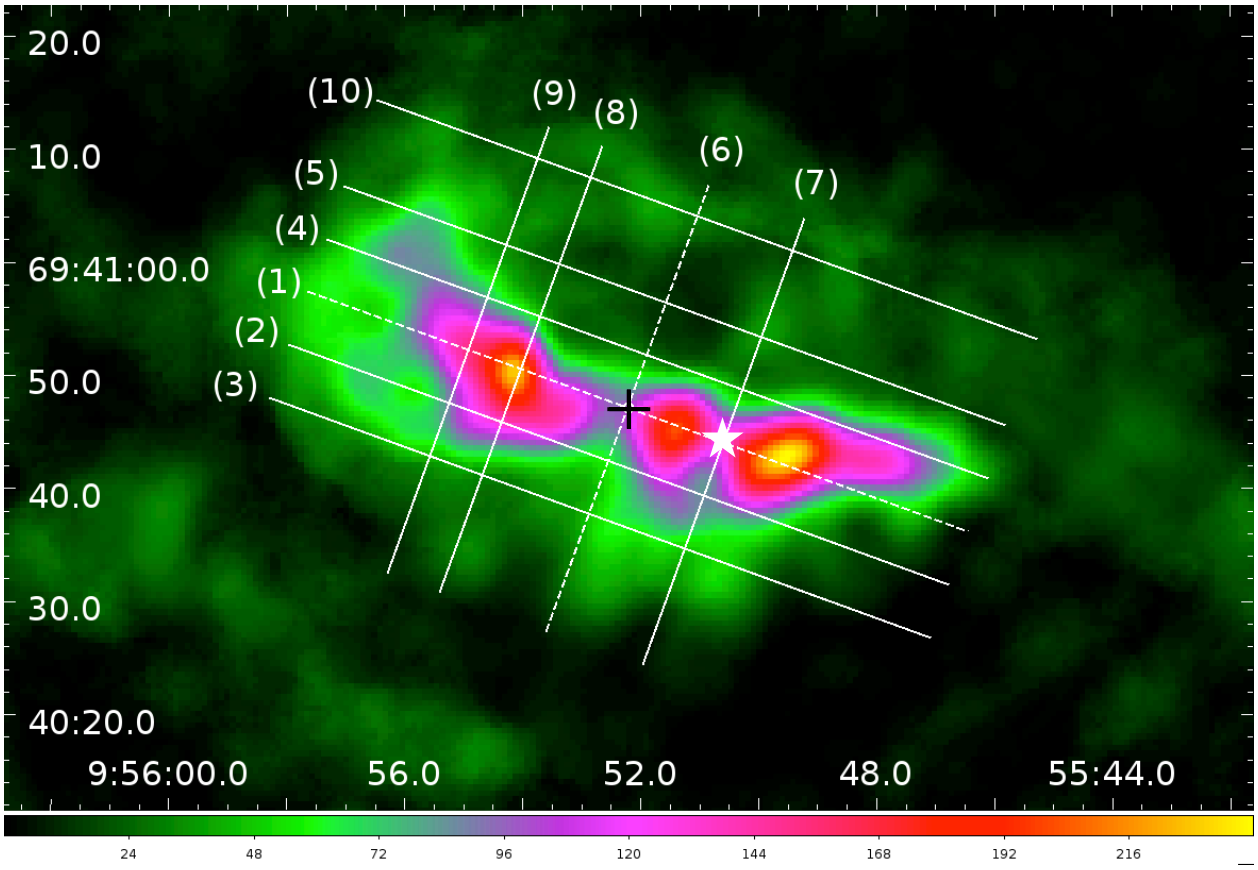

Figure 5.16: Slices of the data cube presented as PVDs in the figures below. The black cross where the dashed lines (major and minor galactic axes) intersect is at $(\alpha, \delta)_{\mathrm{J2000}} = (9^{\mathrm{h}}55^{\mathrm{m}}52.2^{\mathrm{s}}, 69^{0}40'47.1'')$ from Walter et al. (2002). The white star indicates X-2, the brightest X-ray source in M82 (Stevens et al. 1999).

5.3 Nascent 300-pc outflows of molecular gas

In this section, we present evidence for young outflows of molecular gas in the region $\sim$ 300 pc from the nuclear ring. The line of evidence consists of kinematical features of the CO emission revealed in position-velocity diagrams (PVDs) and velocity dispersion maps. We begin discussion by exploring the PVDs at various slices of the data cube. Then, we identify the outflows and investigate their structure, kinematics and energetics. Lastly, we compare the CO (1-0) integrated intensity map with hot gas tracers (X-rays and Hα), radio continuum (SN remnants and H II regions), and the shocked gas tracer SiO (2-1).

5.3.1 Position-velocity diagrams

The data cube of the composite image of M82 was first analyzed by generating PVDs along different directions. The directions are shown in figure 5.16, and the result in figures 5.17 through 5.26. Slices (1) and (6) intersect at the center of the galaxy as major and minor axes; slices (2) and (3) provide evidence for a newly discovered outflow; slice (10) shows rotation 300 pc above the galactic plane. In addition, slices (1), (4) and (7) confirm previously found superbubble and reveal its complex structure which is observed north and south of the galactic plane; the outflow is found to be larger (300 pc) than previously reported (130 pc in Weiß et al. 1999; 105 pc in Matsushita et al. 2000).

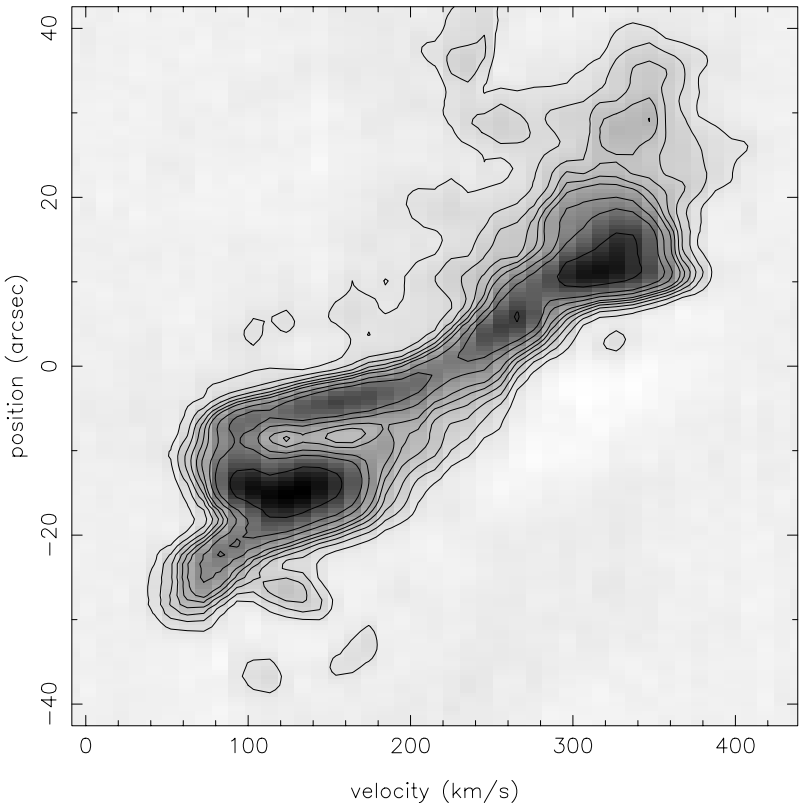

Figure 5.17: PVD at $(\Delta\alpha, \Delta\delta) = (0'', 0'')$ and P.A. $= 70^0$. Contours: 5%, 10%, 15%, 20%, 25%, 30%, 40%, 50%, and 75% of the peak value which is 2.6 Jy beam^{-1}, where Jy K^{-1} = 6.95. The position angle (P.A.) is defined as increasing from north to east. Slice (1) in figure 5.16.

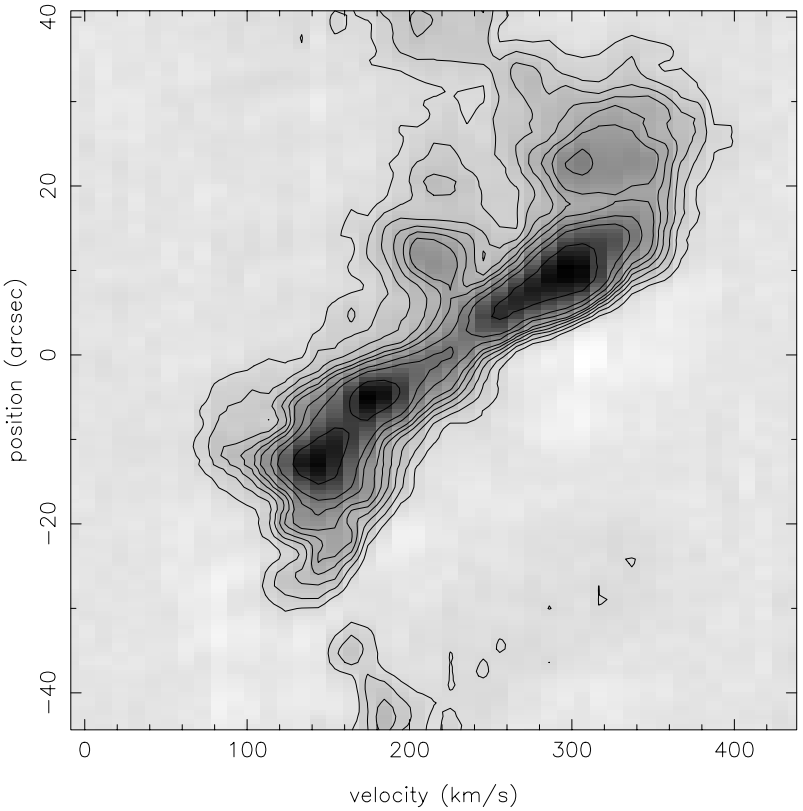

Figure 5.18: PVD at $(\Delta\alpha, \Delta\delta) = (+1.71'', -4.70'')$ and P.A. $= 70^0$; $Y = -5''$. The peak is 1.71 Jy beam^{-1}. Slice (2) in figure 5.16.

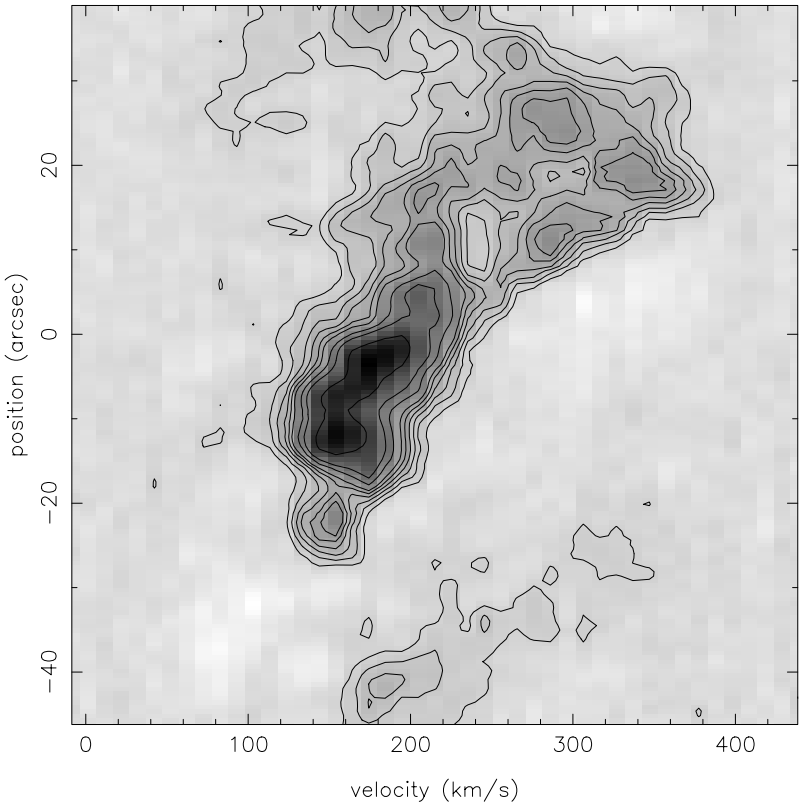

Figure 5.19: PVD at $(\Delta\alpha, \Delta\delta) = (+3.42'', -9.40'')$ and P.A. $= 70^0$; $Y = -10''$. The peak is 1.05 Jy beam^{-1}. Slice (3) in figure 5.16.

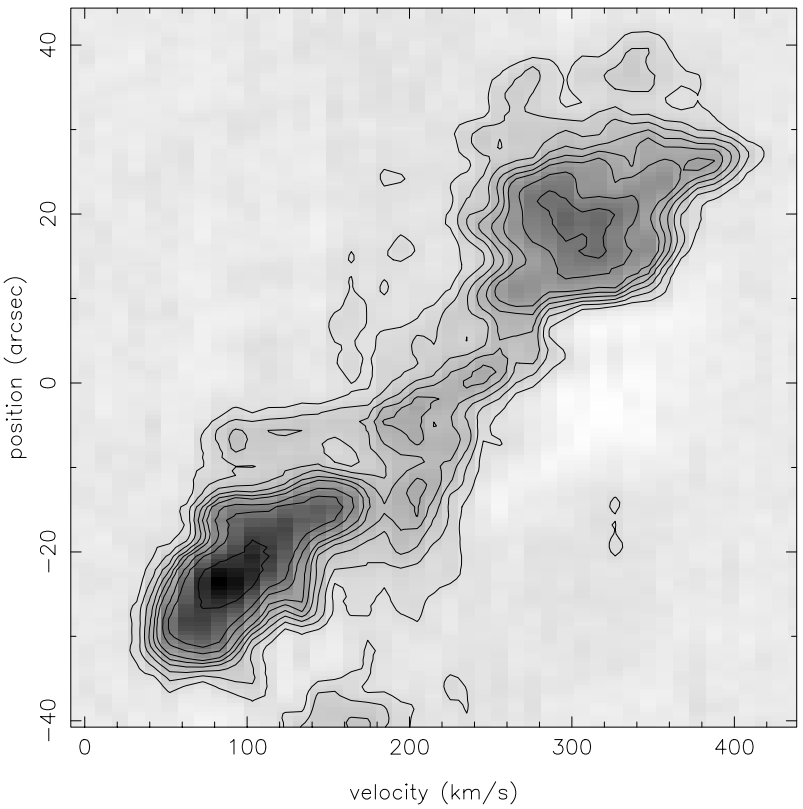

Figure 5.20: PVD at $(\Delta\alpha, \Delta\delta) = (-1.71'', +4.70'')$ and P.A. $= 70^0$; $Y = +5''$. The peak is 1.70 Jy beam^{-1}. Slice (4) in figure 5.16.

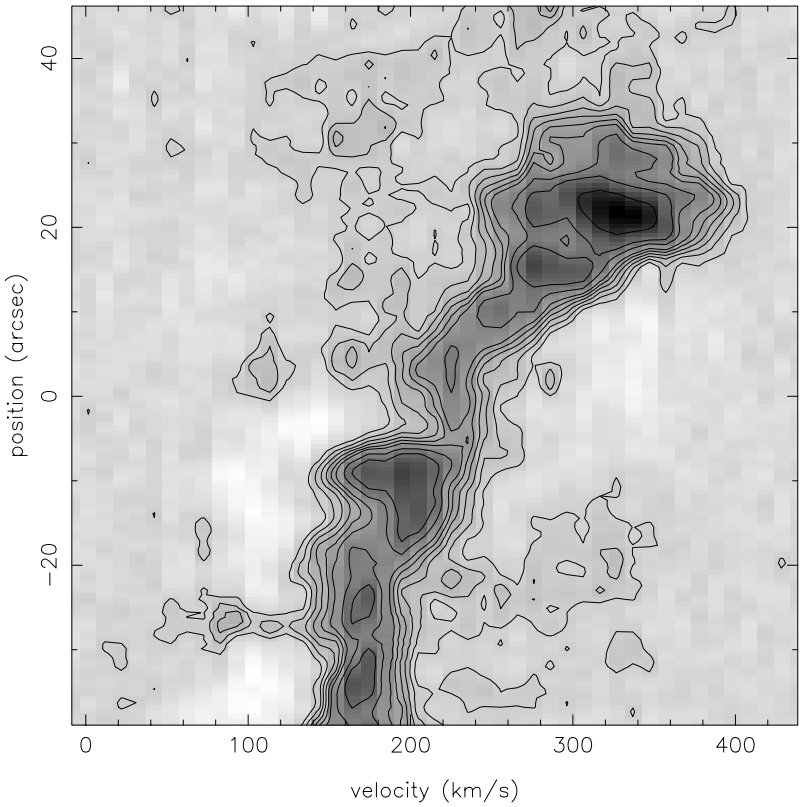

Figure 5.21: PVD at $(\Delta\alpha, \Delta\delta) = (-3.42'', +9.40'')$ and P.A. $= 70^0$; $Y = +10''$. The peak is 0.80 Jy beam^{-1}. Slice (5) in figure 5.16.

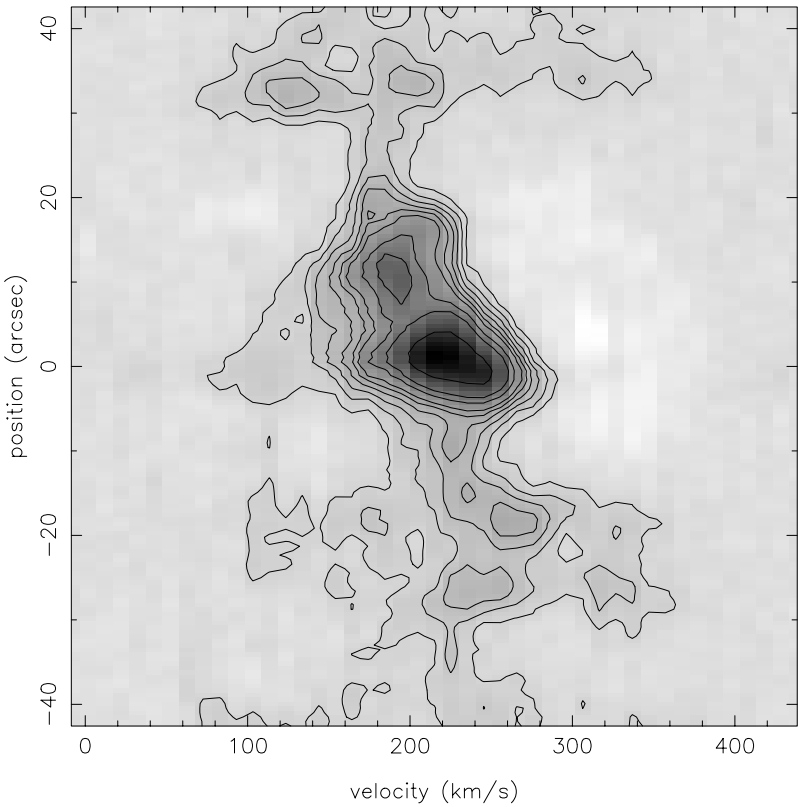

Figure 5.22: PVD at $(\Delta\alpha, \Delta\delta) = (0'', 0'')$ and P.A. $= 160^0$; $X = 0$. Note that negative values correspond to the northern side of the galactic plane. The peak is 1.34 Jy beam^{-1}. Slice (6) in figure 5.16.

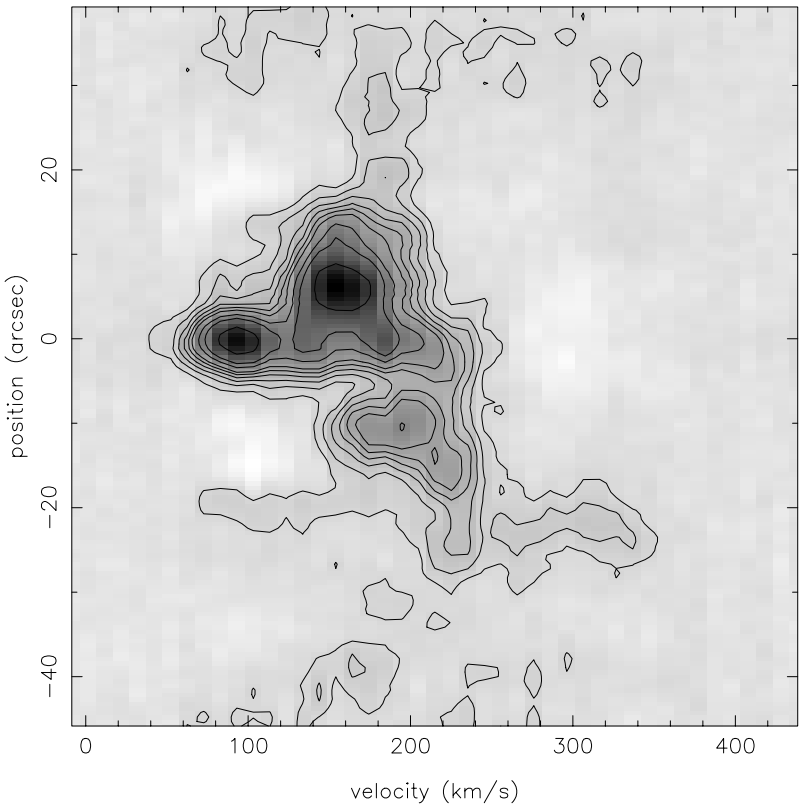

Figure 5.23: PVD at $(\Delta\alpha, \Delta\delta) = (-8.46'', -3.08'')$ and P.A. $= 160^0$; $X = -9''$. The peak is 1.40 Jy beam^{-1}. Slice (7) in figure 5.16.

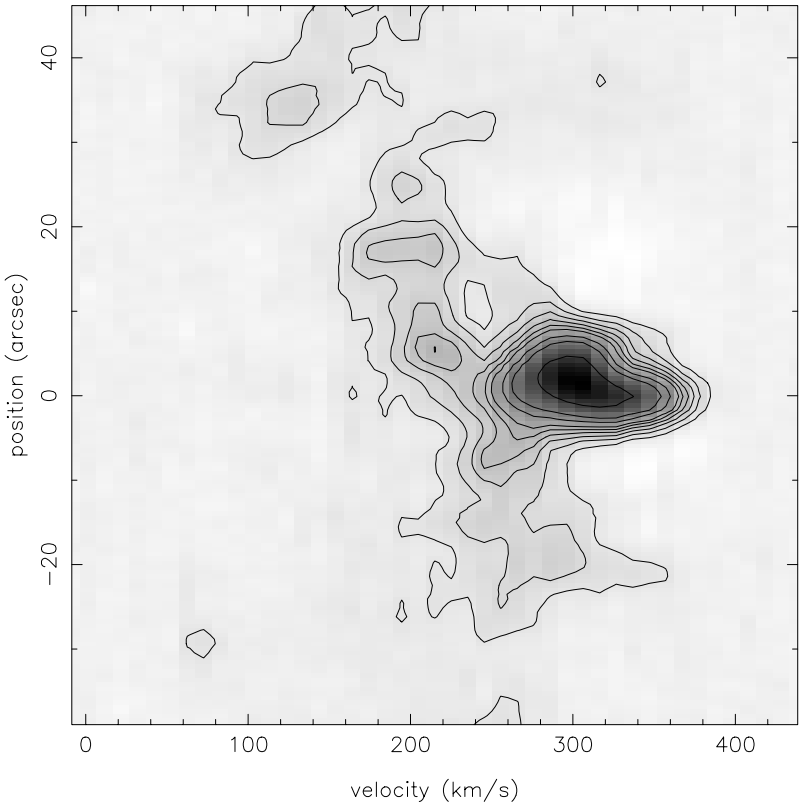

Figure 5.24: PVD at $(\Delta\alpha, \Delta\delta) = (9.40'', 3.40'')$ and P.A. $= 160^0$; $X = +10''$. The peak is 2.41 Jy beam^{-1}. Slice (8) in figure 5.16.

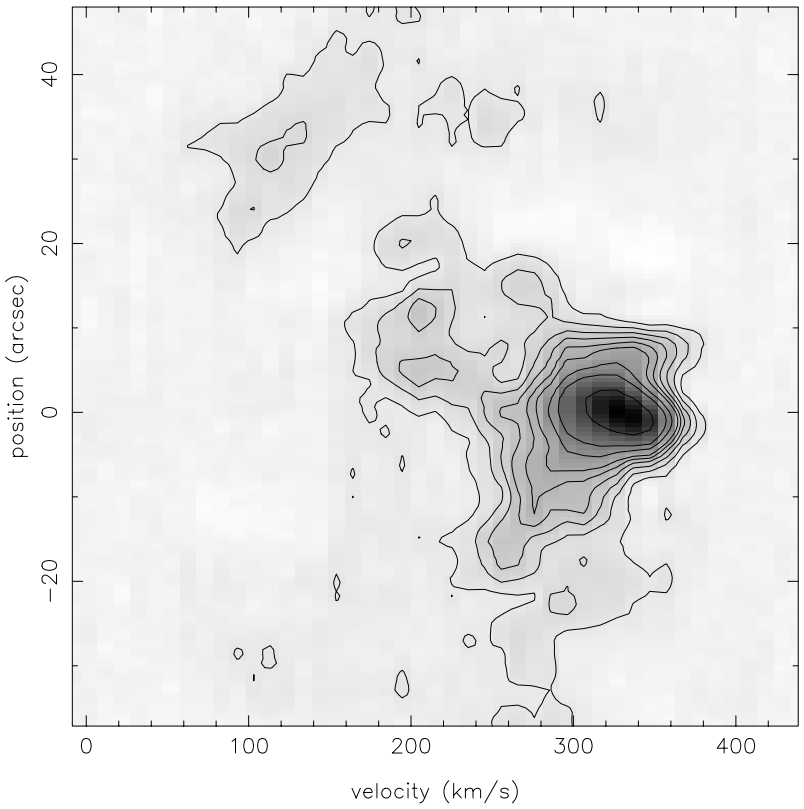

Figure 5.25: PVD at $(\Delta\alpha, \Delta\delta) = (14.1'', 5.1'')$ and P.A. $= 160^0$; $X = +15''$. The peak is 2.11 Jy beam^{-1}. Slice (9) in figure 5.16.

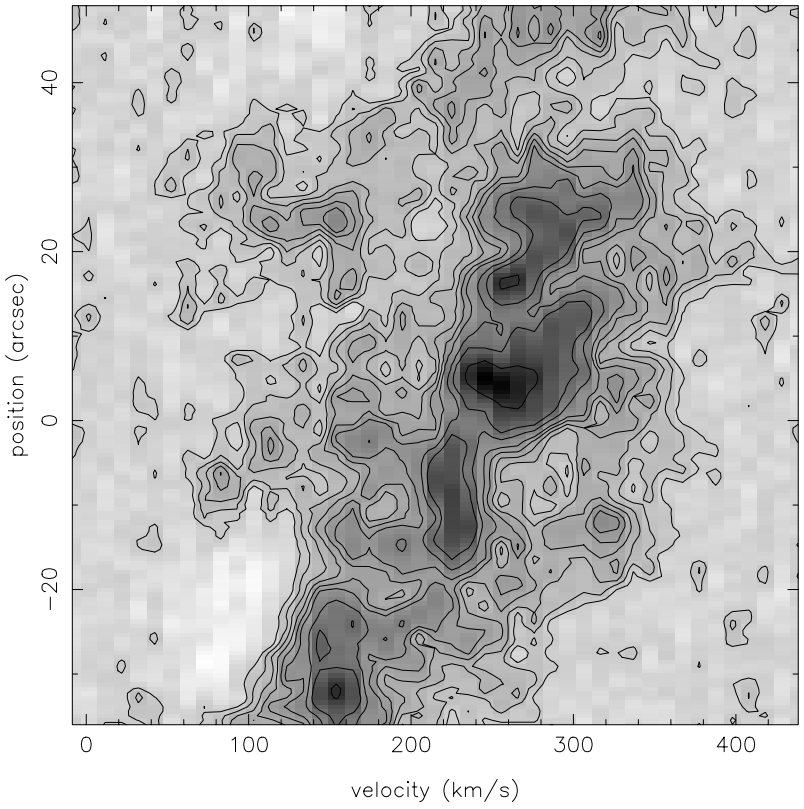

Figure 5.26: PVD at $(\Delta\alpha, \Delta\delta) = (-6.16'', +16.91'')$ and P.A. $= 70^0$; $Y = +18''$. The peak is 0.50 Jy beam^{-1}. Slice (10) in figure 5.16.

5.3.2 Superbubble around SNR 41.9+58 in the western lobe

Figures 5.17 and 5.23 show PVDs with slices through the data cube that intersect at the position of the brightest radio and X-ray source in M82, SNR 41.9+58. Most notably, in the PVD along the major galactic axis we recognize a large semi-circular structure with velocities strongly deviating from the expected rigid-body rotational velocity forming a "superbubble" (white star in figure 5.16). This feature was observed, e.g., in Hα, [N II] (O'Connell & Mangano 1978; Saito et al. 1984), [S II], [S III], O I, Ca II (McKeith et al. 1993), [Ne II] (Achtermann & Lacy 1995), radio continuum (Wills et al. 1999), CO (1-0) (Shen & Lo 1995; Matsushita et al. 2000), ^{13}CO (1-0), C^{18}O (1-0), CO (2-1) (Weiß et al. 1999), HCN (1-0) (Matsushita et al. 2000), as well as H I (Wills et al. 2002). Our data are in good agreement with all those by exhibiting a very similar position-velocity distribution. Weiß et al. (1999) suggested that the expansion velocity of the molecular gas shell is ≈ 45 km s^{-1}, with the bubble diameter of 130 pc and the mass of $\approx 8 \times 10^6\ M_\odot$. The age of the superbubble is $\simeq 1 \times 10^6$ yr, and its kinetic energy 2×10^{54} erg. Matsushita et al. (2000) similarly found $\simeq (1-2) \times 10^6$ yr, although with a higher expansion velocity of 50-100 km s^{-1}.

We find compelling evidence that the expanding shell in the outer layer of the superbubble has been broken, so that the expansion at higher distances (up to $20''$ or approximately 340 pc) from the superbubble center is observed as two prominent spurs (figure 5.27 (b)), in addition to the arc-like structure found in Weiß et al. (1999) and Matsushita et al. (2000). Also, our PVD suggests a maximum expansion velocity of ~ 70 km s^{-1}, in agreement with previous studies. The expansion velocity of 70 km s^{-1} yields a timescale of $t_{\rm dyn} \sim 4.6 \times 10^6$ yr (assuming the maximum distance of $20''$), several times larger than estimated in Weiß et al. (1999) and Matsushita et al. (2000). Another implication is the energy of the shell. Weiß et al. (1999) estimated $E_{\rm k} \approx 1.6 \times 10^{53}$ erg as 10% of the energy in the bubble's hot gas. This was calculated by using $8 \times 10^6\ M_\odot$ as the H_2 mass (with the conversion factor $X_{\rm CO} = 1.2 \times 10^{20}$ cm^{-2} K^{-1} km^{-1} s). Since the CO emission detected in the superbubble of our map is several times more extended, the energy of the shell is correspondingly higher, as shown below.

For the first time, we find evidence of expanding structure north of the galactic plane with respect to the center of the superbubble (white star in figure 5.16). This is obvious from the integrated intensity map (e.g., figure 5.16), but also from the PVD 5.23 where a horizontal feature is observed $-10''$ from the slice center (SNR 41.9+58). The symmetry between the structure south and north of the SNR can be easily explained only as originating from the same source and expanding toward both directions perpendicular to the galactic plane. Although fainter compared to the southern component, the northern shell is observed to behave similarly: velocity width $\simeq 140$ km s^{-1} which gives an expansion velocity of 70 km s^{-1} at a height from the galactic plane of $\simeq 20''$ corresponding to 340 pc. Additional evidence for the northern shell is found in figure 5.20, where we note an arc-like structure at $V_{\rm LSR} \simeq 200$ km s^{-1} and $-15''$. This PV slice is $5''$ north of the galactic plane and parallel to it (position angle 70^0). The northern shell is in good spatial correlation with the ROSAT HRI X-ray image published in Bregman et al. (1995) and compared with CO in Weiß et al. (1999). Weiß et al. (1999) did not detect CO emission in the northern X-ray spur, where our maps clearly show the molecular gas counterpart. Therefore, we conclude that the western lobe of the nuclear ring hosts a 300-pc outflow of molecular gas formed $\sim 4.6 \times 10^6$ years ago.

5.3.3 Discovery of a molecular-gas outflow in the eastern lobe

In figures 5.17, 5.18 and 5.19, we present PVDs of slices through the data cube parallel to the major galactic axis at distances $0''$, $5''$ and $10''$ from the midplane (all at the position angle 70^0). As discussed above, slice (1) revealed the superbubble in the western lobe of the nuclear ring. In the eastern part, we find broadened velocity line width at $X \sim 15''$ from the center, although dominated by rigid rotation characterized by linear distribution of CO emission in the PVD. However, when slices are inspected

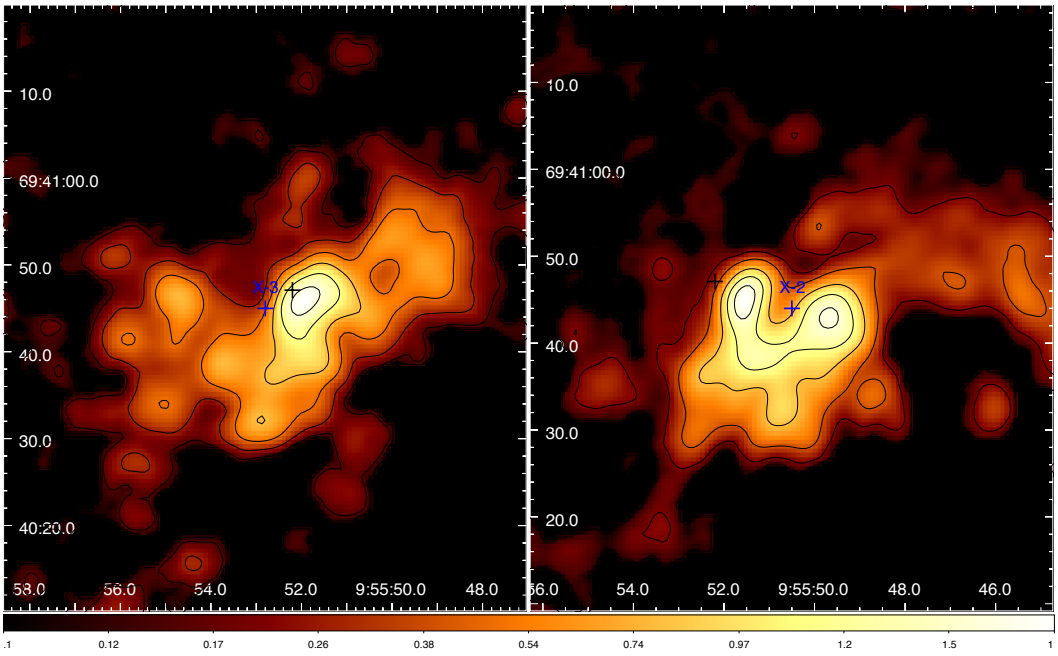

Figure 5.27: Nuclear molecular-gas outflows unveiled in channel maps: eastern lobe at $V_{\rm LSR} = 205$ km s^{-1} (left), and western lobe at $V_{\rm LSR} = 164$ km s^{-1} (right), integrated as one channel of width 10.16 km s^{-1}. Contours: 0.1, 0.2, 0.4, 0.8, 1.2, 1.6 Jy beam^{-1}. The black cross marks the galactic center; the blue crosses mark the most luminous X-ray sources from Stevens et al. (1999).

at larger distances, 5″ and 10″ from the plane, the presence of large deviation from rigid rotation and line splitting becomes clear. This structure is newly discovered because CO emission was detected to a larger spatial extent and higher sensitivity in our combined CARMA-NRO 45m data compared with previous interferometer maps of Shen & Lo (1995), Weiß et al. (1999) and Matsushita et al. (2000).

Near position 20″ in PVDs 5.17, 5.18 and 5.19, we note extended velocity feature from 200 to nearly 400 km s^{-1}. The blueshift component (200-260 km s^{-1}) is rather weak in figure 5.17, becomes stronger in figure 5.18, and finally connects into two remarkable molecular gas arcs in figure 5.19. Figure 5.27 shows two channel maps where the outflows can be clearly seen. In subsections below, we focus on the new outflow in the eastern lobe, and then discuss the energetics of both outflows.

5.3.4 Expansion velocity, mass, and energy of the molecular gas outflows

In order to calculate the kinetic energy of the molecular gas outflow, we need to know its expansion velocity and total mass. First, we begin by estimating the expansion velocity, V, from a geometrical model.

We assume that the outflow has spherical symmetry in the nuclear ring, as shown in figure 5.28. Thus, the line width at the base of the outflow visible in PVDs in figures 5.17 and 5.28 (bottom panel) should reveal the maximum velocity present in the molecular gas. This would be the upper limit for the outflow. On the other hand, figure 5.28 shows the projected velocities in the midplane and south of it. The velocity widths are similar and suggest a maximum deprojected expansion velocity of 80 km s^{-1}. Note that most of the molecular gas in the outflow has lower velocities, close to the average of ~ 50 km s^{-1} in the eastern, and ~ 45 km s^{-1} in the western outflow, the latter in agreement with Weiß et al. (1999) and closer to the estimates for an expanding shell of atomic gas of 29 km s^{-1} observed in the H I 21-cm line (Wills et al. 2002). The lower values will be used in deriving the kinetic energy and momentum.

The derived expansion velocity suggests that the age of the outflows is of the order of 5 Myr.

This is larger than previously estimated ($\sim$ 1 Myr), and is a significant fraction of the time that takes the gas to complete a circle around the center. At a distance of 340 pc (20″) from the center, the rotational velocity is $\simeq$ 120 km s^{-1}, so it takes $\approx$ 24 Myr for the gas to complete its orbit. During this time, SN explosions would be able to create more shells and continuously supply the outflow with momentum within the nuclear ring rather than at one position. In addition, optical data (figure 5.31 below) indicate that the outflows consist of several shells and filaments that may have originated in a series of continuous ejections (SN explosions and stellar winds) and appear blended in the CO data. Therefore, it is likely that we observe a multitude of shells and filaments that form the outflows and expand from the energy-injection zone where much of the starburst activity is taking place. Resolving individual features would require sub-arcsecond resolution, so we discuss the structure simply as an outflow rather than a "shell". In all this complexity, however, we may distinguish one dominating shell which appears to be the one with a radius of about 100 pc in the western lobe, detected previously in [Ne II], CO, and H I (Achtermann & Lacy 1995; Weiß et al. 1999; Wills et al. 2002).

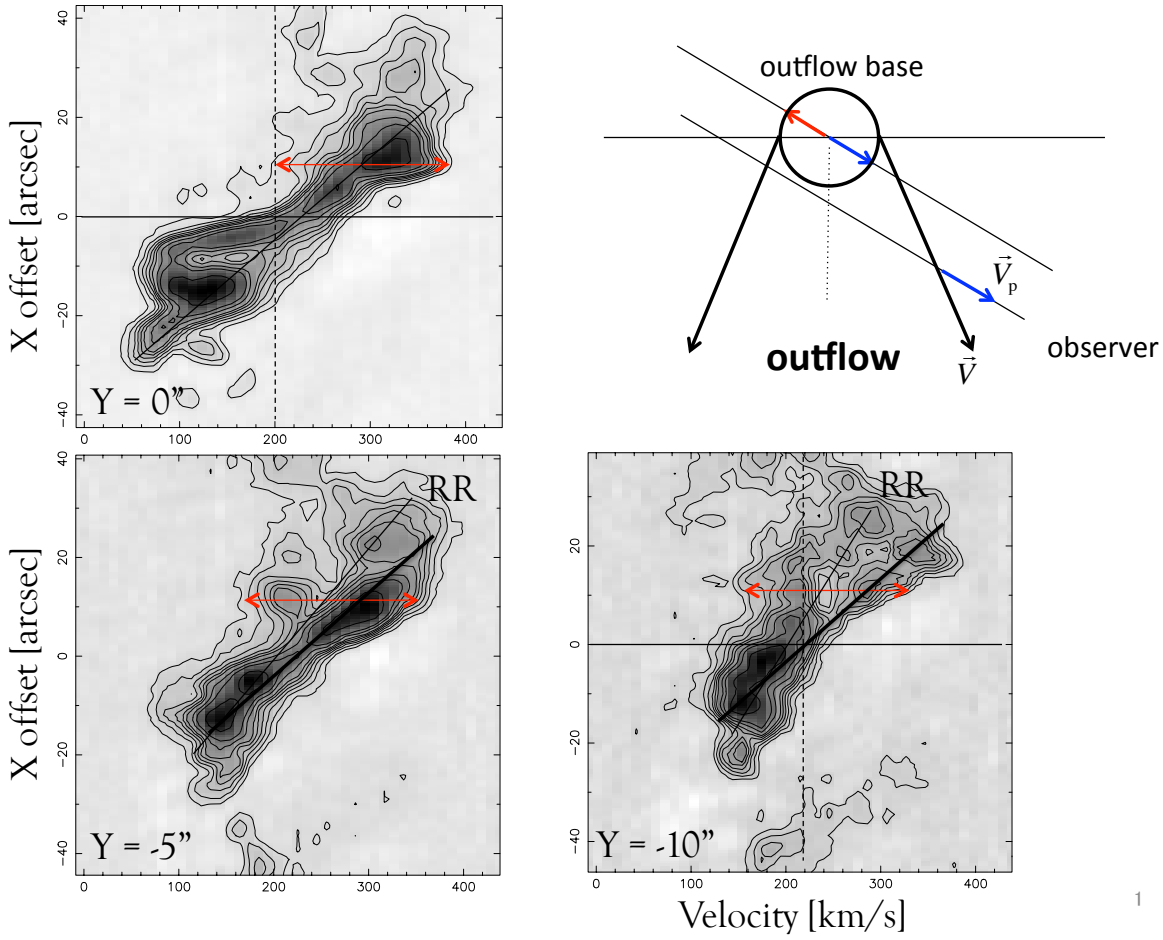

Figure 5.28: Geometry and expansion velocity of the eastern outflow. "RR" = rigid-body rotation. Note the decrease in average rotational velocity with distance from the midplane; this was interpreted as a consequence of the conservation of angular momentum (Seaquist & Clark 2001; Walter et al. 2002). The red line shows the velocity width. The presence of a redshifted component with the same gradient (bold black line) suggests that the rotational velocity up to $Y = -10''$ does not change and that the blueshifted component is part of the outflow.

The mass of the outflow can be calculated by applying a standard conversion formula that relates molecular gas mass (corrected for helium abundance) and CO luminosity, such as that in Bolatto et al. (2013a):

$$M_{\rm mol} = 1.05 \times 10^4 \left(\frac{X}{X_{\rm MW}}\right) D_L^2 (1+z)^{-1} S_{\rm CO}\Delta V. \tag{5.6}$$

Here, the adopted conversion factor of the Milky Way is $X_{\rm MW} = 2 \times 10^{20}$ cm^{-2} (K km s^{-1})$^{-1}$. The conversion factor for the nuclear region of M82 was measured by Weiß et al. (2001b) to be $X = 0.5 \times 10^{20}$ cm^{-2} (K km s^{-1})$^{-1}$, which is adopted here. $D_L = 3.53$ Mpc is the luminosity distance, z is redshift and $S_{\rm CO}\Delta V$ is the velocity-integrated flux density in Jy km s^{-1}. The flux density was calculated directly by using CASA Viewer after masking the regions where the expansion was detected. This is shown in figure 5.29.

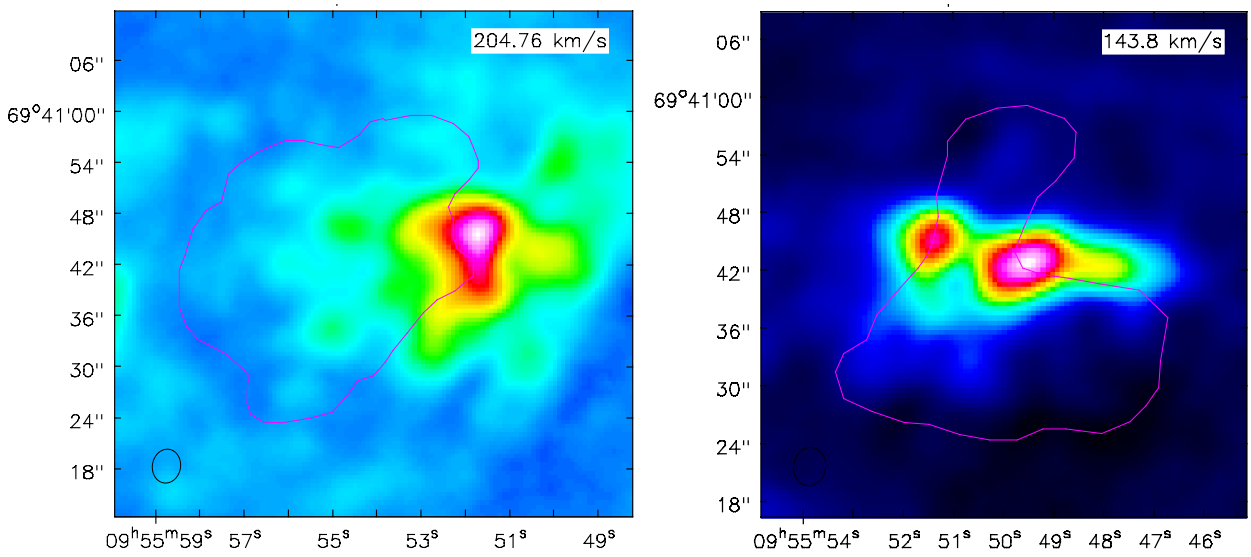

Figure 5.29: Integrated intensity maps of the molecular gas outflows. The integrated velocity range is: $V_{\rm LSR} = (160, 250)$ km s^{-1} for the eastern outflow (left panel), and $V_{\rm LSR} = (50, 240)$ km s^{-1} for the western outflow (right panel). Contours indicate the masked regions where the integrated flux density, $S_{\rm CO}\Delta V$, was calculated. The size and shape of these regions was estimated from the position-velocity diagrams and comparison with the B-band image (figure 5.31).

The kinetic energy is given by

$$E_{\rm k} = \frac{1}{2} M_{\rm mol} V^2, \tag{5.7}$$

and the mass outflow rate is

$$\dot{M} \approx \frac{M_{\rm mol}}{t_{\rm dyn}}. \tag{5.8}$$

The derived outflow properties are given in table 5.1.

The molecular gas outflows have similar maximum expansion velocities (70-80 km s^{-1}) and age (4-5 Myr) which suggests that the structures were formed in the same epoch. The mass and energy of the western outflow are a factor of two larger, but the size of ($20''$), derived from the PVDs and integrated intensity maps, is similar.

Strickland & Heckman (2009) have calculated the mass outflow rate in the hot (10^7 K) gas phase of the "wind fluid" in the inner 500 pc of the galaxy as $\dot{M}_{\rm h} \simeq 2.5\ M_\odot$ yr^{-1}. This number includes the initially cool and cold gas that was vaporized and added to the hot plasma. The hot outflow itself originates in SN ejecta and shocked stellar winds. Interestingly, although the mass outflow rate is a

Table 5.1: Properties of the molecular-gas outflows.

Parameter	Eastern outflow	Western outflow
Maximum expansion velocity $V_{\rm max}$ [km s^{-1}]	80	70
Average expansion velocity V [km s^{-1}]	50	45
Size d [arcsec]	20	20
Age $t_{\rm dyn}$ [yr]	4.0×10^6	4.6×10^6
Integrated flux density $S_{\rm CO}\Delta V$ [Jy km s^{-1}]	948	2008
Molecular-gas mass M [$M_\odot$]	3.4×10^7	6.7×10^7
Molecular-gas outflow rate $\dot{M}$ [$M_\odot$ yr^{-1}]	9	14
Kinetic energy $E_{\rm k}$ [erg]	0.8×10^{54}	1.2×10^{54}

Note. Conversion factor $X = 0.5\times10^{20}$ cm^{-2} (K km s^{-1})$^{-1}$.

factor of few lower than that of the molecular gas, its *momentum* deposition rate is comparable, because the outflow velocity of the hot gas is estimated to be of the order 1400-2200 km s^{-1} (Strickland & Heckman 2009). By comparison, the velocity of the Hα-emitting warm ionized gas is 600-650 km s^{-1} up to 2 kpc above the midplane (McKeith et al. 1995; Shopbell & Bland-Hawthorn 1998). While the hot gas has velocity higher than the escape velocity ($V_{\rm e} = 200-460$ km s^{-1}), the molecular gas is largely unable to climb the potential well and hence is likely to fall back to the disk.

5.3.5 Feedback on star formation in the molecular gas ring

In order to compare the mass of the molecular gas in the outflows with that in the entire nuclear ring, we derive the ring mass from the total integrated intensity map (figure 5.30). The extended molecular gas ring within the integrated region ($S_{\rm CO}\Delta V = 7461$ Jy km s^{-1}) is shown in figure 5.30. When converted to mass, we find 2.3×10^8 $M_\odot$ where $X = 0.5\times10^{20}$ cm^{-2} (K km s^{-1})$^{-1}$ was assumed. This is in agreement with the mass given in Walter et al. (2002). Note that the flux density in the outflows is 2956 Jy km s^{-1} (table 5.1), which is $\sim 40\%$ of the total mass in the ring: nearly one half of the mass of ring's molecular gas is in the young outflows! Since the outflow mass, $M_{\rm mol}$, cannot exceed the total mass in the ring, this gives us a natural upper limit for $M_{\rm mol}$.

With the current mass outflow rate of 23 $M_\odot$ yr^{-1} in the outflows combined, the ring may lose at least one half of its total molecular gas in $\sim 1\times10^7$ yr. Comparing with the escape velocity, $V_{\rm e} \gtrsim 200$ km s^{-1}, we can predict that most of the ejected gas cannot escape from the galaxy, and is likely to re-supply star formation in the future.

The flux density integrated over the entire area where CO was detected is 13682 Jy km s^{-1}.

5.3.6 The streams

The molecular gas streamers were first reported by Walter et al. (2002) as one in the east (S1) and three in the west (S2-S4) part of the galaxy). We confirm the existence of the streamers in addition to a new feature in the west part that was revealed already from our single dish data as the "western arm". As shown in figure 5.30, most of the CO emission arises from the nuclear ring, but there is substantial component in the streams, which could contribute a comparable mass of the molecular gas if a higher conversion factor ($X_{\rm CO}$) is used, as proposed by Walter et al. (2002). Which $X_{\rm CO}$ is appropriate will, on the other hand, depend on the nature of streams and the physical conditions of its

gas. The nature of the streams and their importance in feeding the nuclear ring is discussed further below.

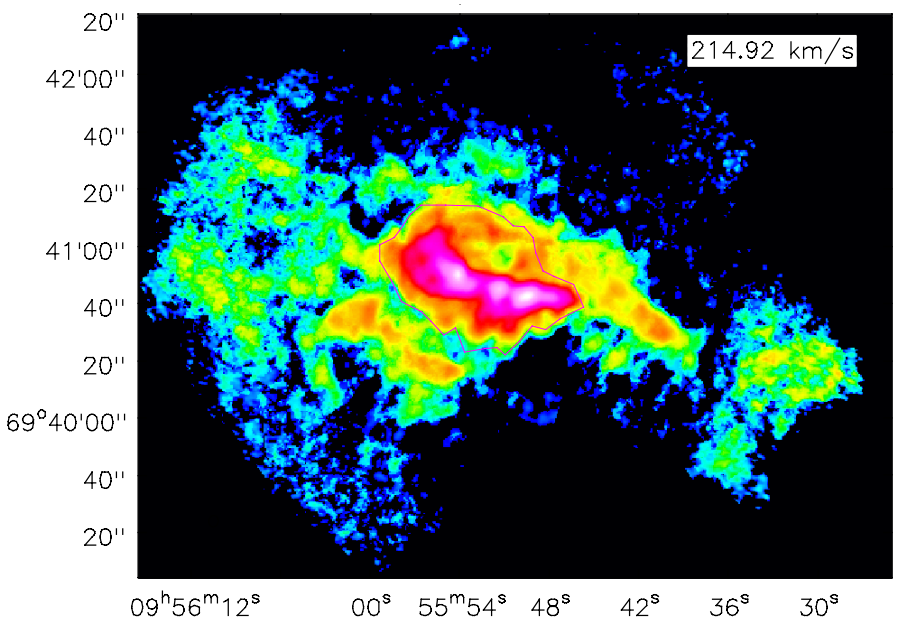

(a)

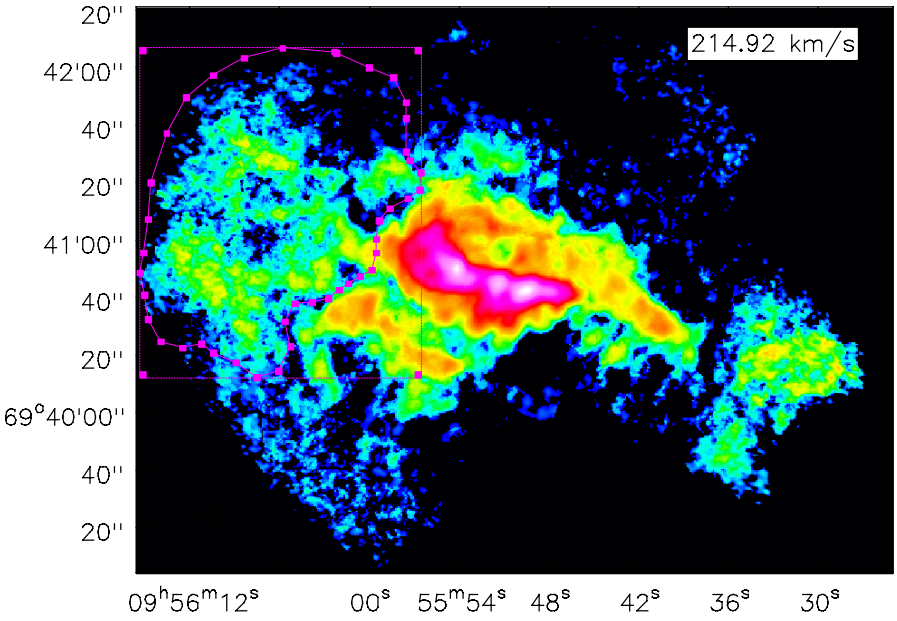

(b)

Figure 5.30: *Top.* Nuclear ring; the flux density is 7708 Jy km s^{-1}. *Bottom.* Eastern streamer; the flux density is 1757 Jy km s^{-1}.

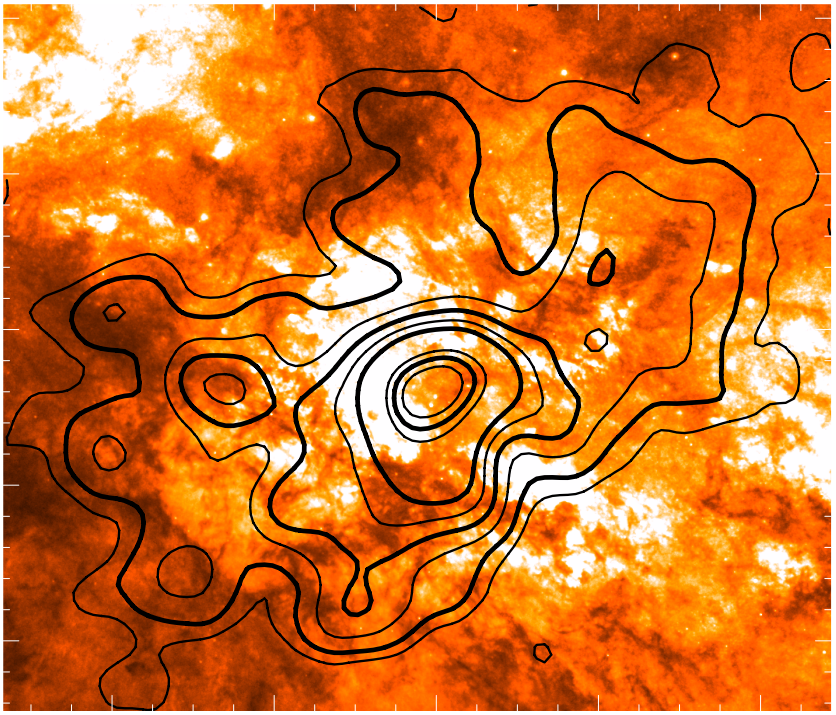

(a)

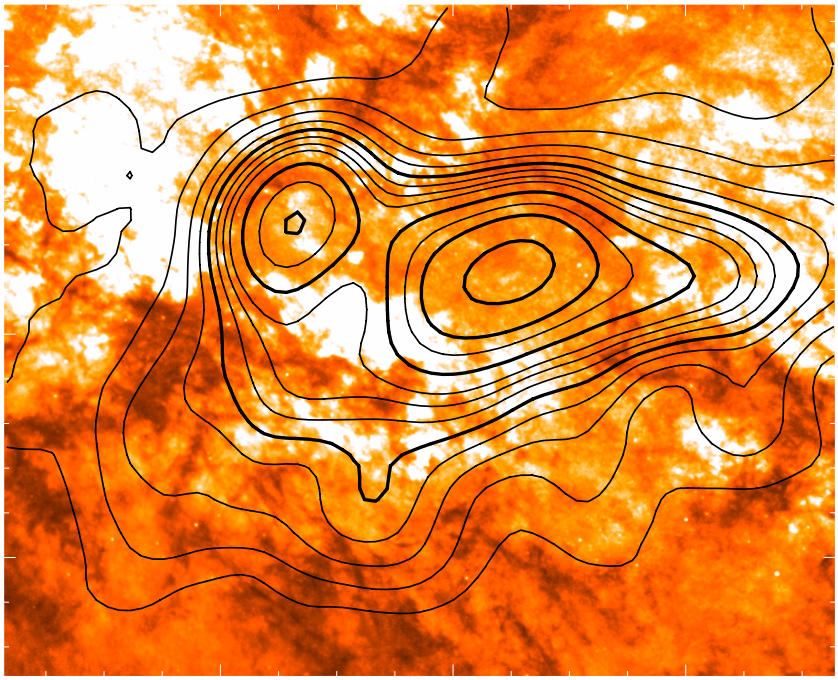

(b)

Figure 5.31: Young nuclear outflows: CO (1-0) contours superimposed on a B-band image (credit: Hubble Heritage Team); cf. figure 5.12. The integrated intensity maps of the outflows are the same as in figure 5.27. Dark regions trace absorption by dust grains.

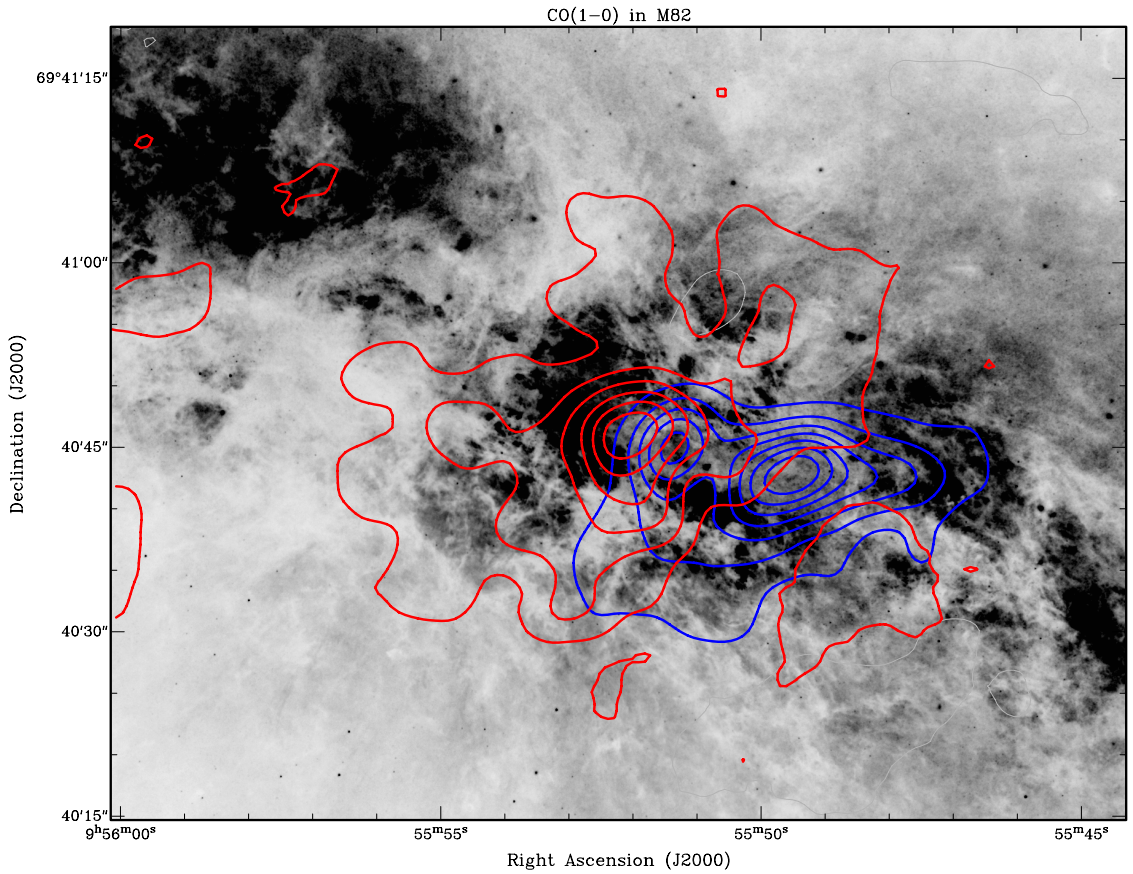

Figure 5.32: CO (1-0) contours of the eastern (red) and western (blue) shells overlaid on a B-band image (negative) taken with the Hubble Space Telescope (Image credit: Hubble Heritage Team). Bright regions trace the dust.

5.3.7 Age of the starburst

The age of the starburst in M82 is crucial to study the relation between star formation and galactic wind feedback. O'Connell et al. (1995) suggested a timescale no older than 50 Myr. In comprehensive studies of the nuclear region, Rieke et al. (1993) proposed a two-burst model with starburst episodes that peaked between 40 and 5 Myr ago; one of their successful models allows peaks at 13 and 5 Myr ago. Similarly, Förster Schreiber et al. (2003) constrain the starburst episodes to peaks 10 and 5 Myr ago. The later study was done by using observational data from their IR instrument and from Infrared Space Observatory (ISO) and compared with model predications for radiation in the range from 1 to 45 μm. For instance, the ratio of [Ne III]/[Ne II] and the ratio of the bolometric luminosity of OB stars to Ly continuum, $L_{\rm bol}^{\rm OB}/L_{\rm Lyc}$ was used as a tracer of young massive stars, i.e., the young starburst. Old stellar populations were examined by using the equivalent widths of CO in near-IR, as well as the mass-to-light ratio, $M_{\rm stars}/L_K$. The latter is about 1 which suggests the presence of many red supergiants with an upper limit of 50 Myr for their age. The best fit for the model yielded a *first starburst episode* between 8 and 15 Myr ago (peak at 10 Myr ago), and a *second starburst episode* 4 to 6 Myr ago. We adopt the two-burst models of Rieke et al. (1993) and Förster Schreiber et al. (2003) with starburst ages of 10 (first) and 5 (second) Myr ago. However, it should be noted that star formation in M82 probably has been *continuous* even before the first episode due to a number of observational evidence that include the Hα "Cap region" 11 kpc deep in the galactic halo and the fact that star clusters older than 10 Myr are difficult to detect (see Strickland & Heckman 2009). Also, since starburst needs time to propagate, it is reasonable that the first episode did not entirely end when

the second started. To accomodate the observations, we adopt that the timescale of the first starburst is between 8 and 50 Myr ago.

5.3.8 Molecular-gas outflow and hot diffuse gas

Molecular gas outflows are being driven from the galactic nuclear region at a velocity of ≈ 50 km s^{-1}. Although the central region of M82 cannot be seen clearly because the galaxy is inclined by $\sim 80^0$ with respect to the observer, extra-planar regions can be investigated because there is less contamination from the galactic disk. Figure 5.33 shows CO contours superimposed on a Chandra image of diffuse hot gas radiating soft X-rays from 0.7 to 1.1 keV (Kilgard et al. NASA, CXC). This emission is related to the starburst and hot-gas outflow from the central 400-pc region. Young massive stars create H II regions and blow strong stellar winds, SN explosions eject layers of gas and dust into the ISM and heat the ambient medium by shocks (collisions); perhaps as much as 90% of the released kinetic energy is radiated away, although Strickland & Heckman (2009) suggest that at least 30% of the energy is used to heat the ambient ISM. The dusty nuclear ring absorbs much of this high-energy radiation, including that coming from the northern side of the galaxy (far side), but we can see the southern side and compare with the distribution of the molecular gas. Curiously, there is a correlation between the outflows of molecular and hot gas. We see two major plumes of hot gas which appear to correlate with the CO emission contours as if pushing/breaking through the molecular gas. From figure 5.34, we note that these plumes clearly extend farther out than the CO emission, which suggests that the hot gas has broken the molecular-gas shells and vented out, in agreement with observations of warm ionized gas, which has expansion velocities of ~ 600 km s^{-1} (Shopbell & Bland-Hawthorn 1998). In figure 5.27 we note that the brightest X-ray sources in M82, denoted by X-2 and X-3, lie at the base of the outflows. The origin of the hot and cold outflows is clearly related to the inner side of the nuclear ring.

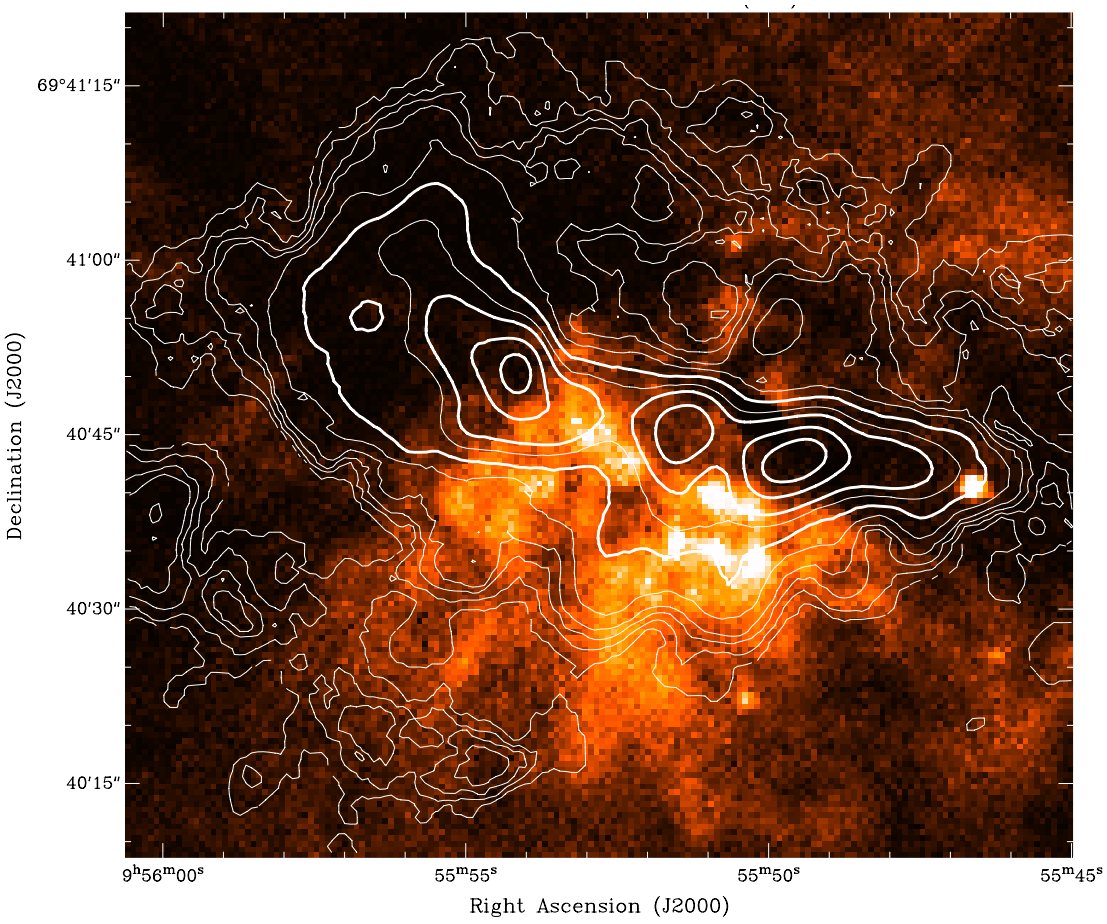

Figure 5.33: CO (1-0) contours from this work superimposed on a soft-X-ray image (0.7-1.1 keV) taken with Chandra (Kilgard et al. NASA, CXC).

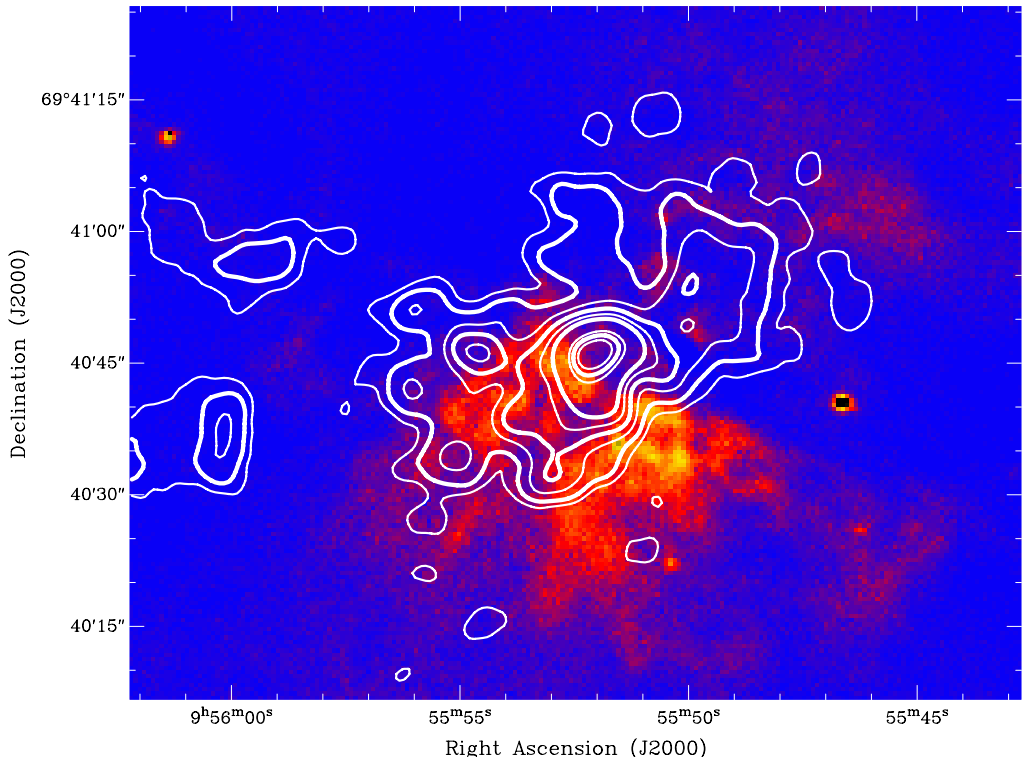

(a)

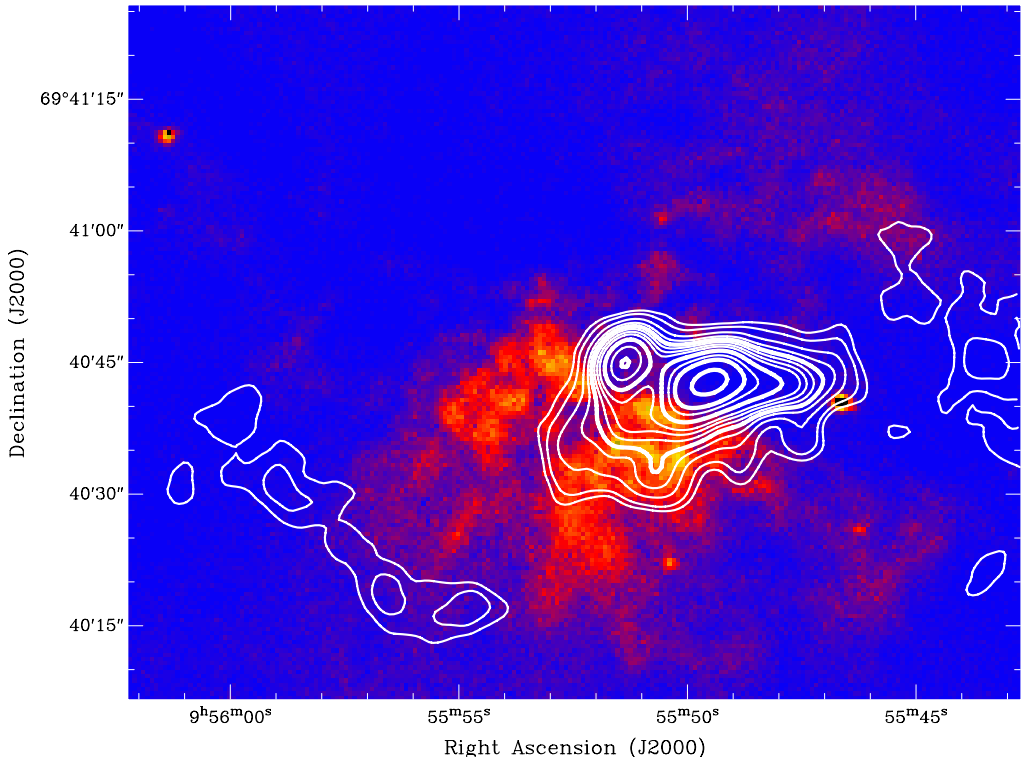

(b)

Figure 5.34: Expanding molecular gas outflows unveiled in channel maps. CO contours are superimposed on a 0.7-1.1 keV Chandra image (NASA/CXC/Wesleyan/R. Kilgard et al.).

5.3.9 Supernova remnants

Since M82 is a starburst galaxy, the state of the ISM is strongly influenced by feedback from vigorous star formation. The most powerful energy sources in an advanced starburst are SN explosions. Figure 5.35 shows the distribution of SN remnants in the disk of M82 observed at 1.7 GHz with an interferometer (Fenech et al. 2010). Most of the remnants have total flux densities $S_\nu < 10$ mJy, but several of them are as bright as $10 < S_\nu/\mathrm{mJy} < 30$. The brightest of them is located between the western peaks, with a flux density of $S_\nu = 38.25$ mJy. These SN remnants were not responsible for the outflow of molecular gas because they are relatively young (~ 100 yr), but reveal the starburst zone within the past several million years. Since frequent SN explosions occur in regions where massive stars are born, dense population of SN remnants is related to regions of massive-star formation. On the other hand, in such regions (e.g. young star clusters), we also expect strong stellar winds and radiation pressure. Figure 5.35 reveals that the distribution of SN remnants in the nuclear ring is fairly uniform, and there is marginal anti-correlation between the most powerful ones ($S > 10$ mJy) and CO peaks.

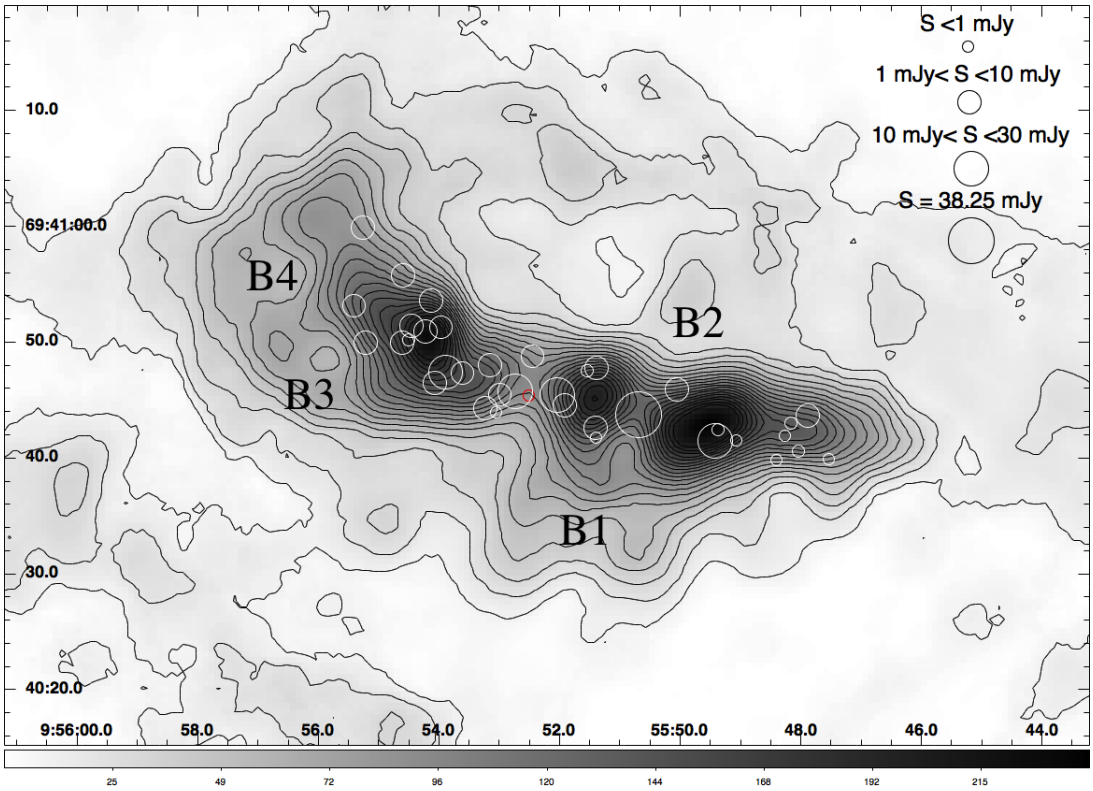

Figure 5.35: Supernova remnants in M82 observed at 1.7 GHz with MERLIN (Fenech et al. 2010). The circle size indicates the total flux density as shown in the upper right corner. The small red circle marks the position of the peculiar source reported in Muxlow et al. (2010). Extended structure of CO emission is denoted by B1-B4.

5.3.10 Shocked molecular gas in the outflow

Following the discovery of molecular gas outflows in our Galaxy and other galaxies, it became evident that while some molecular species show enhancement in such interstellar environments, others are under-abundant (Schilke et al. 1997b). In particular, theoretical and observational studies of elemental abundance and emission brightness show discrepancies that lead to the conclusion that some chemical elements are locked into dust grains and depleted from the gas phase. This is observed for most

species: even abundant molecules such as CO can become depleted by a factor of a few in dusty, dense (dark) molecular clouds (Draine 2011).

One molecular species that exhibits bright emission from rotational transitions mostly in *dense shocked gas* is the silicon-monoxide (SiO). The abundance and production of SiO in shocks was discussed in Schilke et al. (1997b), where it was concluded that fast shocks (shock velocity $v_s > 25$ km s^{-1}) significantly increase the brightness of SiO emission. This is a consequence of energetic collisions between heavy atomic nuclei (heavier than He) and dust grains in shocked gas. The grains are composed of Si-bearing cores and easy-evaporating mantles. Although the mantles can be eroded even at low velocities of $v_s < 15$ km s^{-1}, higher projectile energies are necessary to inflict *mechanical sputtering* on grain cores. Once the cores have been dissolved into constituent atoms, SiO is created mainly via the oxidation reactions:

$$\begin{aligned} \mathrm{Si} + \mathrm{O_2} &\rightarrow \mathrm{SiO} + \mathrm{O} \\ \mathrm{Si} + \mathrm{OH} &\rightarrow \mathrm{SiO} + \mathrm{H} \end{aligned} \tag{5.9}$$

SiO has allowed rotational transitions in the microwave regime. and thus has been used as a tracer of the gas disturbed by fast shocks in several Galactic and extra-galactic studies [e.g., García-Burillo et al. (2010), for NGC 1068; Usero et al. (2006), for IC 342; and the references therein]. Unlike fast shocks, slow shocks merely destroy the grain mantle, hence increase the abundance (and brightness) of species such as the methanol CH_3OH.

Figure 5.36 shows contours of the SiO (2-1) emission superimposed on the combined integrated intensity image of CO (1-0); "RC" indicates the radio continuum chimney discussed in García-Burillo et al. (2001). This result shows that SiO is abundant in planar and extra-planar regions including those of the outflows discussed in this work, although the sensitivity and image fidelity in their measurement was insufficient to match up to our CO data.

5.3.11 Shells at the edge of the eastern lobe

Inspection of the integrated intensity map and channel maps lead us to notice shell-like structure in the westernmost part of the nuclear ring. To locate the shells, we have integrated the velocity range from 245 to 265 km s^{-1}. The result is shown in figure 5.37.

5.3.12 Flux density in the nuclear ring and outflow

In figure 5.38, we show an integrated flux density map of the emission related to the nuclear ring and outflow. The component was separated from the rest of the emission by inspecting the channel maps. The excluded regions consist of the western stream (connected nearly to the galactic nucleus), eastern stream, and eastern arm. The eastern stream is disregarded as part of the outflow because it is not correlated kinematically with the eastern side of the rotating ring. The geometry of the outflow (outflow walls and filamentary structure) is indicated in figure 5.39.

The flux density of this emission is 8810 Jy km s^{-1}, or about 65% of the total CO flux in M82. The total CO flux outside the nuclear ring is $\sim$ 3300 Jy km s^{-1}. Therefore, although we have investigated only the outflow closest to the ring, including the inner outflow up to 1 kpc above the midplane would increase the total mass for less than a factor of 1.5. This is of the same order as the uncertainty in the CO-H_2 conversion factor, and so we conclude that most of the molecular gas mass is within $|Y| = 20''$ from the nuclear ring. By comparison, flux density in the eastern stream is only 1803 Jy km s^{-1}, but if we use a Galactic conversion factor $X_{\mathrm{MW}} = 1.8 \times 10^{20}$ cm^{-2} K^{-1} (km s^{-1})$^{-1}$, the

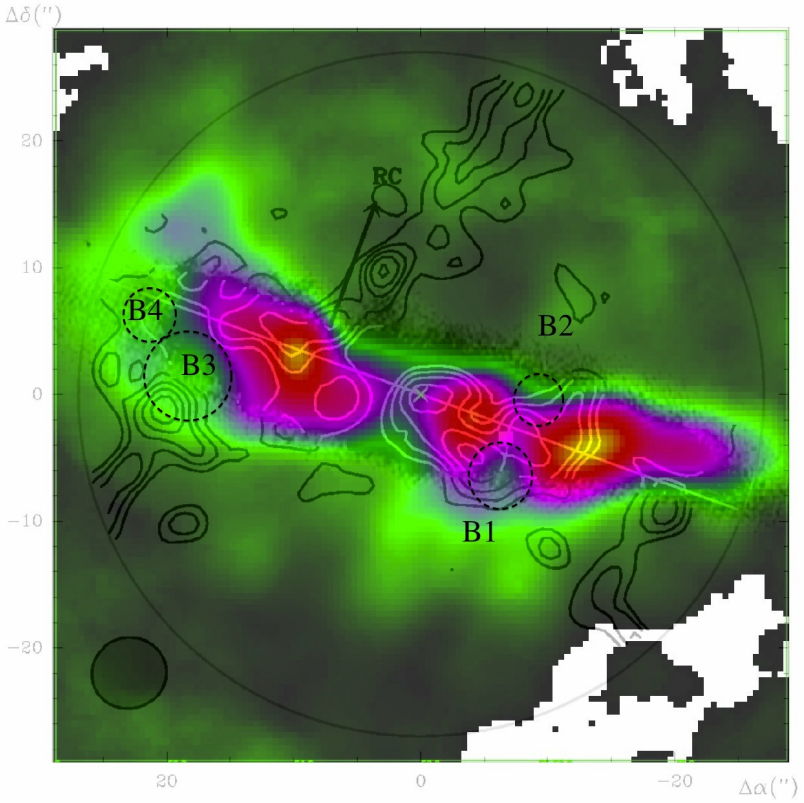

Figure 5.36: SiO (2-1) contours superimposed on the CO (1-0) image. The SiO map is from García-Burillo et al. (2001). The dashed lines indicate the molecular gas bubbles.

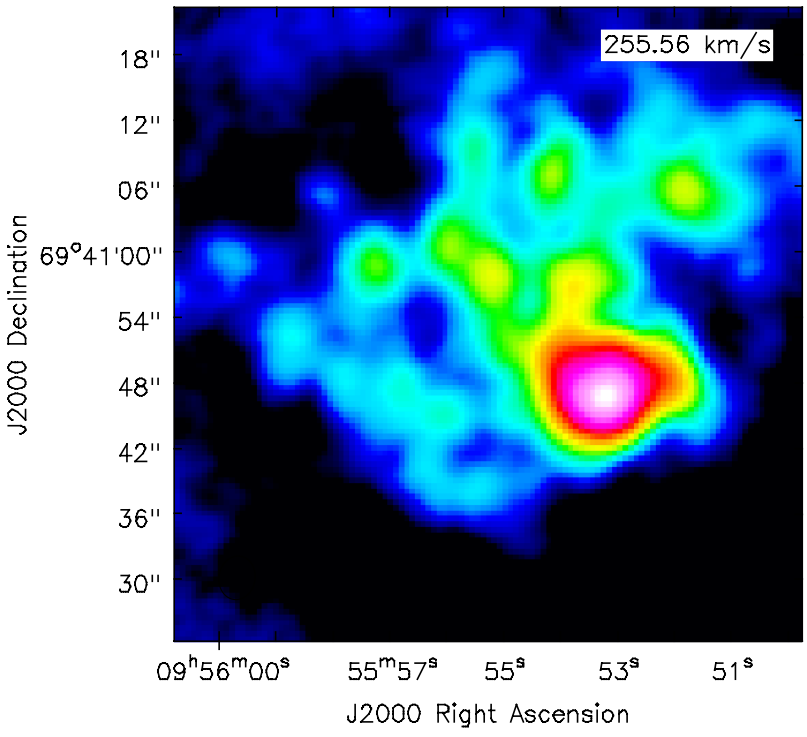

Figure 5.37: Molecular gas shells at the western edge of the nuclear ring. The intensity was integrated from 245 to 265 km s^{-1}.

masses become comparable. Including the western stream and arm too, the molecular gas mass in non-starburst regions becomes even larger than that in the nuclear ring and outflow. Further below, we discuss the possibility that the streams are related to supplying the nuclear ring with fresh molecular gas and maintaining the starburst.

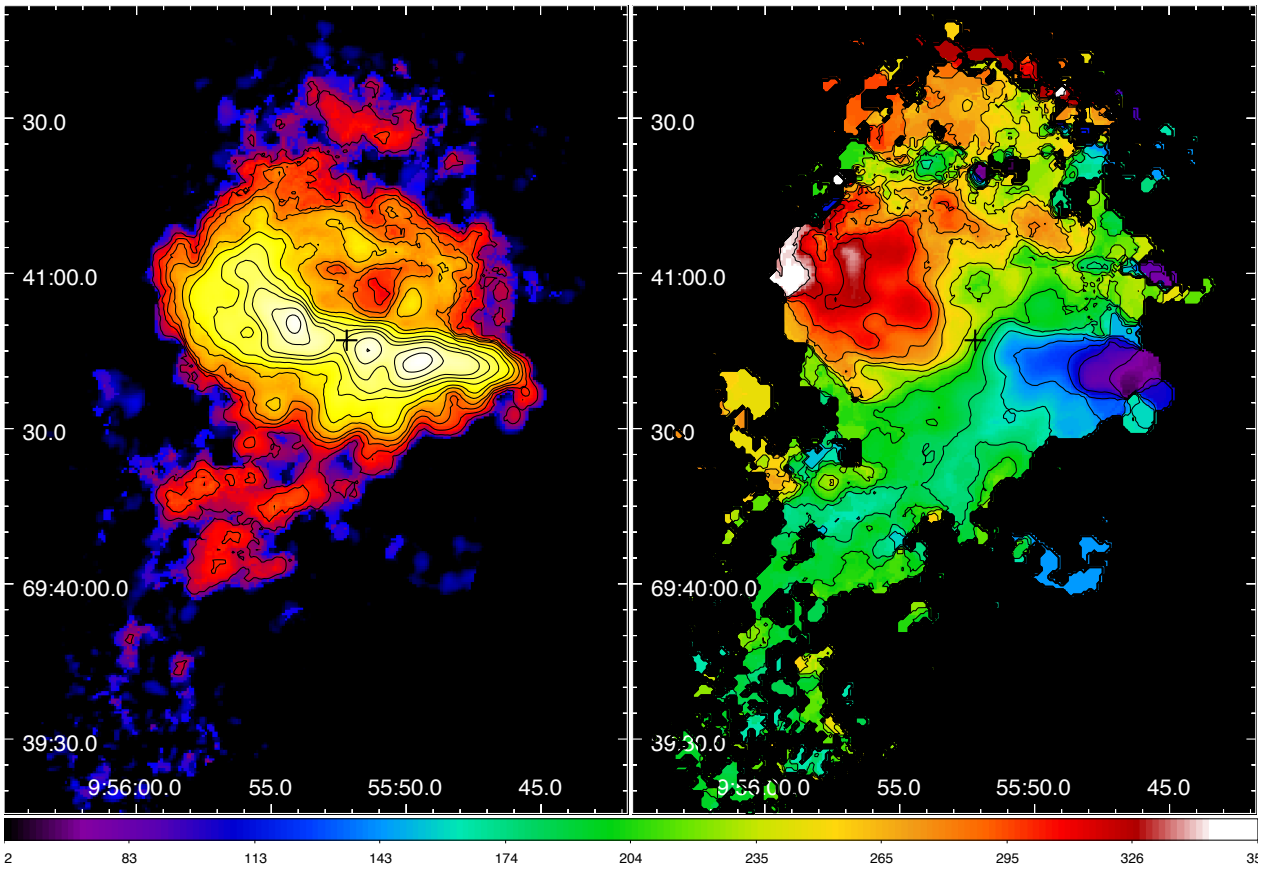

Figure 5.38: *Left.* Integrated intensity map of the nuclear ring and outflow displayed on a logarithmic scale. *Right.* Velocity field. Contours are the same as in figures 5.7 and 5.8.

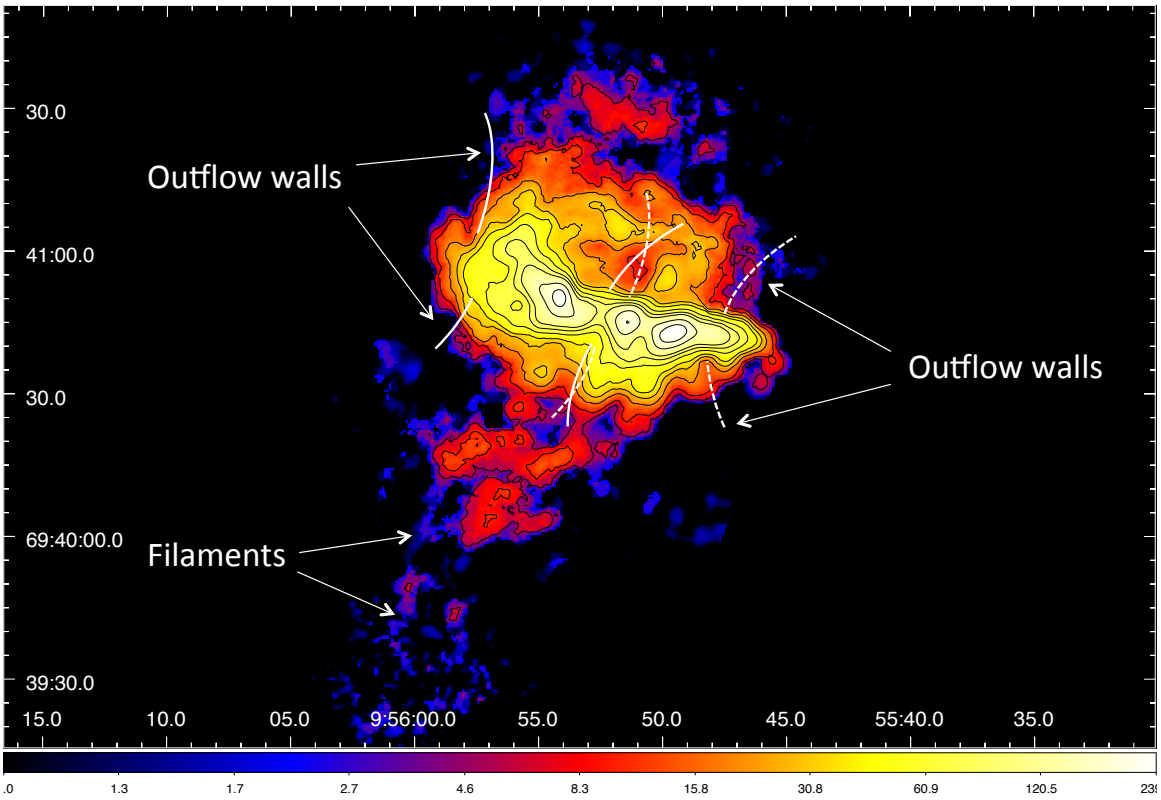

Figure 5.39: Outflow walls and filaments.

5.4 Outflow dynamics

In this section we analyze the energetics in mechanisms that are driving the nuclear 300-pc outflows of molecular gas. We have seen that the outflow ages are of the order $(4-5) \times 10^6$ yr, which constrains the origin to relatively recent events - the youngest episode of starburst that happened 5 Myr ago (Förster Schreiber et al. 2003). The older episode occurred throughout the bulge (500 pc) with most activity going on in the vicinity of the galactic center, while the younger occurred in the nuclear ring. We investigate the energy and momentum deposition rates from SN explosions, radiation, and stellar winds, and compare with observations. The spatial scale is $\pm$300 pc within the mid-plane and we ignore gravitational and magnetic forces[1].

5.4.1 Thermal energy deposition

Let us assume that a typical SN explosion releases $E_0 = 1 \times 10^{51}$ erg of kinetic energy. Current SN rate in M82 was observationally constrained to $R_{\rm SN} \approx 0.1$ yr^{-1} (Fenech et al. 2010), so the energy released per year is $\dot{E}_{\rm SN} = 1 \times 10^{50}$ erg yr^{-1}. The rate of thermal energy deposition to the ISM is given by

$$\dot{E}_{\rm T} \equiv \varepsilon_{\rm E} E_0 R_{\rm SN} = 1 \times 10^{50} \varepsilon_{\rm E} \ [\rm erg\ yr^{-1}]. \tag{5.10}$$

Here, $\varepsilon_{\rm E}$ is the thermalization efficiency - percentage of the SN kinetic energy that is used to heat the ambient gas, mainly by shocks between the SN blastwaves and the surrounding ISM; the typical values are between 0.01 and 0.2 (Veilleux et al. 2005; Murray et al. 2011). The presence of shocked gas was confirmed from the observations of SiO discussed above. Note that $\varepsilon_{\rm E}$ is poorly constrained from observations.

The first starburst episode in the 500-pc nuclear region began 15 Myr ago (Rieke et al. 1993; Förster Schreiber et al. 2003), although we keep in mind that it may have begun as early as 50 Myr ago (O'Connell et al. 1995). Starburst models of Leitherer et al. (1999) show that the number of SN explosions rapidly increases after $\sim 5 \times 10^6$ Myr (figure 5.40). Since we are analyzing the effect of SN explosions on the young, 5-Myr-old outflows, we adopt a SN timescale of $t_{\rm SN} \sim 5.0 \times 10^6$ Myr. The rate of thermal energy deposition during $t_{\rm SN}$ is

$$E_{\rm T} = E_0 \int_{t_{\rm SN}} \varepsilon_{\rm E}(t) R_{\rm SN}(t)\, {\rm d}t \approx \varepsilon_{\rm E} E_0 R_{\rm SN} t_{\rm SN} \sim 5 \times 10^{56} \varepsilon_{\rm E} \ [\rm erg]. \tag{5.11}$$

Here, we assume that $\varepsilon_{\rm E}$ and $R_{\rm SN}$ are constant during $t_{\rm SN}$. The SN rate is actually not constant but changes as shown in models by Leitherer et al. (1999). However, the presence of SN remnants in the nuclear ring (figure 5.35) suggests conditions of an advanced starburst where the contribution from SNe does not vary rapidly as in young starburst environments.

The thermalization efficiency is difficult to constrain because it depends on the local properties of the ISM and varies with time, but if we assume a range of values $0.3 \leq \varepsilon_{\rm E} \leq 1$ suggested in Strickland & Heckman (2009), the total kinetic energy from SNe that has been used to thermalize the ambient medium during the starburst becomes[2]

$$E_{\rm T} \sim (1-5) \times 10^{56} \ \rm erg. \tag{5.12}$$

[1] M82 is known to have a Keplerian rotation curve, which suggests that the total mass budget is dominated by stars and gas (Sofue 1998).

[2] High thermalization efficiency in M82 can be justified because numerous SNe during the starburst history have on average decreased porosity in the ISM.

Thus, we get $E_k/E_T \sim 0.01$ (see table 5.1) and the thermal energy is sufficiently high compared to the kinetic energy in the young molecular outflows. However, most of this energy is carried by the hot and warm ionized gas and warm neutral gas (atomic gas). Shopbell & Bland-Hawthorn (1998) find that the kinetic energy of the ionized gas outside $\pm 8''$ from the mid-plane is $\sim 2 \times 10^{55}$ erg, and higher if the central region is included; this is comparable to E_T. Whether cold molecular gas can survive after being entrained in the outflow together with ionized gas by ram pressure is a matter of debate because hot gas tends to evaporate neutral clouds and escape out of the galactic disk through channels of low density (e.g., Marcolini et al. 2005; Murray et al. 2011)[3]. Note that the adopted value of ε_E means that most of the remaining SN kinetic energy is radiated away. The efficiency is strongly dependent on the environment: it is low in dense gas where the radiative losses are high (Thornton et al. 1998; Efstathiou 2000).

5.4.2 Momentum deposition by radiation

Now, let us consider momentum deposition provided by radiation from the nuclear starburst. An example of this situation is a young super star cluster (= potential progenitor of a future globular cluster) embedded in a dusty, gas-rich ISM. Since most of the stars in galaxies are formed in clusters, and most of the massive stars ($> 8\ M_\odot$) that inject momentum and energy into the surrounding ISM form in dense clusters (Miller & Scalo 1978), we consider radiation pressure as an important mechanism that disrupts GMCs and blows outflows (e.g., Murray et al. 2005; Nath & Silk 2009; Murray et al. 2010; Shetty et al. 2011; Murray et al. 2011).

The momentum of a single photon is

$$p = \frac{h\nu}{c}. \tag{5.13}$$

The momentum deposition rate (= force) from radiation pressure is

$$\dot{p}_{\rm rad} \equiv F_{\rm rad} = \left(\frac{\Delta p}{\Delta t}\right)_{\rm SB} = \left(\frac{\Delta E}{c\Delta t}\right)_{\rm SB}. \tag{5.14}$$

We can introduce the starburst luminosity related to the emitted photons as $L_{\rm SB} = \Delta E/t_{\rm SB}$. Then,

$$\dot{p}_{\rm rad} = \frac{\tau L_{\rm SB}}{c}, \tag{5.15}$$

where τ is the optical depth. In the ISM, radiation pressure is acting on dust grains via absorption and scattering, and we assume that the molecular gas is hydrodynamically well coupled with the dust. Clearly, dusty neutral medium would intercept more photons than diffuse neutral medium, and this is determined only by τ. Note that the contribution of radiation pressure is distance-dependent, because the radiation flux is inversely proportional to distance (d) squared: $\tau = \kappa M_{\rm d}/(4\pi d^2)$. Here κ [cm^2 g^{-1}] is the mass absorption coefficient and $M_{\rm d}$ is the mass of the absorbing material.

Opacity of the ISM strongly depends on the wavelength of radiation. High-luminosity sources and dust-rich medium are located mostly in young (embedded) star clusters where molecular gas is forming stars. In such clusters, the bolometric luminosity is dominated by UV photons from young massive stars. In the case of UV radiation, the opacity is $\kappa_{\rm UV} \sim 10^3$ cm^2 g^{-1}, and since the gas density is at least 10^4 cm^{-3}, we can safely adopt $\tau_{\rm UV} > 1$. Note that the interstellar grains *do not* absorb infrared radiation; only radiation at shorter wavelengths is effectively absorbed (optical, UV), but the energy is then re-radiated isotropically at infrared wavelengths. Therefore, radiation will

[3]Murray et al. (2011) show that star clusters can drive cool gas from its host GMCs up to several tens of kiloparsecs above the galactic plane. However, the "cool gas" in their study is rather warm ($T \sim 10^4$ K), typical for atomic and partially ionized gas in photoionization equilibrium with radiation from hot stars.

transfer most of its momentum in regions where UV emission is strong and dust extinction large. In M82, UV radiation measured with GALEX is considerable and may be driving the wind in the starburst region (Coker et al. 2013).

The star formation rate (SFR) in the starburst region can be considered as a "mass accretion rate" and related to the starburst luminosity by the Einstein equation of mass-energy equivalence:

$$L_{\rm SB} = \varepsilon_{\rm M} \left(\frac{{\rm d}M}{{\rm d}t}\right)_{\rm SB} c^2 = \varepsilon_{\rm M}\ {\rm SFR}\ c^2. \tag{5.16}$$

Here, $\varepsilon_{\rm M}$ is the mass-to-light conversion efficiency, which depends on the low-mass cutoff in the Salpeter initial mass function (IMF, see appendix I; Salpeter 1955). The efficiency is given by $\varepsilon_{\rm M} \sim 10^{-3}$ for stellar masses from 1 to 100 $M_\odot$ (Murray et al. 2005). It should be noted that the IMF of super star clusters in M82 is rather shallow, ${\rm d}N/{\rm d}M_{\rm cluster} \propto M_{\rm cluster}^{-1.9}$ (McCrady & Graham 2007), so the luminosity of the starburst region is dominated by star clusters and their SFR. Combining the last two equations yields

$$\dot{p}_{\rm rad} = \tau \varepsilon_{\rm M}\ {\rm SFR}\ c. \tag{5.17}$$

If we assume that $\dot{p}_{\rm rad} = \dot{p}_{\rm mol}$, i.e., that radiation pressure is providing all the momentum in the molecular gas outflows, we can predict the necessary SFR. The total momentum injection rate in the outflow is (see table 5.1)

$$\dot{p}_{\rm mol} = \dot{M}_{\rm mol,1} V_1 + \dot{M}_{\rm mol,2} V_2 \sim 1 \times 10^3\ M_\odot\ {\rm yr}^{-1}\ {\rm km\ s}^{-1}. \tag{5.18}$$

The star formation rate of an optically thick medium ($\tau = 1$) is then

$${\rm SFR} = \frac{\dot{p}_{\rm rad}}{\tau \varepsilon_{\rm M} c} \sim 3\ M_\odot\ {\rm yr}^{-1}. \tag{5.19}$$

Observations and modeling by Förster Schreiber et al. (2003) give an average star formation rate during the last 15 Myr as ${\rm SFR} = (13-33)\ M_\odot\ {\rm yr}^{-1}$, depending on the low-mass cutoff of the Salpeter ISM within $m_{\rm low} = (0.1-1)\ M_\odot$. In their study, SFR had two peaks of 18 $M_\odot$ yr^{-1} and 6 $M_\odot$ yr^{-1} at 9 and 5 Myr ago. Other studies suggest the following values, some of which are for the current or time-averaged SFR: $\sim 3\ M_\odot$ yr^{-1} (Rodriguez-Rico et al. 2004) from the luminosity of the Lyman continuum assuming a Miller-Scalo IMF (1-100 $M_\odot$); $\sim 2\ M_\odot$ yr^{-1} from 1.7 GHz assuming a Miller-Scalo IMF (1-100 $M_\odot$) (Fenech et al. 2010); $(4.7-46)\ M_\odot$ yr^{-1} from the Lyman continuum by using a Miller-Scalo IMF (1-60 $M_\odot$) (Kronberg et al. 1985); $(2.6-4.3)\ M_\odot$ yr^{-1} from Hα line emission and $(9.1-19.6)\ M_\odot$ yr^{-1} from far-infrared continuum (Grimm et al. 2003). Finally, Strickland & Heckman (2009) derive SFRs between 4.4 and 6.1 $M_\odot$ yr^{-1} from 50 Myr to 10 Myr ago. They assumed a Salpeter IMF (1-100 $M_\odot$); in the case of a Kroupa IMF (0.01-100 $M_\odot$) (Kroupa 2001), SFRs are larger by a factor of 1.76. The current SFR is 3.9 $M_\odot$ yr^{-1}.

The numbers above are of the same order of magnitude as our estimate and allow the possibility of radiation-driven outflow from dusty and dense regions in the nuclear ring.

5.4.3 Momentum deposition by supernova ejecta

Typical SN explosions release a kinetic energy of $E_0 \sim 1 \times 10^{51}$ erg. The momentum of ejecta from a single SN is $M_0 V_0$ where $M_0 = 10\ M_\odot$ is the typical ejecta mass (corresponding to an average between Ia and II types), and V_0 is the ejecta velocity. The r.m.s. velocity can be calculated as

$$\langle V_0^2 \rangle^{1/2} = \left(\frac{2E_0}{M_0}\right)^{1/2} \sim 3000\ {\rm km\ s}^{-1}. \tag{5.20}$$

SN ejecta collide with the surrounding ISM (gas and dust), hence transfer momentum. Since the total momentum must be conserved, $M_0V_0 = MV$, even if the kinetic energy is radiated away, the velocity of the ejecta will decrease but the total mass will increase as the ejecta sweep the ambient material. The derived momentum deposition rate is

$$\dot{p}_{\rm SN} = M_0 V_0 R_{\rm SN} \sim 3 \times 10^3 \, M_\odot \, {\rm yr}^{-1} \, {\rm km \, s}^{-1}. \tag{5.21}$$

Comparison with our calculations of $\dot{p}_{\rm mol}$ shows that $\dot{p}_{\rm SN} \sim \dot{p}_{\rm mol}$. This result suggests that the gas outflow can be driven by the momentum in SN ejecta in addition to radiation pressure, although it does not discriminate between hot and cold outflows. Which mechanism is dominating is likely determined by the local porosity of the ISM and thermalization efficiency (see subsection 5.4.5). This implies that the outflow can be triggered by radiation pressure and supported by subsequent SN explosions. The SNe provide momentum in addition to the thermal energy deposited to the ISM. Depending on the local conditions, hot and cold ISM could be driven by different processes, and propagate side by side into the galactic halo. This is in agreement with the analytical results from Murray et al. (2011), where it was shown that radiation pressure dominates until the outflow reached a certain height outside the galactic plane; then, it is overtaken by ram pressure from hot gas. Interaction between these phases in the outflow may lead to shocks and charge exchange reactions that can be investigated by X-ray observations.

Note, however, that since the SN material is ejected in all directions, only a fraction will propagate in the direction perpendicular to the galactic plane. Thus, the above result should be regarded as an upper limit when compared to the molecular gas outflow.

5.4.4 Momentum deposition by stellar winds

Energy and momentum carried by stellar winds (SWs) in massive stars have been studied and modeled by Leitherer et al. (1999) and others. In stellar winds, radiation pressure is acting on electrons in the stellar ejecta by Thomson scattering, and not only on dust (Osterbrock & Ferland 2006). The importance of SWs is high in young ($\sim 10^6$ yr) starbursts where many luminous stars (mostly Wolf-Rayet and O stars) exist and disrupt their natal GMCs before SNe explode. For example, O stars typically have wind velocities $1500 \lesssim V_{\rm w}/{\rm km \, s}^{-1} \lesssim 2500$ and mass outflow rates of $(10^{-6.5}-10^{-5}) \, M_\odot \, {\rm yr}^{-1}$ (Markova et al. 2004); velocities in B stars are a factor of few smaller. Cooler stars are virtually irrelevant because the momentum in their winds is two orders of magnitude smaller, although stars like the asymptotic-giant-branch (AGB) class provide dusty and metal-rich material. SWs are mainly driven by radiation pressure from hot stars, but the gas is shocked and hot ($\sim 10^7$ K), thus contributing to thermal heating of the ISM around the star. This hot gas had previously been suggested to be driving the bubbles, but recent observations and analysis have shown that the gas either cools rapidly or escapes through holes, hence does not affect the bubble dynamics from inside by ram pressure (Harper-Clark & Murray 2009; Murray et al. 2011).

Figure 5.40 shows that for a starburst model that integrates instantaneous and continuous star formation which lasts up to 10^9 yr, the contribution from SN explosions becomes the dominant mass-injection source after $t \sim 10^{6.7}$ yr since the beginning. Radiation pressure (including SWs) is more significant up to that time. Thus, it is likely that M82 originally had outflows driven by radiation pressure in dusty star-forming clouds where UV/optical opacity was large and many massive stars were forming. Murray et al. (2011) show that star clusters of $M \gtrsim 10^6 \, M_\odot$ can launch galactic winds, while near-IR observational studies of M82 confirm the presence of 10-Myr old, $\sim 10^6 \, M_\odot$ super star clusters in the central 500 pc (McCrady & Graham 2007). Eventually, the outflows were magnified by dramatic series of SN explosions that provided additional momentum to already ejected ISM. As the starburst age is $(5-15) \times 10^6$ yr in M82 (Rieke et al. 1993; Doane & Mathews 1993; Förster Schreiber et al. 2003), we propose that the first starburst episode that peaked 10 Myr ago was dominated by

radiation pressure until several Myr ago, when the number of SNe rapidly increased. The SNe have been exploding since that time. The second starburst episode that peaked 5 Myr ago provided an influx of radiation in the nuclear ring but the number of SNe is yet to increase. We conclude that the wind in M82 has been dominated comparably by SN explosions and radiation pressure, in agreement with recent theoretical analyses (e.g., Nath & Silk 2009; Shetty et al. 2011; Murray et al. 2010; Murray et al. 2011). Wind evolution from star clusters to radiation pressure and SN-driven shells is illustrated in figure 5.41.

5.4.5 Forces in ram pressure and radiation pressure

In previous subsections, we have investigated the overall contribution of SN explosions, radiation pressure, and stellar winds on the ISM in M82 and its relation to the galactic wind. Here, we show that the forces that act on a single cloud of cold gas essentially depend on four parameters: the thermalization efficiency (percentage of kinetic energy released in SN explosions and SWs that heat the gas, $\varepsilon_{\rm E}$), mass loading parameter $\beta \geq 1$ (defined by $\dot{M}_{\rm h} = \beta \dot{M}_*$ where $\dot{M}_{\rm h}$ is the deposition rate of the hot gas, and $\dot{M}_*$ is the mass deposition rate by SNe and SWs), drag coefficient (efficiency of ram pressure on the cloud, $c_{\rm d}$), and optical depth, τ. The derivation below is based on Murray et al. (2011).

The ram pressure is defined as the force acting on the cross section ($A = R^2\pi$) of the cloud: $P_{\rm ram} = F_{\rm ram}/A$. The force is given by

$$F_{\rm ram} = c_{\rm d} A \rho_{\rm h} \left(v_{\rm h} - v_{\rm cl}\right)^2 \approx c_{\rm d} A \rho_{\rm h} v_{\rm h}^2. \tag{5.22}$$

Here, $\rho_{\rm h}$ is the density of the hot gas, $v_{\rm h}$ and $v_{\rm cl}$ are the initial velocities of the hot gas and cold cloud, respectively, and $v_{\rm cl} \ll v_{\rm h}$. The kinetic energy of the hot gas can be related to the luminosity of SNe reduced by the thermalization efficiency:

$$\frac{1}{2}\dot{M}_{\rm h} v_{\rm h}^2 = \varepsilon_{\rm E} L_{\rm SN}. \tag{5.23}$$

We may rewrite the ram force as

$$F_{\rm ram} = c_{\rm d} \frac{A}{4\pi r^2} \dot{M}_{\rm h} v. \tag{5.24}$$

Here, we have used the following transformation:

$$\rho_{\rm h} v_{\rm h}^2 = \frac{{\rm d}m}{{\rm d}V} v_{\rm h}^2 = \frac{{\rm d}m}{r^2 \sin\theta \, {\rm d}\theta \, {\rm d}\phi \, {\rm d}r} \frac{{\rm d}r}{{\rm d}t} v_{\rm h} = \frac{1}{4\pi r^2} \dot{M}_{\rm h} v_{\rm h}. \tag{5.25}$$

Murray et al. (2011) find that for a Chabrier IMF, $\dot{M}_{\rm h} = 0.2\beta$ SFR. Expressing the velocity as

$$v_{\rm h}^2 = \frac{2 L_{\rm SN} \varepsilon_{\rm E}}{\dot{M}_{\rm h}} = \frac{2 L_{\rm SN} \varepsilon_{\rm E}}{0.2\beta \ {\rm SFR}}, \tag{5.26}$$

we may write

$$F_{\rm ram} = c_{\rm d} \frac{A}{4\pi r^2} \dot{M}_{\rm h} \left(\frac{2 L_{\rm SN} \varepsilon_{\rm E}}{0.2\beta \ {\rm SFR}} \right)^{1/2} = c_{\rm d} \frac{A}{4\pi r^2} \frac{\dot{M}_{\rm h}}{\beta} \left(\frac{2 L_{\rm SN} \varepsilon_{\rm E} \beta}{0.2 \ {\rm SFR}} \right)^{1/2} \tag{5.27}$$

$$= 0.2 c_{\rm d} \frac{A}{4\pi r^2} \ {\rm SFR} \left(\frac{2 L_{\rm SN} \varepsilon_{\rm E} \beta}{0.2 \ {\rm SFR}} \right)^{1/2} = 0.2 c_{\rm d} \frac{A}{4\pi r^2} \ {\rm SFR} \left(\frac{10 L_{\rm SN} \varepsilon_{\rm E} \beta}{\rm SFR} \right)^{1/2}. \tag{5.28}$$

The radiation force is

$$F_{\rm rad} = \frac{A}{4\pi r^2}\frac{\tau L_{\rm SB}}{c}, \tag{5.29}$$

hence the ratio of the forces is

$$\frac{F_{\rm ram}}{F_{\rm rad}} = \frac{0.2 c_{\rm d}\sqrt{\varepsilon_{\rm E}\beta}}{\tau}\frac{\sqrt{10 L_{\rm SN}\ {\rm SFR}}}{\varepsilon_{\rm M}\ {\rm SFR}\ c}. \tag{5.30}$$

Since $L_{\rm SN} \propto L_{\rm SB} = \varepsilon_{\rm M}\ {\rm SFR}\ c^2$, we get

$$\frac{F_{\rm ram}}{F_{\rm rad}} \propto \frac{c_{\rm d}\sqrt{\varepsilon_{\rm E}\beta}}{\tau}. \tag{5.31}$$

In the previous subsections, it was discussed that the thermalization efficiency is expected to be low in dense regions because of radiative losses. Therefore, the ratio of forces will be very low inside embedded star clusters, and will increase as the outflow has reached low-density regions outside the cluster and toward the halo. Murray et al. (2011) have estimated that ram pressure becomes dominant at $0.3-1$ kpc above the midplane in a galaxy like M82. Our observations agree with this result, since we find that the molecular gas clouds are largely shattered into filaments and diffuse medium already at a height of ~ 0.5 kpc.

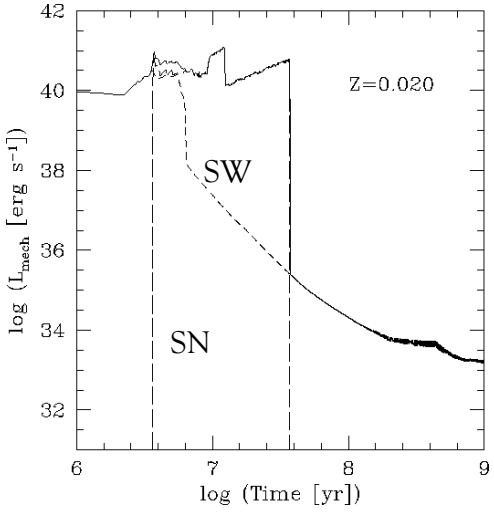

FIG. 113*b*

FIG. 113.—Mechanical luminosity vs. time. Star formation law: instantaneous; IMF: $\alpha = 2.35$, $M_{\rm up} = 100\ M_\odot$; *solid line*, total; *long-dashed line*, supernovae; *short-dashed line*, stellar winds; (*a*) $Z = 0.040$; (*b*) $Z = 0.020$; (*c*) $Z = 0.008$; (*d*) $Z = 0.004$; (*e*) $Z = 0.001$.

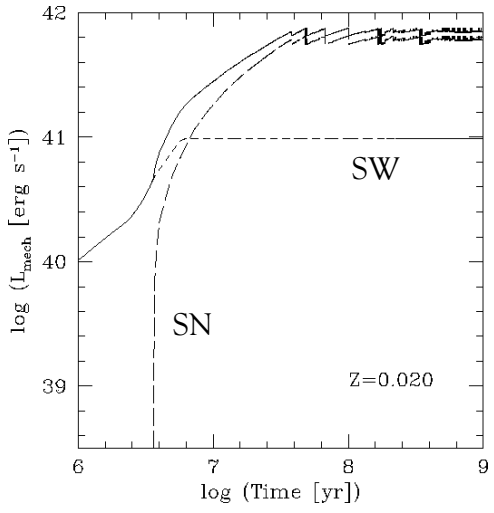

FIG. 114*b*

FIG. 114.—Mechanical luminosity vs. time. Star formation law: continuous; IMF: $\alpha = 2.35$, $M_{\rm up} = 100\ M_\odot$; *solid line*, total; *long-dashed line*, supernovae; *short-dashed line*, stellar winds; (*a*) $Z = 0.040$; (*b*) $Z = 0.020$; (*c*) $Z = 0.008$; (*d*) $Z = 0.004$; (*e*) $Z = 0.001$.

Figure 5.40: "Starburst 99" model (figures 113 and 114) from Leitherer et al. (1999). The mechanical luminosity in instantaneous (left) and continuous (right) star formation low is plotted against time. The initial mass function index is $\alpha = 2.35$, the stellar mass is up to $M_{\rm up} = 100\,M_\odot$, and the metallicity is $Z = 0.02$. The long dashed line is the contribution from SN explosions; short dashed line is from stellar winds; solid line shows both.

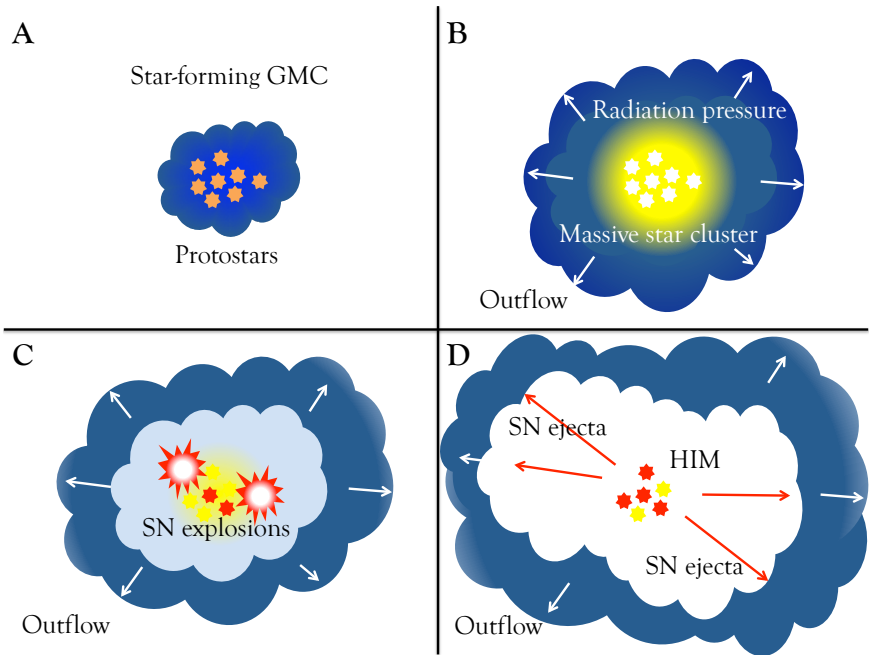

Figure 5.41: Star clusters and outflow evolution: A) massive star formation in a giant molecular cloud (GMC); B) young super star cluster is formed - radiation from hot stars (H II regions and SWs) exerts force on the ISM, disrupts the natal GMC and drives an outflow; C) first SN explosions; D) SN ejecta supply additional momentum to the outflow. The cluster region is overpressurized by hot ionized gas. The hot gas expands adiabatically and exerts ram pressure on surrounding cool gas.

5.4.6 Stellar bar and the ISM in the central 1 kpc

Observations of near-infrared emission, nebular lines, and stellar absorption lines led a number of authors to propose that M82 hosts a stellar bar and to model its shape and orientation (Telesco et al. 1991; Achtermann & Lacy 1995; Neininger et al. 1998; Seaquist et al. 1998; Wills et al. 2000; Greve et al. 2002; Westmoquette et al. 2007). In addition to evidence from 2-μm data from Telesco et al. (1991), McKeith et al. (1993) have found that the rotation of stars (traced with absorption in Ca II) and ionized gas (Hα, [Ne II], [S III]) has much in common in the central 500 pc. Achtermann & Lacy (1995) have interpreted this tentatively as the presence of a bar where the neutral gas is mostly in a ring marginally corresponding to the outer x1 orbits, whereas the ionized gas might be in x2 orbits inside the ring. Neininger et al. (1998) and Seaquist et al. (1998) have come to similar conclusions from their CO and HCO^+ observations, although the issue remained inconclusive due to the presence of a "superbubble" noticed by Neininger et al. (1998), and later studied by Weiß et al. (1999), Matsushita et al. (2000), and Wills et al. (2002). In the meanwhile, Wills et al. (2000) and Greve et al. (2002) developed new models of the nuclear bar that can explain the observed rotation curve without a superbubble. The presence of an expanding bubble in the western lobe was, however, confirmed from H I observations where a shell was located nearly coincident with the CO shell (Wills et al. 2002).

We find three observational features in our data that support the presence of outflows from the ring and disagree with the hypothesis that the CO kinematics can be explained purely by obeying x1 and x2 orbits. The kinematics of CO gas (PVD) is shown in figure 5.42 together with indications of rigid-body rotation (blue line, RR) and x2 orbits of a bar (red line, x2) based on the analyses of ionized-gas lines. Firstly, rigid rotation is a plausible explanation for most of the CO gas. If the steep component at $-5'' < X < 0''$ is part of x2 orbits, then it is clearly one-sided because we do not see a "figure eight" emission pattern at $X > 0''$. Secondly, CO intensity in channel maps that correspond to the proposed nuclear outflows (PVDs and 5.27) clearly exhibit shell-like geometry extended outside the ring. And thirdly, both peaks in the western ring are seen in absorption in B-band (figure 5.31b), and therefore belong to the near side part of the ring contrary to the bar geometry in Wills et al. (2000) and Greve et al. (2002). However, since the overall state of the ISM and stars was influenced by intergalactic tidal interaction, we cannot rule out that some of the molecular gas is in non-circular orbits that obey a bar potential or a nuclear spiral arm, and that the stellar and gas disks are significantly warped.

5.4.7 Streams and inflow channels toward the nuclear ring

In the previous subsections, we have presented integrated intensity maps, velocity field maps, and PVDs in high angular resolution. We found that the nuclear ring has the steepest rotational gradient, and that molecular gas is being ejected above the galactic plane as a consequence of vigorous starburst in the ring. Below, we discuss two unsettled problems.

First, it remains unclear what mechanism supplied large quantities of molecular gas to the galactic nucleus. Tidal interaction between M82 and M81 has clearly disrupted the outer disk of M82 as seen in H I (Yun et al. 1994), but such encounter is unlikely to disrupt the central region of the galaxy. It is most likely that the gas was brought from outside as a consequence of asymmetrical potential produced during the interaction. The gas concentrated in the galactic nuclear region and the starburst began. Even so, it is curious that the starburst is still going on and that, despite the fact that a significant portion of molecular gas has been expelled into an outflow by stellar feedback, the nuclear ring is still very gas-rich and produces stars. In other words, how is it possible to have a large-scale outflow of interstellar matter and a significant reservoir of molecular gas still at the base of the outflow? In an environment of widespread supernova explosions and superbubbles, further star formation cannot be sustained.

Second, southeast of the nuclear ring, we find prominent streams of molecular gas. This gas

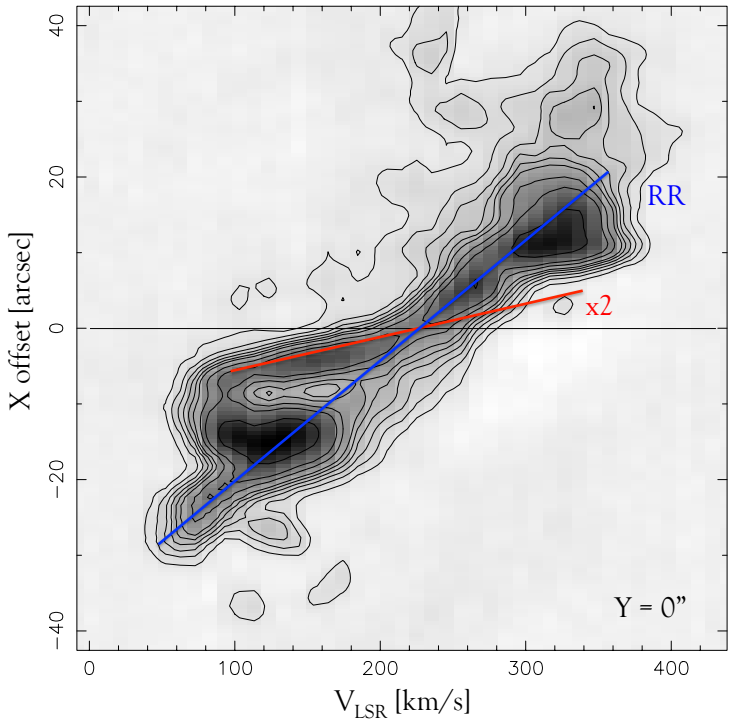

Figure 5.42: Rotation of the molecular gas at $Y = 0$ and P.A. $= 70^0$. Red line is based on stellar Ca II absorption from McKeith et al. (1993). Similar steep rotation at $|X| = 5''$ is also observed in [Ne II] which traces ionized gas (Achtermann & Lacy 1995).

appears to be connected to the ring, but it is *kinematically* decoupled. Although the east part of the ring is redshifted due to rotation, the streams do not share the same kinematics. In the case of an outflow in this direction, we would expect to see predominantly redshifted emission, which is not observed. However, we do observe rotation in some of the streams. The rotation curve is nearly flat and only 30-40 km s^{-1} different from the systemic velocity. Because such low rotational velocity cannot keep the gas in a circular orbit, there is a possibility that some of the streams are channeling molecular gas and dust *toward* the nuclear ring.

5.4.8 Starburst history and the galactic wind in M82

To summarize our main results from this section: we find that two young molecular-gas outflows were formed 4-5 Myr ago, timescale that corresponds to the latest starburst episode in the nuclear ring of M82. The overall morphology of the outflow in the inner 1 kpc from the nuclear ring clearly shows that most of the gas is currently being ejected from the nuclear ring in a biconical shape toward the halo, showing no evidence of an outflow from the galactic center. In our previous study with the NRO 45-m telescope (Salak et al. 2013), we have detected a 2-kpc outflow of molecular gas and derived its expansion velocity. Inserting starburst timescales (5 and 10 Myr) and distances (300 pc for the young outflows discussed in this work, and 2 kpc from our previous work), we come to a conclusion that the large-scale outflow of molecular gas was triggered during the first starburst episode, while the young, 300-pc outflow discussed here was formed during the second starburst episode. This is illustrated in figures 5.43 and 5.44.

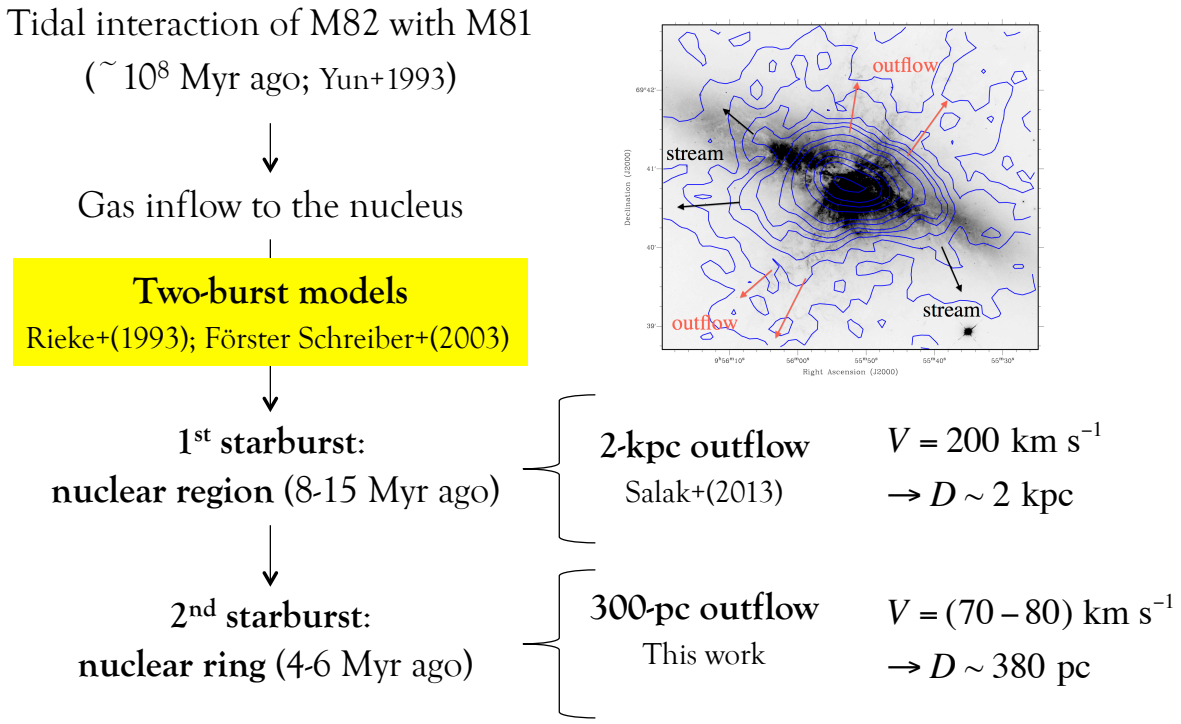

Figure 5.43: Starburst history and CO observations of the galactic wind.

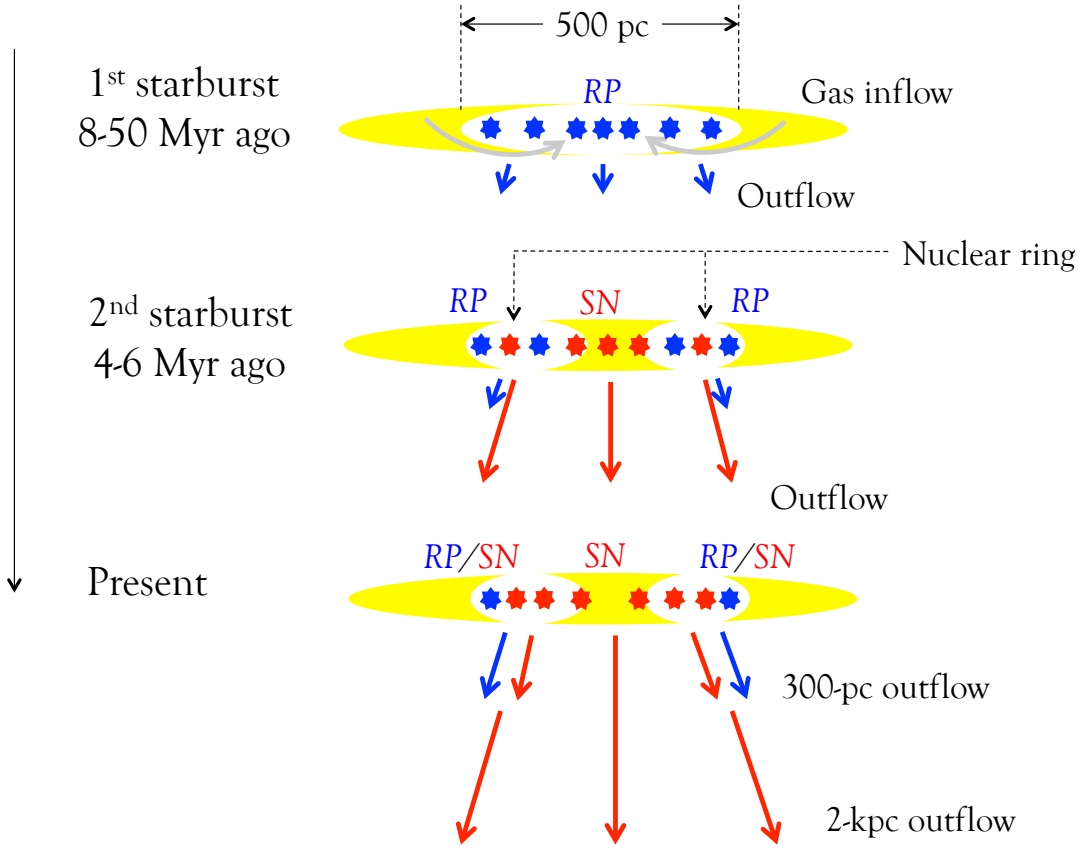

Figure 5.44: Starburst history and feedback on the molecular gas. During the first starburst episode, the wind was dominated by radiation pressure from the starburst in the central $\sim$ 500-pc region, with the highest activity toward the galactic center. By the time the second starburst begun, SNe had started to explode in the entire region. The second starburst occurred in the nuclear ring where new sources of radiation pressure were formed. At present, SNe whose progenitor stars were formed in the second episode have begun to explode, hence the 300-pc outflow is driven by both radiation pressure, stellar winds, and SN explosions. SNe from the first episode whose progenitor stars were least massive ($\lesssim 30\ M_\odot$) are still active. White elliptical regions mark the starburst regions; SN or RP indicate whether the wind is supported mainly by SN explosions or radiation pressure from star clusters denoted by stars, respectively, or both.

5.5 Line intensities of CO, CN and CS

Observations of CO (1-0), described in previous sections, have shown us the distribution and kinematics of the molecular gas on large scale (several kpc) and on small scale (angular resolution 60 pc) by combining single dish OTF mapping and interferometric mosaic imaging. The molecular gas is clearly abundant in the disk and halo of M82, and our next aim was to investigate its physical conditions in a variety of environments.

Owing to its proximity and large quantities of molecular gas, M82 is one of the best studied extragalactic sources. However, all previous single dish studies of the molecular gas were focused either on CO molecular lines (e.g., Nakai et al. 1987; Mao et al. 2000; Seaquist & Clark 2001; Weiß et al. 2005), or on the bright nuclear ring alone (e.g., Aladro et al. 2011a; Aladro et al. 2011b). Although these line surveys at 1.3 mm and 3 mm have deepened our understanding of the physical conditions of the ISM in the nuclear region, we still lack observational data of the molecular gas halo. Weiß et al. (2005) probed the halo by observing CO emission lines, and realized that the physical conditions of the molecular gas are likely different than in the galactic nucleus. Their study included CO 1-0, 2-1 and 3-2 along with the rare isotopic species ^{13}CO of 1-0 and 2-1.

In this section, we present the first multi-species molecular line survey toward extra-planar regions of M82. The main aim was to probe the molecular gas conditions in the outflow and compare it with the disk of the galaxy. To accomplish this, we observed CO (1-0), ^{13}CO (1-0), C^{18}O (1-0), CN (1-0), and CS (2-1) toward the nuclear region, the inner outflow, and the outer outflow, which was observed for the first time. We have detected all lines in the inner regions, while in the outer parts of the halo only CO (1-0) was detected, although with a high signal-to-noise ratio. The observed positions are summarized in table 5.2 and indicated in figure 5.45.

5.5.1 Data presentation

The positions observed with the 45-m telescope were chosen as representative regions for the galactic nuclear region and outflow (table 5.2). The nuclear region of the galaxy consists of a rotating, edge-on, 200-pc molecular gas ring seen as a triple peak. One of the CO (1-0) peaks in the ring, with the integrated intensity of 228.0 Jy beam^{-1} km s^{-1} as derived from our combined NRO-CARMA map (previous section), is at the position of the eastern lobe (hence referred to as the *eastern peak*). This position represents the nuclear star-forming ring.

In order to compare the molecular line emission in the nuclear ring with that in the outflow, a position with peak CO (1-0) emission was selected in the northern part of the outflow. This position corresponds to the brightest peak (39.9 Jy beam^{-1} km s^{-1}) in the clumpy inner outflow, hence referred to as the *inner outflow*, and represents the molecular gas blown out from the nuclear ring.

The eastern peak and inner outflow are indicated in figure 5.45, where the circles show the telescope beam at 115 GHz with a diameter of 15″.

To select additional observing positions farther from the central region, we used our OTF data cube, 250 μm data from Roussel et al. (2010), and 7 μm data from Kaneda et al. 2010. The positions are referred to as the *outer outflow* - located 2 kpc above the galactic plane (filament "F" in figure 5.1 (b)), the *NW clump* - located 3.5 kpc above the plane (see figure 5.1 (b)), the *western stream* - located in a stream of molecular gas in the galactic plane, and the *western arm*, in the newly discovered arm farther out in the disk. Properties of the NW clump and western arm were reported in Salak et al. (2013).

The observed positions are shown in figures 5.45 and 5.46, superimposed on the moment 0 data cubes of the CO (1-0) OTF and combined maps.

In 2011, we observed CO (1-0) toward one position in the Cap region (for the Cap, see, e.g., Tsuru et al. 2007; Kaneda et al. 2010), but without detection.

Table 5.2: Observed positions.

Position[a]	α (J2000.0)	δ (J2000.0)	Observation date
Eastern peak	$09^h55^m54.1^s$	$+69^o40'50.8''$	2013
Inner outflow	$09^h55^m51.9^s$	$+69^o41'05.7''$	2013
Outer outflow	$09^h55^m37.5^s$	$+69^o42'17.5''$	2013
NW clump	$09^h55^m18.0^s$	$+69^o42'52.0''$	2013
Western stream	$09^h55^m40.5^s$	$+69^o40'29.0''$	2013
Western arm	$09^h55^m32.0^s$	$+69^o40'19.5''$	2013
Cap region[b]	$09^h55^m00.0^s$	$+69^o50'15.0''$	2011

a) A common systemic velocity of 220 km s^{-1} was adopted for all positions. The velocity was calculated in the radio definition with respect to the LSR.
b) Salak et al. (2013).

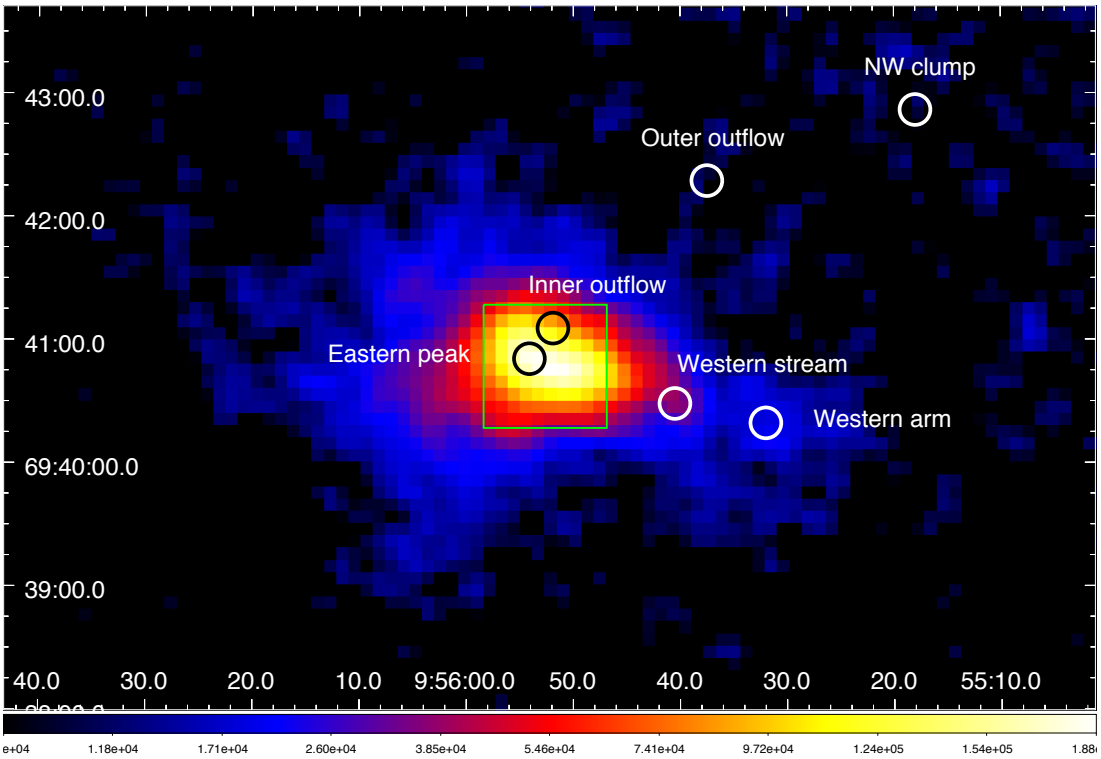

(a)

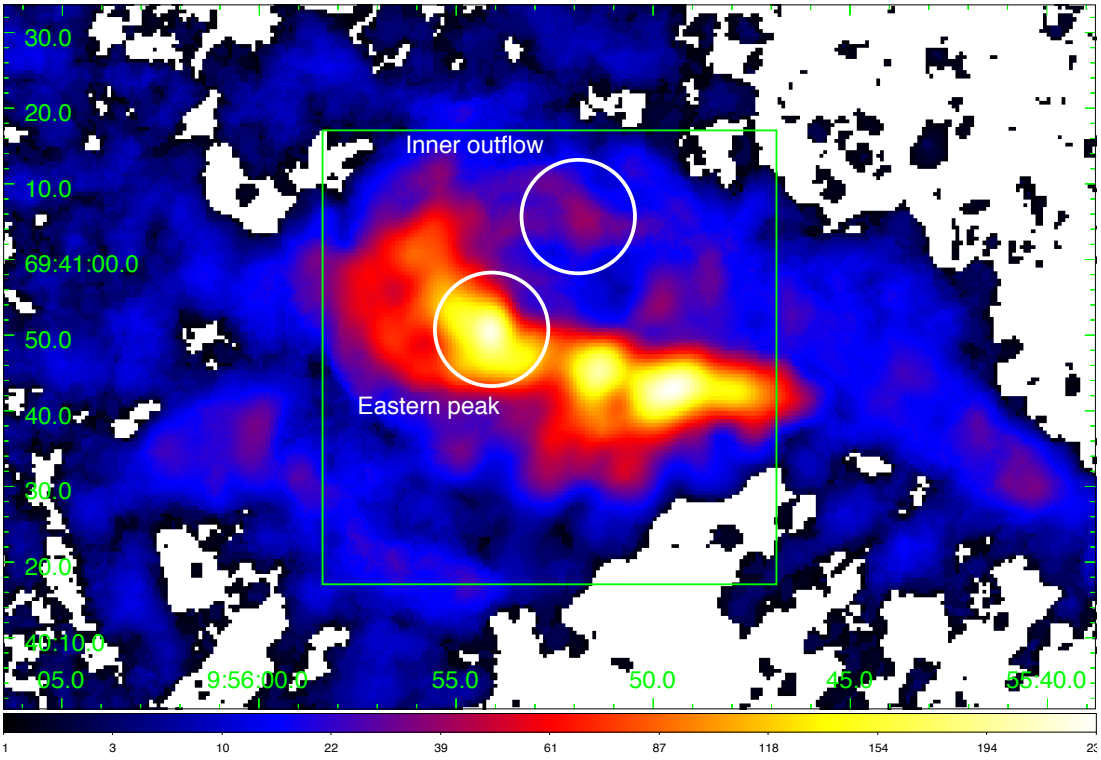

(b)

Figure 5.45: (a) Observed positions in the disk and halo of M82 (white and black circles). The telescope beam was 15″ at 115 GHz for the line-survey observations (circle size), while it was 22″ in the OTF mapping. (b) Observed positions in the nuclear ring and the inner outflow of M82. The size of the green rectangle is 60″ × 60″.

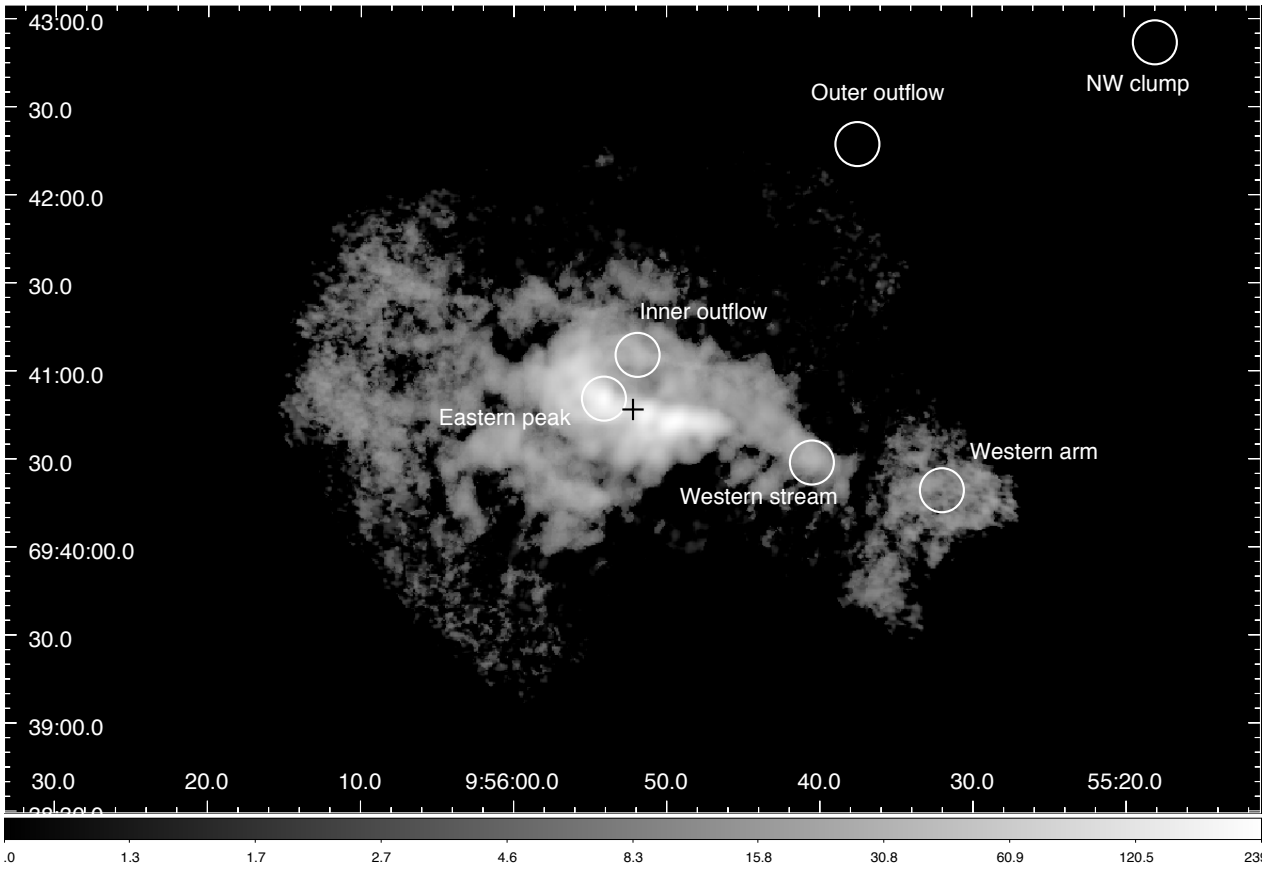

Figure 5.46: Observed positions (continued).

In the following subsections, the spectra of the molecular lines at all positions are presented. In the nuclear ring and inner outflow, all observed lines were detected with a signal-to-noise ratio above 5σ in integrated intensity. In all other regions, only CO (1-0) was clearly detected.

The size of the telescope beam (angular resolution) for CO (1-0), ^{13}CO (1-0), C^{18}O (1-0) and CN (1-0) varies for less than $1''$ (wavelengths differ from 2.61 to 2.73 mm), hence can be considered nearly equal. In the case of CS (2-1) at 3.06 mm, the resolution is $17.6''$, which is for $\approx 2.5''$ larger than that of CO (1-0). Since we have spectra at only one observing point we cannot smooth the data to correct for the angular resolution. Therefore, the data should be interpreted after converting $T_{\rm mb}$ to the brightness temperature $T_{\rm b}$ by correcting for the beam filling factor $f_{\rm b}$. The relation is

$$T_{\rm mb} \equiv f_{\rm b} T_{\rm b} = \frac{\Omega_{\rm s}}{\Omega_{\rm b} * \Omega_{\rm s}} T_{\rm b}. \tag{5.32}$$

Here, $\Omega_{\rm s}$ is the angular size of the source, and $\Omega_{\rm b}$ is the size of the telescope beam.

To a first approximation, we compare the data by neglecting the difference in the beam size. In general, for all lines, $f_{\rm b}^{\rm EP} \neq f_{\rm b}^{\rm IO}$ due to optical depth effects and astrochemistry in different environments.

To estimate the beam filling factor, we must make an assumption of the excitation temperature of CO (1-0), $T_{\rm ex}$. The brightness temperature is given by

$$T_{\rm b} = \left[J_\nu(T_{\rm ex}) - J_\nu(T_{\rm bg})\right]\left(1 - {\rm e}^{-\tau}\right), \tag{5.33}$$

where

$$J_\nu(T) = \frac{h\nu}{k} \frac{1}{{\rm e}^{h\nu/kT} - 1} \tag{5.34}$$

is the radiation temperature. $T_{\rm bg} = 2.73$ K is the temperature of the cosmic microwave background, and τ is the optical depth of CO (1-0). Since CO (1-0) is usually optically thick and it was found that $\tau > 1$ in the disk of M82 (Weiß et al. 2001b), we may write

$$T_{\rm b} \approx J_\nu(T_{\rm ex}) - J_\nu(T_{\rm bg}) = \frac{h\nu}{k}\left[\frac{1}{{\rm e}^{h\nu/kT_{\rm ex}}-1} - \frac{1}{{\rm e}^{h\nu/kT_{\rm bg}}-1}\right] \approx T_{\rm ex} - T_{\rm bg}. \tag{5.35}$$

Note that in the case of CO (1-0), in general, we cannot use the Rayleigh-Jeans approximation literally for low temperatures. In the case of higher temperatures (60 K, see below), $h\nu/kT_{\rm k} \simeq 0.09$, hence the approximation can be used to make simple estimates. In Galactic molecular clouds, $T_{\rm ex} \simeq 10$ K (Maloney 1990). The dust temperature is considerably higher in the nuclear ring of M82, and if we assume that CO molecules are in thermal equilibrium with H_2 molecules and dust grains, then $T_{\rm ex} \simeq 40$ K might be a more appropriate value (e.g., Nakai et al., 1987). However, observations of the ammonia molecule (Weiß et al. 2001a) and LVG analysis of CO lines (Weiß et al. 2005) show that the kinetic temperature of the molecular gas in the nuclear ring is at least 60 K, implying that the dust temperature is not necessarily equivalent to the excitation temperature of the gas. This implies a beam filling factor of $f_{\rm b} = T_{\rm mb}/T_{\rm b} \simeq 0.1$.

The critical density of CO (1-0) is $n_{\rm c} \sim 10^3$ cm^{-3}. This is lower than typical densities in molecular clouds in the center of M82 as found by Weiß et al. (2001b) and Weiß et al. (2005), which range from 10^3 to 10^5 cm^{-3}. Therefore, CO (1-0) should be thermalized and gas properties are close to LTE.

In positions other than the eastern peak, $T_{\rm mb}$ is much lower while $T_{\rm ex}$ is not likely to be below 10 K, so the beam filling factor is even smaller. Therefore, for CO-emitting molecular clouds, $f_{\rm b} \simeq 0.1$ for the eastern peak and $f_{\rm b} \ll 1$ for all other positions are reasonable estimates.

5.5.2 Eastern peak

Spectra of ^{12}CO (1-0), ^{13}CO (1-0), C^{18}O (1-0), CN (1-0) and CS (2-1) toward the eastern peak are shown in figures 5.47, 5.48, 5.49, 5.50, and 5.51, respectively. The line properties of Gaussian fits at the spectral resolution of about 5 km s^{-1} are given in table 5.3.

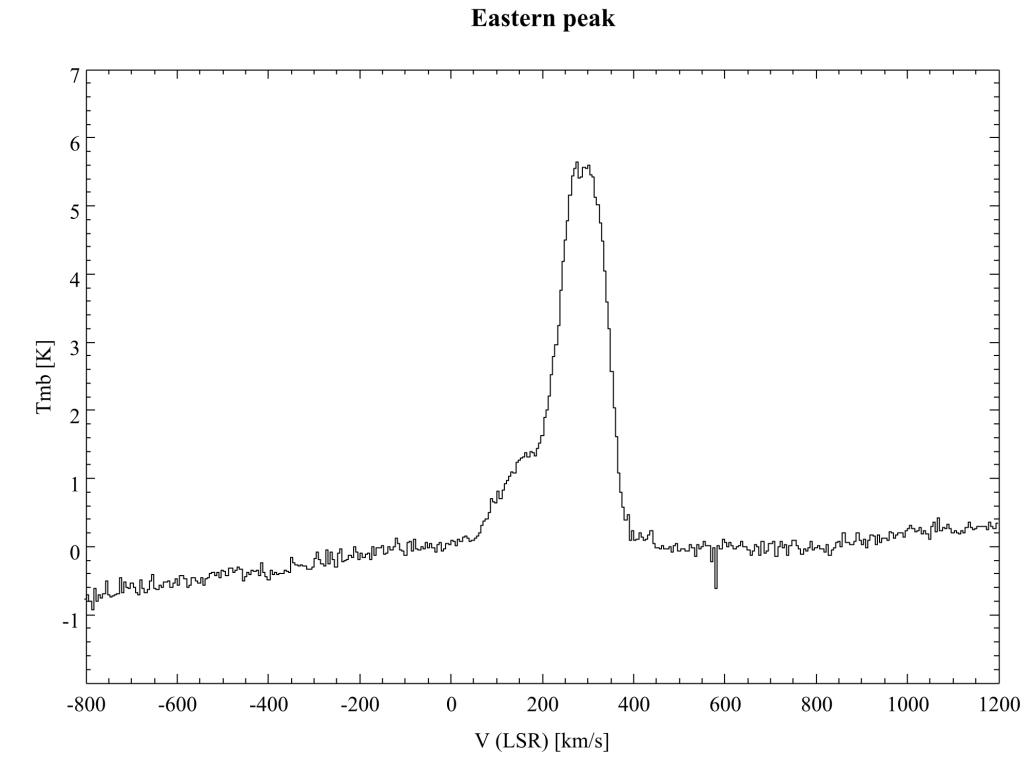

Figure 5.47: ^{12}CO (1-0) emission spectrum at the position of the eastern peak in the nuclear ring.

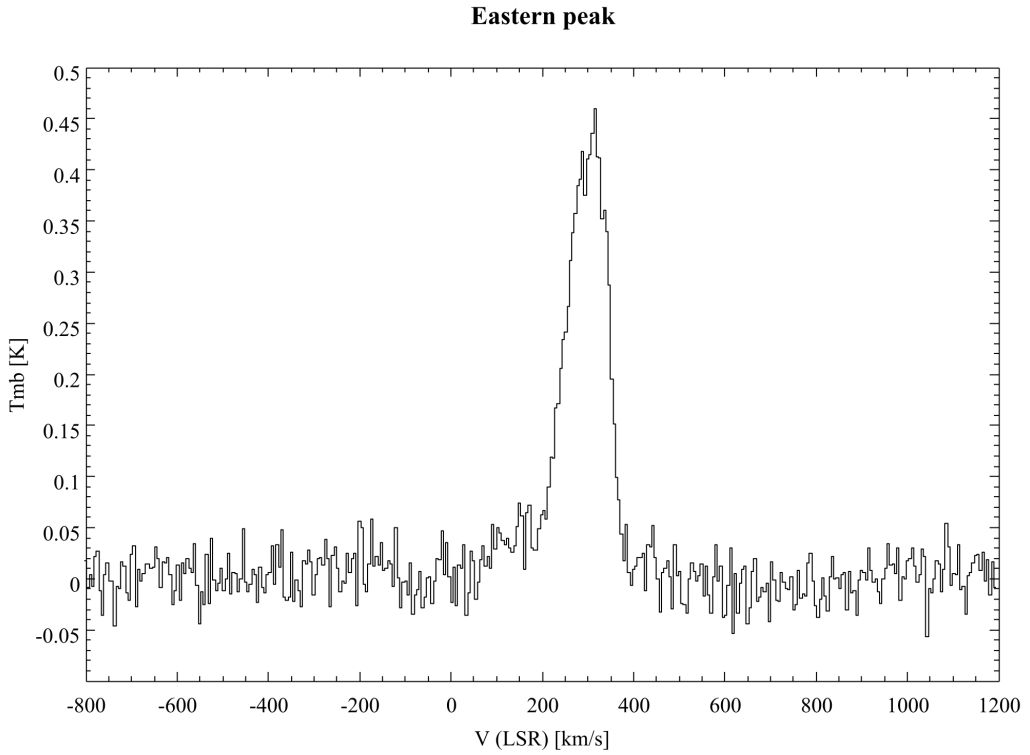

Figure 5.48: ^{13}CO (1-0) emission spectrum at the position of the eastern peak in the nuclear ring.

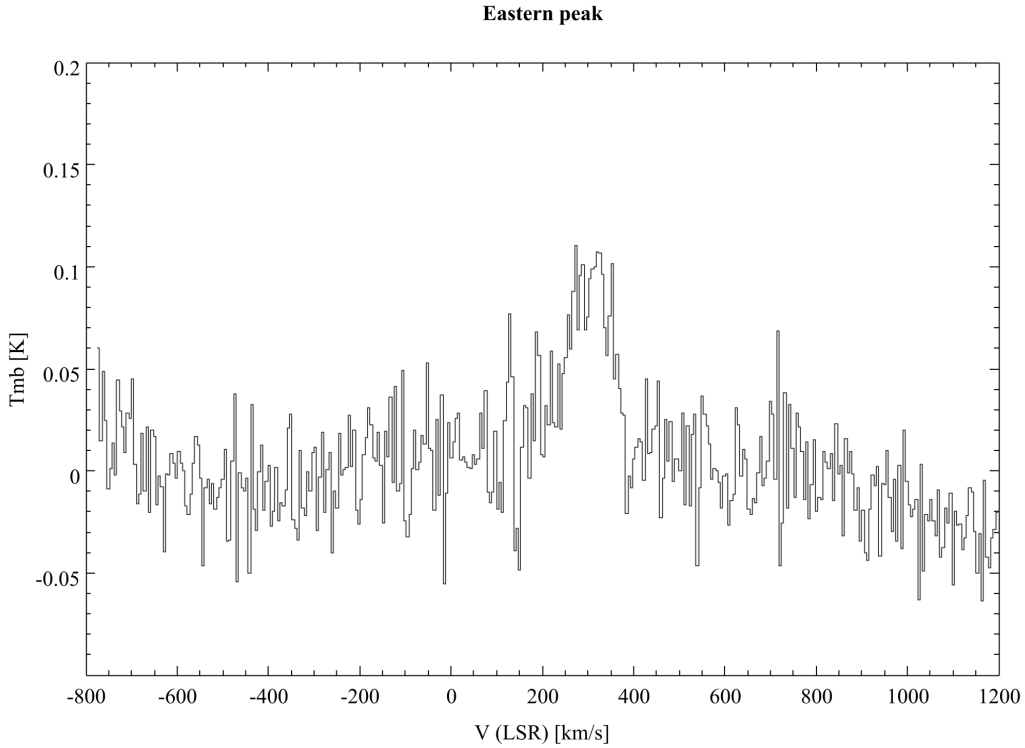

Figure 5.49: $C^{18}O$ (1-0) emission spectrum at the position of the eastern peak in the nuclear ring.

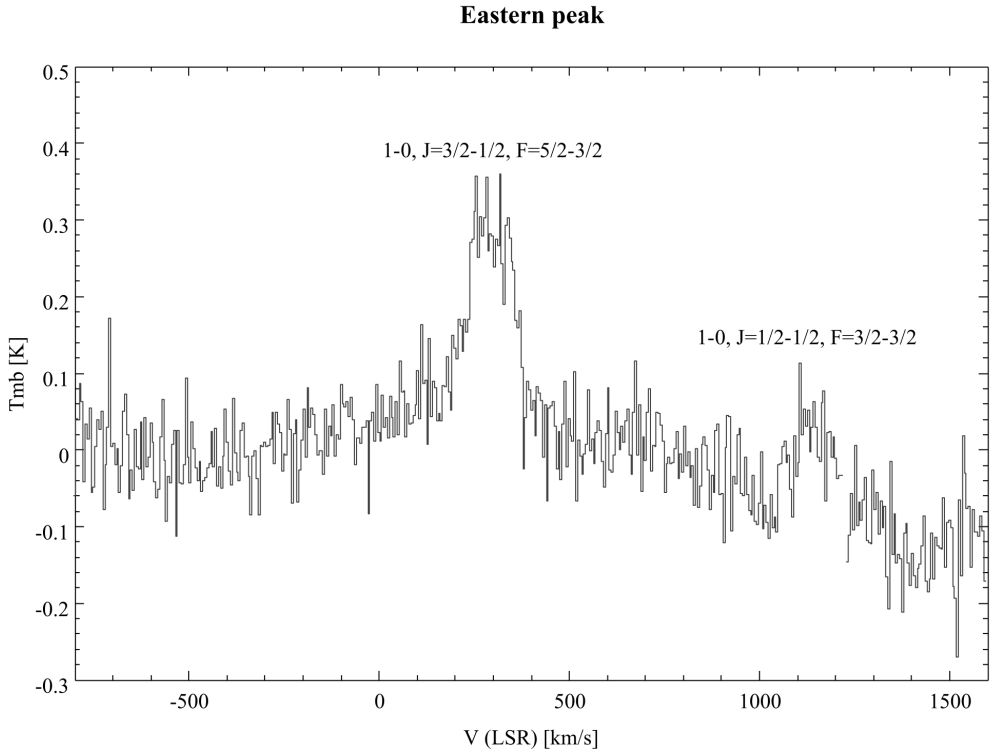

Figure 5.50: CN (1-0) emission spectrum at the position of the eastern peak in the nuclear ring. Two strongest fine structure lines are indicated.

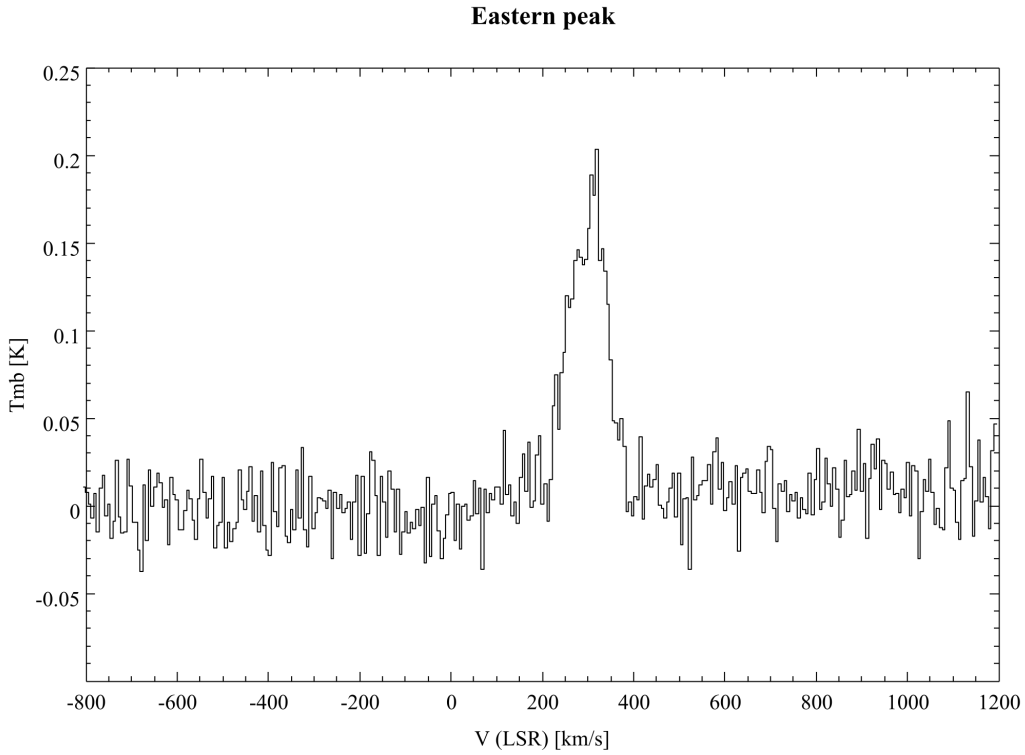

Figure 5.51: CS (2-1) emission spectrum at the position of the eastern peak in the nuclear ring.

The main beam brightness temperature of CO (1-0) is 5.7 K. This is in agreement with previous observations with the NRO 45-m telescope (Nakai et al. 1987), where 5.8 K was reported as the peak brightness temperature. The integrated intensity of CO (1-0) is 828.8 K km s^{-1}. In Salak et al. (2013), the brightness temperature and integrated intensity peaks were at 3 K and 507 K km s^{-1}, respectively; taking into account the uncertainty of measurement (20%), the difference is attributed to the larger effective size of the telescope beam in the OTF observations (22″ compared to 15″ in position switching).

The central velocities of the emission line profiles (V_c) are very close to each other, in the range between 290 and 301 km s^{-1}, with a variation less than 10% of the line FWHM. Slight differences arise from intrinsic variations in the molecular gas distribution and pointing errors. CO (1-0) and CN (1-0) lines were observed simultaneously, as well as ^{13}CO (1-0), C^{18}O (1-0) and CS (2-1). Our results show that the pointing error between the two measurement sets has negligible effect on line ratios. The pointing error was no larger than 2″ during observations.

The line profiles are broad (FWHM>100 km s^{-1}) and can be fitted with more than one Gaussian functions. This is a consequence of observing unresolved, beam-averaged molecular clouds with different velocities in a rotating edge-on ring. Integrated intensities were calculated by covering the entire emission range of the spectra, while T_{mb} peaks were obtained by fitting Gaussian functions only to the main component of the complex profile. This was necessary only for the ^{12}CO (1-0) line where the profile deviates from a single Gaussian due to a blueshifted component.

The molecular gas conditions in the nuclear ring are beyond the scope of this work because the subject was studied in numerous previous works (Rieke et al. 1980; Nakai et al. 1987; Shen & Lo 1995; Weiß et al. 2001b; Seaquist & Clark 2001). Instead, this work is focused on the comparison with the extended halo regions by using the line ratios discussed below.

Table 5.3: Line parameters for the eastern peak.

Line	I [K km s^{-1}]	T_{mb} [K]	V_c [km s^{-1}]	FWHM [km s^{-1}]	Δv_{int}	Δv_{ch}
^{12}CO (1-0)	828.8 ± 7.0	5.739 ± 0.167	290.6 ± 0.6	128.9 ± 2.4	349	5.08
^{13}CO (1-0)	51.6 ± 0.8	0.441 ± 0.021	298.1 ± 1.3	103.7 ± 3.0	302	5.31
C^{18}O (1-0)	13.0 ± 0.8	0.095 ± 0.023	300.1 ± 4.8	128.0 ± 11.2	216	5.33
CN (1-0)^a	39.0 ± 1.9	0.274 ± 0.046	288.5 ± 3.0	133.5 ± 7.2	350	5.16
CN (1-0)^b	25.8 ± 2.0	0.127 ± 0.046	-	190.6 ± 26.0	380	5.17
CS (2-1)	18.4 ± 0.6	0.172 ± 0.017	301.1 ± 2.1	101.8 ± 5.6	217	5.98

Note. The data were smoothed by 4 channels to the velocity resolution of ≈ 5 km s^{-1}. The CN molecule has two sets of hyperfine-structure transition lines: a) $N = 1-0, J = 3/2-1/2$ between 113.488 and 113.520 GHz and b) $N = 1-0, J = 1/2-1/2$ between 113.123 and 113.191 GHz.

5.5.3 Inner outflow

All molecular lines were detected at the position of the inner outflow. The position is $20''$ separated from the eastern peak, with a deprojected distance of 345 pc into the halo (where $i = 80^0$). The spectra are shown in figures 5.52, 5.53, 5.54, 5.55, and 5.56. The line properties are given in table 5.4.

The main beam brightness temperature and integrated intensity of CO (1-0) are 2.1 K and 307.8 K km s^{-1}, respectively. This is a factor of 3 lower than in the eastern peak. Other lines are much weaker, with ^{13}CO (1-0) and CN (1-0) having comparable integrated intensities of 11.4 and 15.2 K km s^{-1}, respectively. Similarly, C^{18}O (1-0) and CS (2-1) show comparable line intensities.

The central velocities of the line profiles are in good agreement with each other - the variation is between 258 and 266 km s^{-1}, with the exception of CN (1-0). Note that V_c is for ≈ 50 km s^{-1} lower than in the eastern peak - this suggests that contamination from the error beam and side lobes is not dominant in the profiles of the inner-outflow lines. Our velocity-field map (figure 5.9) confirms that the velocity is lower at the position northwest of the nuclear ring. Furthermore, observations toward the inner outflow were made in excellent weather conditions (wind speed less than 3 m s^{-1}), which resulted in a measured pointing error of $< 1.5''$. See also discussion below about the error beam of the 45-m telescope.

The line widths (FWHM) in the inner outflow are broad and similar to those in the eastern peak. This suggests that the molecular clouds are in turbulent motion and that the overlap along the line of sight is still large.

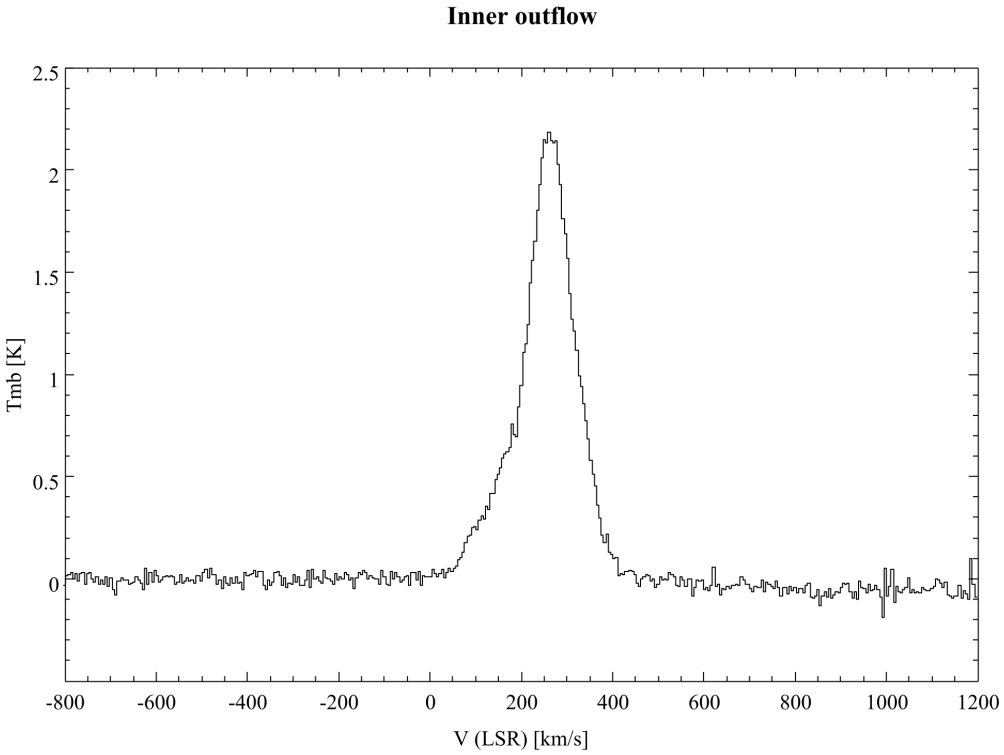

Figure 5.52: ^{12}CO (1-0) emission spectrum at the position of the inner outflow.

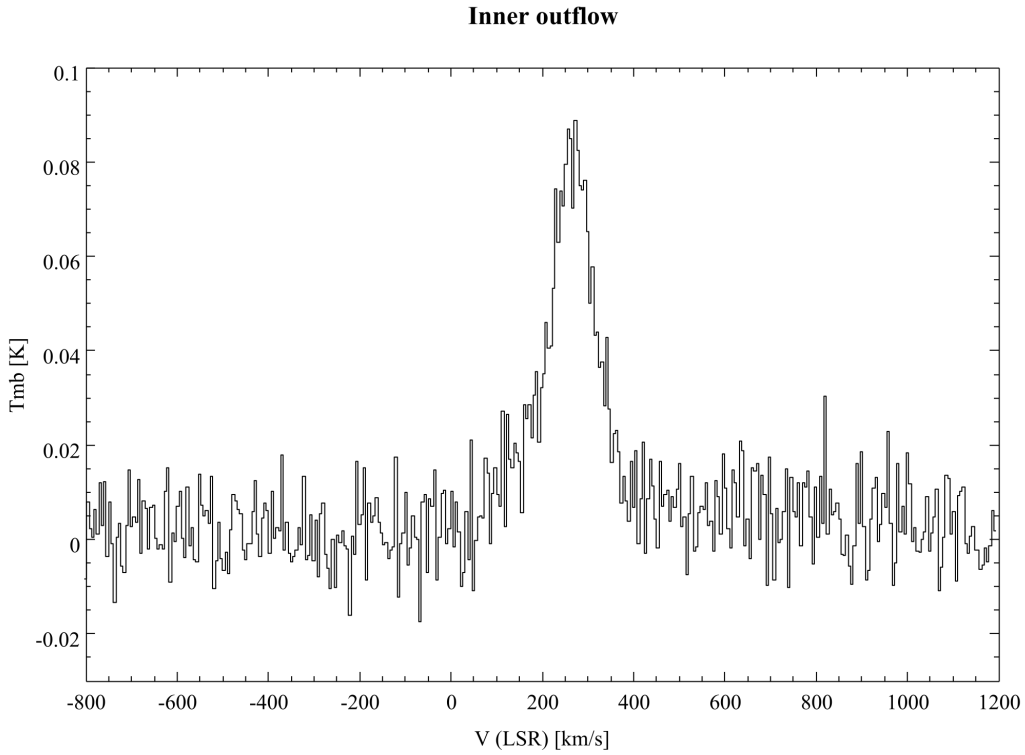

Figure 5.53: ^{13}CO (1-0) emission spectrum at the position of the inner outflow.

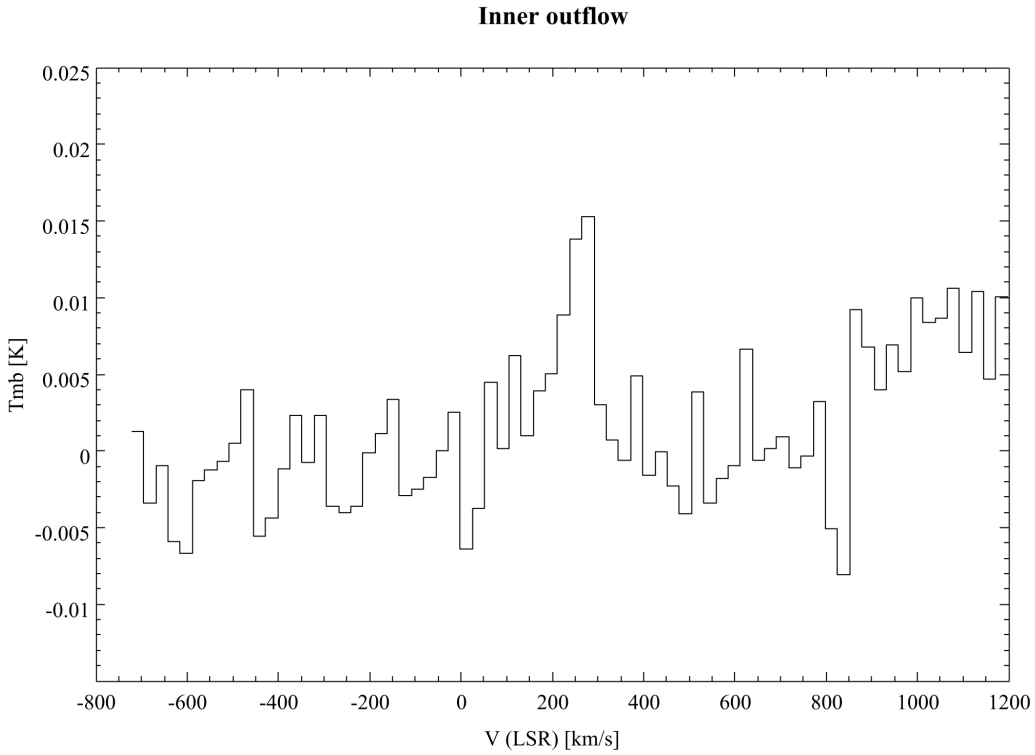

Figure 5.54: C^{18}O (1-0) emission spectrum at the position of the inner outflow.

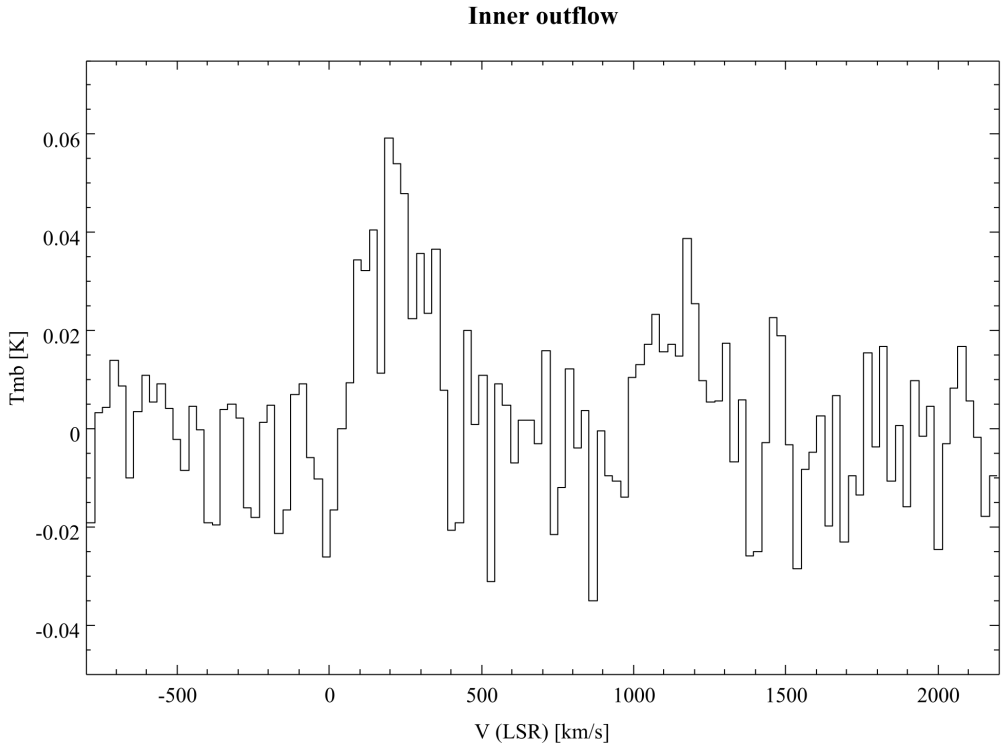

Figure 5.55: CN (1-0) emission spectrum at the position of the inner outflow.

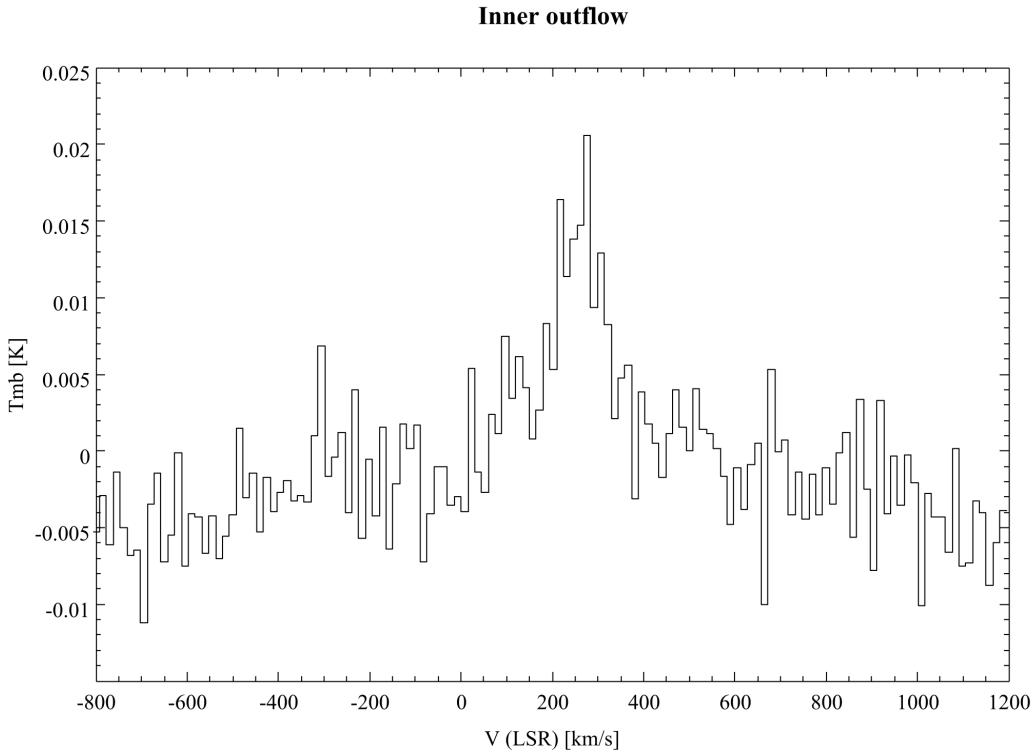

Figure 5.56: CS (2-1) emission spectrum at the position of the inner outflow.

Compared to CO (1-0), emission from the dense gas tracer CS (2-1) is weak. The Einstein coefficient for this transition is $A_{21} = 2.2 \times 10^{-5}$ s^{-1}, which is large compared to CO (1-0). Consequently, the critical density is $n_c \sim 10^5$ cm^{-3}. Therefore, while CO can radiate strongly in low- and high-density medium, CS (2-1) is bright only in dense molecular clouds. Studies of nearby galaxies suggest that CS lines are probing the densest gas very well (Baan et al. 2008), although Galactic studies have also found low-density sub-thermally excited CS emission (McQuinn et al. 2002). These authors found that CS (2-1) and ^{13}CO (1-0) lines can be used to probe the physical conditions (density) of the interstellar gas. We will see below that the ^{13}CO (1-0)/CS (2-1) ratio is significantly different in the nuclear torus and the inner outflow. On the contrary, ^{13}CO (1-0)/CN (1-0) ratio is nearly the same. Implications on this result are discussed in the subsection on excitation.

As mentioned above, we must carefully examine whether emission in the inner outflow is contaminated by the error beam of the 45-m telescope. The CS (2-1) intensity in the outflow is $\simeq 12\%$ its value in the nuclear ring. The error beam contamination at the position of the inner outflow is estimated to be about 5% and certainly lower than 10%. This is lower than observed, hence we interpret the CS (2-1) emission line as clear detection. This is supported by V_c in the inner outflow, which is as expected from our interferometer map. Therefore, we use this result in our discussion.

The intensity of the CN (1-0) line is only 4.4 times weaker in the outflow. This rules out any significant contamination from the error beam. Similar is for the CO lines, except the weak C^{18}O (1-0) line. Interestingly, the intensity ratio of C^{18}O (1-0) and CS (2-1) in the eastern peak compared to the inner outflow is nearly the same.

Table 5.4: Line parameters for the inner outflow.

Line	I [K km s^{-1}]	T_{mb} [K]	V_c [km s^{-1}]	FWHM [km s^{-1}]	Δv_{int}	Δv_{ch}
^{12}CO (1-0)	307.8 ± 1.7	2.138 ± 0.038	264.2 ± 0.3	118.1 ± 0.9	385	5.08
^{13}CO (1-0)	11.4 ± 0.3	0.084 ± 0.008	266.5 ± 1.8	105.5 ± 7.1	287	5.31
C^{18}O (1-0)	1.3 ± 0.2	0.016 ± 0.003	258.8 ± 5.5	75.0 ± 13.1	166	26.7
CN (1-0)^a	10.3 ± 1.2	0.048 ± 0.013	218.2 ± 15.9	204.8 ± 37.4	310	25.8
CN (1-0)^b	4.9 ± 1.1	0.024 ± 0.013	-	191.8 ± 68.4	261	25.8
CS (2-1)	2.0 ± 0.2	0.016 ± 0.003	261.8	124.1 ± 20.5	221	14.9

Note. The data were smoothed by 4 channels to the velocity resolution of ≈ 5 km s^{-1}, except C^{18}O (1-0) and CN (1-0) which were smoothed by 20 channels and CS (2-1), which was smoothed by 10 channels. The CN molecule has two sets of hyperfine-structure transition lines: a) $N = 1 \rightarrow 0$, $J = 3/2 \rightarrow 1/2$ between 113.488 and 113.520 GHz and b) $N = 1 \rightarrow 0$, $J = 1/2 \rightarrow 1/2$ between 113.123 and 113.191 GHz.

5.5.4 NW clump and outer outflow

The north-west clump (NW clump) is an extra-planar region of molecular and atomic gas discovered in CO (1-0) and H I lines (Salak et al. 2013; Yun et al. 1994), located in the galactic halo 3.5 kpc above the midplane (see figure 5.1 (b)). The NW clump is a peculiar region because of its bright emission arising from both atomic and molecular gas with no detected stellar counterpart. By comparing with X-ray emission, which is widely extended in the halo (Stevens et al. 2003), we find that the clump is faint in X-rays - it coincides with an X-ray "dark lane". The anticorrelation was discovered by Stevens et al. (2003), who suggested that two processes can be responsible: (1) absorption of X-rays by ambient neutral gas, or (2) interaction between X-ray emitting plasma from the outflow and the neutral gas. In either case, the X-ray halo originates in the superwind outflow, whereas the NW clump is part of a tidal stream.

The strong CO (1-0) emission (4σ in $T_{\rm mb}$ in our OTF map) led us to investigate the region by observing ^{12}CO (1-0), ^{13}CO (1-0), CN (1-0) and CS (2-1) to probe the physical conditions of the molecular gas. Spectra of the CO (1-0), ^{13}CO (1-0) and CS (2-1) in the NW clump are shown in figures 5.57, 5.58, and 5.59. The line parameters are given in table 5.5.

With high sensitivity (2 mK and 3 mK r.m.s. in $T_{\rm mb}$ for CS 2-1 and ^{13}CO 1-0, respectively), the weak lines were not detected. ^{12}CO (1-0) was detected with $T_{\rm mb} = 0.183 \pm 0.029$ mK. In our OTF map, the line peak was $T_{\rm mb} = 142 \pm 34$ mK at the resolution of 20 km s^{-1} and the telescope beam of $22''$; here, it is $T_{\rm mb} = 142 \pm 13$ mK at the similar resolution and the beam of $15''$. The beam size was different but the data are in good agreement within the positional and intensity uncertainty.

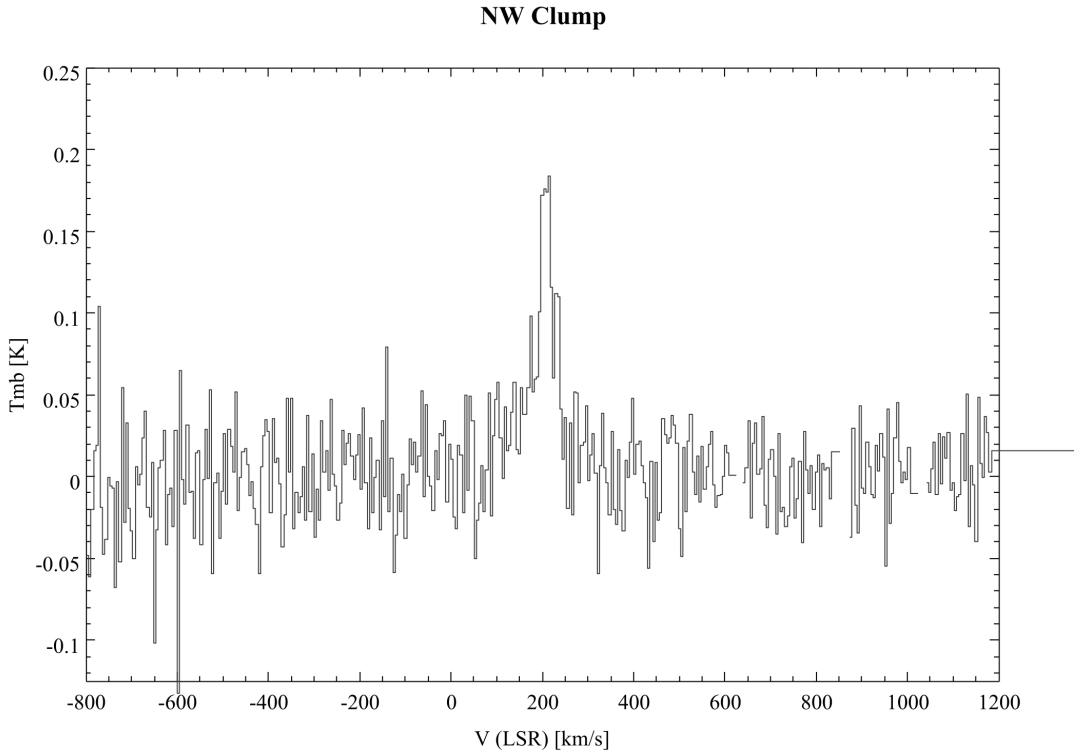

Figure 5.57: ^{12}CO (1-0) emission spectrum at the position of the NW clump.

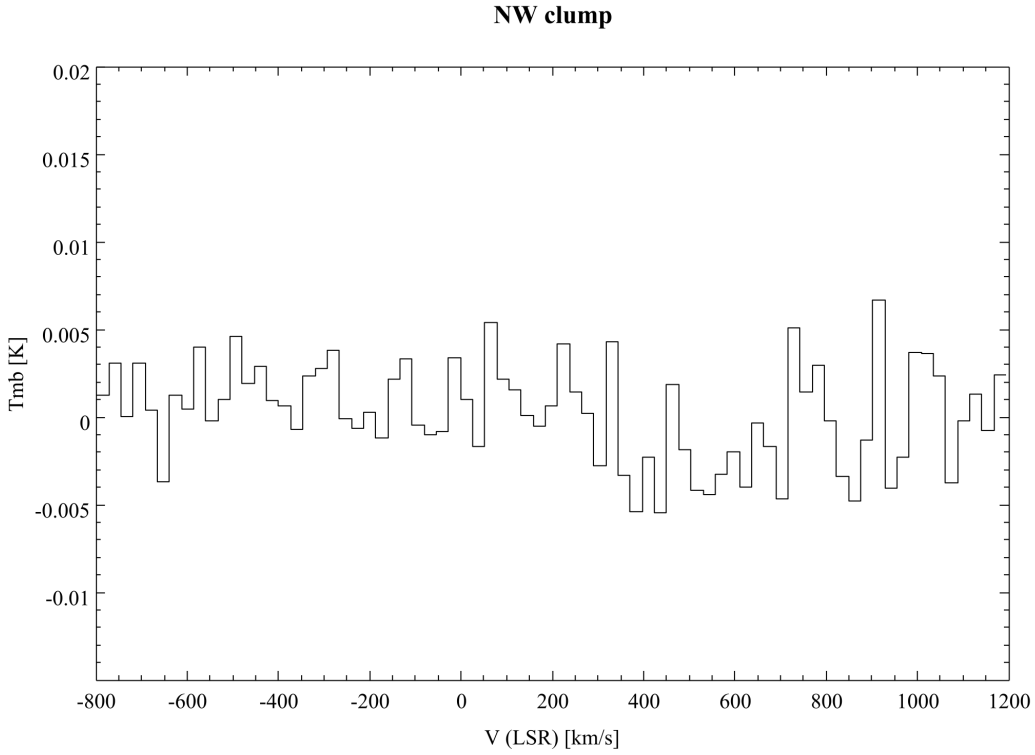

Figure 5.58: ^{13}CO (1-0) emission spectrum at the position of the NW clump smoothed by 20 channels to the spectral resolution of 26.6 km s^{-1}.

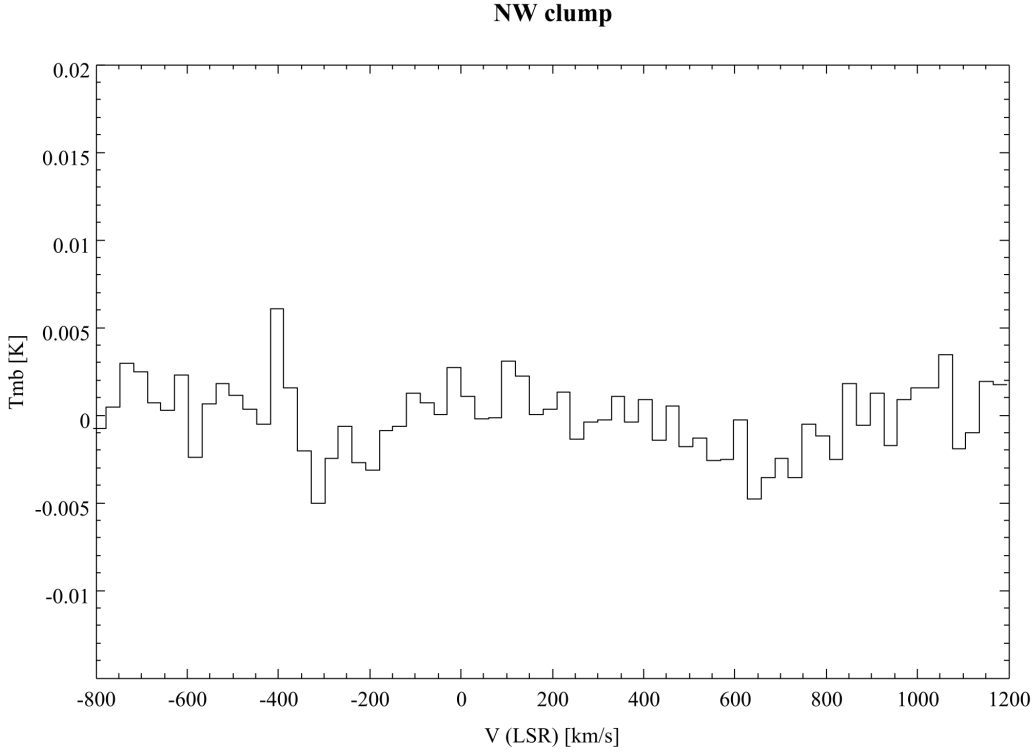

Figure 5.59: CS (2-1) emission spectrum at the position of the NW clump smoothed by 20 channels to the spectral resolution of 29.9 km s^{-1}.

The outer outflow is a position selected between the NW clump and the galactic center; it is part of a CO filament in the north part of the molecular gas outflow, denoted "F" in figure 5.1 (b). Spectra of ^{12}CO (1-0) and CN (1-0) are shown in figures 5.60 and 5.61. ^{13}CO (1-0) and CS (2-1) were not observed at this position.

The CO (1-0) emission is brighter in the outer outflow than in the NW clump. The peak brightness temperature of the line is 256 ± 39 mK, and the integrated intensity is 13.3 ± 1.1 K km s^{-1}. We note in table 5.5 the following comparison between the two regions: (1) $V_c \approx V_{sys}$ in the outer outflow, while it is lower in the NW clump; (2) the line widths (FWHM) are nearly the same; (3) the integration range is larger for the line profile of the outer outflow - there is noticeable line broadening (wing) in the spectrum of the outer outflow. The broadening shows that the spectrum can be fitted with two components - one narrow Gaussian, and the other for the broad wing at lower velocities. FWHM in table 5.5 corresponds to the narrow component.

With an r.m.s. noise of 9 mK, CN (1-0) was not detected.

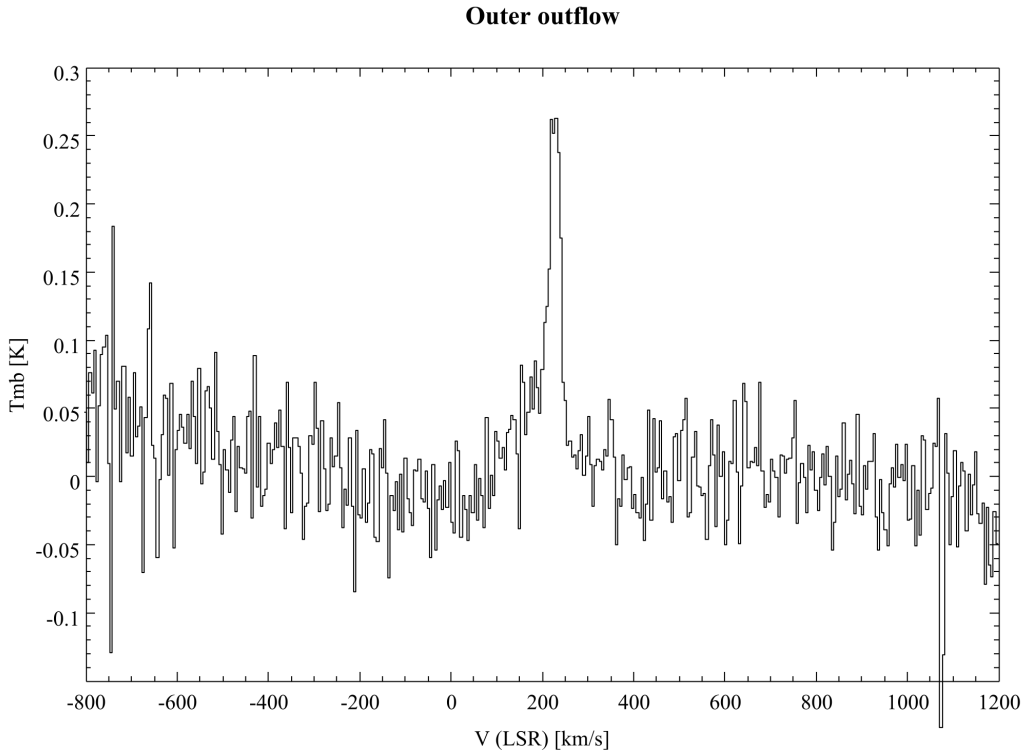

Figure 5.60: ^{12}CO (1-0) emission spectrum at the position of the outer outflow smoothed by 4 channels to the spectral resolution of 5.08 km s^{-1}.

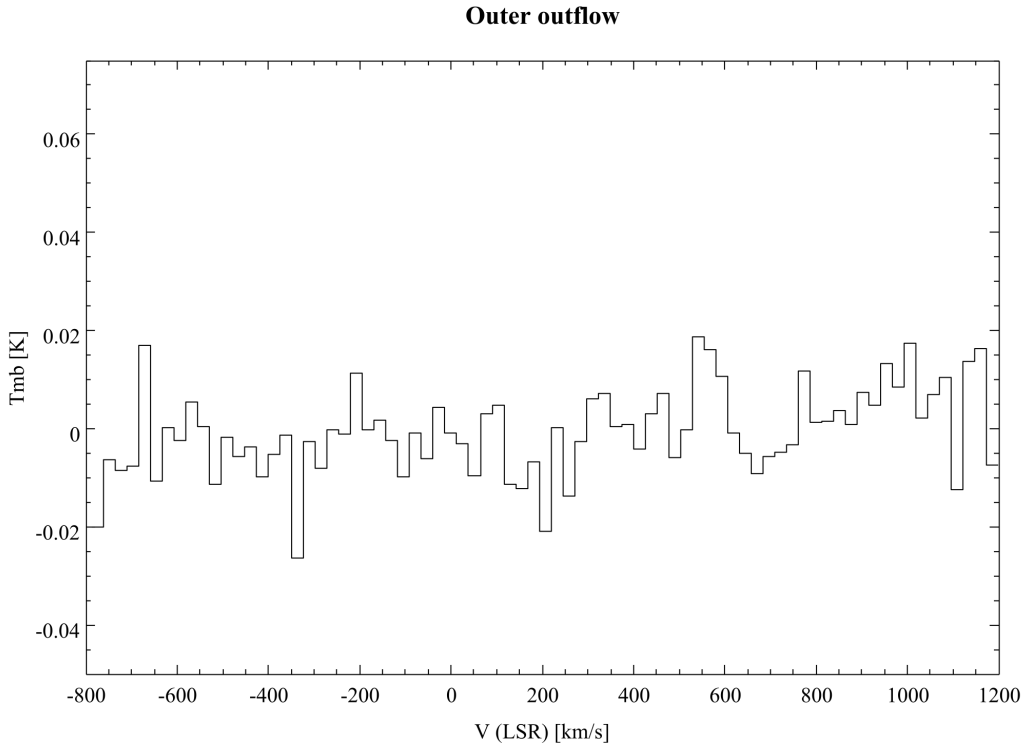

Figure 5.61: CN (1-0) emission spectrum at the position of the outer outflow smoothed by 20 channels to the spectral resolution of 25.8 km s^{-1}.

Table 5.5: Line parameters for the NW clump and outer outflow.

Line	I [K km s^{-1}]	$T_{\rm mb}$ [K]	$V_{\rm c}$ [km s^{-1}]	FWHM [km s^{-1}]	$\Delta v_{\rm int}$	$\Delta v_{\rm ch}$
NW clump						
^{12}CO (1-0)	8.2(0.6)	0.183 ± 0.029	208.6 ± 1.5	34.3 ± 3.4	86	5.08
^{13}CO (1-0)	<0.4	<0.009(0.003)	-	-	-	26.6
CS (2-1)	-	<0.006(0.002)	-	-	-	29.9
Outer outflow						
^{12}CO (1-0)	13.3 ± 1.1	0.256 ± 0.039	225.8 ± 1.3	36.4 ± 3.2	163	5.08
CN (1-0)	-	<0.027(0.009)	-	-	-	25.8

Note. ^{12}CO data (1-0) were smoothed by 4 channels to the velocity resolution of 5.08 km s^{-1}. When smoothed by 20 channels, then $T_{\rm mb} = 0.142 \pm 0.013$ K in the NW clump.

5.5.5 Western stream and western arm

CO (1-0) was clearly detected in the regions labeled as western stream (WS) and western arm (WA). In these regions we simultaneously observed CN (1-0), but without detection at a noise level of 13-16 mK in $T_{\rm mb}$ (table 5.6).

The line intensity in WS is 146 K km s^{-1} with the peak brightness temperature as high as 1.624 ± 0.05 K. The emission is clearly blueshifted with respect to $V_{\rm sys}$, with $V_{\rm c} = 132.2 \pm 0.9$ km s^{-1}. The line FWHM is 58.5 ± 4.4 km s^{-1}, which is an intermediate value between those in the nuclear region and the halo. Since WS is near the midplane, rotation pattern affects its line width. Note from figure 5.62 that the line does not have the shape of a regular Gaussian. The peak belongs to a narrow blueshifted component at 132 km s^{-1}, whereas the weaker component is near 180 km s^{-1}. The complex profile suggests that the weak component is part of the galactic disk, contrary to the low-velocity component that was resolved as a molecular gas stream in our high-resolution map, and in Walter et al. (2002) as S1.

The integrated intensity of the CO (1-0) line in WA is 50.9 K km s^{-1}, with a bright peak of 0.916 ± 36 K at $V_{\rm c} = 110.2 \pm 1$ km s^{-1}. The line width FWHM is 47.3 ± 2.1 km s^{-1}, while the profile can be fitted with a single Gaussian function. Note from figure 5.1 (b) that WA corresponds to the only bright peak detected outside the nuclear ring.

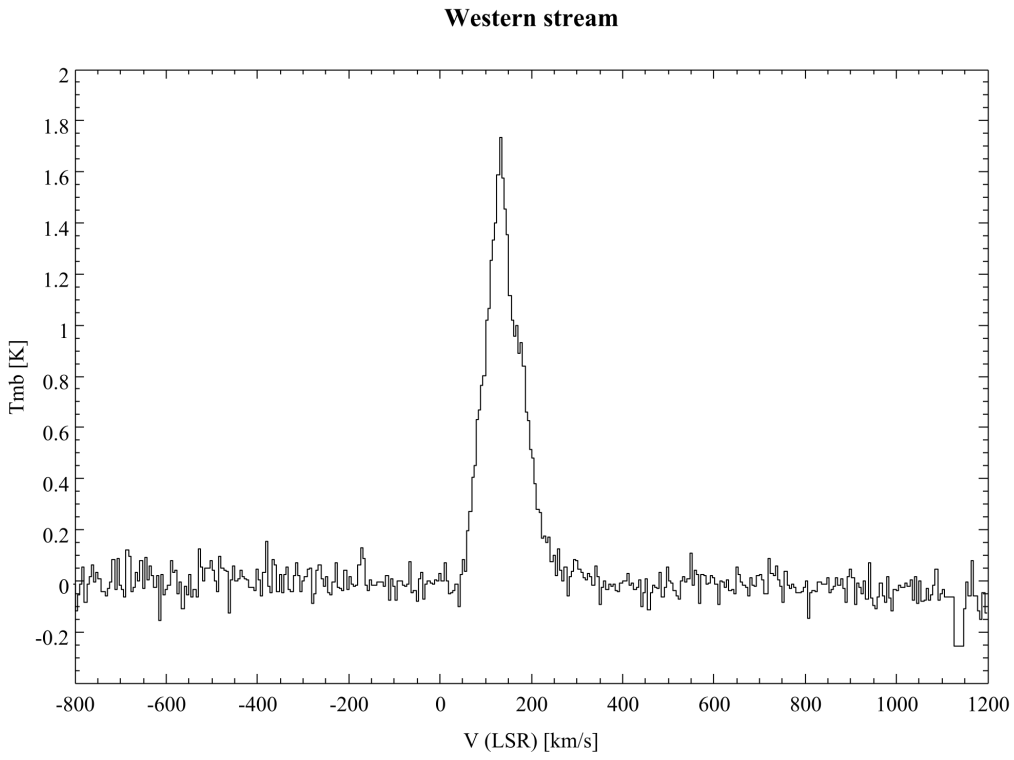

Figure 5.62: ^{12}CO (1-0) emission spectrum at the position of the western stream.

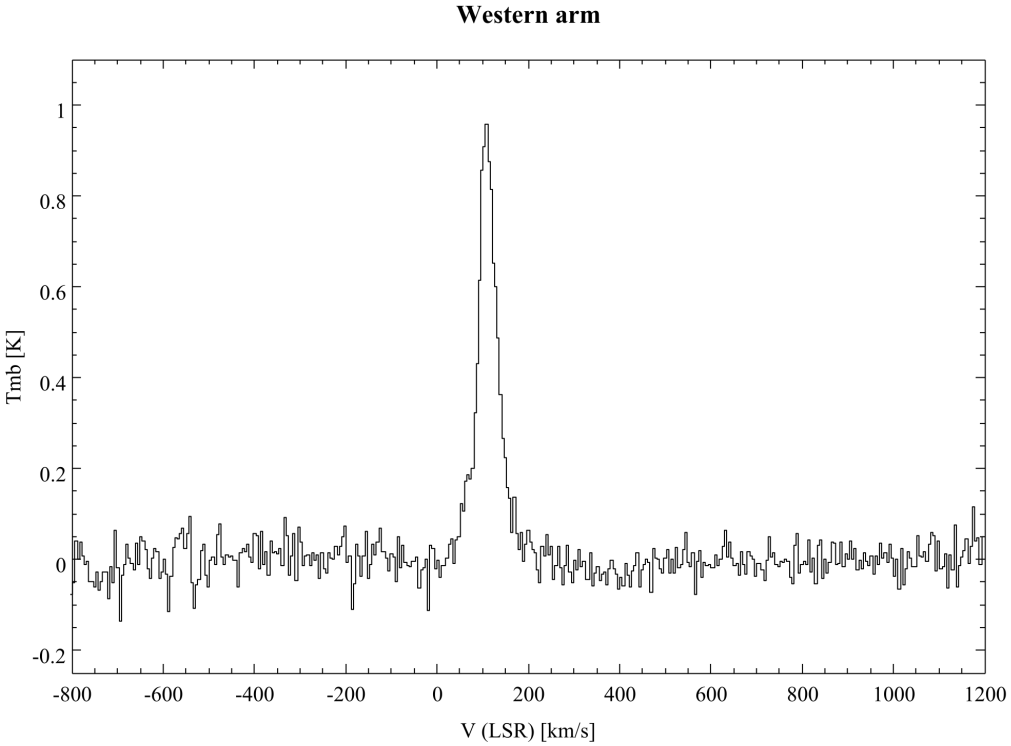

Figure 5.63: ^{12}CO (1-0) emission spectrum at the position of the western arm.

Table 5.6: Line parameters for the western arm and western stream.

Line	I [K km s^{-1}]	$T_{\rm mb}$ [K]	$V_{\rm c}$ [km s^{-1}]	FWHM [km s^{-1}]	$\Delta v_{\rm int}$	$\Delta v_{\rm ch}$
Western arm						
^{12}CO (1-0)	50.9 ± 1.0	0.916 ± 0.036	110.2	47.3 ± 2.1	154	5.08
CN (1-0)	-	<0.039(0.013)	-	-	-	25.8
Western stream						
^{12}CO (1-0)	146.0 ± 1.6	1.624 ± 0.050	132.2 ± 0.9	58.5 ± 4.4	201	5.08
CN (1-0)	-	<0.048(0.016)	-	-	-	25.8

5.5.6 Line ratios

In previous sections, we have presented the data of our single-dish and interferometer imaging and 3-mm line survey. In addition to the image of CO (1-0), the lines of rare isotopic species of CO, in combination with CN and CS in the nuclear region and the halo, give us a set of tools to study the physical conditions of the molecular gas. In this subsection, we present the ratios of line intensities, and information that can be deduced from their analysis. In all comparisons, integrated intensity is used instead of brightness temperature because of its higher signal-to-noise ratio for weak lines.

The integrated intensity $I \equiv \int T_{\rm mb} {\rm d}v$ of the observed lines is summarized in table 5.7, along with the ratio "EP/IO" of the intensity of each line in the eastern peak (EP) and inner outflow (IO). The most interesting result here is the different EP/IO for different molecular species. Even among the CO lines, we see a decreasing tendency toward the most abundant isotopic species: EP/IO (CO 1-0) is lower than EP/IO (^{13}CO 1-0), which is in turn lower than EP/IO (C^{18}O 1-0). Also, we note that EP/IO's are similar for ^{13}CO (1-0) and CN (1-0) on one hand, and between C^{18}O (1-0) and CS (2-1) on the other. Considering that CS is a tracer of dense gas, and that C^{18}O (1-0) requires significant column density to be detected, this tendecy indicates a decrease in the beam filling factor of the dense component of the molecular gas in the inner outflow compared to the nuclear ring. The line ratios suggest that the molecular gas is increasingly diffuse in the outflow. If we model the molecular gas as having two phases - dense (DSP) and diffuse (DFP), an analysis of the line ratios can yield the change of the relative volume filling factors of DSP and DFP.

Table 5.7: Comparison of integrated intensities (in K km s^{-1}) in the nuclear ring, inner outflow, and NW clump.

Line	EP	IO	CL	EP/IO
^{12}CO (1-0)	775.1 ± 11.5	294.2 ± 2.7	10.3 ± 0.6	2.6 ± 0.1
^{13}CO (1-0)	49.0 ± 1.0	12.5 ± 0.4	<0.4	3.9 ± 0.2
C^{18}O (1-0)	13.3 ± 0.8	1.7 ± 0.3		7.8 ± 1.8
CN (1-0)	68.4 ± 2.1	15.5 ± 1.1		4.4 ± 0.4
CS (2-1)	18.5 ± 0.7	2.2 ± 0.2	<0.3	8.4 ± 1.1

Note. EP = eastern peak, IO = inner outflow, CL = NW clump. All lines were smoothed by 20 channels to a comparable spectral resolution. All values were derived from Gaussian fitting of the spectra. The upper limits were calculated as 3σ of the integrated intensity assuming the same line width as that of CO (1-0).

Table 5.8: Comparison of integrated intensities of different transitions in the nuclear ring, inner outflow, and NW clump.

Ratio	EP	IO	CL
^{12}CO (1-0)/^{13}CO (1-0)	15.8 ± 0.6	23.5 ± 1.0	>25.7
^{13}CO (1-0)/C^{18}O (1-0)	3.7 ± 0.3	7.3 ± 1.5	
^{12}CO (1-0)/C^{18}O (1-0)	58.3 ± 4.0	173.1	
^{12}CO (1-0)/CN (1-0)	11.3 ± 0.5	19.0 ± 1.5	
^{12}CO (1-0)/CS (2-1)	41.9 ± 2.2	133.7 ± 13.4	>34.3
CN (1-0)/CS (2-1)	3.7 ± 0.3	7.0 ± 1.1	
CN (1-0, 3/2-1/2)/CN (1-0, 1/2-1/2)	1.8	2.0	

Note. EP = eastern peak, IO = inner outflow, CL = NW clump. All lines were smoothed by 20 channels to a comparable spectral resolution. All values were derived from Gaussian fitting of the spectra.

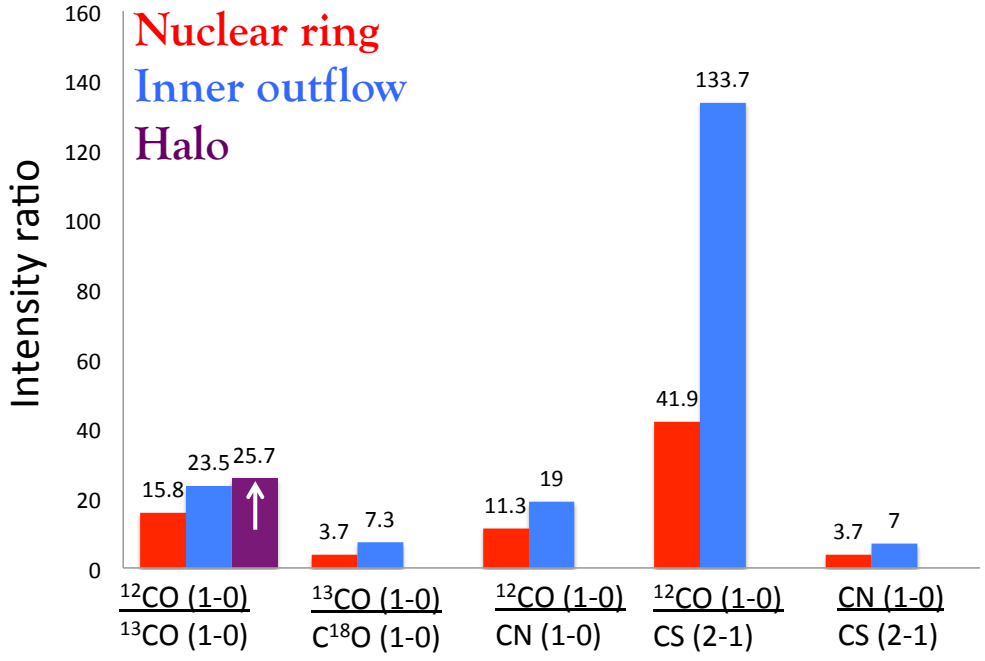

Figure 5.64: Line intensity ratios. "Halo" corresponds to the NW clump.

Error beam

The main beam efficiency of the 45-m telescope at 110-115 GHz is 0.30 (NRO web page). This means that about 70% of the received power arrives in solid angles outside the main beam. In order to investigate the possibility that the observed emission lines in the inner outflow are instrumental artifacts from the error beam and power side lobes, we have used the result of measurement of the telescope beam at NRO (N. Kuno, priv. comm.). The inner outflow position is separated by $\approx 20''$ from the bright nuclear ring. From figure 5.65, it can be deduced that the intensity level could be as high as ≈ 5 % at this position. Hence, the emission lines in the outflow cannot be attributed to the error beam, because all ratios of the line intensities (nuclear ring)/(inner outflow) are less than 10. Although strong influence may be expected for the CS (2-1) line, for which the telescope beam is largest, the line profile and the peak velocity of the spectrum do not resemble that of the nearby eastern peak. If the emission were solely due to the nuclear ring, we would expect to see a double peak, since both bright peaks of the nuclear ring are at similar distance from the inner outflow position.

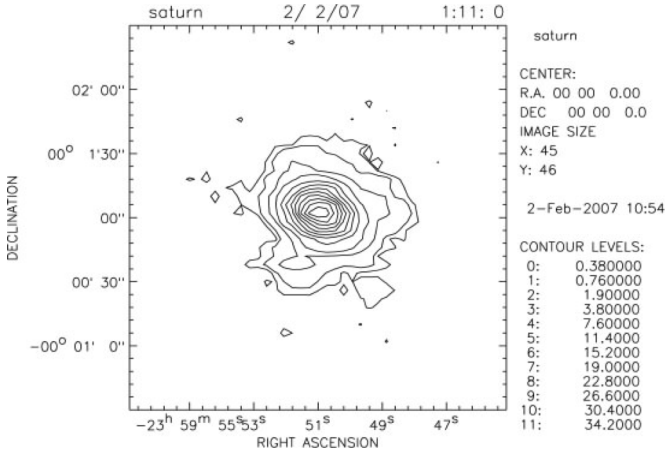

Figure 5.65: Beam pattern of the 45-m telescope measured in 2007 at 110 GHz by observing the planet Saturn which has an apparent diameter of $15''-20''$. The contours are: 1%, 2%, 5%, 10%, 20%, 30%,... of the peak intensity. (Received from N. Kuno, priv. comm.)

5.6 Excitation conditions

5.6.1 Isotopic species of CO

Observations of the CO isotopic species in nearby galaxies have established an important result: the ratio of CO (1-0) and ^{13}CO (1-0), which is defined $\mathscr{R}_{23} = I(^{12}\mathrm{CO}\ J = 1 \rightarrow 0)/I(^{13}\mathrm{CO}\ J = 1 \rightarrow 0)$, is increasing with dust temperature, T_d (Young & Sanders 1986). Emission of CO (1-0) arises mostly from outer layers of molecular clouds, with a photon mean free path of $\tau = 1$, because it is optically thick. Similarly, UV photons coming from outside will be efficiently absorbed, and CO is said to be self-shielded. ^{13}CO (1-0) is only moderately optically thick $\tau \simeq 1$, and UV photons which can lead to dissociation of ^{13}CO can penetrate deeper into the cloud. This is referred to as the *selective dissociation*. Therefore, ^{13}CO (1-0) emission arises mostly from inner parts of the cloud.

The ratio $\mathscr{R}_{23}$ was found to be $\simeq 8$ on average in our Galaxy (Young & Sanders 1986), while larger in a number of other galaxies, especially interacting systems and mergers, where > 20 was found (Aalto et al. 1995; Costagliola et al. 2011). Costagliola et al. (2011) have found $\mathscr{R}_{23} \simeq 28$ in NGC 6240 and NGC 1614, which can be explained by high gas temperature and diffuse medium.

Another scenario that may enhance $\mathscr{R}_{23}$ is in starburst galaxies where molecular gas is strongly concentrated in a particular region. There, cloud-cloud collisions, crowding and non-circular motion increase the line width of CO, hence allowing more photons to escape without being absorbed. In that case, the optical depth is decreased because $\tau \propto (\Delta v)^{-1}$, which results in a large $\mathscr{R}_{23}$.

In regions where ^{13}CO (1-0) is moderately optically thick, it is safe to assume that C^{18}O (1-0) is optically thin, with $\tau \ll 1$. Therefore, the C^{18}O (1-0) emission arises from even denser regions, and if we define $\mathscr{R}_{38} = I(^{13}\mathrm{CO}\ J = 1 \rightarrow 0)/I(\mathrm{C}^{18}\mathrm{O}\ J = 1 \rightarrow 0)$, the ratio $\mathscr{R}_{38}$ will follow a similar tendency as discussed above for $\mathscr{R}_{23}$.

The relative abundance of the isotopic species of CO is influenced by environmental effects such as starburst activity or gas infall toward the central galactic region (Henkel & Mauersberger 1993). These authors argue that advanced starburst stage of a galaxy, with a star formation history including many massive ($> 8\ M_\odot$) stars, should decrease the abundance ratio of ^{16}O/^{18}O, but only slightly affect ^{12}C/^{13}C. The latter is likely to be increased by gas infall, because molecular gas outside the galactic center resides in environment which has not experienced much massive-star formation. The formation of massive stars is the most important reservoir of ^{18}O, because during He-burning ^{14}N is "processed" into ^{18}O. Class O stars, Wolf-Rayet stars and SN explosions of type II are the main generators.

5.6.2 Ratio map of CO (3-2) and CO (1-0) intensities

The physical parameters of the molecular gas in the central region of M82 were studied in a number of previous studies (e.g., Seaquist & Clark 2001; Weiß et al. 2005), which demonstrated the importance of a multi-line approach. We have derived a 2×2 arcmin^2 ratio map of the CO integrated intensity from this work and I_CO (3-2) from Seaquist & Clark (2001), defined as $R_{31} \equiv I_\mathrm{CO}(J = 3 \rightarrow 2)/I_\mathrm{CO}(J = 1 \rightarrow 0)$ (figure 5.66; Salak et al. 2013). The intensity maps were corrected for the difference in angular resolution and channel width.

The line ratio is high ($R_{31} \gtrsim 1.0$) in the starburst nucleus, and decreases gradually outward down to $R_{31} = 0.5 \pm 0.2$ at $Y = +30''$ and $Y = -40''$. The decline is more rapid along the minor axis compared to the major axis, where it retains a value of 0.7 up to $|X| = 50''$ east of the nucleus. This tendency is in agreement with previous measurements of the line ratios in Weiß et al. (2005), where it was found that the ratios are higher in the disk and streams than in the outflow.

The gradual decrease in R_{31} along the minor axis in the outflow suggests that the physical conditions of the molecular gas are not constant throughout the outflow. The CO (3-2) line is a tracer of warm and/or dense molecular gas. Beyond $|Y| = 40''$ we find $R_{31} \lesssim 0.5$, which clearly reflects decreasing excitation with distance from the central region.

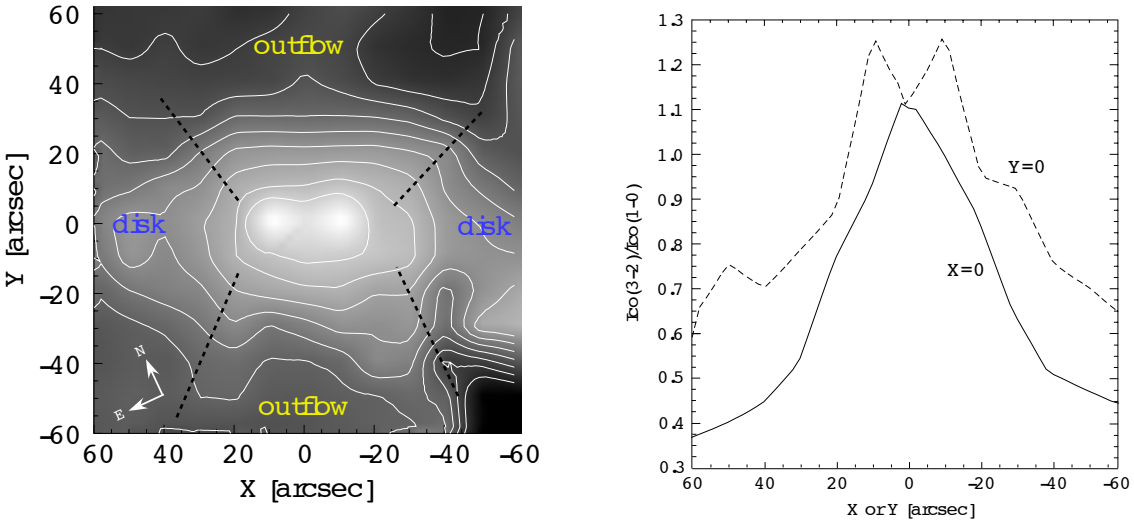

(a) (b)

Figure 5.66: Ratio of integrated intensities of the CO lines 3-2 and 1-0 in the central region of M82 (Salak et al. 2013): a) ratio map of the CO lines, and b) X- and Y-axis profiles of the ratio.

5.6.3 Two-phase model in LTE

The velocity-integrated main beam temperature of an observed species can be expressed as

$$I = \int T_{\rm mb} {\rm d}v = f_{\rm d} \Delta V_{\rm d} T_{\rm d} \left(1 - {\rm e}^{-\tau_{\rm d}}\right) + f_{\rm t} \Delta V_{\rm t} T_{\rm t} \left(1 - {\rm e}^{-\tau_{\rm t}}\right), \tag{5.36}$$

where d and t denote dense and translucent phases of the molecular gas. In the LTE, we can assume that the abundance ratio is nearly equal to the optical depth ratio. The abundance ratios in the nuclear ring were derived by Weiß et al. (2001b) to be $[{\rm CO}]/[^{13}{\rm CO}] \sim 70$ and $[{\rm CO}]/[{\rm C}^{18}{\rm O}] \sim 215$. We obtain three equations with eight unknown parameters:

$$\begin{aligned} I_1 + I_2 &= A_1 \left(1 - {\rm e}^{-\tau_{\rm d}}\right) + A_2 \left(1 - {\rm e}^{-\tau_{\rm t}}\right) = 100 \\ I_3 + I_4 &= A_3 \left(1 - {\rm e}^{-\tau_{\rm d}/70}\right) + A_4 \left(1 - {\rm e}^{-\tau_{\rm t}/70}\right) = 6.2 \\ I_5 + I_6 &= A_5 \left(1 - {\rm e}^{-\tau_{\rm d}/215}\right) + A_6 \left(1 - {\rm e}^{-\tau_{\rm t}/215}\right) = 0.6, \end{aligned} \tag{5.37}$$

where $A \equiv f \Delta V T$. The solutions are shown in table 5.9. The results show that most of the CO (1-0) and ^{13}CO (1-0) emission comes from the translucent phase, while C^{18}O (1-0) emission arises primarily from the dense phase. The assumed optical depths of 100 and 1 for the dense and translucent components, respectively, accommodate the observed properties of moderately optically thick CO (1-0) throughout the nuclear ring (Weiß et al. 2001b).

5.6.4 Optical depth of CN (1-0)

As discussed in Introduction, the CN (1-0) line has two sets of hyperfine transitions. Let us denote the transitions $N = 1 \rightarrow 0$, $J = 3/2 \rightarrow 1/2$ with hf(3/2) and the transitions $N = 1 \rightarrow 0$, $J = 1/2 \rightarrow 1/2$ with hf(1/2). The observed brightness temperatures, assuming equal beam filling factors, are

Table 5.9: Relative LTE solutions for a two-phase molecular gas.

Line	A_1	I_1	τ_1	A_2	I_2	τ_2	I_1+I_2
^{12}CO (1-0)	0.5	0.5	100	157	99.5	1	100
^{13}CO (1-0)	0.66	0.5	1.43	402	5.7	0.014	6.2
C^{18}O (1-0)	1.34	0.5	0.46	21.5	0.1	0.005	0.6

$$T_{\rm b,32} = \left(T_{\rm ex,32} - T_{\rm bg}\right)\left(1 - {\rm e}^{-\tau_{32}}\right) \qquad (5.38)$$
$$T_{\rm b,12} = \left(T_{\rm ex,12} - T_{\rm bg}\right)\left(1 - {\rm e}^{-\tau_{12}}\right).$$

If we assume that the excitation temperatures are the same, i.e., $T_{\rm ex,32} = T_{\rm ex,12}$, we may write

$$\frac{T_{\rm b,32}}{T_{\rm b,12}} = \frac{1 - {\rm e}^{-\tau_{32}}}{1 - {\rm e}^{-\tau_{12}}}, \qquad (5.39)$$

where the only unknowns are optical depths τ_{12} and τ_{32}. In LTE, $\tau_{12} = \tau_{32}/2$ and

$$\frac{T_{\rm b,32}}{T_{\rm b,12}} = \frac{1 - {\rm e}^{-\tau_{32}}}{1 - {\rm e}^{-\tau_{32}/2}}. \qquad (5.40)$$

This equation is plotted in figure 5.67. From table 5.8, we find that the optical depth is of CN is low, $\tau_{32} \approx 0.5$ in the eastern peak and $\tau_{32} \ll 1$ in the outflow. Therefore, the optical depth of CN (1-0) in LTE is estimated to be $\tau < 1$ in beam-averaged environment of the nuclear ring and inner outflow.

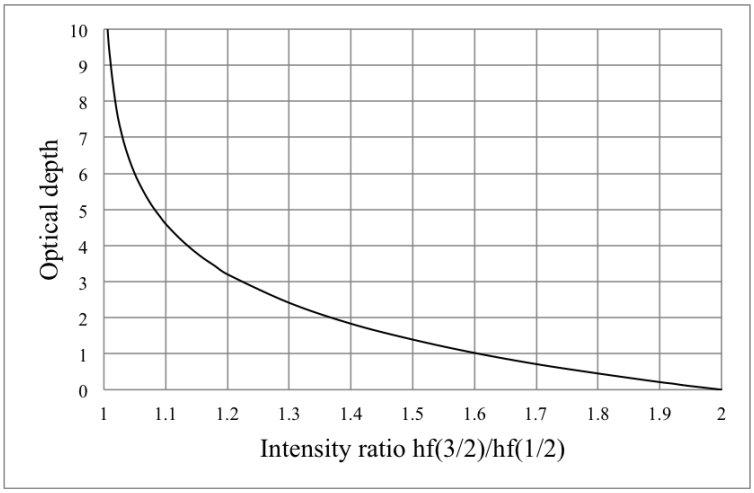

Figure 5.67: Optical depth vs. ratio of the hyperfine transitions of CN: hf(3/2) denotes the $N = 1 \rightarrow 0$, $J = 3/2 \rightarrow 1/2$ set of lines, and hf(1/2) denotes the $N = 1 \rightarrow 0$, $J = 1/2 \rightarrow 1/2$ set of lines.

5.6.5 Dense and diffuse molecular gas

The 3-mm line survey presented in this section provided us with information on relative molecular line intensities in the nuclear and extra-planar regions in M82. Although detailed analysis of physical conditions requires several transitions of the same molecule which are not available, the strength of this observation is in first detections of dense-gas tracers CN and CS in the inner outflow, confirmed

CO emission deep in the halo, and derived relative intensities of the lines of different molecular species. The ratios can be interpreted by a physical picture illustrated in figures 5.68 and 5.69. In this illustration, we emphasize particular regions which are traced with CO, CN, and CS in molecular clouds. For a comprehensive introduction on observations of CN and CS in external galaxies, see, e.g., Baan et al. (2008) and Costagliola et al. (2011). Below, we summarize some observational results.

The CN molecule. Observations of Orion KL show that cyano radical (CN) is enhanced in the *outer* regions of dense molecular clouds, with intensity rapidly decreasing toward the cloud interior (Jansen et al. 1995a; Jansen et al. 1995b). This is illustrated in figure 5.68 as a green line. However, the critical density of CN (1-0) is rather high, $n_c \sim 10^5$ cm^{-3}, and it would be dissociated outside of molecular medium (see table 1.2). Thus, CN (1-0) is a good probe of photodissociation regions (PDR), between dense and diffuse molecular-gas phases in the boudary region where C and CO coexist (see figure 1.8).

The CS molecule. The carbon monosulfide molecule (CS) is another dense-gas tracer with high critical density of CO (2-1) $n_c \sim 10^5$ cm^{-3}. Observations of our and external galaxies have demonstrated that CS is bright in dense regions, whereas low column densities do not contribute significantly to observed intensities (Baan et al. 2008). Thus, we illustrate optically thin CS (2-1) emission in figure 5.68 as coming directly from the cloud interior.

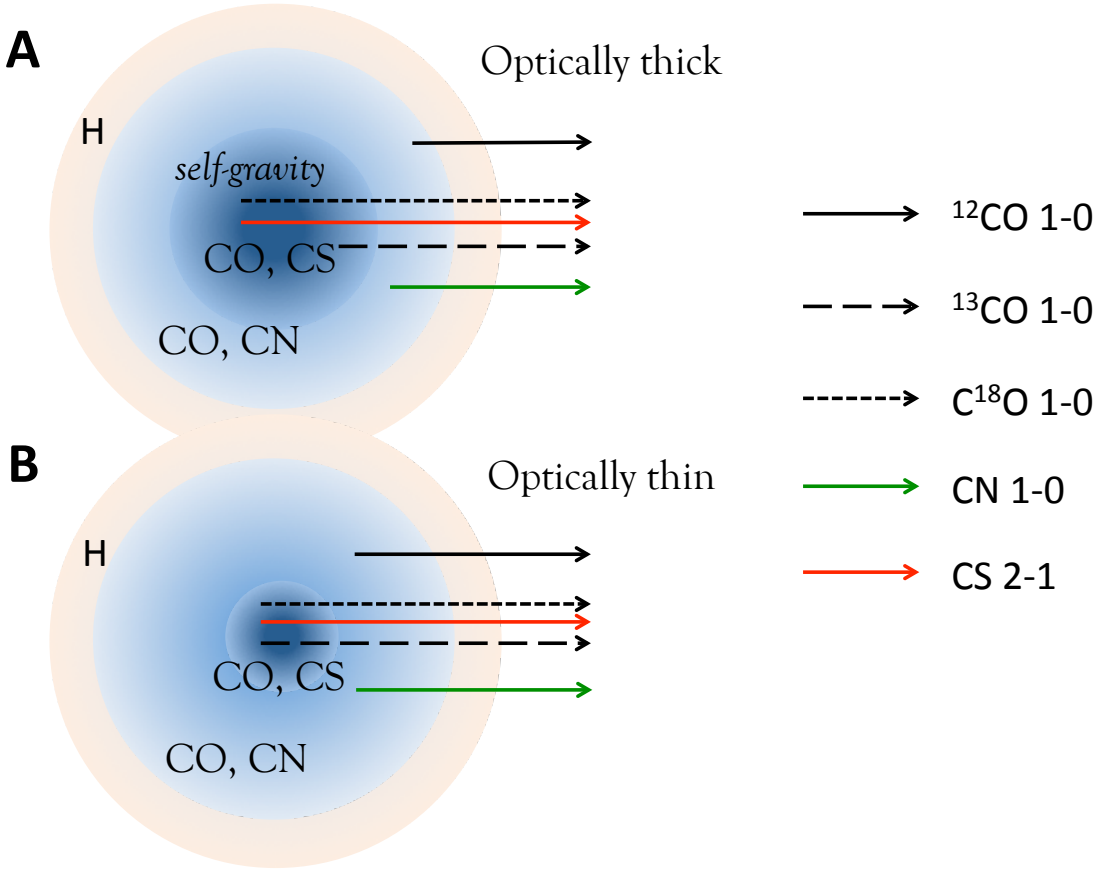

Figure 5.68: Molecular cloud composition in optically thick (A) and thin (B) gas. The arrows indicate from which regions the corresponding emission arises. In case A, CO (1-0) is tracing the outer envelopes of the cloud, while ^{18}CO (1-0) and CS (2-1) trace the cores. In case B, most of the emission penetrates through the entire cloud. CN is a molecule abundant in intermediate regions.

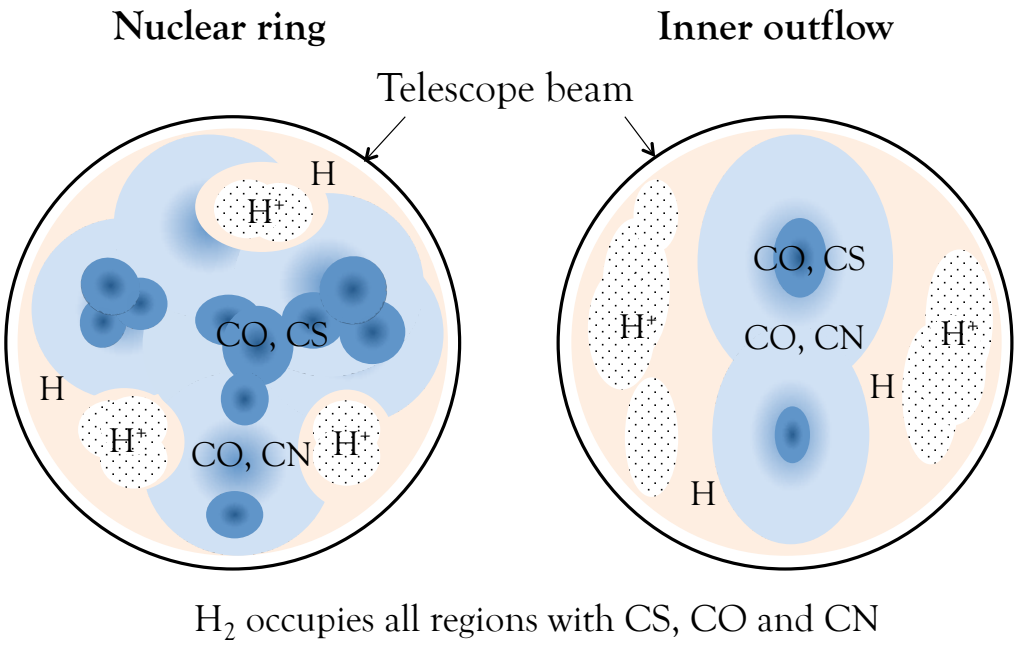

Figure 5.69: Molecular clouds of the nuclear region and inner outflow projected inside the beam of the NRO 45-m telescope.

Chapter 6

Observations of NGC 1808 with the VLA

6.1 VLA imaging of the galactic nucleus

6.1.1 Observations

The Very Large Array (VLA) observations of NGC 1808 took place on September 8 and 13, 2012, in the 2012B season, during the Expanded VLA (=EVLA) project to improve the capabilities of the old VLA interferometer. The spatial configuration of the interferometer array was BnA, with all 27 antennas operational with installed K- and Ka-band receivers. The BnA configuration is a hybrid configuration that has one arm of the Y-shape extended to the typical configuration A baselines, whereas the remaining two arms are in configuration B. In such arrangement, it is possible to achieve a (u, v) coverage for low-declination objects which is similar to that of the pure configuration B. Since NGC 1808 is at $\delta \approx -37^{\circ}$, BnA is the configuration that provides the highest angular resolution (equivalent to that of configuration B).

The observation proposal to NRAO was accepted in 2012, and NGC 1808 was observed in the same year with a total of 3.5 hours allocated to our project (table 6.1). The observing schedule was prepared in the NRAO's web application Observation Preparation Tool (OPT), divided into three scheduling blocks: one 1-hour block for K-band observations and two 1.25-hour blocks for Ka-band. The Ka-band was given more time because it is in a higher frequency band where radio continuum is expected to decline with a law $\propto \nu^{\alpha}$, where α is the spectral index. On the other hand, higher frequency provides higher resolution, because the resolution is inversely proportional to frequency, hence there was substantial merit to increase the integration time, i.e., sensitivity and (u, v) coverage in the Ka-band.

Table 6.1: Observational summary.

Date of obs.	Bands	Array	Duration	MS size
2012/09/08	K, X	BnA	60 min.	35.59 GB
2012/09/08	Ka, X	BnA	75 min.	46.30 GB
2012/09/13	Ka, X	BnA	75 min.	46.54 GB

Note. The bands are listed in the following order: main observation, reference pointing. All data can be found in NRAO's Data Archive.

The coordinates of the observed targets (the main target NGC 1808, and two calibrators J0424-3756 and 3C147) are given in table 6.2; the correlator configuration, integration time, bandwidth, etc.

are shown in tables 6.3, 6.4 and 6.5. The setup utilized three receivers: two for main observations (K and Ka) and one for reference pointing (X).

Table 6.2: Coordinates of the observed sources.

Source	α (J2000.0)	δ (J2000.0)	Reference
NGC 1808	$05^h07^m42.343001^s$	$-37^o30'46.98''$	VLA archive (2MASS peak)
J0424-3756	$04^h24^m42.243727^s$	$-37^o56'20.78423''$	VLA archive
0542+498=3C147	$05^h42^m36.137916^s$	$+49^o51'7.23356''$	VLA archive

Table 6.3: Instrument configuration.

Observation	Band	Integ. time	Bandwidth (AC, BD)	Frequency (AC, BD)
Primary pointing	X	1 s	128.0 MHz, 128.0 MHz	8.46 GHz, 8.588 GHz
K wide band	K	1 s	1.024 GHz, 1.024 GHz	20.7 GHz, 21.7 GHz
Ka wide band	Ka	1 s	1.024 GHz, 1.024 GHz	32.52 GHz, 31.52 GHz

Due to the low declination of the target, observations required careful planning of time intervals (LST = local sidereal time) when NGC 1808 was observable. At its peak, the galaxy does not rise above elevation $= 20^0$ as seen from the VLA site, which poses a challenge for high frequency observations. Figures 6.1, 6.2 and 6.3 show elevation vs. LST and azimuth vs. LST diagrams for all targets. To make reliable calibration of the complex gain (amplitude and phase), it was necessary to select a calibrator that was at similar elevation as the target itself. On the other hand, the calibrator had to be at reasonable elevation to allow high S/N measurements (solutions) in short time intervals because interferometric observations comprise of observations of the target and the calibrator alternately. Unlike the gain calibrator, however, the only available calibrator for flux density was 3C147, which was at much higher elevation (figure 6.3). Flux calibration was done with respect to this calibrator.

Observations of the gain calibrator were conducted every four minutes. The flux calibrator was observed only once near the end of each scheduling block.

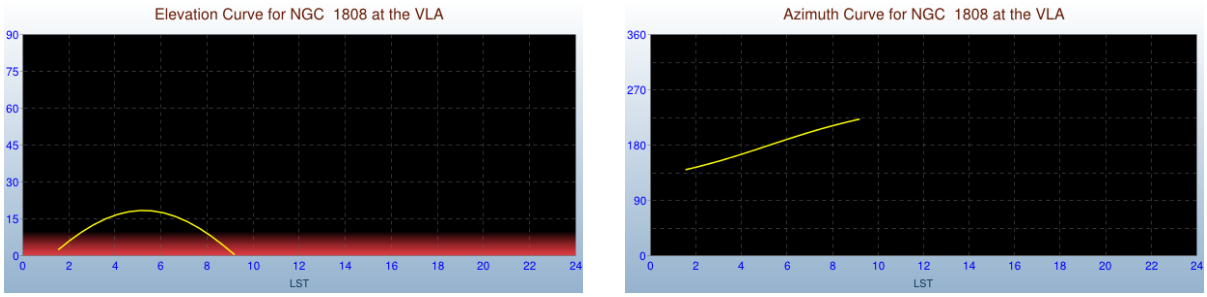

(a) (b)

Figure 6.1: (a) Elevation and (b) azimuth of NGC 1808 as a function of LST at the VLA site.

Table 6.4: K-band observational setup.

Spw	Ch.	Freq. [GHz]	Ch. BW [MHz]	Tot. BW [MHz]	Correlations
A/C 0	64	20.188	2.0	128.0	RR RL LR LL
A/C 1	64	20.316	2.0	128.0	RR RL LR LL
A/C 2	64	20.444	2.0	128.0	RR RL LR LL
A/C 3	64	20.572	2.0	128.0	RR RL LR LL
A/C 4	64	20.700	2.0	128.0	RR RL LR LL
A/C 5	64	20.828	2.0	128.0	RR RL LR LL
A/C 6	64	20.956	2.0	128.0	RR RL LR LL
A/C 7	64	21.086	2.0	128.0	RR RL LR LL
B/D 8	64	21.188	2.0	128.0	RR RL LR LL
B/D 9	64	21.316	2.0	128.0	RR RL LR LL
B/D 10	64	21.444	2.0	128.0	RR RL LR LL
B/D 11	64	21.572	2.0	128.0	RR RL LR LL
B/D 12	64	21.700	2.0	128.0	RR RL LR LL
B/D 13	64	21.828	2.0	128.0	RR RL LR LL
B/D 14	64	21.956	2.0	128.0	RR RL LR LL
B/D 15	64	22.084	2.0	128.0	RR RL LR LL

Note. Spw: spectral window, Ch: channels, Freq: sub-band center frequency, Ch. BW: channel bandwidth, Tot. BW: total bandwidth of a sub-band A/B, C/D: see Overview of the EVLA.

Table 6.5: Ka-band observational setup.

Spw	Ch.	Freq. [GHz]	Ch. BW [MHz]	Tot. BW [MHz]	Correlations
A/C 0	64	32.008	2.0	128.0	RR RL LR LL
A/C 1	64	32.136	2.0	128.0	RR RL LR LL
A/C 2	64	32.264	2.0	128.0	RR RL LR LL
A/C 3	64	32.392	2.0	128.0	RR RL LR LL
A/C 4	64	32.520	2.0	128.0	RR RL LR LL
A/C 5	64	32.648	2.0	128.0	RR RL LR LL
A/C 6	64	32.776	2.0	128.0	RR RL LR LL
A/C 7	64	32.904	2.0	128.0	RR RL LR LL
B/D 8	64	31.008	2.0	128.0	RR RL LR LL
B/D 9	64	31.136	2.0	128.0	RR RL LR LL
B/D 10	64	31.264	2.0	128.0	RR RL LR LL
B/D 11	64	31.392	2.0	128.0	RR RL LR LL
B/D 12	64	31.520	2.0	128.0	RR RL LR LL
B/D 13	64	31.648	2.0	128.0	RR RL LR LL
B/D 14	64	31.776	2.0	128.0	RR RL LR LL
B/D 15	64	31.904	2.0	128.0	RR RL LR LL

Note. Abbreviations are the same as in the previous table.

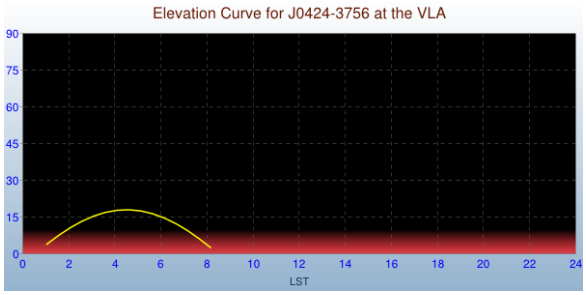

(a)

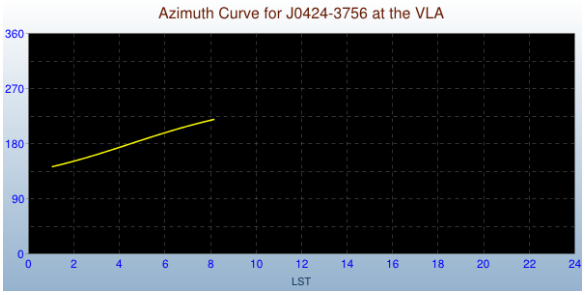

(b)

Figure 6.2: (a) Elevation and (b) azimuth of the calibrator J0424-3756 as a function of LST at the VLA site.

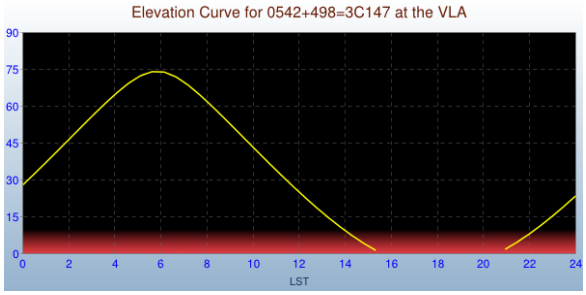

(a)

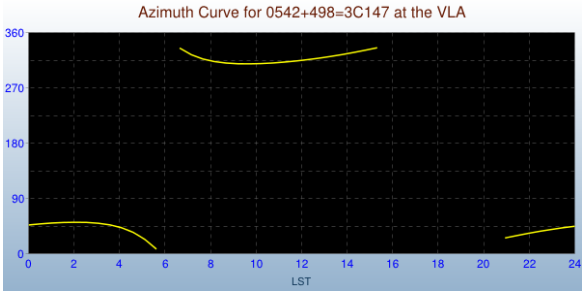

(b)

Figure 6.3: (a) Elevation and (b) azimuth of the calibrator 3C147 as a function of LST at the VLA site.

6.1.2 Data reduction

Reduction of the acquired data was performed using CASA (Common Astronomy Software Application) with tasks appropriate for interferometric observations[1]. In this subsection, we introduce some of the main steps.

Firstly, the data consisted of three measurement sets (MS) labelled K.ms, KA1.ms and KA2.ms. The extension .ms refers to the measurement set data format. In this notation, K refers to the K-band data set, KA's to the Ka-band data sets. The two KA data sets were obtained on different days by using a single script. Note that a measurement set delivered to the archive is basically one scheduling block, and the data consisted of three scheduling blocks.

Below is a list of the main steps in the reduction process:

1. Hanning smoothing: hanningsmooth
2. Inspecting the MS: ploweather,plotants,listobs,plotms
3. Deterministic flagging: flagcmd,flagdata,flagmanager
4. Flux calibration: setjy
5. Prior calibrations - initial delay and bandpass calibrations: gencal,gaincal
6. Initial bandpass calibration: gaincal,bandpass

[1]The reduction of the NRO 45-m data was done in CASA version 4.0.1, but the reduction of EVLA data was carried out in version 4.1.0 to meet the recommended requirements and upgrades.

7. Apply calibration: applycal
8. Identify bad deformatters/RFI, flag spectral windows with no calibration: flagdata
9. Semi-final delay calibration: gaincal
10. Semi-final bandpass calibration: gaincal
11. Apply calibration: applycal
12. Bootstrap flux densities: setjy
13. Final calibration tables (delay and bandpass): gaincal
14. Apply calibration: applycal
15. Split the calibrators: split
16. Find short solint phase solutions: gaincal
17. Apply final calibrations: applycal
18. Additional flagging: flagdata,flagmanager
19. Calculate weights per spectral window: statwt
20. Image/CLEAN: clean

Listobs

The first step to take is to inspect the data. This task prints a summary of observations in the log window and includes the following information: the observed sources, observation date and time, data amount, spectral windows, fields, scan details, frequencies, etc (figure 6.4). Three portions of the listobs result are given below as screen shots. The task to list the K.ms data set (visibilities) is run from the terminal by executing

listobs(vis='K.ms')

Flagdata

The listobs task gave us detailed information about the measurement set. For example, the first two scans on the list are "dummy" scans (technical requirement at the time), which can be safely deleted. Similarly, we do not need the pointing scan (number 4). The first scientific data were taken during scan number 5. Non-important data were flagged:

flagdata(vis='K.ms',flagbackup=T,mode='manual',scan='1,2,3,4')

By using flagbackup=T, a backup file was created (flagdata_1), to inable us to return to the original data by using flagmanager.

From the observing log provided by VLA operators, we learned that antenna 20 had a problem with optical fibers. The downtime was 15 minutes, but since the report stated that fringe amplitudes and delays appeared normal during the observation, we did not flag this antenna initially.

The interferometer takes some time (a few seconds) to settle before acquiring scientific data. Therefore, it is always recommended to flag several few integrations. The integration time was 1 s, and we choose to flag the first 1 s integration of all scans by executing the following command:

flagdata(vis='K.ms',mode='quack',quackinterval=1.0,quackmode='beg')

Here, mode='quack' refers to the sampling interval of 1 s, and quackmode='beg' instructs flagging at the beginning of each scan.

```
================================================================================
           MeasurementSet Name:  /Users/tenmon/EVLA-K/K.ms      MS Version 2
================================================================================
   Observer: Mr. Dragan Salak Salak     Project: uid://evla/pdb/11473178
Observation: EVLA
Data records: 16675308       Total integration time = 3559 seconds
   Observed from   08-Sep-2012/13:28:58.5   to   08-Sep-2012/14:28:17.5 (UTC)

   ObservationID = 0         ArrayID = 0
  Date        Timerange (UTC)          Scan  FldId FieldName             nRows   Int(s)   SpwIds      ScanIntent
  08-Sep-2012/13:28:58.5 - 13:29:28.5     1      0 J0424-3756            174096 1        [0, 1, 2, 3, 4, 5, 6, 7, 8, 9, 10, 11, 12, 13, 14, 15]
              13:29:29.5 - 13:30:27.5     2      0 J0424-3756             41418  1       [16, 17]                      OBSERVE_TARGET#UNSPECIFI
              13:30:29.5 - 13:32:41.5     3      1 J0424-3756             93366  1       [16, 17]                      UNSPECIFIED#UNSPECIFIED
              13:32:43.5 - 13:40:26.5     4      1 J0424-3756            310284 1        [16, 17]                      CALIBRATE_POINTING#ON_SO
              13:40:27.5 - 13:41:55.5     5      2 J0424-3756            499824 1        [0, 1, 2, 3, 4, 5, 6, 7, 8, 9, 10, 11, 12, 13, 14, 15]
              13:41:57.5 - 13:46:54.5     6      3 NGC  1808             16735681        [0, 1, 2, 3, 4, 5, 6, 7, 8, 9, 10, 11, 12, 13, 14, 15]
              13:46:56.5 - 13:48:24.5     7      2 J0424-3756            499824 1        [0, 1, 2, 3, 4, 5, 6, 7, 8, 9, 10, 11, 12, 13, 14, 15]
              13:48:26.5 - 13:53:23.5     8      3 NGC  1808             16735681        [0, 1, 2, 3, 4, 5, 6, 7, 8, 9, 10, 11, 12, 13, 14, 15]
              13:53:25.5 - 13:54:53.5     9      2 J0424-3756            499824 1        [0, 1, 2, 3, 4, 5, 6, 7, 8, 9, 10, 11, 12, 13, 14, 15]
              13:54:55.5 - 13:59:52.5    10      3 NGC  1808             16735681        [0, 1, 2, 3, 4, 5, 6, 7, 8, 9, 10, 11, 12, 13, 14, 15]
              13:59:54.5 - 14:01:22.5    11      2 J0424-3756            499824 1        [0, 1, 2, 3, 4, 5, 6, 7, 8, 9, 10, 11, 12, 13, 14, 15]
              14:01:24.5 - 14:06:21.5    12      3 NGC  1808             16735681        [0, 1, 2, 3, 4, 5, 6, 7, 8, 9, 10, 11, 12, 13, 14, 15]
              14:06:23.5 - 14:07:51.5    13      2 J0424-3756            499824 1        [0, 1, 2, 3, 4, 5, 6, 7, 8, 9, 10, 11, 12, 13, 14, 15]
              14:07:53.5 - 14:12:50.5    14      3 NGC  1808             16735681        [0, 1, 2, 3, 4, 5, 6, 7, 8, 9, 10, 11, 12, 13, 14, 15]
              14:12:52.5 - 14:14:20.5    15      2 J0424-3756            499824 1        [0, 1, 2, 3, 4, 5, 6, 7, 8, 9, 10, 11, 12, 13, 14, 15]
              14:14:22.5 - 14:19:19.5    16      3 NGC  1808             16735681        [0, 1, 2, 3, 4, 5, 6, 7, 8, 9, 10, 11, 12, 13, 14, 15]
              14:19:21.5 - 14:28:17.5    17      4 0542+498=3C147        30157921        [0, 1, 2, 3, 4, 5, 6, 7, 8, 9, 10, 11, 12, 13, 14, 15]
            (nRows = Total number of rows per scan)
Fields: 5
  ID   Code Name                RA               Decl           Epoch   SrcId nRows
  0    NONE J0424-3756          04:24:42.24373 -37.56.20.7842 J2000   0     215514
  1    P    J0424-3756          04:24:42.24373 -37.56.20.7842 J2000   1     403650
  2    D    J0424-3756          04:24:42.24373 -37.56.20.7842 J2000   2     2998944
  3    NONE NGC  1808           05:07:42.34300 -37.30.46.9800 J2000   3     10041408
  4    Q    0542+498=3C147      05:42:36.13792 +49.51.07.2336 J2000   4     3015792
```

Figure 6.4: Some basic parameters of the observations displayed by using listobs. J0424-3756 was the source used for reference pointing and gain calibration, 3C147 was the flux and bandpass calibrator, and NGC 1808 was the main target.

Plotants

This task is useful to get a sense of the array configuration (figure 6.5). By executing

plotants(vis='K.ms',figfile='myfile.ps') we can plot a 2-D map and export it to a file. Below is a plot of the configuration in these observations created in CASA. Note that the array extends up to more than 20 km, and that in general all baselines are long enough so that antenna shadowing can be neglected. From the array configuration we can also deduce that the reference antenna near the center of the array (although not clearly seen in the plot) is the antennas labeled ea25 and ea07; we take antenna ea25 for reference.

Gencal: antenna positions

Each time antennas are moved from one position to another due to transformation to another array configuration, it is necessary to accurately measure the new positions in order to derive the antenna-to-antenna baselines. This is done by the VLA staff, and we only search and apply new positions to the data:

gencal(vis='K.ms',caltable='K.antpos',caltype='antpos')

This task writes a table called K.antpos, and the calibration type is antpos, i.e., antenna positions. We will load this table in later stages of reduction. In this observation, antennas 1, 2, 8, 10, 16, 20, 23, and 28 had incorrect baselines because they had been moved recently. Note from figure 6.5 that many of these antennas constitute the northern arm of the VLA in configuration BnA. They were previously in configuration B, and then were moved to new positions. The configuration after BnA, starting from late September 2012, was configuration A, when the SE and SW arms of the array were extended.

Plot (u,v) coverage

The (u,v) coverage is plotted by using the following command:

plotuv(vis='K.ms',field='3',maxnpts=40165632) where field 3 corresponds to NGC 1808, and the total number of visibility data is 40165632. The result is shown in figure 6.6.

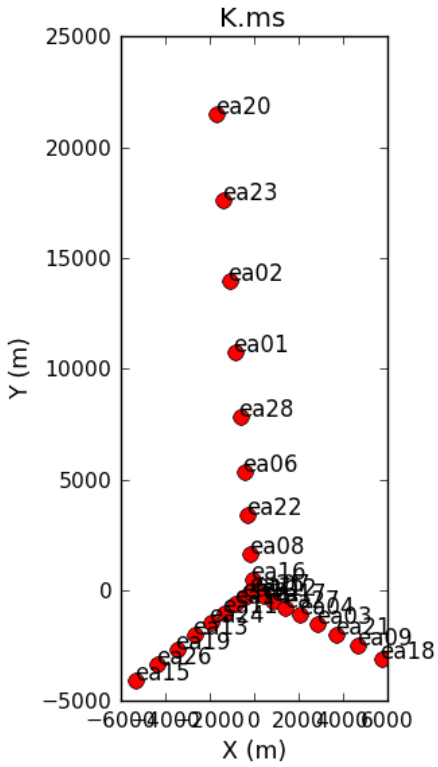

Figure 6.5: BnA configuration during the observations. X and Y correspond to offsets in geographic longitude and latitude, respectively.

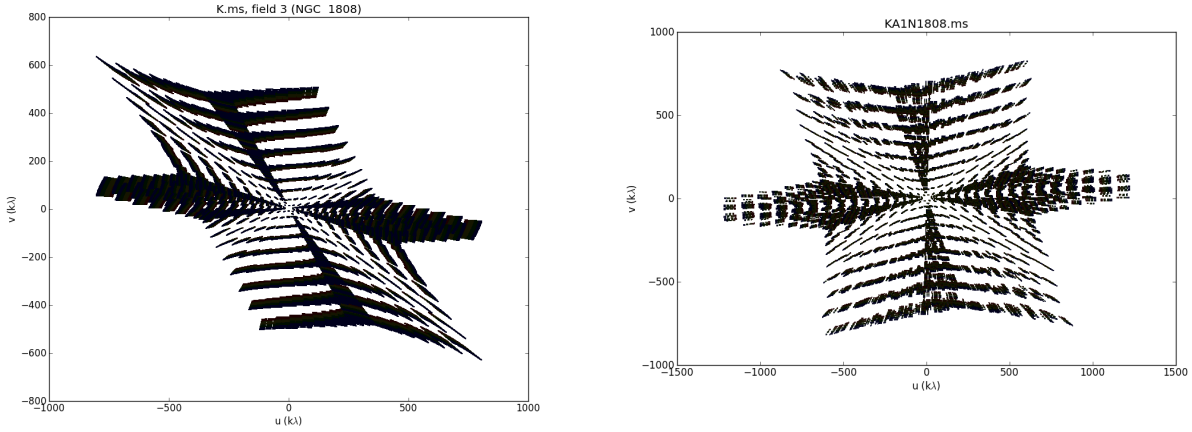

(a) (b)

Figure 6.6: (u, v) coverage of NGC 1808 in (a) band K, and (b) band Ka.

Gain curves

Since the antenna gain varies with elevation, it is necessary to correct for this effect. In this observation, the antennas were pointed at very low elevation. The calibration is done by using gencal, as follows:

```
gencal(vis='K.ms',caltable='K.gaincurve.cal',caltype='gc')
```

Opacity

Depending on elevation and weather conditions, it is imporant to take into account the atmospheric opacity. The opacity, τ_z [Np][2], is obtained from the weather summary of the observation, which displays the solar elevation, wind speed, and pwv [mm] in addition to opacity. The weather plot for K.ms is shown in the figure below.

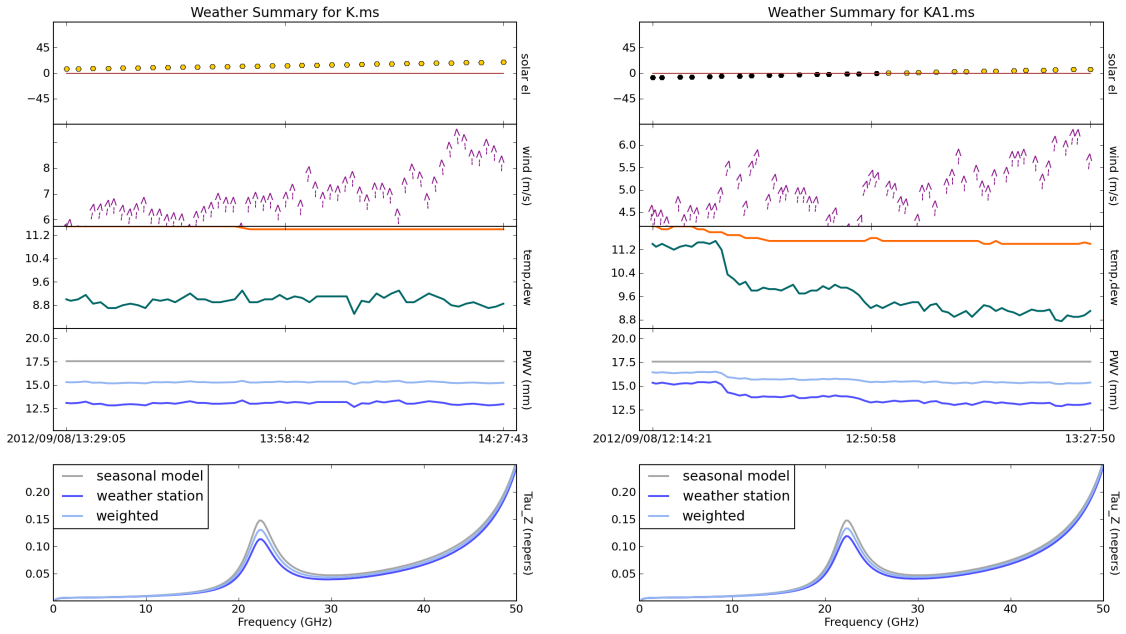

(a) (b)

Figure 6.7: Weather log for: a) K-band observations, and b) Ka-band observations (first SB).

The task which corrects for the opacity is:

```
gencal(vis='K.ms',K.opacity.cal','opac',parameter=[0.05])
```

Here, the opacity of 0.05 Np was estimated from the weather summary. According to the weather information, the average opacities at 23 GHz are 0.051 Np at the VLA.

Plotms

plotms is a useful task which runs a separate GUI window for data manipulation and plotting. It is very important for inspecting the data visually. For example, we can create a plot of the visibility amplitude or phase versus baseline or time. The data can be displayed in wide variety of options, selecting all data or only specified parts (e.g., only some antennas, fields, scans and spectral windows). A caveat about this task is that it requires a powerful machine to compute and plot parameters since the VLA

[2]The neper (Np) is a dimensionless, non-SI, logarithmic unit, named after J. Napier, the inventor of logarithms. Unlike the decibel, it is defined with the natural logarithm: $X = \ln(x_2/x_1)$ [Np].

data are usually heavy, typically of the order 30-50 GB per MS. First, to make processing faster, we can plot only the scans of NGC 1808, which is field=3, as follows:

plotms(vis='K.ms',xaxis='',yaxis='',averagedata=F,transform=F, extendflag=F,plotfile='',selectdata=T,field='3')

Even this might be slow, but further selections can be made in the GUI. For example, we can select only antenna 0 and the first scan.

In figure 6.8, plots of elevation vs. time made in plotms are shown.

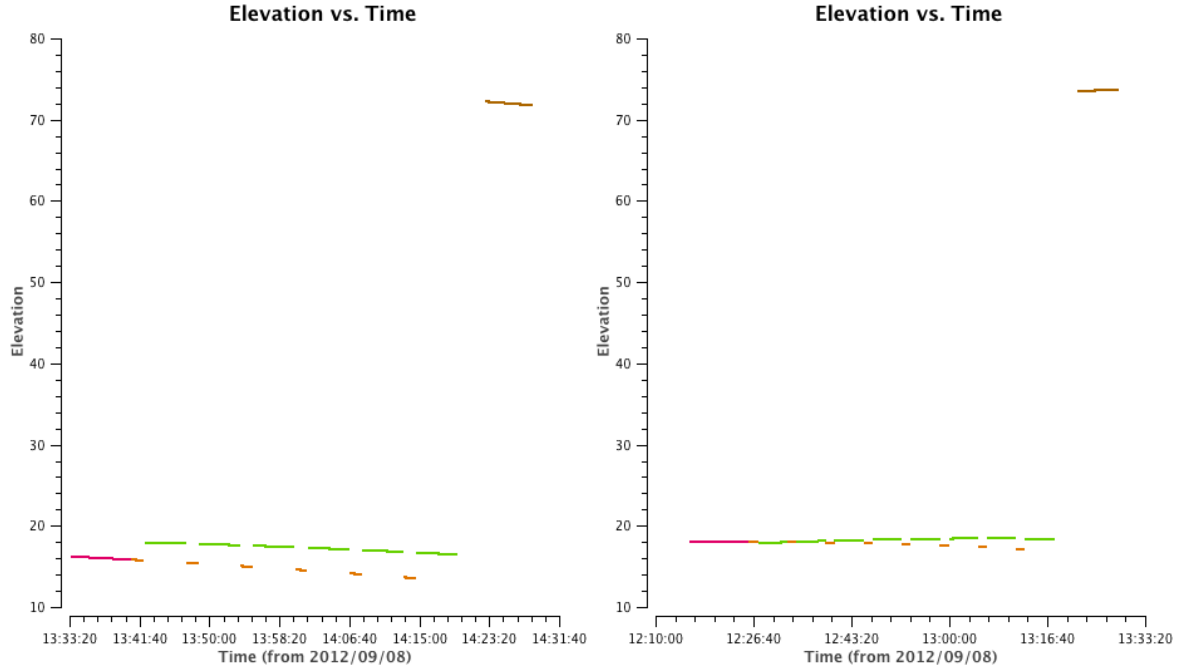

(a) (b)

Figure 6.8: Elevation vs. time for: a) K-band observations, and b) Ka-band observations (first SB).

Amplitude and phase anomalies

By using plotms, we can check the amplitude and phase as a function of frequency for each antenna. It is useful to use the strong calibrator, such as 3C147, for this purpose. Bad antennas are usually those with low amplitudes, as low as 0. Spectral windows with large roll-offs and radio-frequency interference (RFI) are important too.

Setjy

Setjy is a task to calculate the absolute flux density scale. It is a necessary step to determine the intensity of the observed source. The task is applied to the flux calibrator 3C147:

setjy(vis='K.ms',field='4',modimage='3C147_K.im',listmodels=False,standard='Perley-Butler 2010',usescratch=False,scalebychan=True,spw='')

Here, a model image named 3C147_K.im, which can be downloaded from the VLA database, was used, and the calculation was done per channel by setting scalebychan=True, and for all spectral windows by letting spw=''.

Split

Before imaging, we split the data to create an MS which contains only the data of the galaxy with corrected (calibrated) parameters:

split(vis='K.ms',outputvis='KN1808.ms',field='3')

Here, field 3 belongs to NGC 1808.

Calibrated data

The calibrated phase for all calibrators is shown in figure 6.9. After final calibrations, the variations that were as large as 180^0 over the observing time, are now reduced to about $\pm 5^0$. The phase jumps were relatively large due to two effects: 1) clouds and atmospheric fluctuations over the 20-km field of the BnA array, and 2) low elevation (below 20^0). However, the amplitude of the complex gain was calibrated to a stable condition, with most antennas having nearly constant value of 1.0 throughout the observations.

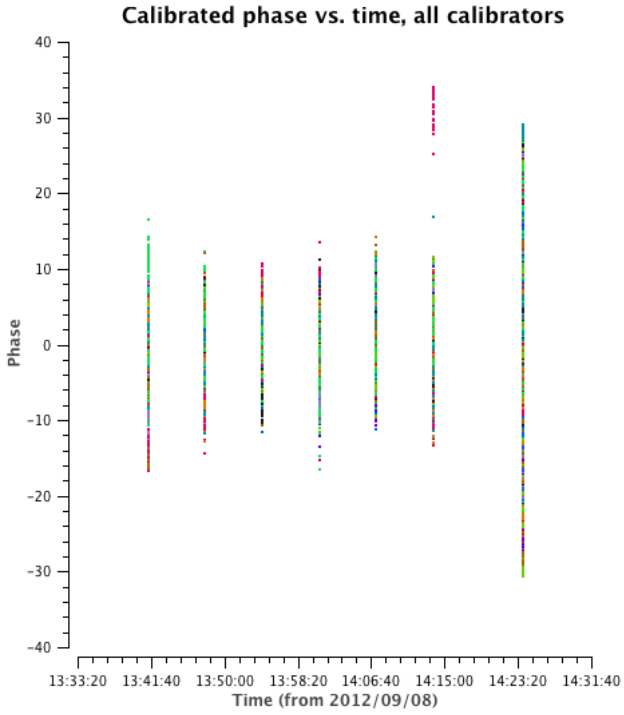

Figure 6.9: Calibrated phase vs. time for all calibrators.

Figures 6.10, 6.11 and 6.12 show the amplitude of the complex visibility vs. the *uv*-distance. Note that 3C147 is resolved at this frequency and configuration of the array. This is obvious from the large difference between amplitudes at various (u,v) ranges. Therefore, it was essential to use an emission model provided by NRAO.

Imaging

CASA's task clean has two main integrated operations to create images from visibilities: Fourier transform of the data (invert) and deconvolution of the resulting image.

From figure 6.12 we note that the longest baseline for the K-band was $u \simeq 1 \times 10^6\ \lambda$, where $\lambda = 1.3$ cm. Therefore, the angular scale (resolution) is $\lambda/D \sim 1/10^6$ rad, i.e., $10^{-6} \times 3600 \times 360/(2\pi) \approx 0.21''$. We oversample the image by setting the size of a pixel to $0.05''$ to achieve the most effective cleaning at 3-5 pixels across the synthesized beam.

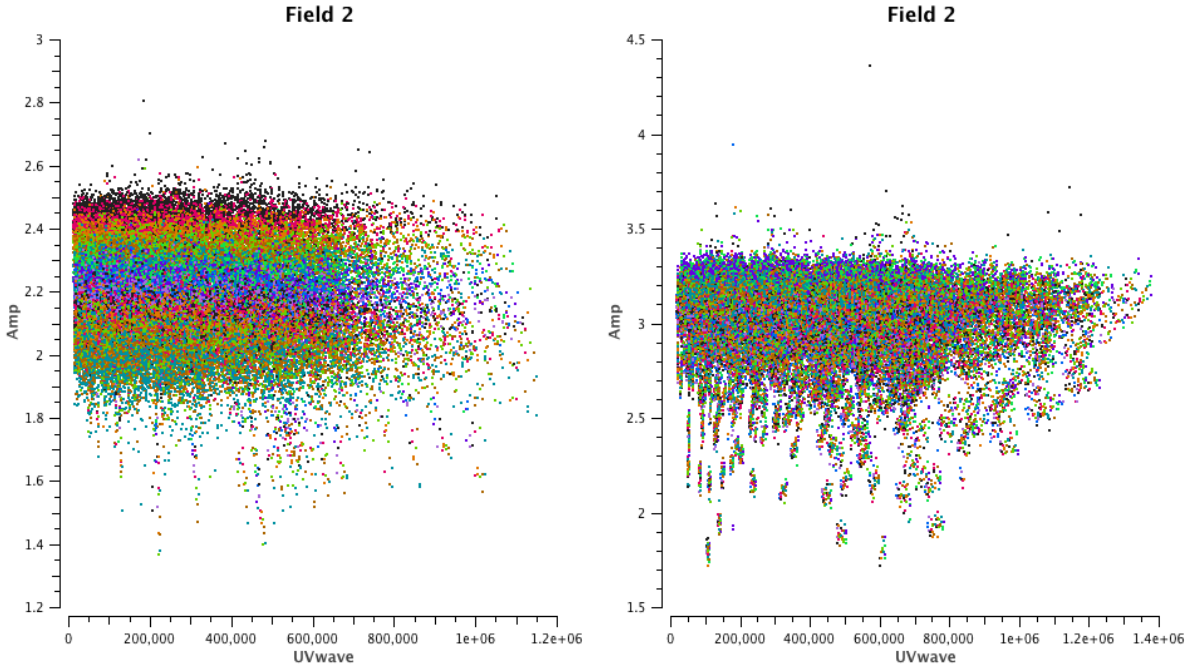

(a) (b)

Figure 6.10: Amplitude vs. (u,v) distance in a) K and b) Ka bands for the gain calibrator J0424-3756.

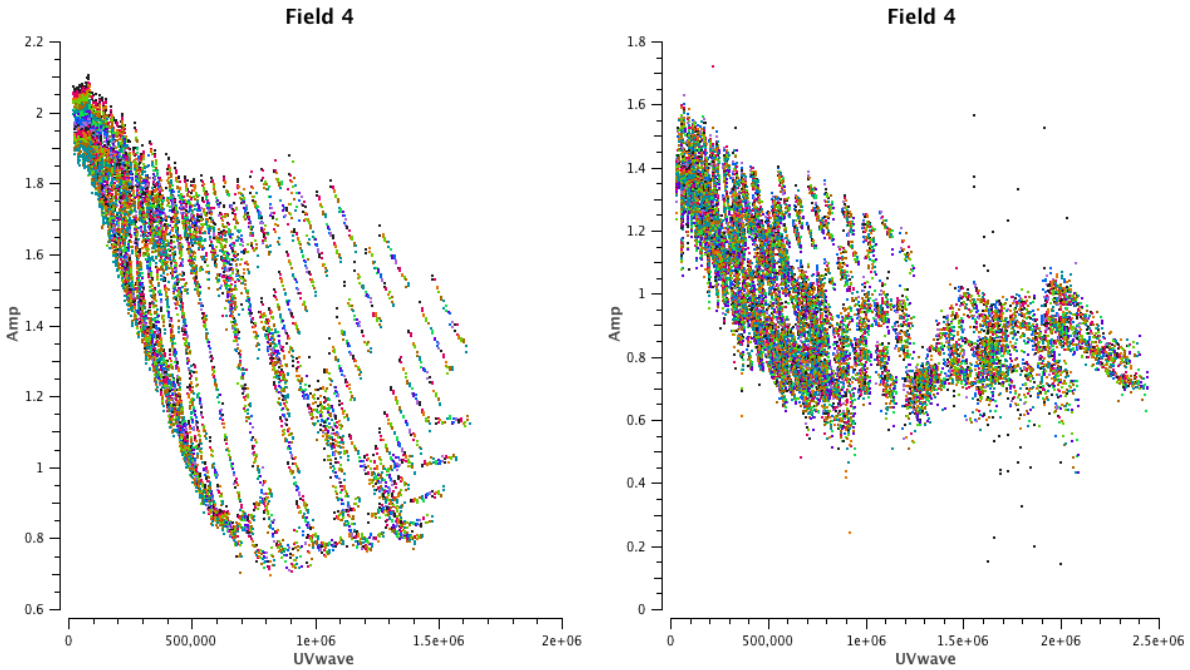

(a) (b)

Figure 6.11: Amplitude vs. (u,v) distance in a) K and b) bands for the flux and bandpass calibrator 3C147.

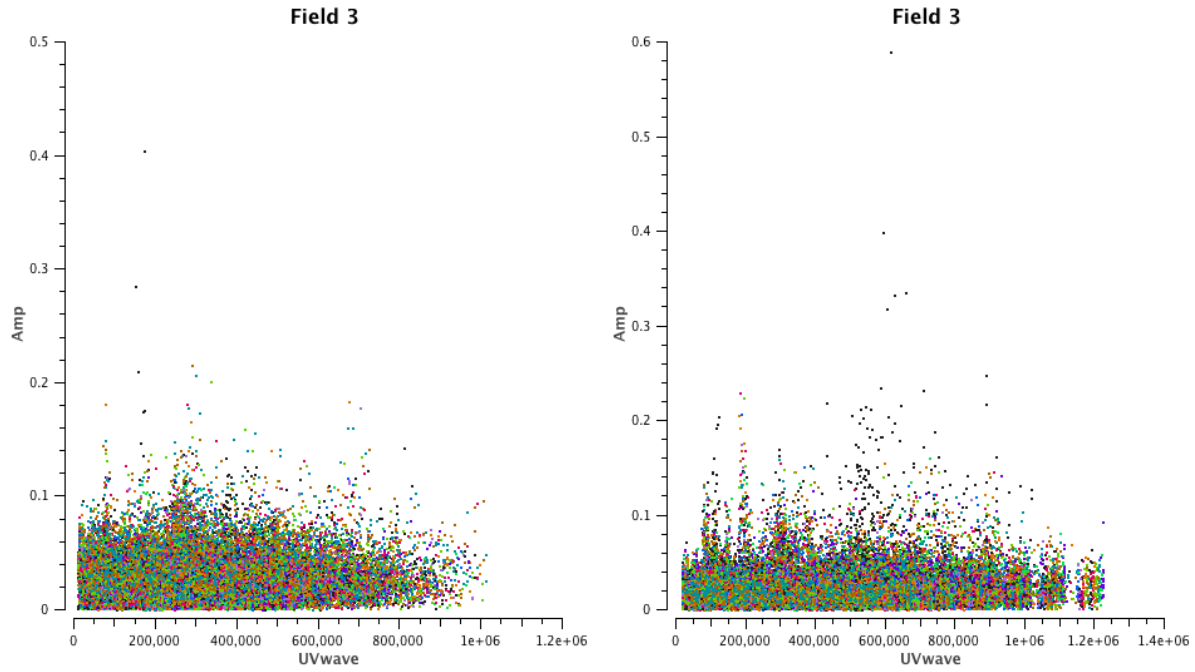

(a) (b)

Figure 6.12: Amplitude vs. (u,v) distance in a) K and b) Ka bands for NGC 1808.

clean(vis='KN1808.ms', imagename='KIM.ms', mode='mfs', nterms=2, imagermode='csclean', imsize=480, cell=['0.05arcsec'], weighting='briggs', robust=0.5, interactive=T)

Below is an explanation of each step in the clean task. Note that clean can handle more than one MS. Two MS' were combined in the reduction of Ka data.

mode='mfs' instructs multi-frequency synthesis (MFS) imaging. Each visibility channel with baseline $\mathbf{D}_k$ at wavelength λ_k is gridded at $\mathbf{u}_k = \mathbf{D}_k/\lambda_k$ in the uv-plane. If nterm=2, then multi-scale MFS is triggered, and the result is two images. The first image plane is at the frequency given by the midpoint between $\nu_{\rm min}$ and $\nu_{\rm max}$ in the input spectral windows, ν_0. The wide-band sky is modeled as a linear combination of Gaussian-like functions whose amplitudes follow a Taylor-polynomial in frequency. The output is

$$I_\nu = \sum_t I_t \left(\frac{\nu-\nu_0}{\nu_0}\right)^t, \tag{6.1}$$

where t is the Taylor coefficient. When nterm=2, we get an image for tt0 (total intensity at ν_0) and for tt1. The spectral index is given by

$$I_\nu = I_{\nu_0}\left(\frac{\nu}{\nu_0}\right)^{\alpha+\beta\log(\nu/\nu_0)}. \tag{6.2}$$

Multi-frequency synthesis mode is important for short-interval observations (nearly snapshot) because it improves the (u,v) coverage by treating different frequencies as different sets of (u,v). The only requirement to use this option efficiently is to do wide band observations.

imagermode='csclean' utilizes the Cotton-Schwab cleaning algorithm.

imsize=480 makes the image size $480'' \times 480''$. For unequal sides of the map, we write, e.g., imsize=[160,240].

cell='0.05arcsec' makes the size of a cell (pixel) $0.05''$. It is possible to set two unequal values.

weighting='briggs' runs the Briggs weighting which is useful to suppress instrumental artifacts. With robust=0.5, we make weighting halfway between uniform and natural.

interactive=T makes cleaning interactive. This is useful when inspecting the source brightness distribution for the first time because we can infer the noise and choose by hand which regions to clean.

The point spread function of the synthesized beam and the flux response function of the primary beam are shown in figure 6.13.

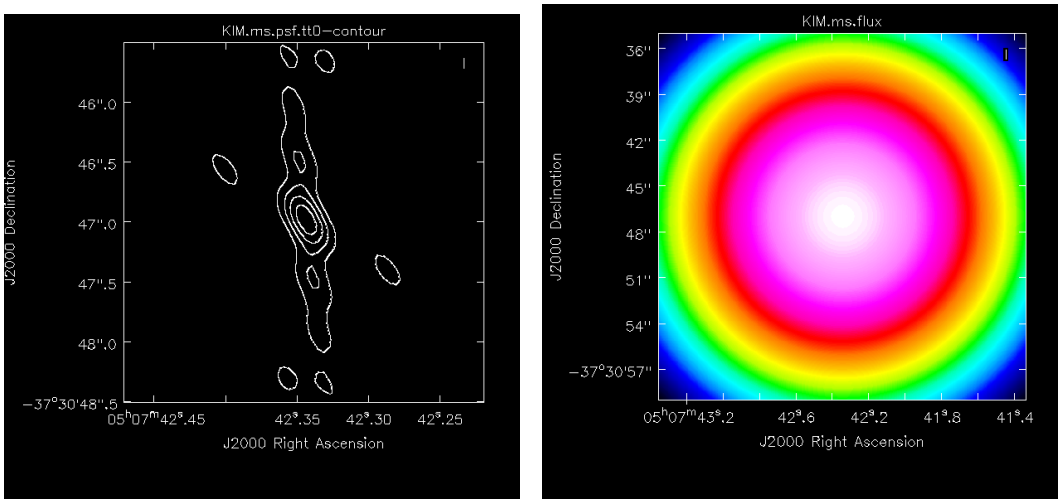

(a) (b)

Figure 6.13: (a) Point spread function of the synthesized beam ("dirty" beam, contours: 0.1, 0.325, 0.55 and 0.775 of the peak); (b) the primary beam response function (above 99% of the phase center peak in pink and white regions).

In total, the following data products are created in the cleaning process:

1. K1808.image : final restored image (or dirty map if the number of iterations was set to zero), with clean components convolved with a restoring beam and added to the remaining residuals at the end of the imaging process
2. K1808.psf : point spread function (dirty beam), deconvolved from the true sky brightness during clean
3. K1808.model : image (sum) of the clean components
4. K1808.residual : residual image after subtracting clean components - useful to judge whether more cleaning is necessary or not
5. K1808.flux : primary beam response function[3]

[3]If pbcor=F, which is default, the produced cleaned image has correct flux only at the position of the phase center. To calculate accurate fluxes across the image, .image should be divided by .flux, or set pbcor=T.

Chapter 7

Observations of NGC 1808 with ASTE

7.1 Observations and data reduction

The observations of NGC 1808 were carried out using the Atacama Submillimeter Telescope Experiment (ASTE) - a 10-m telescope located at 4862 m altitude in the Atacama desert in northern Chile. The telescope is operated by the National Astronomical Observatory of Japan, and the observations were conducted remotely from Mitaka campus in Tokyo. The telescope's location in the southern hemisphere provides unique opportunity to observe southern objects, and NGC 1808 at the declination of -37^0 is a most suitable target. Furthermore, ASTE site is close to ALMA, hence closely related observations are possible. For example, high-resolution observations with ALMA in combination with large-field observations with ASTE.

The observations were carried out on September 18, 19 and 20, and October 7, 2013. The total allocated time was 15+5 hours, 5 hours per day (night in Chile) from LST=0h to LST=5h. The central region of NGC 1808 was mapped in position-switching mode across the area of about 5×4 kpc^2. There were 9×7 observing points, each separated by $10''$ which is slightly less than the beam size of ASTE ($22''$). The map position angle was 140^0, along the major axis of the galaxy, in agreement with previous observation of CO (1-0) and CO (2-1) made by Aalto et al. (1994) with the Swedish ESO 15-m Submillimeter Telescope (SEST). The beam size of SEST was $24''$ at the frequency of CO (2-1) but the position separation was the same ($10''$), hence our data can be directly compared with theirs.

The frontend was the 2SB receiver CATS 345, which was employed only in the upper sideband (USB) for CO (3-2), and in lower sideband (LSB) for ^{13}CO (3-2). The corresponding rest frequencies are 345.79599 GHz, and 330.58796 GHz, respectively. The system noise temperature was measured by the standard chopper wheel method, which yielded the antenna temperature, $T_{\rm A}^*$, corrected for atmospheric and ohmic losses (Ulich & Haas, 1976). Typical system noise temperature was between 150 and 300 K, depending mostly on the elevation of the source; all three nights had clear sky and low opacity of ~ 0.05 as measured at 220 GHz. Pointing accuracy was checked every one hour by observing the nearby red giant variable star R Dor in the constellation of Dorado (peak CO intensity ~ 2 K). The relative uncertainty was typically better than $1.5''$ despite moderately strong wind (7-15 m s^{-1}); experimental system for wind correction "ASPIRIN" was used. All data have pointing accuracy better than $2.5''$. Absolute intensity of the measurement was calibrated by observing Orion KL, with typical antenna temperatures of $T_{\rm A}^* \sim 80$ K for ^{12}CO (3-2) and $T_{\rm A}^* \sim 35$ K for ^{13}CO (3-2). The data were scaled to the intensities of standard spectra of Orion KL provided in Schilke et al. (1997a). This comparison with standard spectra taken with a telescope of the same 10-m aperture as ASTE allowed correcting for the main beam efficiency $\eta_{\rm mb}$ and flux variations.

The backend comprised in a digital XF-type[1] millimeter autocorrelator spectrometer (MAC) with

[1]XF-type backends perform autocorrelation of the input voltage, $V(t)$, to derive the autocorrelation function (ACF), $R(\tau)$, where τ is the time delay. According to the Wiener-Khinchin theorem, the ACF $R(\tau)$ and the power spectral density,

a total bandwidth of 512 MHz. The total number of channels is 1024, with a spectral resolution of 0.5 MHz (0.43 km s^{-1} at 345 GHz), and a velocity coverage of 445 km s^{-1}. The data were smoothed with a hanning window. This insures that the first side lobe is only about 2.6% of the peak (Wilson, Rohlfs & Hüttemeister, 2010), at a cost of twice the lower resolution.

Data reduction was done by using the software package NEWSTAR developed by Nobeyama Radio Observatory. The raw data were first flagged with the task FLAG to eliminate bad spectra. Then, baselines were fitted by a first-order polynomial and subtracted by using BASELINE. The map was created in MAP and image analysis was done by using DS9.

The adopted observational properties of NGC 1808 and a summary of observations are given in table 7.1.

Table 7.1: NGC 1808 and observation parameters.

Basic parameters of NGC 1808	
Right ascension (B1950.0)[a]	$05^h05^m58.3^s$
Declination (B1950.0)[a]	$-37^0 34' 35.0''$
Distance[b]	10.8 Mpc
Systemic velocity[a]	965 km s^{-1}
Position angle[a]	140^0
Inclination angle[c]	57^0
Morphological type[c]	(R)SAB(s)a
Observation summary	
Telescope	ASTE 10m
Observing date	Sep. 18, 19, 20, Oct. 7, 2013
Receiver	CATS 345
Spectrometer bandwidth	512 MHz (445 km s^{-1})
Spectral resolution	0.5 MHz (0.43 km s^{-1})
Integration time for ^{12}CO (3-2) map	5.2 h
Integration time for ^{13}CO (3-2)	49 min.
Angular resolution	$22''$
Map grid	9×7 obs. points (spacing $10''$)
Map size	$100'' \times 80''$ (5×4 kpc)
Intensity calibrator	Orion KL
Pointing calibrator	R Dor

Note. [a]Aalto et al. (1994); [b]Tully (1988); [c]de Vaucouleurs et al. (1991). The morphological type is based on the de Vaucouleurs system where (R) indicates an outer ring, (s) indicates inner spiral structure (no rings), SABa means spiral galaxy with a weak bar and closely wound spiral arms.

$S(\nu)$ are Fourier pairs, so this kind of spectrometer performs Fourier transform $R(\tau) \rightleftharpoons S(\nu)$. In XF, X=correlation and F=Fourier transform. For more details, see sections 4.1 and 5.4 of Wilson, Rohlfs & Hüttemeister (2010).

Chapter 8

Results and analysis of NGC 1808

8.1 Radio continuum in the galactic nucleus

In this section we introduce the results of our radio-continuum observations. The observations were carried out at 21 and 32 GHz as explained in chapter 6. At both frequencies, emission was detected from the galactic nucleus (figure 8.1).

Figure 8.1 shows continuum maps of the nucleus at 21 and 32 GHz. The red cross in the figure marks the center of the continuum peak from Saikia et al. (1990); it is nearly coincident with the center determined in this work. In our observations, the angular resolution was higher, hence the determination of the galactic center is more accurate. Note that the black cross marks the 2MASS galactic center. This position is significantly separated from the radio nucleus; a likely cause for this is larger uncertainty ($1.5''$) in the optical data.

The two blue crosses in figure 8.1 mark the position of the X-ray double peak from Jiménez-Bailón et al. (2005). The double peak was previously observed by Veron-Cetty & Veron (1985) and Awaki et al. (1996) with similar results: there is a luminous, hard X-ray source (the western cross in the image) and a much less luminous, mostly soft source (the eastern cross). X-ray properties of the sources are given in table 8.1. The peculiar X-ray emission from the galactic nucleus lead several authors to conclude that NGC 1808 hosts a low-luminosity active galactic nucleus (LLAGN). Curiously, the position of the hard X-ray peak does not have a counterpart in radio emission. Radio continuum emission has not been detected yet. This suggests that the S1 source is the candidate LLAGN, and figure 8.1 shows that it coincides with the radio-continuum peak to within several parts of an arcsecond. Leaving S2 behind as an unknown object that could be an X-ray binary, ultra-luminous X-ray source (ULX), or an obscured LLAGN, we focus in this section on the properties of the source S1.

Table 8.1: Luminosity of the X-ray sources indicated with blue crosses in figure 8.1.

Source	$L_{0.1-2.4\ \mathrm{keV}}$ $\times 10^{39}$ erg s^{-1}	$L_{2-10\ \mathrm{keV}}$ $\times 10^{39}$ erg s^{-1}
S1	3.9	1.5
S2	$(< 6 \times 10^{4})$	9.2

Note. Reference: Jiménez-Bailón et al. (2005).

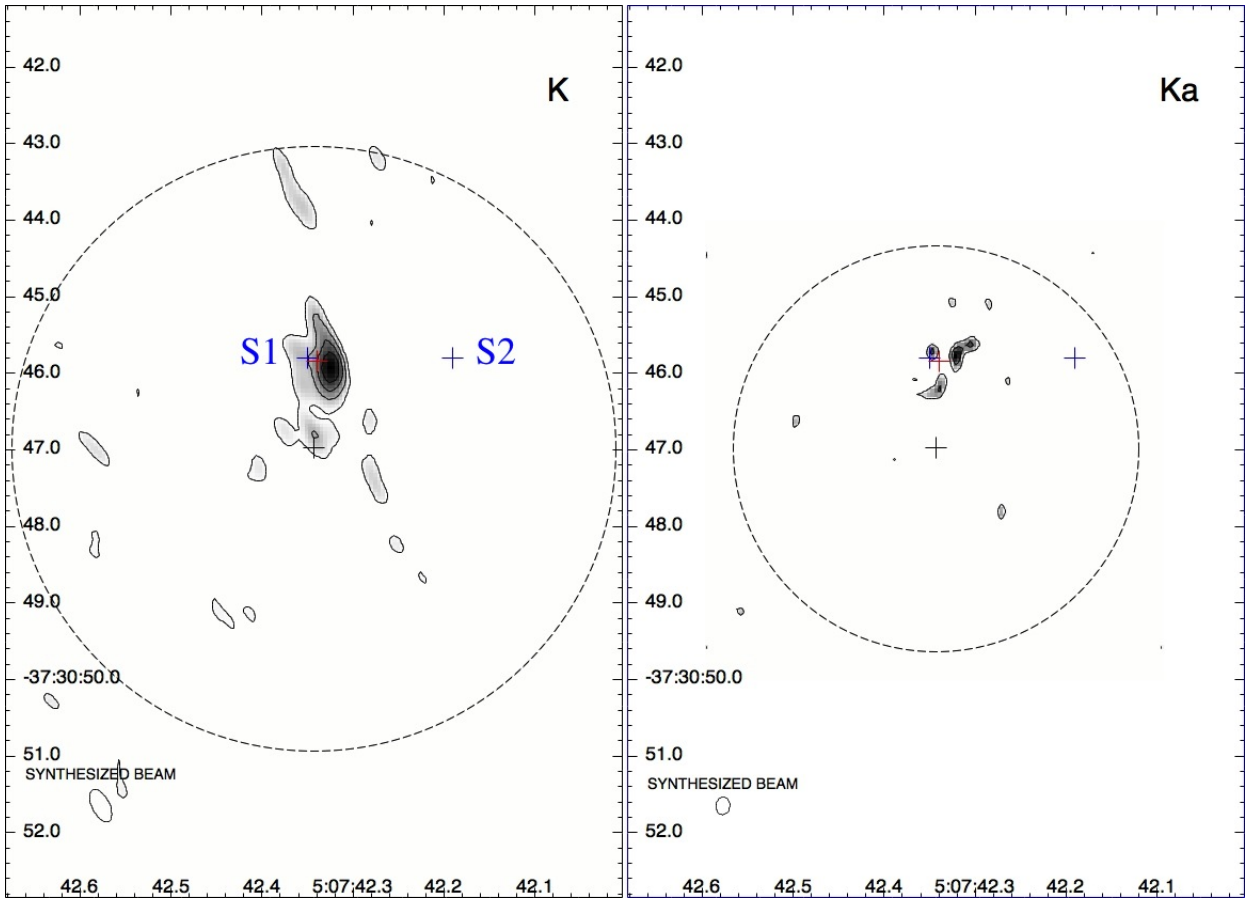

Figure 8.1: Radio continuum in the central region of NGC 1808 (coordinates given in $\alpha_{\rm J2000}, \delta_{\rm J2000}$). K and Ka correspond to 21- and 32-GHz observations. The synthesized beams are $0.47'' \times 0.23''$ at P.A. $= 28^0$, and $0.25'' \times 0.17''$ at P.A. $= -174^0$, respectively. At the adopted distance of 10.8 Mpc, $1''$ corresponds to about 50 pc. The black cross marks the phase center; red is the brightest peak from Saikia et al. (1990); blue crosses are the positions of X-ray sources S1 and S2 from Jiménez-Bailón et al. (2005). The dashed lines show the regions of highest imaging fidelity in configuration B (see text). The contours are: K) 0.27, 0.56, 0.86 and 1.15 mJy beam^{-1}; Ka) 0.18 and 0.26 mJy beam^{-1}. The lowest contour is at 3σ of the noise level.

8.1.1 Properties of the nucleus

Table 8.2 shows a comparison of radio-continuum observations at various frequencies, from the lowest at 1.5 GHz to 32 GHz. The core is only marginally resolved at 32 GHz when displayed at a significance of $> 3\sigma$ (figure 8.2). Fitting a Gaussian profile to the image implies that the size of the nuclear source is of the order $\lesssim 10$ pc.

Table 8.2: Flux density of the radio continuum at the central position of NGC 1808. The total flux density is defined as $S_\nu = \int I_\nu \, d\Omega$, where S_ν is in Jy and the brightness I_ν is in Jy beam^{-1}.

Frequency [GHz]	I_ν (peak) [mJy beam^{-1}]	S_ν [mJy][a]	Reference
1.4649	54.4 ± 0.12	425	(1)
4.8351	16.6 ± 0.06		(1)
8.4649	8.96		(2)
15	5.8 ± 0.2	8.3	(1)
21	1.45 ± 0.09	7.84	This work
32	0.35 ± 0.06	1.92	This work

Note. a) The total flux density was obtained by selecting the region where emission $> 3\sigma$ was detected. References: (1) Saikia et al. (1990); (2) Collison et al. (1994).

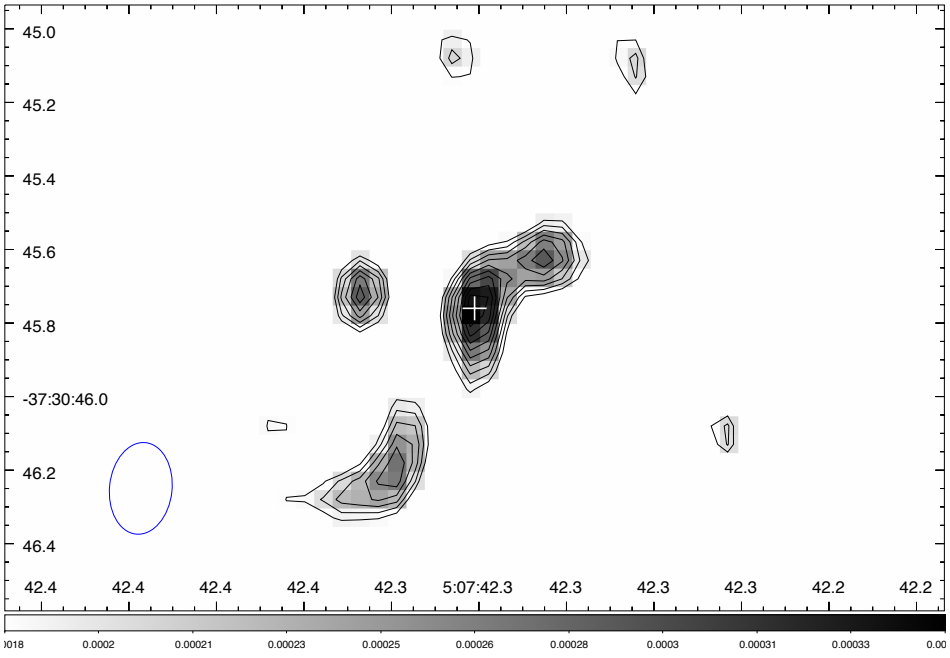

Figure 8.2: Nuclear source at 32 GHz. The lowest contour is 0.18 mJy beam$^{-1} \approx 3\sigma$. The coordinates are equatorial for J2000. At the adopted distance of the galaxy (10.8 Mpc), $0.2'' \approx 10$ pc.

8.1.2 Position of the nucleus

Observations at 32 GHz have provided data in the highest angular resolution made so far. Thus, we can determine the coordinates of the galactic center with accuracy higher than in previous studies. The central position is determined to be at

$$(\alpha, \delta)_{\mathrm{J2000}} = (05^{\mathrm{h}}07^{\mathrm{m}}42.32^{\mathrm{s}}, -37^{0}30'45.76'') \tag{8.1}$$

with an uncertainty less than the FWHM of the synthesized beam $0.25''$.

8.2 Molecular gas in the inner 5 kpc of NGC 1808

The results of ASTE observations are presented in this section: these are the first map of ^{12}CO (3-2) and the first detection of ^{13}CO (3-2) in NGC 1808. A region that contains $9 \times 7 = 63$ positions separated by $10''$ was observed, which is slightly better than Nyquist sampling for a beam FWHM of $22''$. The spectra are shown in figure 8.3. The final map is $100'' \times 80''$ (5×4 kpc^2) in size, at a position angle of P.A. $= 140^0$, corresponding to the galactic position angle adopted in Aalto et al. (1994). The r.m.s. noise $\Delta T_{\rm mb}$ in a channel of 5 km s^{-1} ranges from 9.2 to 17.5 mK throughout the map.

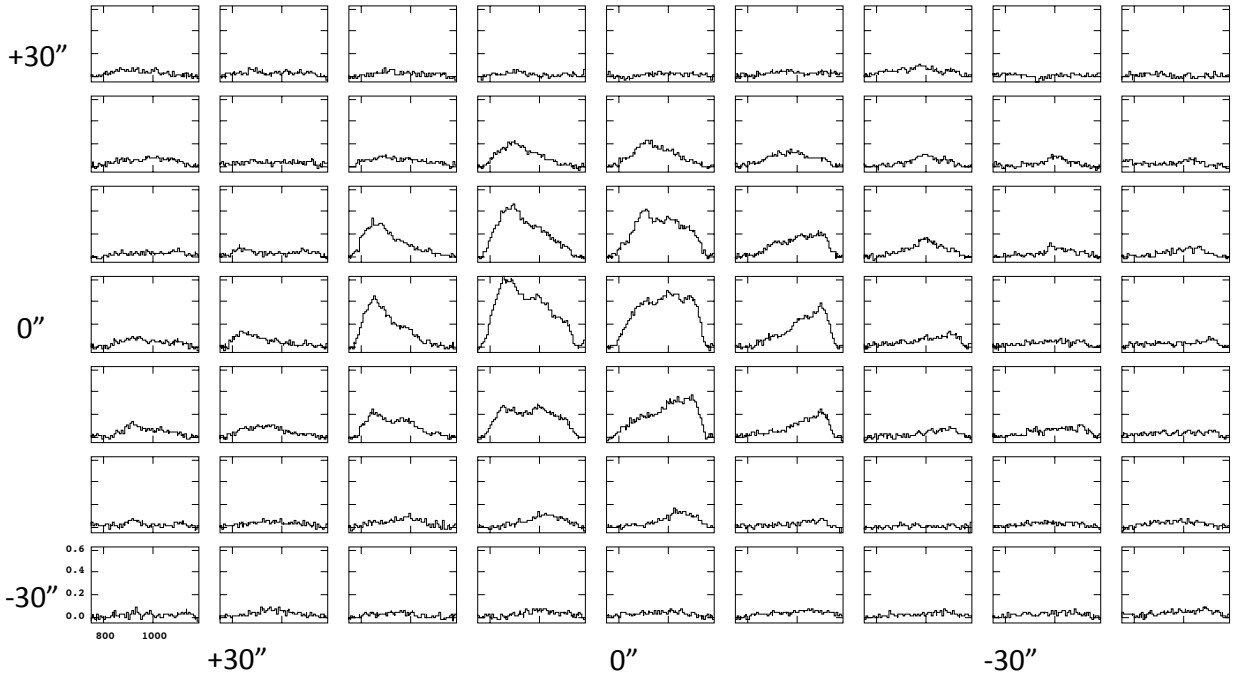

Figure 8.3: Spectra of the observed positions. The scale is in $T_{\rm mb}$ with tickmarks at 0.0, 0.2 and 0.4 K, and velocity $V_{\rm LSR}$ in km s^{-1}.

From figure 8.3 it is clear that CO (3-2) emission was detected in nearly every part of the observed region. The integrated intensity is shown in figure 8.4. Emission is relatively strong in the nuclear region where it reaches 127 K km s^{-1}, whereas it decreases tenfold 2 kpc outwards. Note that there are spurs in the intensity distribution: in the SE-NW direction, that coincides with the galactic bar (disk), but also in the perpendicular (polar) direction. The nature of this feature is discussed below.

A map of the velocity field (velocity peaks) is shown in figures 8.4 and 8.5 (right panel). The rotation pattern is clearly visible, with the eastern part of the galaxy exhibiting redshifted and the western part exhibiting blueshifted motion, although apparently there is strong deviation from purely circular motion.

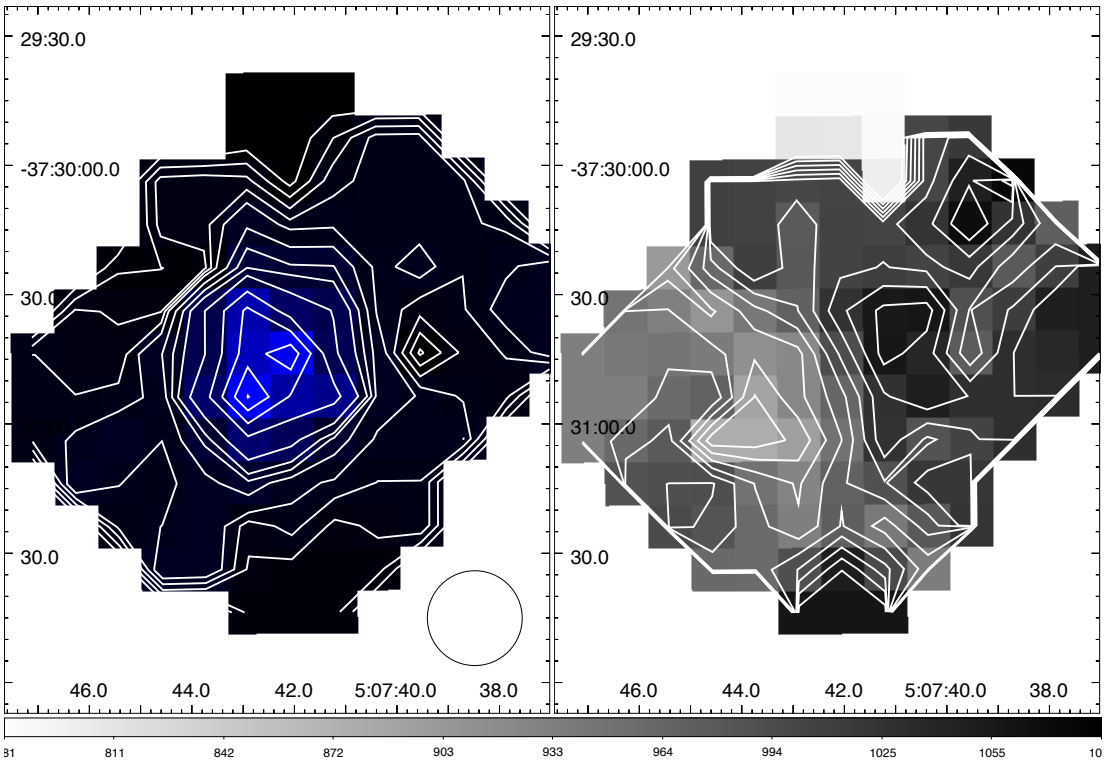

Figure 8.4: *Left.* ^{12}CO (3-2) integrated intensity map defined as $\int T_{\rm mb}\,{\rm d}v$. The contours are 5, 7.5, 10, 12.5, 15, 20, 25, 30, 40, 60, 80, 100, 120 K km s^{-1}. *Right.* Intensity-weighted velocity field of the CO (3-2) line emission. The contours are from 890 to 1050 km s^{-1} separated by 20 km s^{-1} (grey scale). The angular resolution ($22''$) is shown in the bottom right corner. A pixel of the map is $10''$ wide which corresponds to about 500 pc. The coordinates are equatorial in J2000.0.

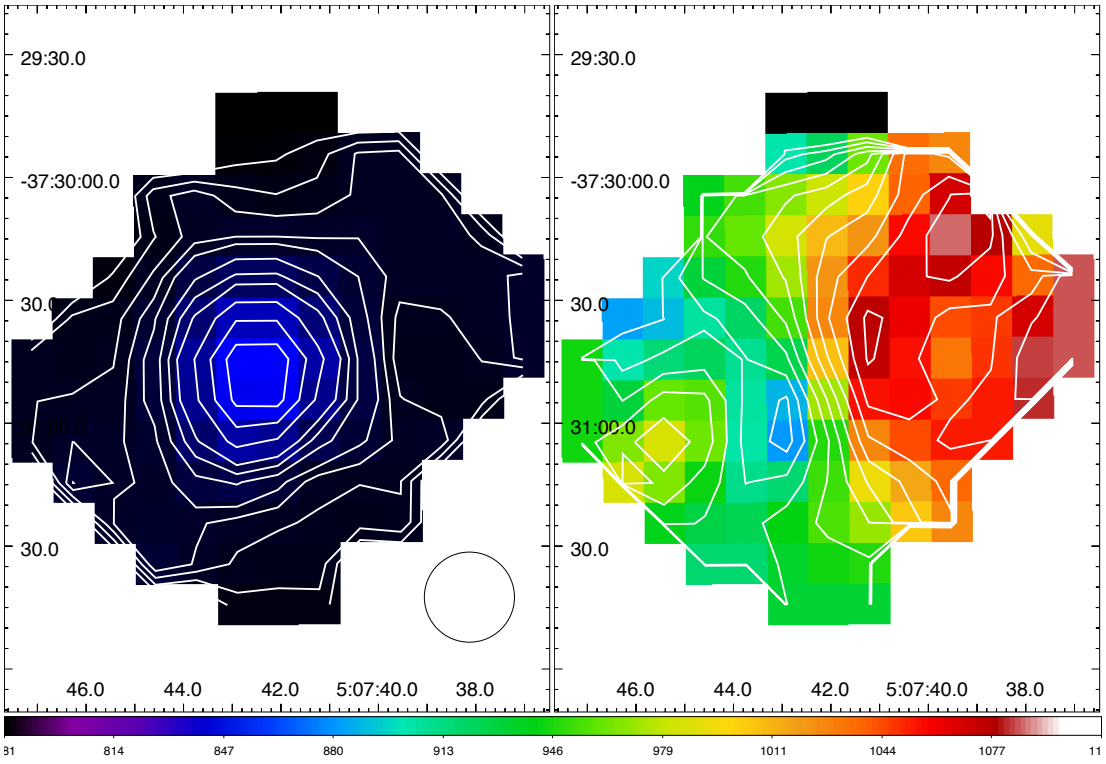

Figure 8.5: *Left.* ^{12}CO (3-2) integrated intensity map convolved with a Gaussian of $22''$. The contours are 5, 7.5, 10, 12.5, 15, 20, 25, 30, 40, 60, 80 K km s^{-1}. *Right.* Velocity peaks with contours from $V_{\rm LSR} = 890$ to 1090 km s^{-1} separated by 20 km s^{-1}.

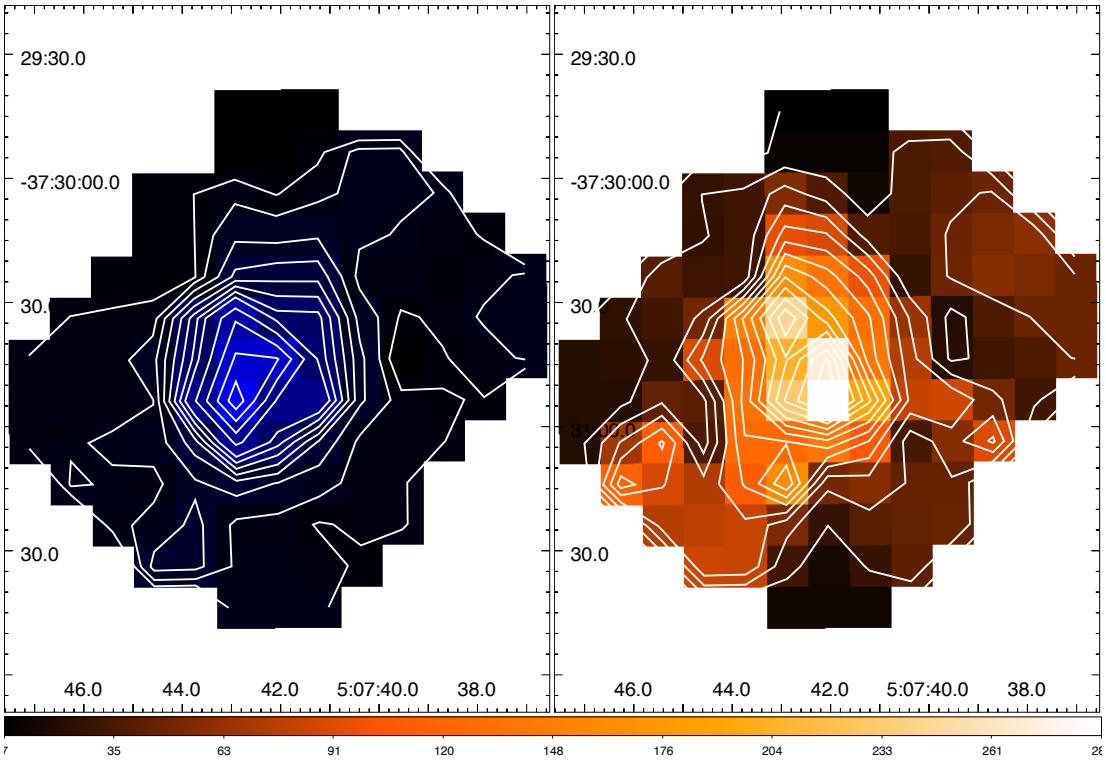

Figure 8.6: *Left.* Main-beam brightness temperature $T_{\rm mb}$ with contours 0.07, 0.09, 0.12, 0.15, 0.18, 0.21, 0.27, 0.33, 0.39, 0.45, 0.51 K. *Right.* Velocity dispersion from 6 to 266 km s^{-1} with an increment of 20 km s^{-1}.

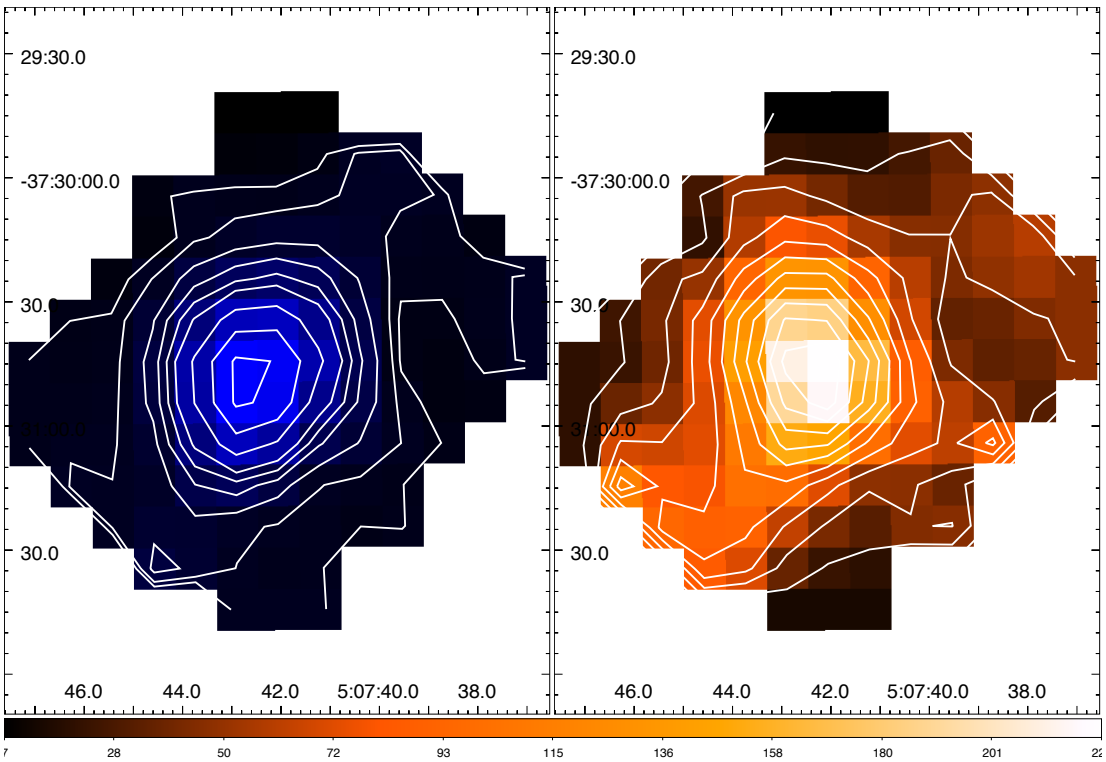

Figure 8.7: *Left.* Main-beam brightness temperature $T_{\rm mb}$ map of the smoothed data with contours 0.075, 0.09, 0.12, 0.15, 0.18, 0.21, 0.27, 0.33, 0.39 K. The threshold of 75 mK corresponds to 5σ in $T_{\rm mb}$ throughout the map. *Right.* Velocity dispersion from 5 to 205 km s^{-1} with an increment of 20 km s^{-1}.

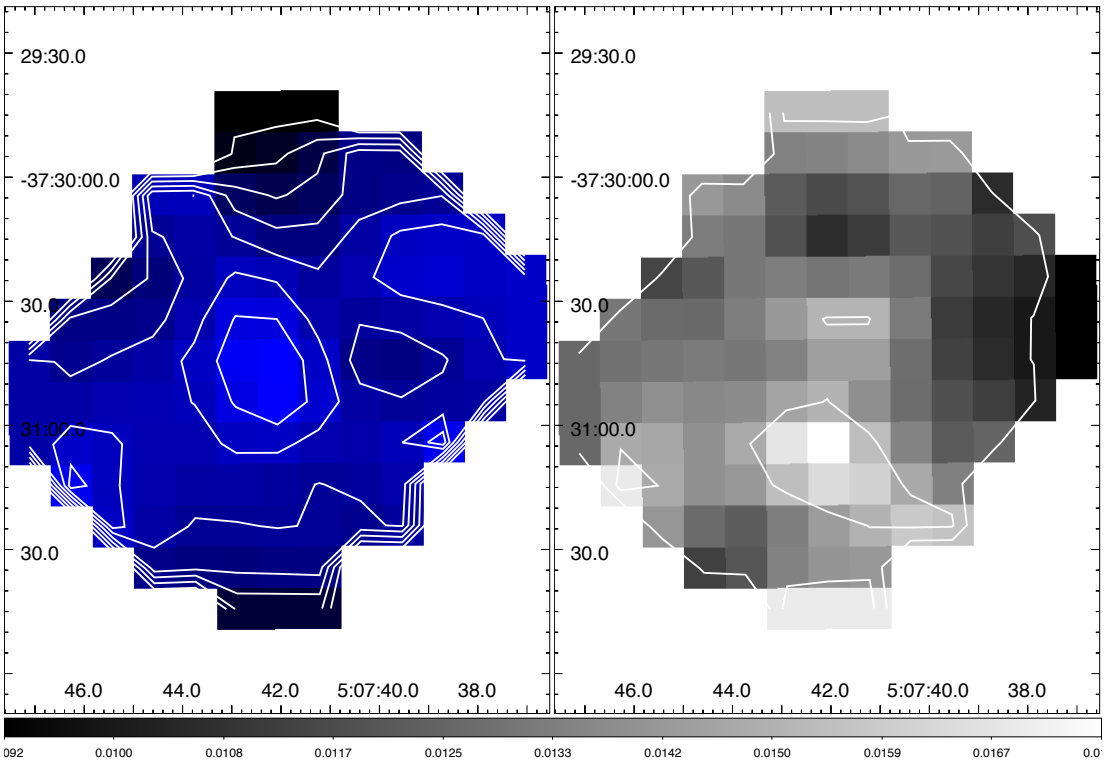

Figure 8.8: *Left.* Ratio of the integrated intensity and main-beam brightness temperature of the smoothed data with contours from 70 to 190 km s^{-1} separated by 20 km s^{-1}. *Right.* r.m.s. noise with contours at 10 and 15 mK. The r.m.s. in the map spans from 9.2 to 17.5 mK in $T_{\rm mb}$.

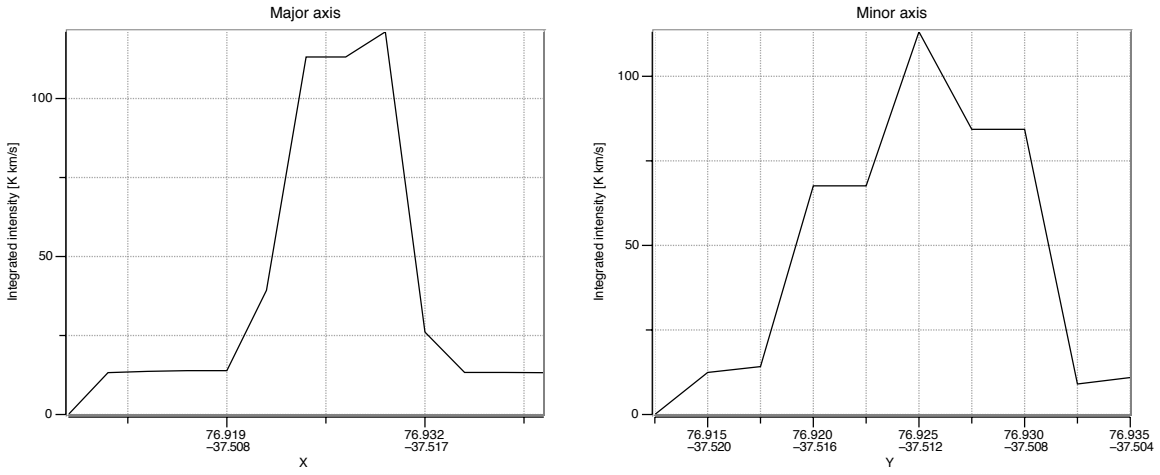

(a) (b)

Figure 8.9: Projections of the integrated intensity along the major axis (a) and minor axis (b).

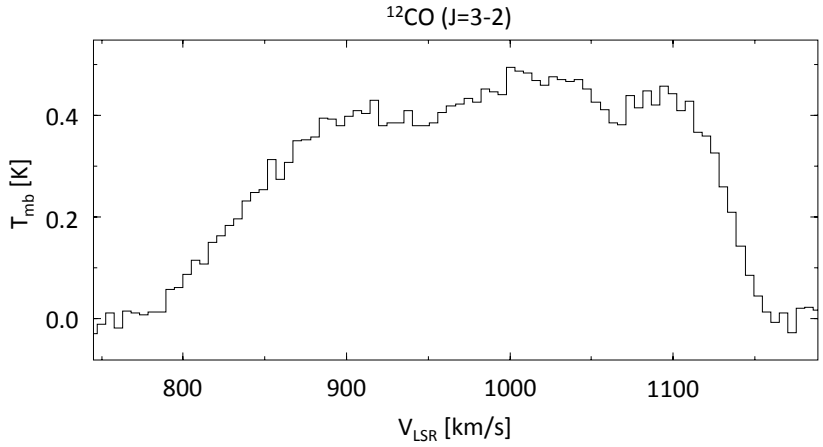

(a)

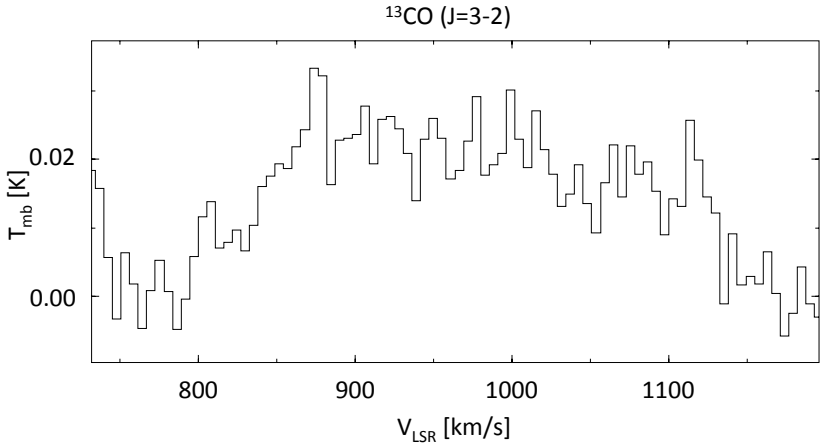

(b)

Figure 8.10: Spectra of a) ^{12}CO (3-2) (integ. time 5 minutes, $\Delta T_{\rm mb} = 17.4$ mK) and b) ^{13}CO (3-2) (integ. time 49 minutes, $\Delta T_{\rm mb} = 3.9$ mK) at the central position $(X,Y) = (0'',0'')$, $(\alpha,\delta)_{\rm B1950} = (05^{\rm h}05^{\rm m}58.3^{\rm s}, -37^0 34' 35.0'')$. The width of a velocity channel is 5 km s^{-1}.

Table 8.3: Properties of the observed molecular lines at the central position.

Line	peak $T_{\rm mb}$ [K]	Integrated intensity I [K km s^{-1}]
^{12}CO (3-2)	0.494 ± 0.017	127.15 ± 0.75
^{13}CO (3-2)	0.033 ± 0.004	6.46 ± 0.20

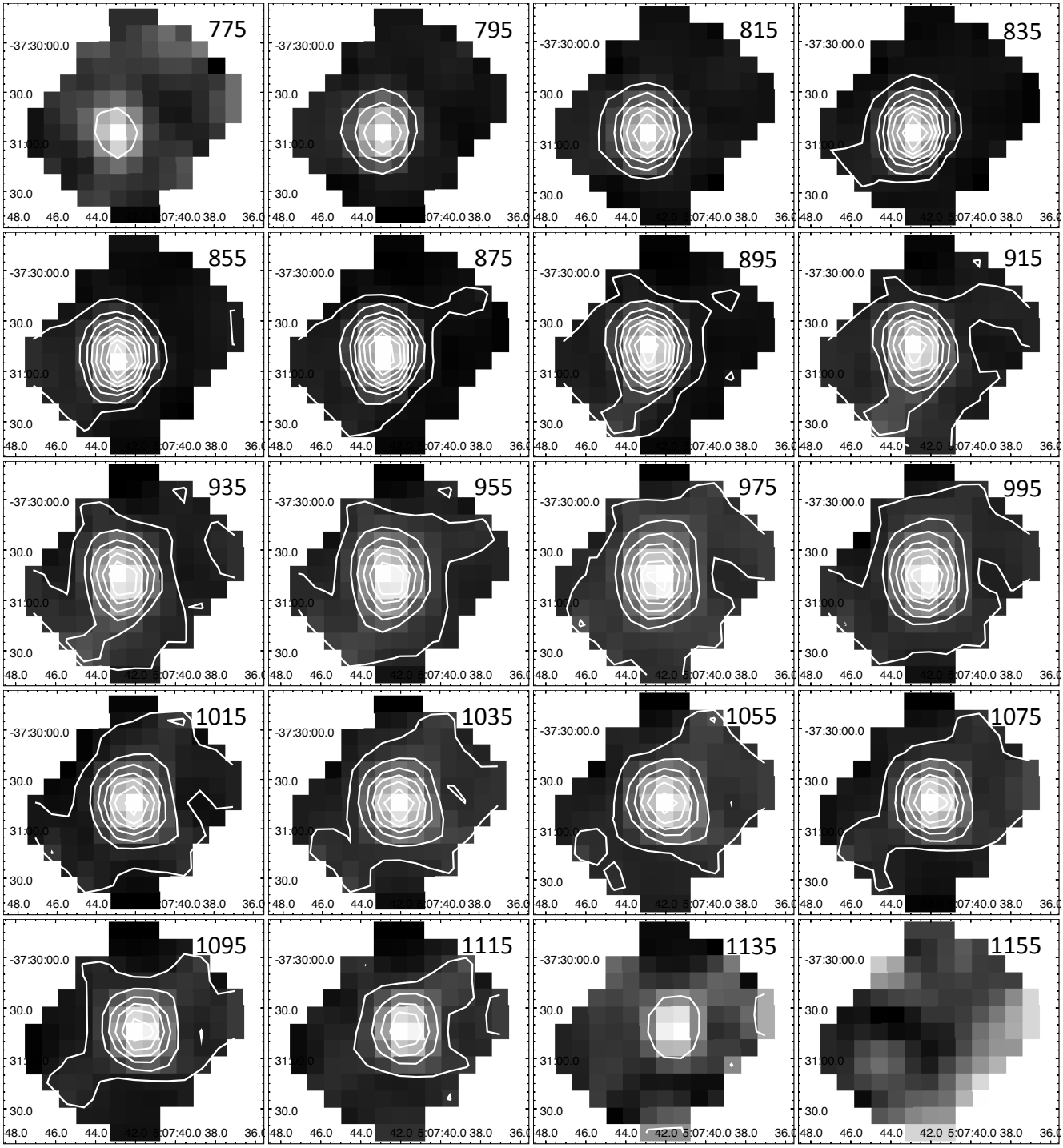

Figure 8.11: Channel maps of the smoothed data from $V_{\rm LSR} = 775$ to1155, with a separation of 20 km s^{-1}. The contours run from 0.03 K with an increment of 0.03 K in $T_{\rm A}^*$. The coordiantes are equatorial in J2000.

8.2.1 Is there a molecular-gas outflow in NGC 1808?

In figure 8.12, we show a comparison of the CO (3-2) integrated intensity map with optical and UV images. The Hα emission line in the optical regime (6564.6 Å) is a tracer of ionized gas present mostly in H II regions, i.e., in star forming regions. The B-band image traces a population of main-sequence stars, hence appears in the whole stellar disk of the galaxy. The near-UV image traces star-forming regions.

The comparison shows two noteworthy features of the CO gas: (1) wide distribution in the inner 4 kpc, with elongated structure in the direction of the galactic bar; (2) presence of the molecular gas in the polar direction (spur marked by arrows), coincident with the dust lanes that are most clearly seen in the B-band image. Note that this region is heavily obscured in the near-UV image; this is because UV radiation is easily absorbed by dust.

These results indicate that both dust and molecular gas are present in an outflow from the nuclear region of NGC 1808. Further investigation with ALMA is promising to reveal the properties of the outflow (size, velocity, etc).

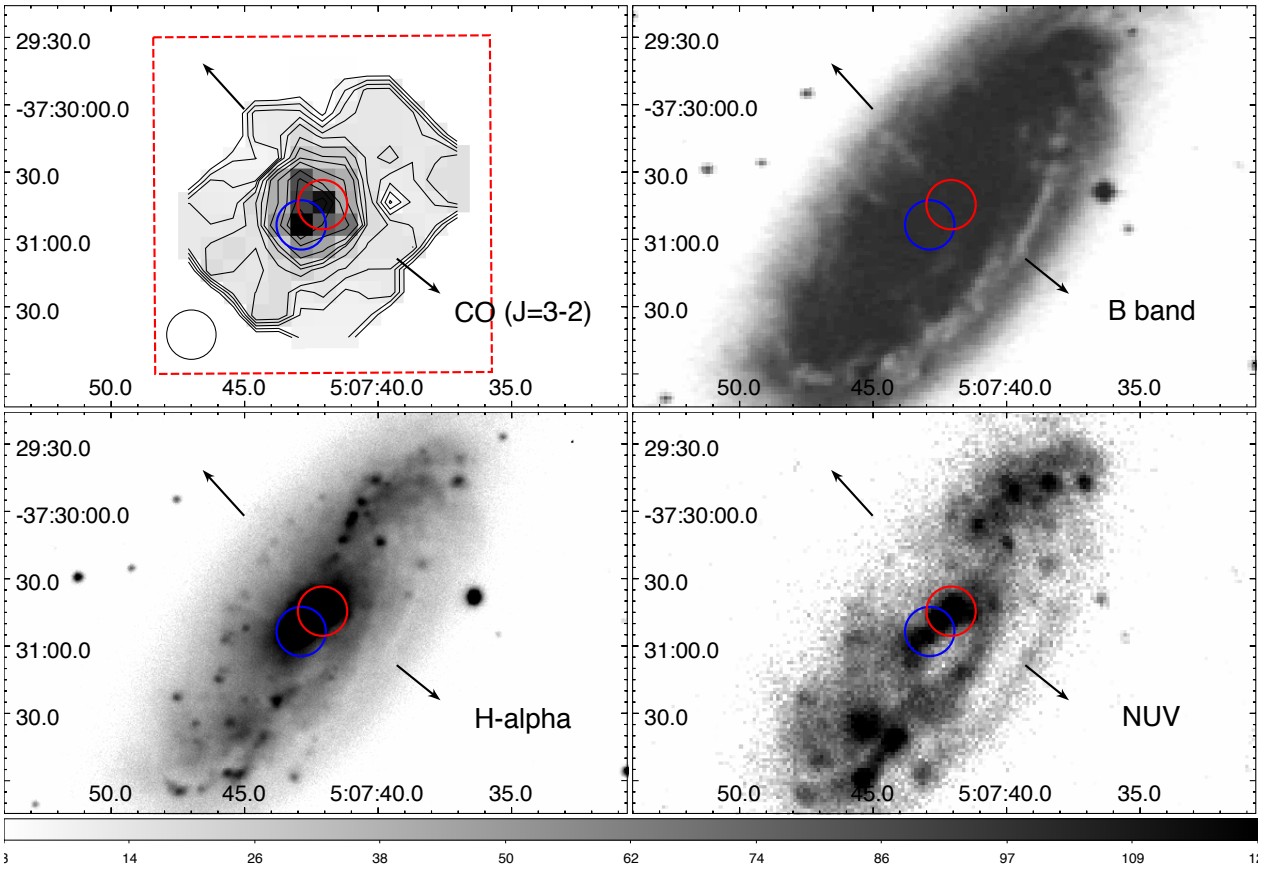

Figure 8.12: Comparison of the CO (3-2) integrated-intensity image with images on other wavelengths (acquired from NED). Red and blue circles indicate double peak at the center of NGC 1808. Black arrows mark the proposed direction of the outflow. The red rectangle shows the mosaicking region of ALMA CO (1-0) observations. The coordiantes are equatorial in J2000.0.

In a recent work, Sharp & Bland-Hawthorn (2010) have analyzed optical data of NGC 1808 (although observed in poor atmospheric conditions). These data include Hα ($\lambda = 6564.6$ Å) and [N II]6585.3. A comparison between the flux ratio [N II]/Hα and CO (3-2) is shown in figure 8.13. Although the angular resolutions differ by an order of magnitude, it is clear that the direction of the outflow of ionized gas coincides with the spur detected in CO (3-2). The relatively increased [N II]/Hα ratio in the nucleus and along the minor galactic axis is an indicator of shocked gas. Since we

cannot clearly resolve the structure both spatially and kinematically, it is important to note that the optical data show that the extended emission in this direction is not due to the disk component on the far side of the disk but emission from extra-planar regions.

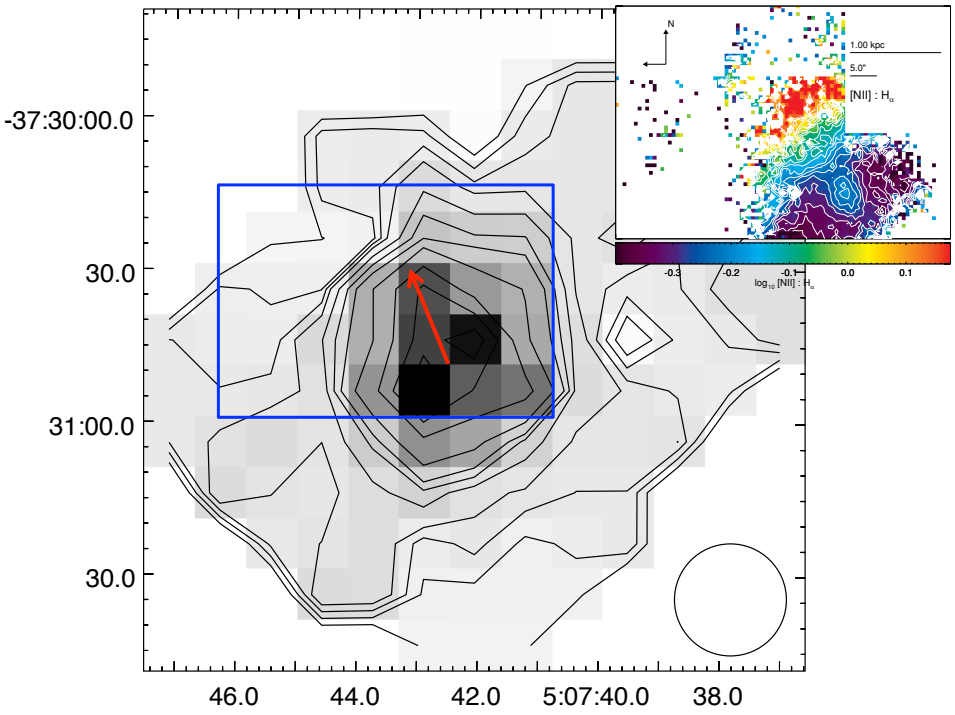

Figure 8.13: Comparison of the CO (3-2) integrated-intensity image with the ratio of [N II]6585.3 and Hα from Sharp & Bland-Hawthorn (2010).

8.3 Physical conditions of the molecular gas

In this section we estimate the physical conditions (kinetic temperature $T_{\rm k}$ and density $n(\mathrm{H_2})$) of the molecular gas in the starburst nucleus (radius ≈ 550 pc from the center) of NGC 1808. The calculation was carried out by using the computer program RADEX (van der Tak 2007). Description of the basic steps in the calculation is given in the following subsection. For more details on the program, refer to the paper cited above or to the home page: http://home.strw.leidenuniv.nl/∼moldata/radex.html.

In order to compile a large set of input data, line intensity ratios of ^{12}CO and ^{13}CO were derived (table 8.4). Data of $J = 1 \rightarrow 0$ and $J = 2 \rightarrow 1$ were taken from Aalto et al. (1994); data of $J = 3 \rightarrow 2$ are from this work.

Table 8.4: Integrated intensity ratios at the central position.

Molecule	Transition	Value	Reference
^{12}CO	2-1/1-0	1.12 ± 0.01	Aalto et al. (1994)
^{12}CO	3-2/2-1	0.56 ± 0.01	This work
^{13}CO	2-1/1-0	1.2^a	Aalto et al. (1994)
^{13}CO	3-2/2-1	0.45	This work
^{12}CO/^{13}CO	1-0	16.4 ± 1	Aalto et al. (1994)
^{12}CO/^{13}CO	2-1	15.5 ± 1	Aalto et al. (1994)
^{12}CO/^{13}CO	3-2	19.8 ± 0.6	This work

Note. ^{a}The ^{13}CO 2-1 and 1-0 data were not convolved to the same angular resolution prior to taking their ratio.

A map of the line intensity ratio of CO (3-2)/(2-1) is shown in figure 8.14. The CO (2-1) data were taken with the Swedish-ESO Submillimeter Telescope (SEST) at an angular resolution of $24''$, and the CO (3-2) data with ASTE at $22''$. The observing positions are identical, centered on $(\alpha, \delta)_{\rm B1950} = (05^{\rm h}05^{\rm m}58.3^{\rm s}, -37^0 34' 35.0'')$ with a position angle of 140^0. The systemic velocity with respect to the local standard of rest (LSR) is 965 km s^{-1} in the radio definition.

The average 3-2/2-1 ratio in the central region is 0.6. Note that there is no clear evidence for a symmetric ratio gradient in the central 4 kpc. The ratio is high (>0.5) in the central region and along the galactic bar, and lower in the outer regions (NW and SE part of the map). There is, however, marginal depression in the ratio in the range from $(X,Y) = (0'',0'')$ to $(X,Y) = (-10'',+30'')$ in the direction of the outflow (see below).

8.3.1 Radiative transfer analysis with low-energy rotational transitions of CO

Overview of RADEX

RADEX is a non-LTE program that allows one to estimate the kinetic temperature ($T_{\rm k}$) and density ($n(\mathrm{H_2})$) of the molecular gas. Input parameters are the column density (N) and velocity width (ΔV). RADEX uses one of the escape probability functions to decouple radiation from level populations. The equation for level 1 can be written as

$$\frac{{\rm d}n_1}{{\rm d}t} = -n_1 \left(B_{12}\bar{J} + C_{12}\right) + n_2 \left(A_{21} + B_{21}\bar{J} + C_{21}\right). \tag{8.2}$$

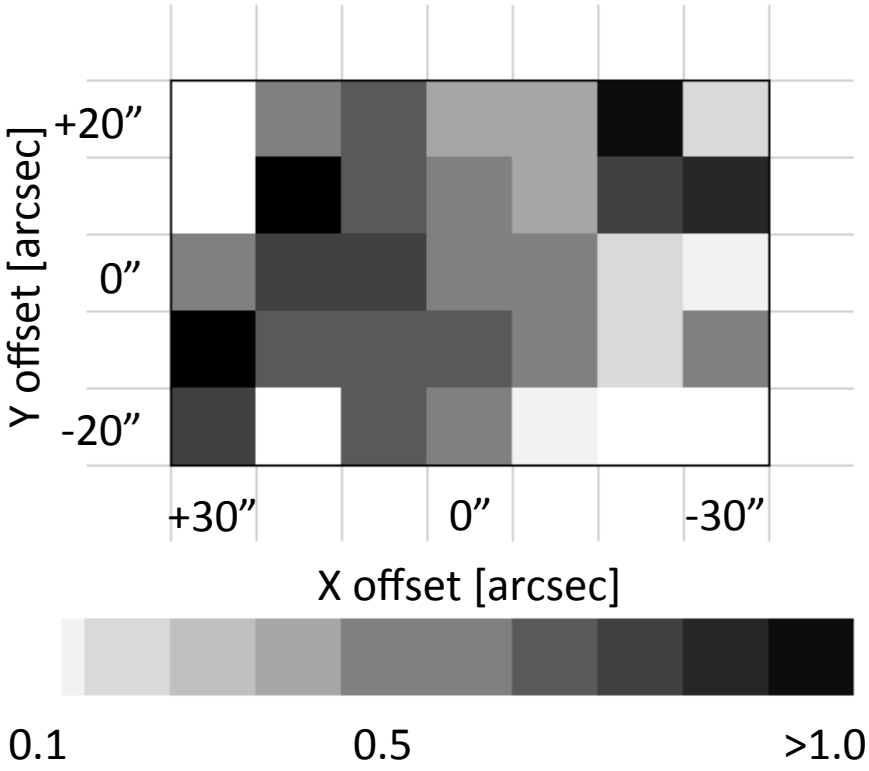

Figure 8.14: CO (3-2)/(2-1) integrated intensity ratio. X and Y axes correspond to the major and minor axes, respectively, with a position angle of 140^0. The CO (2-1) data are from Aalto et al. (1994). The pixels are separated by $10''$, which was the grid spacing in both observations.

The first term on the right side is the decrease of population n_1 due to absorption B_{12} in radiation field $\bar{J}$, while the second term is the increase of population n_2 due to spontaneous emission A_{21}, stimulated emission B_{21}, and collisional deexcitation C_{21}.

Analogously, for level 2:

$$\frac{\mathrm{d}n_2}{\mathrm{d}t} = n_1\left(B_{12}\bar{J}+C_{12}\right) - n_2\left(A_{21}+B_{21}\bar{J}+C_{21}\right). \tag{8.3}$$

Since n's and $\bar{J} = \int J_\nu \mathrm{d}\phi(\nu)$ are both unknown, it is said that the level populations and radiation are coupled. Here, A and B are Einstein's coefficients, and C is the collisional coefficient. If we introduce an escape probability that photons will leave an opaque cloud, the average radiation field becomes

$$\bar{J} = S(1-\beta), \tag{8.4}$$

where S is the source function of the cloud, and β is the escape probability. In the case of a large velocity gradient (LVG, Sobolev 1957) in the cloud,

$$\beta = \frac{1-\mathrm{e}^{-\tau}}{\tau}. \tag{8.5}$$

This is the equation that was used in the calculations below. With β, the equations above can be decoupled:

$$\frac{\mathrm{d}n_2}{\mathrm{d}t} = n_1 C_{12} - n_2 C_{21} - \beta n_2 A_{21}. \tag{8.6}$$

Therefore, calculating the populations and radiation can be done separately. The equations that govern radiation are:

$$I_\nu = I_\nu(0)\mathrm{e}^{-\tau_0} + S_\nu\left(1-\mathrm{e}^{-\tau_0}\right) \tag{8.7}$$

for intensity, and

$$T_\mathrm{R} = \frac{\lambda^2}{2k}\left[I_\nu - I_\nu(0)\right] \tag{8.8}$$

is the radiation temperature. Note that $T_\mathrm{R} = T_\mathrm{b}$ only if the beam size is smaller than the observed source. Otherwise, it should be multiplied by a beam filling factor. When taking line intensity ratios, the beam filling factors cancel if they are the same for both lines.

The level populations are

$$\frac{n_2}{n_1} = \frac{g_2}{g_1}\exp\left(-\frac{E_2-E_1}{kT_\mathrm{ex}}\right), \tag{8.9}$$

where T_ex is the excitation temperature. The optical depth at the line center is

$$\tau_0 = \frac{A_{21}\lambda^3}{8\pi}\frac{N}{\Delta V}\left(n_1\frac{g_2}{g_1} - n_2\right). \tag{8.10}$$

Thus, the results of RADEX calculations depend on $N/\Delta V$. In the case of CO, we can express the relationship between the column density, line width and density as

$$N(\mathrm{CO}) \propto f_\mathrm{CO} n(\mathrm{H_2})\frac{\Delta V}{\mathrm{d}v/\mathrm{d}r} \tag{8.11}$$

where $f_\mathrm{CO} \equiv [\mathrm{CO}]/[\mathrm{H_2}]$ is the abundance of CO relative to $\mathrm{H_2}$ and $\mathrm{d}v/\mathrm{d}r$ is the velocity gradient.

The calculation begins by deriving relative level populations in the optically thin limit. Then, the populations are used to obtain the optical depth in all lines by using the escape probability. Again, the optical depth is used to calculate the relative populations. This process is iteratively repeated until RADEX decides to stop when a consistent solution for the radiation and populations is achieved.

Results

Examples of calculation with RADEX are shown in figures 8.15 and 8.16. The ratios from table 8.4 were implemented with the adopted parameters listed in the caption of the figure. These results reflect the beam-averaged properties of the molecular gas. For example, the velocity width of 5 km s^{-1} is appropriate for typical molecular clouds, but it certainly does not represent the observed value of 250 km s^{-1} in the telescope beam. This velocity was used by assuming that the beams of ASTE and SEST were filled with an ensemble of clouds with an average velocity width of 5 km s^{-1} dominated by turbulence (which is an order of magnitude larger than the thermal width of CO lines). Note that the output of RADEX depends on the ratio $N(\mathrm{CO})/\Delta V$. Thus, the exact values of the column density and velocity width are of secondary importance. The initial values used here are $N(^{12}\mathrm{CO}) = 10^{17}$ cm^{-1} and $\Delta V = 5$ km s^{-1}. This is a reasonable start because in many galaxies column densities of $\mathrm{H_2}$ are of the order $N(\mathrm{H_2}) \sim 10^{21}$ cm^{-2}, which fits in a typical abundance ratio of the order $[\mathrm{CO}]/[\mathrm{H_2}] \sim 10^{-4}$ (see figure 1.8).

Inspection of figures 8.15 and 8.16 indicates that the estimated physical parameters are strongly dependent on the abundance ratio of ^{12}CO to ^{13}CO. The examples show the ratios of 50 and 40. Lower ratio is unlikely if we consider the ratios found in M82 as a typical starburst galaxy (75-80, Weiß et al., 2005). Also, ratios higher than 50 confine the temperatures to very low values of about 5 K. In our Galaxy, different values were found at different Galactocentric distances. Unlike M82, low values of about 30 were found in the region of Sagittarius B2, while the ratios are typically >50 in the solar neighborhood (Goto et al., 2003). Also, note that the parameters cannot be easily constrained by

using the line ratios of a single isotopologue. Therefore, the parameter space was explored by using the ratio of ^{12}CO and ^{13}CO in transitions 2-1 and 3-2, which have the same angular resolution, higher than that of 1-0. The best fits were found for the presented examples where at least three line intensity ratios approach and intersect in one region of the parameter space: at $T_{\rm k} = 20$ K, $n({\rm H_2}) = 10^{3.7}$ cm^{-3} (abundance ratio 50) and $T_{\rm k} = 35$ K, $n({\rm H_2}) = 10^{3.3}$ cm^{-3} (abundance ratio 40), with estimated uncertainty of the r.m.s. noise only. The temperature and density do not vary much within this region and the best solution where five lines intersect at nearly the same point is presented in figure 8.17. The corresponding parameters are $T_{\rm k} = 32$ K and $n({\rm H_2}) = 10^{3.5}$ cm^{-3}.

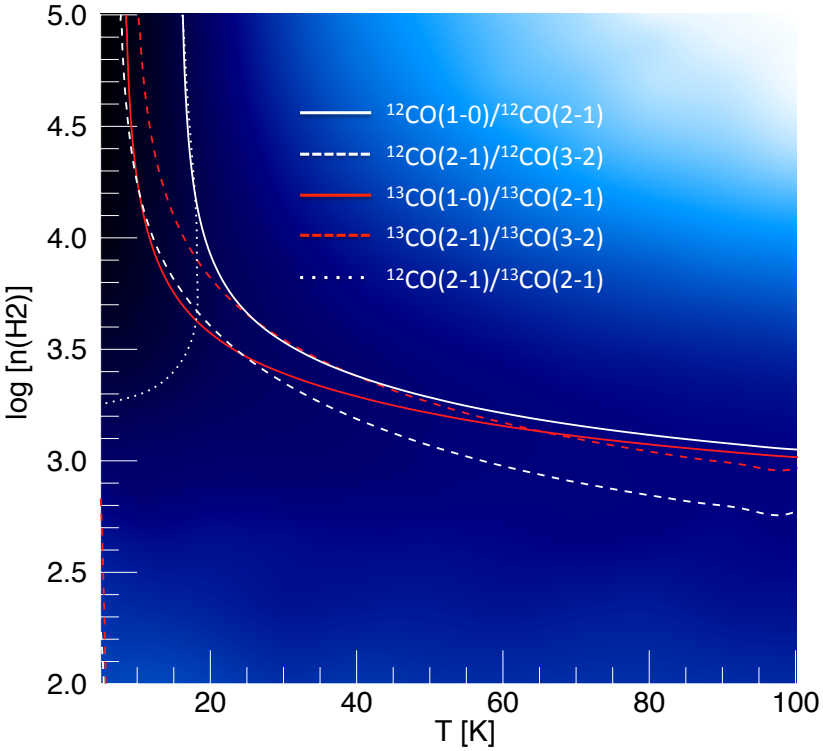

(a)

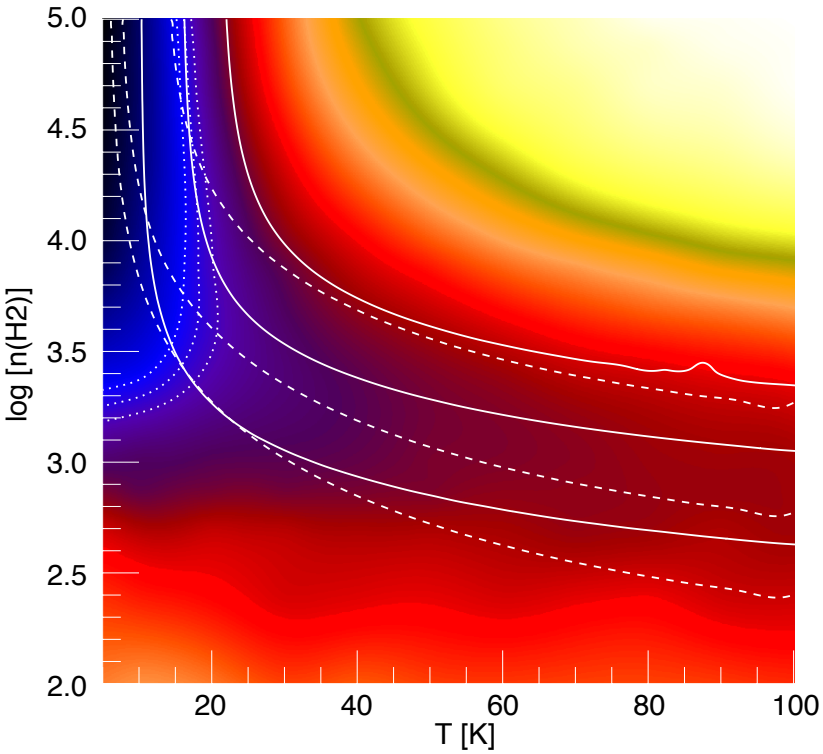

(b)

Figure 8.15: Example result of RADEX calculation. Adopted parameters: abundance ratio $[^{12}\mathrm{CO}]/[^{13}\mathrm{CO}] = 50$, column density/velocity width $N(^{12}\mathrm{CO})/\Delta V = 2 \times 10^{16}$ cm^{-2} (km s^{-1})$^{-1}$. (a) Ratios of all observed lines, and (b) same plot with indicated uncertainties. The color field corresponds to the ^{12}CO(2-1)/^{13}CO(2-1) ratio, where brighter color indicates larger ratio.

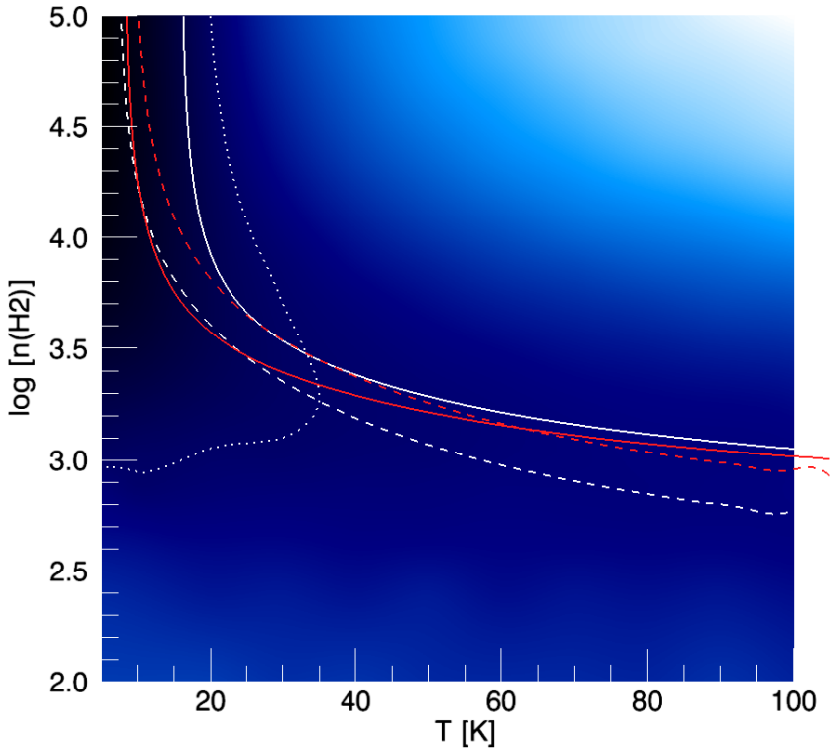

(a)

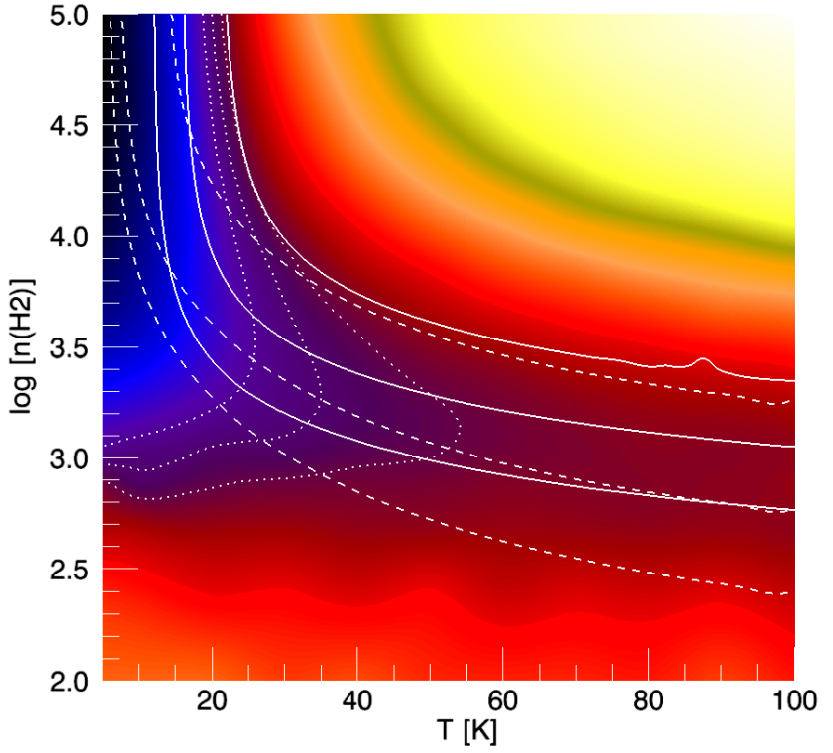

(b)

Figure 8.16: Example result of RADEX calculation. Adopted parameters: abundance ratio $[^{12}\mathrm{CO}]/[^{13}\mathrm{CO}] = 40$, column density/velocity width $N(^{12}\mathrm{CO})/\Delta V = 2 \times 10^{16}$ cm^{-2} (km s^{-1})$^{-1}$. (a) Ratios of all observed lines, and (b) same plot with indicated uncertainties. The color field corresponds to the ^{12}CO(2-1)/^{13}CO(2-1) ratio, where brighter color indicates larger ratio.

The above derivation of physical parameters suffers from three drawbacks. Firstly, it is assumed that the beam dilution is the same for all six lines. Since the molecular clouds are not resolved, we have no way of estimating the beam filling factors for individual lines. Secondly, the line profile in the spectrum of CO (2-1) from Aalto et al. (1994) and our CO (3-2) data seem to be different. Note in figure 8.3 that the emission profile is asymmetric and that the peak intensity is higher at $(\Delta X, \Delta Y) = (+10'', 0'')$ than at the central position. The discrepancy in the line profiles could be due to an error in telescope pointing. The uncertainty in our observations was typically better than $2''$, whereas in the observations with SEST it was $4''$ (Aalto et al., 1994). And thirdly, we have taken into account only the r.m.s. noise uncertainty. Since each measurement has an absolute uncertainty of about 20%, and the lines were not observed simultaneously (although with the same telescope), the relative ratios of lines in different bands have non-negligible uncertainty.

Calibration methods lead us to estimate that the measured ratios in the same frequency band have a total uncertainty no larger than 15%. The RADEX calculation then yields a continuum of values shown in figure 8.17 (a). The result implies that the density and temperature of the molecular gas are confined to $3.0 \lesssim \log(n/\mathrm{cm}^{-3}) \lesssim 4.0$ and $20 \lesssim T_\mathrm{k} \lesssim 100$ K. Molecular gas at $20 \lesssim (T_\mathrm{k}/\mathrm{K}) \lesssim 60$ could belong to GMCs, whereas the high-temperature component ($T_\mathrm{k} \gtrsim 60$ K) could belong to the regions where cosmic ray and mechanical (shock) heating have disrupted GMCs, as well as star formation in H II regions and the central X-ray sources.

The analysis so far has yielded a relatively cool molecular medium. However, we still cannot reproduce the densest molecular clouds (10^{4-5} cm^{-3}) with low temperatures (10 K) observed to exist in the Galaxy. If we could correct for the beam dilution, the produced line intensity ratios should predict these entities. This is shown in figure 8.17 (b): *lower* ratios of ^{12}CO/^{13}CO lines produce lower temperatures and higher densities corresponding to the coldest (10-20 K) and densest ($n \gtrsim 10^4$ cm^{-3}) clouds.

Aalto et al. (1994) have developed a two-population model for the molecular clouds in NGC 1808 based on observations with SEST. Their results suggest two kinds of cloud: "cores" with $n(\mathrm{H_2}) = 1.0 \times 10^5$ cm^{-3} and $T_\mathrm{k} = 15$ K, and "envelopes" with $n(\mathrm{H_2}) = 2.0 \times 10^3$ cm^{-3} and $T_\mathrm{k} = 100$ K. Although this model is a crude simplification since molecular gas does not have well-defined boundary between cores and envelopes, it is generally consistent with our results. Their model fails to reproduce the observed ratio of ^{12}CO (3-2)/^{13}CO (3-2) and assumes that the warm molecular gas is between the dense cores, but neglects the heating sources inside the cores.

We conclude that although RADEX calculations successfully constrain the molecular gas densities and temperatures, interpretation of the result should be done with caution. Higher angular resolution and observations of other molecular lines that can be used to measure the density and temperature are necessary.

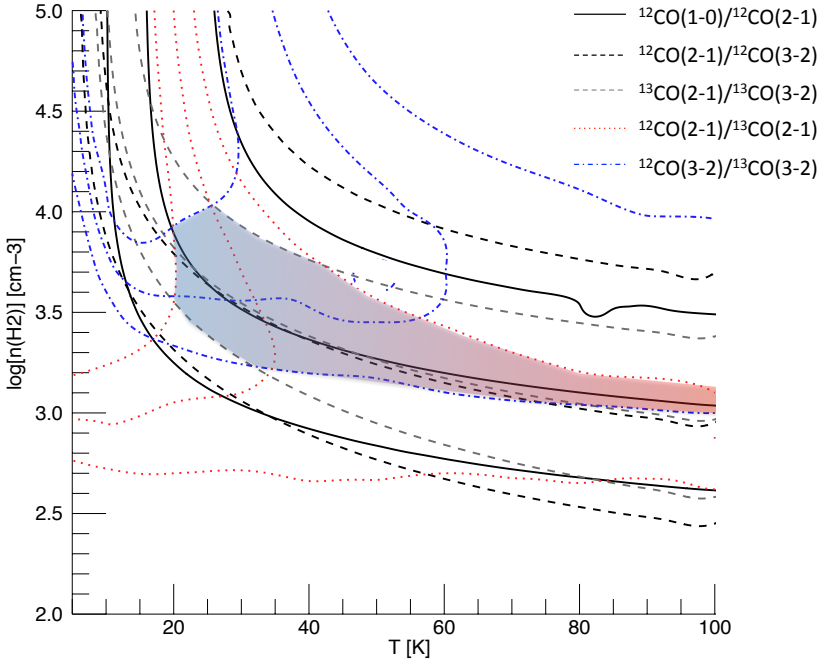

(a)

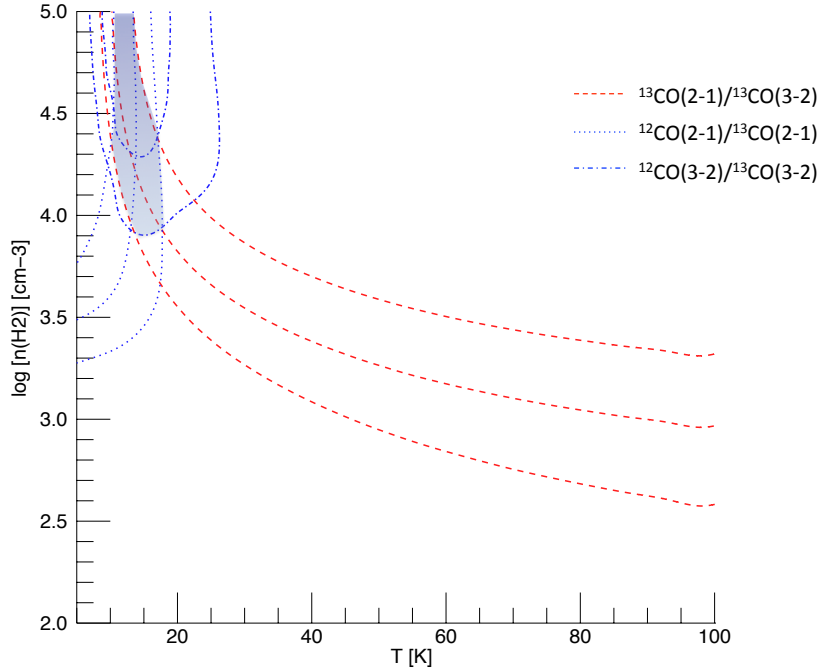

(b)

Figure 8.17: *Top*. Solution for five CO line ratios in RADEX calculations. The adopted parameters are: $N(^{12}\mathrm{CO}) = 10^{17}$ cm^{-2}, $\Delta V = 5$ km s^{-1}, $[^{12}\mathrm{CO}]/[^{13}\mathrm{CO}] = 40$. The ratio ^{13}CO (1-0)/(2-1) is not included because the data were not smoothed to the same angular resolution (Aalto et al., 1994). The uncertainty is 15% for ^{12}CO/^{13}CO ratios and 30% for ^{12}CO(1-0)/^{12}CO(2-1), ^{12}CO(2-1)/^{12}CO(3-2), and ^{13}CO(2-1)/^{13}CO(3-2) ratios. The shaded area shows the overlap region. *Bottom.* Ratios of ^{12}CO(2-1)/^{13}CO(2-1) and ^{12}CO(3-2)/^{13}CO(3-2) assumed to be 2/3 of the measured value to estimate the influence of different beam dilutions for the ^{12}CO and ^{13}CO lines. The ratio ^{13}CO(2-1)/^{13}CO(3-2) is unchanged.

Optical depth of CO (3-2)

Adopting an abundance ratio of $r \equiv [^{12}\mathrm{CO}]/[^{13}\mathrm{CO}] = 45$, the optical depth of the CO (3-2) line can be dervied. Let us begin with an LTE approach. The observed brightness temperatures are

$$\begin{aligned} T_{\mathrm{b},12} &= \left(T_{\mathrm{ex},12} - T_{\mathrm{bg}}\right)\left(1 - \mathrm{e}^{-\tau_{12}}\right) \\ T_{\mathrm{b},13} &= \left(T_{\mathrm{ex},13} - T_{\mathrm{bg}}\right)\left(1 - \mathrm{e}^{-\tau_{13}}\right) \end{aligned} \tag{8.12}$$

for ^{12}CO (3-2) and ^{13}CO (3-2), respectively. $T_{\mathrm{bg}} = 2.73$ K is the cosmic microwave background. If the excitation temperatures are equal, $T_{\mathrm{ex},12} = T_{\mathrm{ex},13}$, the optical depth can be calculated from the ratio of integrated intensities:

$$\frac{I_{12}}{I_{13}} \propto \frac{T_{\mathrm{b},12}}{T_{\mathrm{b},13}} \approx \frac{\left(1 - \mathrm{e}^{-\tau_{12}}\right)}{\left(1 - \mathrm{e}^{-\tau_{12}/r}\right)}. \tag{8.13}$$

Numerically solving this equation gives $\tau_{12} = 2.1^{+0.2}_{-0.1}$ for ^{12}CO (3-2) and $\tau \ll 1$ for ^{13}CO (3-2). For the parameters $n(\mathrm{H_2}) = 10^{3.5}$ cm^{-3}, $T_{\mathrm{k}} = 32$ K, and $[^{12}\mathrm{CO}]/[^{13}\mathrm{CO}] = 45$, RADEX predicts optical depths of $\tau = 3.8$ for ^{12}CO (3-2) and $\tau = 0.09$ for ^{13}CO (3-2). The excitation temperatures are $T_{\mathrm{ex},12} = 14$ K and $T_{\mathrm{ex},13} = 10$ K; thus the lines are subthermally excited. The derivation assumes equal beam filling factors. In figure 8.18, we show optical depths and excitation temperatures of ^{12}CO and ^{13}CO from $J = 1-0$ to $J = 8-7$ calculated with RADEX. Note that $J = 2-1$ and $J = 3-2$ of ^{12}CO are the most opaque lines.

8.3.2 Dust temperature

The dust temperature (T_{d}) can be established as temperature of a source radiating as blackbody. The temperature and radiation flux are related by the Planck formula. Determination of T_{d} can be achieved by using the fluxes at 60 and 100 μm (Solomon et al. 1997; Gao & Solomon 2004). In the case of NGC 1808, the flux ratio is $S_{60\mu\mathrm{m}}/S_{100\mu\mathrm{m}} \sim 0.75$ (IRAS catalog in Sanders et al. 2003) which yields a dust temperature of $T_{\mathrm{d}} \simeq 34$ K. Note that this value is very close to that of the gas kinetic temperature derived from CO. Dust temperatures derived from long wavelengths trace cooler medium compared to those traced with 12 and 24 μm (Mangum et al. 2013), and our radiative transfer analysis traces the same average properties of the molecular gas. Among nearby star-forming galaxies, for example, similar values have been found in: NGC 253 (34 K), NGC 660 (37 K), NGC 1365 (32 K), IC 342 (30 K), NGC 3079 (32 K), M83 (31 K), and NGC 6946 (30 K) (see references in Mangum et al. 2013).

8.3.3 Average conversion factor and column density in the central 500 pc

By using the derived average $\mathrm{H_2}$ density, $n \sim 10^{3.5}$ cm^{-3}, and kinetic temperature, $T_{\mathrm{k}} \sim 32$ K, and assuming that this temperature is equal to the excitation temperature of CO, $T_{\mathrm{k}} = T_{\mathrm{ex}} = 32$ K, we may estimate the CO-$\mathrm{H_2}$ conversion factor X_{CO}. Draine (2011) has shown that the conversion factor can be derived theoretically for spherical, self-gravitating, homogeneous clouds with turbulent velocities (instead of large velocity gradient) as

$$X_{\mathrm{CO}} = \frac{k}{8\pi h\nu}\left(\frac{15}{2.8 G m_{\mathrm{H}}}\right)^{1/2} (n_{\mathrm{H}})^{1/2}\left(\mathrm{e}^{h\nu/kT_{\mathrm{ex}}} - 1\right). \tag{8.14}$$

Inserting the above numbers, we find

$$X_{\mathrm{CO}} \sim 0.5 \times 10^{20}\ \mathrm{cm^{-2}}\ \left(\mathrm{K\ km\ s^{-1}}\right)^{-1}. \tag{8.15}$$

The conversion factor is lower than the Galactic value (Solomon et al. 1987; Young & Scoville 1991; Dame et al. 2001; Liszt et al. 2010), and similar to that in M82 (Weiß et al. 2001b) and ultraluminous starburst galaxies (Downes & Solomon 1998). This low value is in agreement with recent studies where it has been shown that, on average, conversion factors are lower in galactic nuclei (e.g., Sandstrom et al. 2013).

Now, by using this $X_{\rm CO}$, we can go a step further and derive the beam-averaged column density in the central 500 pc of NGC 1808. From the measured intensity ratio of CO (3-2) and CO (1-0), which is $I_{3-2}/I_{1-0} \sim 0.74$, the beam-averaged column density of H_2 gas is

$$N({\rm H_2}) \approx 1.3 X_{\rm CO} I_{3-2} \sim 0.8 \times 10^{22}\ {\rm cm^{-2}}. \tag{8.16}$$

If we express the conversion factor as

$$X_{\rm CO} = \frac{N({\rm CO})}{I_{1-0}} \frac{N({\rm H_2})}{N({\rm CO})} = \frac{N({\rm CO})}{I_{1-0}} \frac{1}{f_{\rm CO}}, \tag{8.17}$$

we find that

$$f_{\rm CO} = \frac{N({\rm CO})}{1.3 X_{\rm CO} I_{3-2}} \sim 1 \times 10^{-5}. \tag{8.18}$$

The abundance $f_{\rm CO}$ may be relatively lower in diffuse gas where $N({\rm H_2}) \sim 10^{20} - 10^{21}\ {\rm cm^{-2}}$ (Shetty et al. 2011), hence our result can be explained if we include low-density gas that originates from PDR surfaces unresolved together with dense molecular clouds ($N({\rm H_2}) \sim 10^{23}\ {\rm cm^{-3}}$) in the telescope beam.

The area of the projected telescope beam is $A = 9.1 \times 10^{42}\ {\rm cm^2}$. The H_2 mass is

$$M({\rm H_2}) = 2 m_{\rm H} A N({\rm H_2}) \simeq 1.2 \times 10^8\ M_\odot \tag{8.19}$$

within 550 pc from the galactic center. Here, $m_{\rm H} = 1.67 \times 10^{-24}$ g is the hydrogen atom mass. Corrected for the He abundance (multiply by 1.36), the total mass of molecular gas is $\simeq 1.6 \times 10^8\ M_\odot$, comparable to the central 500 pc in M82.

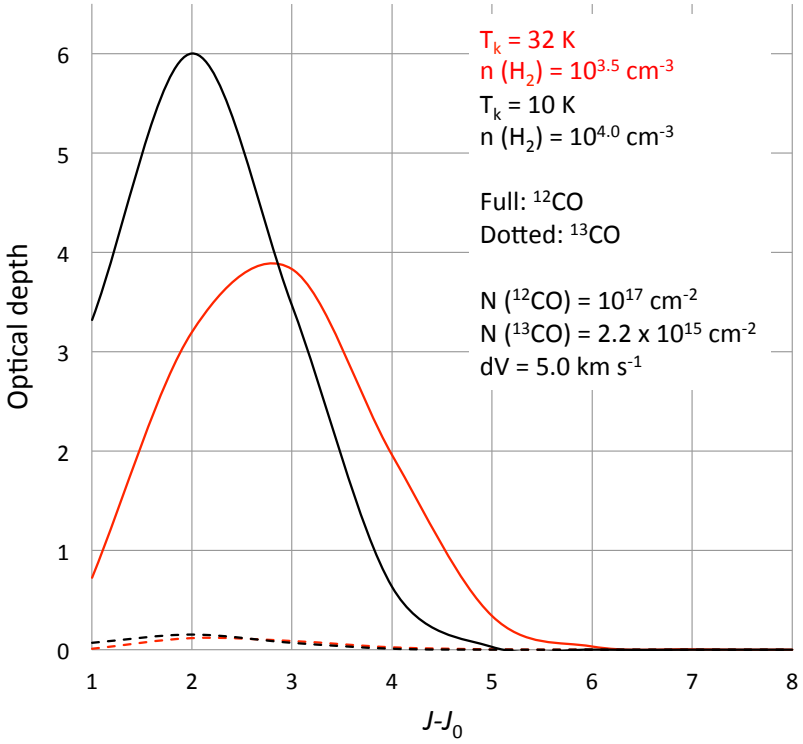

(a)

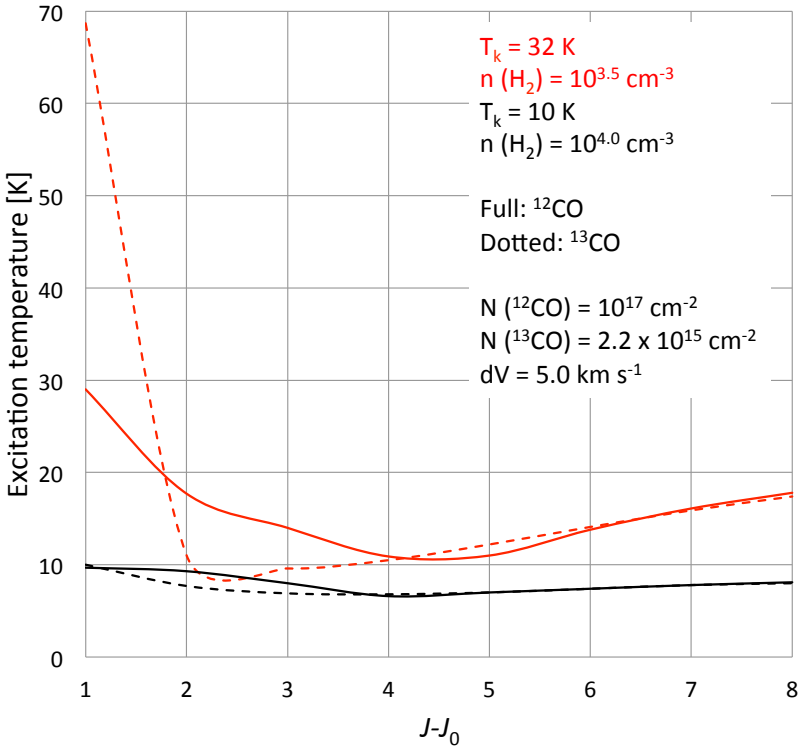

(b)

Figure 8.18: RADEX calculation with LVG geometry. Comparison is made between the derived properties of $T_{\rm k} = 32$ K and $n({\rm H_2}) = 10^{3.5}$ cm^{-3} with $T_{\rm k} = 10$ K and $n({\rm H_2}) = 10^4$ cm^{-3}, typical for Galactic clouds. *Top.* Optical depth (τ) as a function of rotational transition $J - J_0$ where J_0 is the ground state. *Bottom.* Excitation temperature ($T_{\rm ex}$) as a function of rotational transition.

Interpreting derived temperatures

In the last part of this section, we discuss the derived temperatures and their physical meaning. It has been found observationally that deriving temperatures by using different molecular lines can yield significantly different results. In the case of M82, molecular gas temperatures of > 45 K and 58 K were derived from CO and NH_3 measurements, respectively (Weiß et al. 2001b; Mangum et al. 2013). However, a much higher temperature of ~ 200 K was derived by observing the lines of H_2CO (Muehle et al. 2007). On the other hand, observations of dust at 60 and 100 μm usually yield lower values of dust temperatures; in M82, it was found to be 45 K.

We believe that this discrepancy arises from two factors: structure and spectral biases. The structure bias can be best understood if we consider observations of the Orion Nebula. Mangum et al. (1993) have shown that H_2CO abundance is not significantly different in the core compared to the ridge of the cloud. On the contrary, NH_3 is much more abundant in the core and only scarcely in the ridge. Similarly, it is well established that the low transitions of ^{12}CO are often optically thick: emission traces mostly the surface of a cloud. However, the low transitions of ^{13}CO are optically thinner - they probe the cloud interior.

The spectral bias is based on the choice of observed transitions. In the case of M82, T_k derived from NH_3 is similar to the CO and dust temperatures because only low inversion transitions $(J,K) = (1,1)$ and $(J,K) = (2,2)$ were used. However, Mangum et al. (2013) use higher transitions too and find temperatures readily above 100 K for other nearby galaxies. Thus T_k can depend on the lines available in observational data. Concerning the actual size of emitting sources, the beam dilution plays an important role in producing the observed intensities.

We conclude that molecular gas thermometry requires deep understanding of the properties of the observed source. Observations of Galactic and extra-galactic sources indicate that T_k in the dense gas is most reliably determined with a large number of (J,K) transitions of NH_3 (both low and high) and ^{13}CO or C^{18}O. If the gas is diffuse (10^3 cm^{-3}), it is traced with low-J transitions of CO. Unresolved, average gas properties are reflected in the intensities of *low* (J,K) transitions of NH_3 and both low and high transitions of ^{12}CO.

Comparison of CO intensities in NGC 1808 and M82

We have seen that the low-J transitions of ^{12}CO are optically thick while those of ^{13}CO are optically thin. In this subsection we compare the intensities of rare isotopologues ^{13}CO and C^{18}O in NGC 1808 and M82. Table 8.5 shows the line ratios and abundances: clearly, the ratios are very similar in both galaxies.

Table 8.5: CO line intensity ratios in NGC 1808 and M82.

Galaxy	^{13}CO(1-0)/C^{18}O(1-0)	^{12}CO(1-0)/C^{18}O(1-0)	$[^{12}\mathrm{CO}]/[\mathrm{C}^{18}\mathrm{O}]$
NGC 1808	3.3 ± 0.5^a	54 ± 6^a	-
M82	3.7 ± 0.3^b	58.3 ± 4.0^b	160-270^c

Note. ^{a}Aalto et al. (1994); ^{b}This work; ^{c}Weiß et al. (2001b).

General comparison between M82, NGC 1808, and our Galaxy

Table 8.6: Comparison between M82, NGC 1808, and the Milky Way.

	M82	NGC 1808	Milky Way
SFR $[M_\odot\ \mathrm{yr}^{-1}]$	11-33[a]	>2.2[e], 10[f]	1.3[i]
Starburst age (nucleus) [Myr]	8-50[a,b]	40[e], 50[g,h]	-
Starburst age (circum-nuclear) [Myr]	4-6[a]	8-17[e]	-
Density $[\mathrm{cm}^{-3}]$	$10^{(3.0-4.5)}$[c]	$10^{(3.0-4.0)}$	-
Temperature (CO) [K]	>45[c]	>20	30-45[j]
Temperature (dust) [K]	45[d]	34	15[k]
$[^{12}\mathrm{CO}]/[^{13}\mathrm{CO}]$	70[c]	40	30[l]

Note. [a]Förster Schreiber et al. (2003); [b]O'Connell et al. (1995); [c]Weiß et al. (2001b); [d]Sanders et al. (2003); [e] Kotilainen et al. (1996); [f]Junkes et al. (1995); [g]Krabbe et al. (1994); [h]Forbes et al. (1992); [i]Murray & Rahman (2010); [j]Kim et al. (2002); [k]Rodríguez-Fernández et al. (2004); [l]Goto et al. (2003). Values without reference were derived in this work.

Observations of CO (1-0) with ALMA

In cycle 1 of the ALMA early science, we submitted a proposal to make mosaicking observations of CO (1-0) in NGC 1808. The proposal was accepted at highest priority and the observations have begun in November 2013.

Cycle 1 observation consists of mosaicking of a $150'' \times 150''$ field (figure 8.19) with 32 antennas of the 12-m array, 9 antennas of the 7-m Atacama Compact Array (ACA, aka Morita array), and the 12-m total power array (TP). There are 39 pointings for the 12-m array, spaced by $25.9''$ (Nyquist for a HPBW of $53''$), and 14 pointings for ACA, spaced by $44.4''$ (HPBW of $91''$). The expected angular resolution (synthesized beam) is $2''$ (100 pc) or somewhat less, depending on actual configurations.

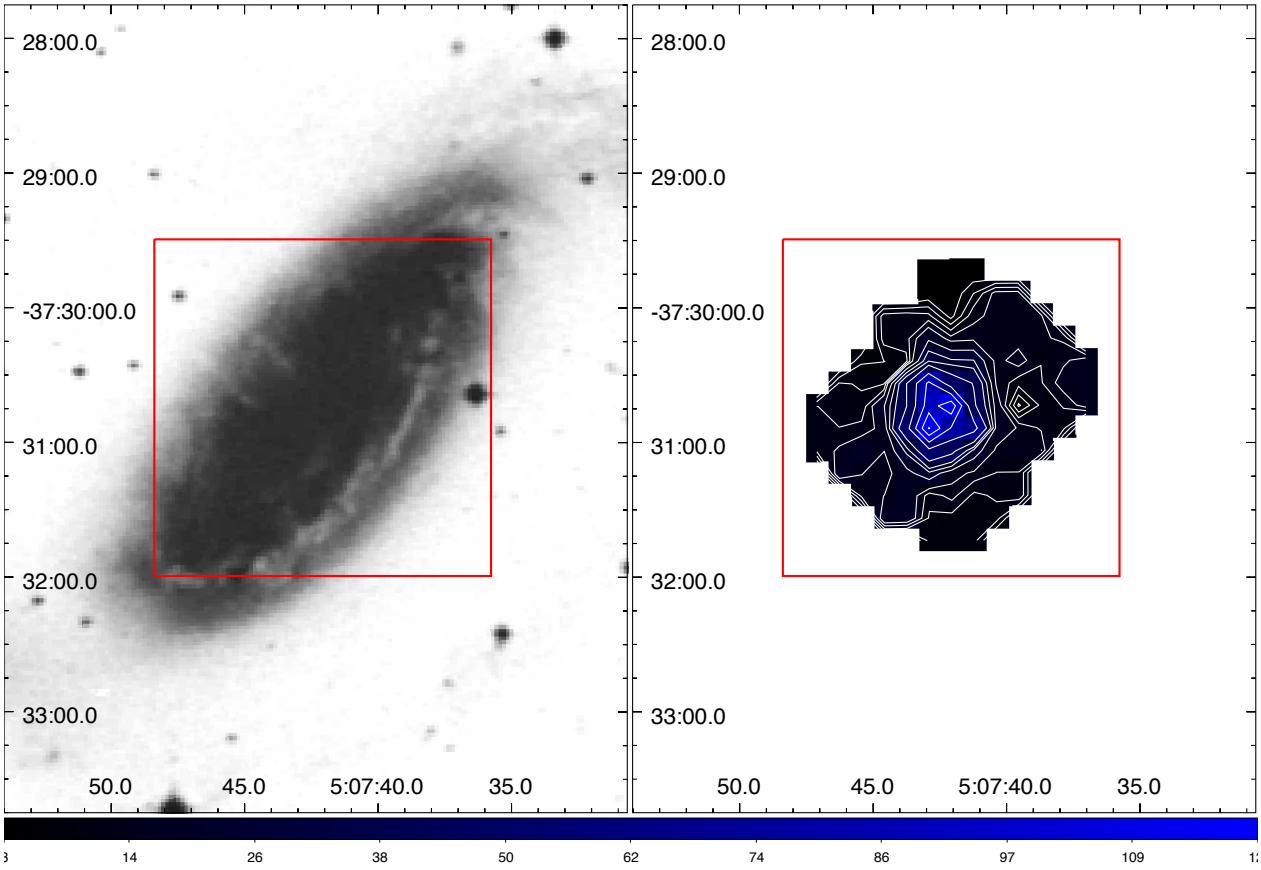

Figure 8.19: Mosaicking region (red rectangle) of CO (1-0) in NGC 1808: (a) B-band image, and (b) CO (3-2). The contours are the same as in figure 8.4.

Summary

In this work we have reported observations of M82 and NGC 1808 - two nearby starburst galaxies with galactic winds. Below is a summary:

1. M82 was mapped in CO (1-0) molecular line with the Nobeyama 45-m telescope and CARMA. Mapping observations with the 45-m telescope took place in 2009 and 2010; the data were combined with CARMA data acquired in 2012. The combining resulted in a sensitive image with high angular resolution ($4.0'' \times 3.3''$ equivalent to about 60 pc).

2. We used the 45-m telescope in 2013 to conduct 3-mm-line survey observations of M82 in ^{12}CO (1-0), ^{13}CO (1-0), C^{18}O (1-0), CN (1-0), and CS (2-1) molecular lines at selected positions in the galactic disk and outflow.

3. NGC 1808 was observed with the VLA in late 2012 at 21 and 32 GHz. Radio continuum was detected at both frequencies with $S/N > 5\sigma$. We have determined the position of the galactic nucleus and the size of the nuclear source to be $D \lesssim 10$ pc.

4. Observations of NGC 1808 in ^{12}CO (3-2) and ^{13}CO (3-2) with the ASTE 10-m telescope were carried out in late 2013. The ^{12}CO (3-2) line was mapped over $100'' \times 80''$ (5×4 kpc^2), while ^{13}CO (3-2) was observed toward the galactic center. Both lines were detected at high significance.

5. The CARMA-NRO 45m combined image of M82 reveals the geometry and kinematics of the molecular gas outflow. Two prominent 300-pc outflows were found to emanate from the nuclear ring with average expansion velocities of 50 km s^{-1}. We have calculated dynamical timescales, kinetic energies and mass outflow rates of both outflows. We show that the outflows were triggered 5 Myr ago during the second starburst episode that took place in the galactic ring. The large-scale (2 kpc) outflow detected previously with our OTF mapping was created after the onset of the first starburst episode in the central 500 pc 10-50 Myr ago.

6. We show that the momentum deposition rate from radiation pressure (with current star formation rate) in the nuclear ring is high enough to provide momentum in the 300-pc molecular gas outflows. Similarly, it can be demonstrated that SN ejecta have comparable momentum with the observed outflow. We propose that the driving mechanism of the outflow (radiation pressure and SN explosions) depends strongly on the local properties of the ISM: the molecular gas is driven by radiation pressure near the base of the outflow, and then re-accelerated by subsequent SN explosions. Once the outflow gas is driven solely by hot gas 1 kpc above the galactic plane, it is disrupted into diffuse medium and retains higher density only in fragments and filaments.

7. We present the first fully sampled map of NGC 1808 in ^{12}CO (3-2) and the first detection of ^{13}CO (3-2) in this galaxy. The molecular gas is strongly concentrated in the galactic nuclear region with prominent extended structure along the galactic bar (major axis) but also along the minor axis. The minor-axis component can be explained as molecular gas entrained in the galactic wind.

8. Our radiative transfer analysis of the excitation conditions of CO in the starburst region (central 500 pc) of NGC 1808 suggests that beam-averaged density and kinetic temperature of the molecular gas can be well fitted at $n \sim 10^{3.5}$ cm^{-3} and $T_{\rm k} \sim 32$ K, with uncertainties within $3.0 \lesssim \log(n/{\rm cm}^{-3}) \lesssim 4.0$ and $20 \lesssim T_{\rm k} \lesssim 100$ K.

9. M82 and NGC 1808 both have increased concentration of molecular gas in the central 500 pc. The molecular gas masses in the central region are comparable: 2.3×10^8 $M_\odot$ in M82 and 1.6×10^8 $M_\odot$ in NGC 1808, derived by using the same CO-to-H_2 conversion factor of $X_{\rm CO} = 0.5 \times 10^{20}$ cm^{-2} $\left({\rm K\ km\ s^{-1}}\right)^{-1}$.

10. In M82, low line intensity ratios of 3.7 ± 0.3 and 58.3 ± 4.0 were found for ^{13}CO/C^{18}O 1-0 and ^{12}CO/C^{18}O 1-0, respectively. This is similar to the values reported previously for NGC 1808 and suggests that the abundance of C^{18}O relative to ^{12}CO is enhanced in both starburst galaxies.

Acknowledgements

I would like to express gratitude to my academic adviser professor Naomasa Nakai for guidance during my study in the doctoral course at the University of Tsukuba.

The research of M82 in high angular resolution would not be possible without the CARMA data provided by the CANON team and their help in data reduction. I wish to thank professor Jin Koda for strong support that led to improvement of this work.

Many thanks go to my colleagues at the university for friendly and working environment that made me feel comfortable and eager to pursue my research.

I am thankful to the staff of the National Astronomical Observatory of Japan, in particular for help during my observations of M82 with the 45-m telescope at Nobeyama Radio Observatory, and NGC 1808 with ASTE 10m at NAOJ headquarters in Tokyo. Also, I am grateful to the staff of the Very Large Array for conducting observations of NGC 1808 at Socorro, USA.

I acknowledge generous financial support (scholarship) from Japan's Ministry of Education, Culture, Sports, Science and Technology during my academic life in Tsukuba.

My deepest thanks go to my father Vladimir, mother Jelica, and sister Svetlana, for encouragement that strengthened me emotionally during the past five years in Japan.

Appendix A

Astronomical constants and units

Information about astronomical constants and units is taken from Draine (2011), Binney & Tremaine (2008), Weinberg (2008), and Bransden & Joachain (2003), giving priority to higher accuracy of measurement.

Following the usual practice in astronomy, the values are expressed in cgs (Gauss) units. Non-standard units (such as debye, D, or parsec, pc) are converted to cgs.

Table A.1: Astronomical constants and units.

Unit	Symbol	Value
age of the universe	t_0	$13.73(16)$ Gyr
astronomical unit	AU	$1.49597871475(30) \times 10^{13}$ cm
Hubble constant	H_0	$70h_7$ km s^{-1} Mpc^{-1}
	h_7	$1.05(5)$
jansky	Jy	10^{-23} erg s^{-1} cm^{-2} Hz^{-1}
parsec	pc	$3.0856775975(6) \times 10^{18}$ cm
		3.2615638 light Julian years
		$648000/\pi$ AU
Solar absolute V-magnitude	M_V	$+4.83$
Solar bolometric luminosity	$L_\odot$	$3.845(8) \times 10^{33}$ erg s^{-1}
Solar mass	$M_\odot$	$1.9884(3) \times 10^{33}$ g
Solar radius	$R_\odot$	$6.9551(3) \times 10^{10}$ cm
year (Julian)		365.25 days
		3.1557600×10^7 s
year (sidereal)		3.15582×10^7 s

Table A.2: Useful conversions.

$\lambda\ [\mu\text{m}] = \frac{300}{\nu\ [\text{THz}]}$
$\text{dB} = 10 \log\left(\frac{P_2}{P_1}\right)$

Standard deviation and r.m.s.

The standard deviation of a variable x is

$$\sigma_x = \sqrt{\langle x^2 \rangle - \langle x \rangle^2}. \tag{A.1}$$

Here, $\langle\rangle$ denotes the expectation value:

$$\langle x \rangle = \int_{-\infty}^{+\infty} x p(x) \mathrm{d}x, \tag{A.2}$$

where $p(x)$ is the probability distribution. On the other hand, the r.m.s. (root-mean-square) value of a variable x is

$$x_{\mathrm{rms}} = \sqrt{\frac{x_1^2 + x_2^2 + \ldots + x_n^2}{n}} = \sqrt{\frac{1}{n}\sum_{i=1}^{n} x_i^2} = \sqrt{\langle x^2 \rangle}. \tag{A.3}$$

Appendix B

Quantum mechanics of diatomic molecules

In this appendix, we introduce the basics of the physics of diatomic molecules. The first part is a brief introduction to definitions and therminology in atomic and molecular spectroscopy, which is followed by the quantum mechanics of vibrational and rotational motion of molecules. For more details, see, e.g., a comprehensive textbook of atomic and molecular physics Bransden & Joachain (2003). A chapter on molecular spectroscopy can be found in Draine (2011), Wilson, Rohlfs & Hüttemeister (2010), Rybicki & Lightman (2004) too, while the vibration and rotation of diatomic molecules is treated in more detail in the classic book on microwave spectroscopy Townes & Schawlow (1955).

B.1 Angular momentum and term symbols

The motion of molecules consists of translational and internal motion. While translational motion is with respect to the surroundings of the molecule, internal motion includes the orbital motion of the electrons and nuclei, their spin, as well as vibration and rotation.

B.1.1 Atoms

In atoms, each electron has orbital angular momentum $\mathbf{l}$ and spin $\mathbf{s}$. The total electronic orbital angular momentum of N electrons given in units $\hbar$ is[1]

$$\mathbf{L} = \sum_{i=1}^{N} \mathbf{L}_i, \tag{B.1}$$

and the total electronic spin angular momentum is

$$\mathbf{S} = \sum_{i=1}^{N} \mathbf{S}_i, \tag{B.2}$$

where the operators of the angular momenta satisfy the eigenvalue equations: $\mathbf{L}^2\psi_l(\theta,\phi) = l(l+1)\hbar^2\psi_l(\theta,\phi)$ and $\mathbf{S}^2\psi_s(\theta,\phi) = s(s+1)\hbar^2\psi_s(\theta,\phi)$ for $l = 0,1,2,...$ and $s = 1/2$. The projections of the angular momenta on an arbitrary axis in space z are $L_z = m_l\hbar$ and $S_z = m_s\hbar$, where $m_l = -l,-l+1,...,0,...l-1,l$ and $m_s = \pm s$.

The total angular momentum of a low-Z atom is given by[2]

$$\mathbf{J} = \mathbf{L} + \mathbf{S}, \tag{B.3}$$

[1] In quantum theory, according to the postulate introduced by N. Bohr, the angular momentum is quantized in descrete units of the Planck constant, i.e., $L = nh/2\pi$, and $\hbar = h/2\pi$ is the natural unit of angular momentum.

[2] We discuss only low-Z atoms here for which the L-S coupling holds.

where $\mathbf{J}^2 = j(j+1)\hbar^2$, $j = 0, 1/2, 1, 3/2, ...$ being the quantum number of the total angular momentum.

In spectroscopy, the magnitudes of total angular momenta can be expressed as J, L and S. For example, if an atom with two electrons (1 and 2) has $m_l(1) = 1$, $m_l(2) = 1$, $s_z(1) = 1/2$ and $s_z(2) = -1/2$, then[3] $L_z = L = 2$ and $S = 0$, so $J = 2$. Alternatively, we may have $s_z(1) = s_z(2)$ in which case $S = 1$ and, e.g., $m_l(1) = 0$ and $m_l(2) = 1$, to satisfy the Pauli exlusion principle which forbids quantum systems with all quantum numbers equal. This yields $L = 1$, and the total angular momentum can take on three values: $J = 0, 1, 2$.

By using these quantities, the electronic states in atoms are usually expressed with term symbols:

$$^{2S+1}L^p_J, \tag{B.4}$$

where $2S+1$ represents *multiplicity*, and p is *parity*. The orbital angular momentum L can take integer values $L = 0, 1, 2, 3, ...$, and each value is denoted with a letter: $L = \mathrm{S, P, D, F, ...}$ The parity p is defined as *even* (no superscript) for $\Pi_i(-1)^{l_i} = 1$, and *odd* (superscript o) for $\Pi_i(-1)^{l_i} = -1$. Note that there are often a number of ways electrons can be arranged in an atom, owing to the fine structure splitting. Therefore, for example, while the ground state of neutral hydrogen atom is ns^1 $^1\mathrm{S}_{1/2}$, the neutral carbon has three fine-structure levels in the ground state, denoted by the following term symbols (with increasing energy): np^2 $^3\mathrm{P}_{0,1,2}$ (ground state), $^1\mathrm{D}_2$ and $^1\mathrm{S}_0$ (first excited states).

In spectroscopy and astronomy, neutral atoms are denoted with a Roman numeral I next to the symbol of the chemical element; for example, the neutral hydrogen H^0 is H I, carbon C^0 is C I, etc. Ions are denoted by numerals II, III, IV, etc. for once-, twice-, trice-, and multi-ionized atoms; for example, the once-ionized carbon C^+ is written as C II. Forbidden transitions are denoted by brackets, e.g., [C II].

B.1.2 Diatomic molecules

Let the total electronic angular momentum of a molecule be denoted $\mathbf{J}$. In general, it is a sum of the orbital angular momentum and the spin angular momentum as given in (B.3). If we fix an axis in space so that it is parallel to the molecular symmetry (internuclear) axis z, we can define projections of the angular momentum on z. The projections of orbital and spin angular momenta are, respectively, $\Lambda \equiv |L_z|$ and $\Sigma \equiv |S_z|$. The projection of the total electronic angular momentum is

$$|\mathbf{J}_z| = J_z\hbar \tag{B.5}$$

$$J_z = \begin{cases} |\Lambda - \Sigma| \\ \Lambda + \Sigma \end{cases} \tag{B.6}$$

The terms of diatomic (heteronuclear)[4] molecular states in spectroscopy are written as

$$^{2\Sigma+1}\mathscr{L}^{(\pm)}_{J_z}. \tag{B.7}$$

Here, $\mathscr{L} = \Sigma, \Pi, \Delta, ...$, for $\Lambda = 0, 1, 2, ...$, in analogy with atomic terms.

In the case of Σ states, a superscript $+$ or $-$ is added to describe whether the wave function is symmetric or antisymmetric under reflection through the planes containing the nuclei. Therefore, for example, the ground state of the CO molecule is $^1\Sigma^+_0$, while for CN it is $^2\Sigma^+_{1/2}$.

[3] Note that the vector summation is $J = L + S$ and $J = |L - S|$, and $L \geq L_z$.

[4] Heteronuclear molecules are molecules composed of different atoms. For example, CO, CS, CN, etc. are heteronuclear, while H_2, N_2, O_2, etc. are called homonuclear.

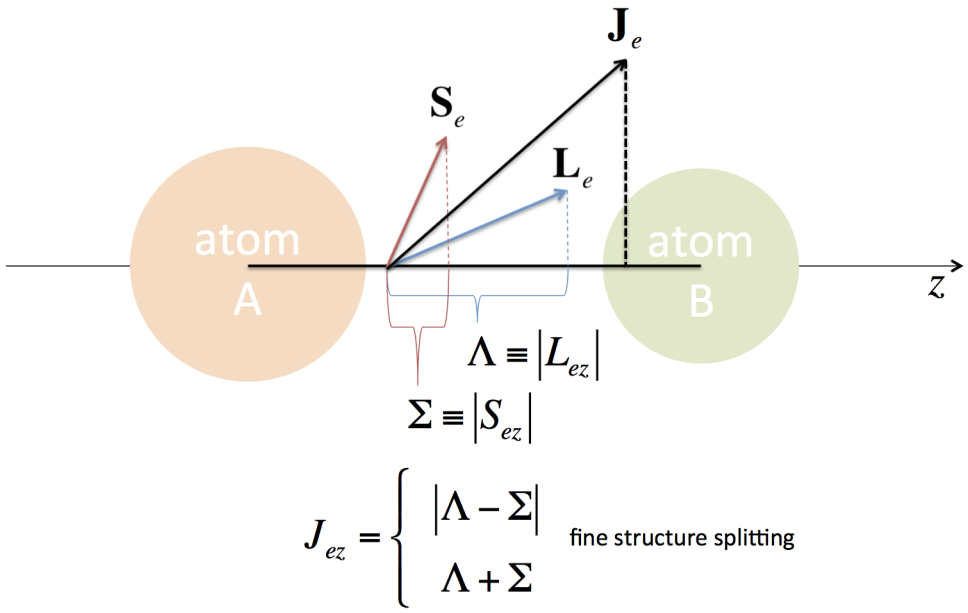

Figure B.1: Electronic angular momentum in a diatomic molecule. The total electronic angular momentum $\mathbf{J}_e$ is a vector sum of the orbital angular momentum $\mathbf{L}_e$ and the spin angular momentum $\mathbf{S}_e$.

The total angular momentum of a diatomic molecule is a sum of all angular momenta: the motion of the nuclei (**N**), orbital angular momentum (**L**), and spin (**S**):

$$\mathbf{J} = \mathbf{N} + \mathbf{L} + \mathbf{S}, \tag{B.8}$$

where the coupling is explained by Hund's cases (see, e.g., p.524 of Bransden & Joachain (2003)). The total angular momentum, electronic plus nuclear, is written as

$$\mathbf{F} = \mathbf{J} + \mathbf{I}, \tag{B.9}$$

where **I** is the nuclear spin. Nuclei with even number of nucleons have $I = 0$, while those with odd number of nucleons can have $I > 0$. For example, the nitrogen nucleus in $^{14}_{7}$CN has $I = 1$, because one proton and one neutron contribute 1/2.

B.2 Rotational and vibrational motion

In addition to the motion of electrons, the nuclei in molecules can rotate and vibrate. In classical mechanics, the angular momentum of rotational motion is expressed by

$$\mathbf{J} = I\omega\mathbf{z}_0, \tag{B.10}$$

where $\mathbf{z}_0$ is the unit vector along the axis of rotation, $\omega = 2\pi/T = 1/\nu$ is the angular velocity, and I is the moment of inertia:

$$I = \int r^2 \mathrm{d}m. \tag{B.11}$$

In the classical quantum theory, represented by N. Bohr and others, the angular momentum was suggested to be quantized in units $\hbar$, namely, $|\mathbf{J}| = J\hbar = Jh/2\pi$. It follows immediately that the frequency of such motion is reversely proportional to I:

$$\nu = \frac{J\hbar}{2I} \propto I^{-1}. \tag{B.12}$$

By calculating the moment of inertia of simple molecules, it is easy to show that the rotational motion falls into the microwave (radio) domain. On the contrary, the electron is much lighter than the nucleus, hence the frequency of motion is much higher.

When discussing the rotation of diatomic molecules, it is customary to introduce a rigid rotor - two nuclei at fixed separation which rotate about the center of mass. Since the electronic motion is much faster than the nuclear, we may assume that the position of nuclei remains constant; this is the *Born-Oppenheimer approximation*.

The time-dependent Schrödinger equation is

$$H\Psi(\mathbf{r},t) = i\hbar\frac{\partial}{\partial t}\Psi(\mathbf{r},t), \tag{B.13}$$

where Ψ is the time-dependent wave function, and

$$H = -\frac{\hbar^2}{2m_\mathrm{r}}\nabla^2 + V(\mathbf{r},t) \tag{B.14}$$

is the Hamiltonian operator. Here, we have used the quanum-mechanical expression for the momentum operator $\mathbf{p} = -i\hbar\nabla$, and m_r is the *reduced mass* of the nuclei m_1 and m_2:

$$m_\mathrm{r} = \frac{m_1 m_2}{m_1 + m_2}. \tag{B.15}$$

The "nabla" squared,

$$\nabla^2 = \frac{\partial^2}{\partial x^2} + \frac{\partial^2}{\partial y^2} + \frac{\partial^2}{\partial z^2}, \tag{B.16}$$

is the Laplacian operator.

Since the potential $V(\mathbf{r})$ does not depend on time, we may write the time-independent Schrödinger equation:

$$H\psi(\mathbf{r}) = E\psi(\mathbf{r}), \tag{B.17}$$

where E is the rotational-vibrational energy of the system. The Schrödinger equation for a molecule with nuclei m_1 and m_2 may be written

$$-\frac{\hbar^2}{2}\left(\frac{1}{m_1}\nabla^2 + \frac{1}{m_2}\nabla^2\right)\psi(\mathbf{r}) = [E - V(\mathbf{r})]\,\psi(\mathbf{r}). \tag{B.18}$$

Expressing ∇^2 in spherical polar coordinates, this becomes

$$\frac{1}{r^2}\frac{\partial}{\partial r}\left(r^2\frac{\partial\psi}{\partial r}\right) + \frac{1}{r^2\sin\theta}\frac{\partial}{\partial\theta}\left(\sin\theta\frac{\partial\psi}{\partial\theta}\right) + \frac{1}{r^2\sin^2\theta}\frac{\partial^2\psi}{\partial\phi^2} + \frac{2m_\mathrm{r}}{\hbar^2}[E - V(r)]\,\psi = 0, \tag{B.19}$$

where $\psi = \psi(r,\theta,\phi)$. The equation may be simplified by separating the variables:

$$\psi = R(r)\Theta(\theta)\Phi(\phi) \tag{B.20}$$

and the radial part becomes

$$\frac{1}{r^2}\frac{\mathrm{d}}{\mathrm{d}r}\left(r^2\frac{\mathrm{d}R}{\mathrm{d}r}\right)+\frac{2m_\mathrm{r}}{\hbar^2}\left[E-V(r)-\frac{\hbar^2 J(J+1)}{2m_\mathrm{r}r^2}\right]R=0, \tag{B.21}$$

where $J(J+1)/r^2$ is the centrifugal contribution to the potential energy. In the above equation, we often use an empirical formula known as the *Morse potential*, for the potential $V(r)$:

$$V(r)=E_\mathrm{d}\left[1-e^{\alpha(r-r_0)}\right]^2, \tag{B.22}$$

where E_d is the molecular dissociation energy, α constant, r_0 the distance at which the nuclei are in equilibrium. For $r>r_0$ the potential is approaching zero, and for $r<r_0$ the internuclear replusion arises. By using the Morse potential it is possible to solve for E. The final result in the first approximation is the sum of the vibrational and rotational motion:

$$E=\hbar\omega\left(v+\frac{1}{2}\right)+BJ(J+1), \tag{B.23}$$

where $v=0,1,2,...$ is the vibrational quantum number, and $J=0,1,2,...$ is the rotational quantum number (see below)[5].

B.3 Rotational energy levels of a rigid rotor

The Hamiltonian of pure rotational motion can be obtained by considering the angular momentum

$$\mathbf{J}=\mathbf{r}\times\mathbf{p}=-i\hbar(\mathbf{r}\times\nabla). \tag{B.24}$$

If $\mathbf{J}^2=J_x^2+J_y^2+J_z^2$, it can be shown that only one component of angular momentum commutes with $\mathbf{J}^2$:

$$[\mathbf{J}^2,J_z]=0, \tag{B.25}$$

the others being $[J_x,J_y]=i\hbar J_z$, $[J_y,J_z]=i\hbar J_x$, and $[J_z,J_x]=i\hbar J_y$. According to the Born's postulate, it means that we can measure simultaneously $\mathbf{J}^2$ and J_z. The two operators in spherical coordinates take the following form:

$$\mathbf{J}^2=-\hbar^2\left[\frac{1}{\sin\theta}\frac{\partial}{\partial\theta}\left(\sin\theta\frac{\partial}{\partial\theta}\right)+\frac{1}{\sin^2\theta}\frac{\partial^2}{\partial^2\phi}\right] \tag{B.26}$$

and

$$J_z=-i\hbar\frac{\partial}{\partial\phi}. \tag{B.27}$$

The eigenvalue equations are:

$$\mathbf{J}^2\psi(\theta,\phi)=J(J+1)\hbar^2\psi(\theta,\phi) \tag{B.28}$$

and

$$J_z\psi(\theta,\phi)=M\hbar\psi(\theta,\phi), \tag{B.29}$$

or

[5]Not to be confused with the total electronic angular momentum discussed above.

$$J_z\Phi(\phi) = M\hbar\Phi(\phi). \tag{B.30}$$

From here, it follows that the normalized wave function for J_z is

$$\Phi_n(\phi) = \frac{1}{\sqrt{2\pi}}\mathrm{e}^{iM\phi} \tag{B.31}$$

The normalization is obtained from the condition

$$\int_0^{2\pi} \Phi(\phi)^*\Phi(\phi)\,d\phi = 1. \tag{B.32}$$

The Hamiltonian for rotational energy is

$$H = \frac{\mathbf{J}^2}{2I}, \tag{B.33}$$

hence

$$-\frac{\hbar^2}{2I}\left[\frac{1}{\sin\theta}\frac{\partial}{\partial\theta}\left(\sin\theta\frac{\partial\psi}{\partial\theta}\right) + \frac{1}{\sin^2\theta}\frac{\partial^2\psi}{\partial\phi^2}\right] = E_J\psi, \tag{B.34}$$

where E_J is the rotational energy. The equation can be separated into

$$\psi(\theta,\phi) = \Theta(\theta)\Phi(\phi). \tag{B.35}$$

Note that

$$\frac{\mathrm{d}^2\Phi}{\mathrm{d}\phi^2} = -M^2\Phi. \tag{B.36}$$

The solutions are obtained for the following energy eigenvalues:

$$E_J = \frac{\hbar^2}{2I}J(J+1), \tag{B.37}$$

where J is the rotational quantum number introduced above, and $|M| \leq J$.

The meaning of the constant M is understood since it follows that the projection of the angular momentum $\mathbf{J}$ on the arbitrary axis in space z is quantized, $J_z = M\hbar$. It should be noted that the components J_x and J_y are not zero even when $J = M$. Their average value is zero because (as can be shown in the vector model of angular momentum), $\mathbf{J}$ precesses around the axis z.

Consider now, for example, two rotational energy levels, E_0 and E_1 corresponding to $J_0 = 0$ and $J_1 = 1$. From the above equations we find that the energy difference is

$$\Delta E = E_1 - E_0 = \frac{\hbar^2}{2I}\left[J_1(J_1+1) - J_0(J_0+1)\right] = \frac{\hbar^2}{I} = 2B. \tag{B.38}$$

Here, B is the rotational constant

$$B = \frac{\hbar^2}{2I}. \tag{B.39}$$

Therefore, the fundamental frequency of rotational motion is

$$\nu_0 = \frac{2B}{h}. \tag{B.40}$$

In the case of $^{12}\mathrm{C}^{16}\mathrm{O}$, we have $\nu_0 = 115.271$ GHz and only $E_\mathrm{r}/k = 5.5$ K, which suggests that CO molecules can undergo excitation to the $J = 1$ level already at low temperatures. Note that because

of the mass-dependence of the frequency through (B.11), the spectral lines of isotopologues, such as ^{12}CO and ^{13}CO will be at different frequencies, which can be easily observed.

The general formula for the rotational energy difference is

$$\Delta E = \frac{\hbar^2}{2I}\left[(J+1)(J+2) - J(J+1)\right] = \frac{\hbar^2}{2I} 2J = 2BJ, \tag{B.41}$$

where J represents the upper state.

The real molecules are not rigid rotors but stretch their bonds while rotating. This introduces additional constants, the so-called stretching constant D. The contribution is small (although not negligible) compared to the rotational constants, but for simplicity it was ignored in this overview.

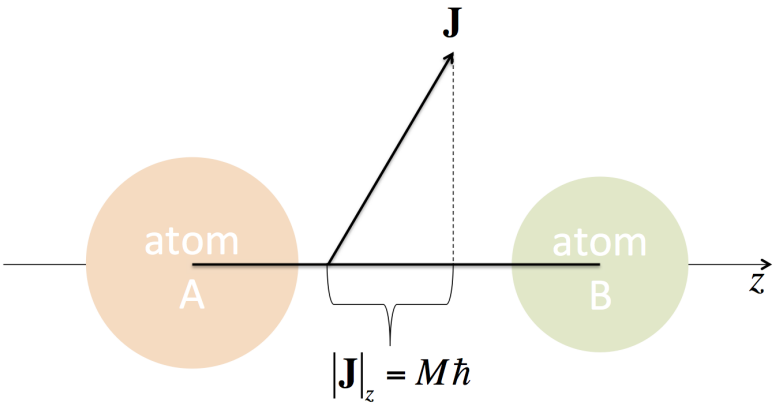

Figure B.2: Quantization of the J_z component of the angular momentum in diatomic molecules.

Table B.1: Properties of the $^{12}C^{16}O$ molecule (from Draine 2011).

Quantity	Value
Electronic configuration of C atom	$1s^2 2s^2 2p^2$
Electronic configuration of O atom	$1s^2 2s^2 2p^4$
Shared p electrons in C	2
Shared p electrons in O	4
Electronic orbital angular momentum L_e	0
Electronic spin angular momentum S_e	0
Ground state term	$^1\Sigma_0^+$
Reduced mass	6.9 amu
Permanent electric dipole moment μ	0.110 D
Fundamental vibrational wavelength	4.6 μm
Fundamental rotational frequency	115.271 GHz

Appendix C

Basics of radiative transfer

C.1 Radiative transfer equation

Consider the *radiative transfer equation*, which relates the effects of absorption and emission on the intensity of electromagnetic radiation I_ν (erg s^{-1} cm^{-2} sr^{-1} Hz^{-1}) during its propagation over distance s:

$$\frac{\mathrm{d}I_\nu}{\mathrm{d}s} = -\alpha_\nu I_\nu + j_\nu. \tag{C.1}$$

Here, α_ν (cm^{-1}) is the *absorption coefficient*, and j_ν (erg cm^{-3} s^{-1} sr^{-1} Hz^{-1}) the emission coefficient. Dividing by α_ν, and defining the *source function* $S_\nu(T) = j_\nu/\alpha_\nu$, we may rewrite the above equation:

$$\frac{1}{\alpha_\nu}\frac{\mathrm{d}I_\nu}{\mathrm{d}s} = -I_\nu + S_\nu. \tag{C.2}$$

If the source is an emitter of thermal radiation, then $S_\nu = B_\nu(T)$, where $B_\nu(T)$ is the *Planck function* of blackbody radiation:

$$B_\nu(T) = \frac{2h\nu^3}{c^2}\frac{1}{\mathrm{e}^{h\nu/kT}-1}. \tag{C.3}$$

Let us define the *optical depth*:

$$\tau_\nu \equiv \int \alpha_\nu \,\mathrm{d}s. \tag{C.4}$$

Equation (C.2) then can be written as

$$\frac{\mathrm{d}I_\nu}{\mathrm{d}\tau_\nu} = -I_\nu + S_\nu. \tag{C.5}$$

In the case of an isothermal medium, the general solution of (C.5) is

$$I_\nu(s) = I_\nu(0)\mathrm{e}^{-\tau_\nu} + S_\nu(1-\mathrm{e}^{-\tau_\nu}). \tag{C.6}$$

We often consider two simplified situations:

1. Optically thin medium $\tau_\nu \to 0$:
$$I_\nu \to \tau_\nu S_\nu. \tag{C.7}$$
2. Optically thick medium $\tau_\nu \to \infty$:
$$I_\nu \to S_\nu. \tag{C.8}$$

Note the difference between the *blackbody* radiation and *thermal* radiation. Blackbody radiation is when $I_\nu = B_\nu(T)$, while thermal radiation is when $S_\nu = B_\nu(T)$. Thermal radiation becomes blackbody radiation when $\tau_\nu \to \infty$.

C.2 Absorption and optical depth

The absorption coefficient, α_ν, was introduced in (C.1). For an emission line with a normalized profile $\int \phi_{21}(\nu)\mathrm{d}\nu = 1$, the absorption coefficient is defined as

$$\alpha_\nu \equiv \frac{h\nu}{4\pi}[n_1 B_{12} - n_2 B_{21}]\phi_{21}(\nu). \tag{C.9}$$

Here, B_{12} (erg^{-1} s^{-1} cm^3) is the *Einstein coefficient* for photon absorption. It is related to the probability for an upward transition from level 1 to level 2 (absorption, or radiative excitation) per unit time in a monochromatic radiation field with energy density u_ν:

$$R_{12} = \frac{cu_\nu}{4\pi} B_{12}. \tag{C.10}$$

B_{21} is the Einstein coefficient for stimulated emission. Introducing A_{21} as the Einstein coefficient for spontanoeus emission from level 2 to level 1 (in unit s^{-1}), the radiative transfer equation can now be fully written as

$$\frac{\mathrm{d}I_\nu}{\mathrm{d}s} = \frac{h\nu}{4\pi}\left[n_2 A_{21} - (n_1 B_{12} - n_2 B_{21})I_\nu\right]. \tag{C.11}$$

In the case of electric dipole transitions, the stimulated emission coefficient is

$$A_{21} = \frac{64\pi^4}{3hc^3}\nu^3 |\mu_{21}|^2, \tag{C.12}$$

where, for emission arising from rotational transitions of diatomic molecules ($\Delta J = 1$, $J \to J-1$),

$$|\mu_J|^2 = \mu^2 \frac{J}{2J+1} \tag{C.13}$$

is the *mean electric dipole moment* of the oscillator in the transition. μ is the permanent electric dipole moment of the molecule, often expressed in units debye (D). ^{12}CO has a very small dipole moment of $\mu(^{12}\mathrm{CO}) = 0.11$ D, while, for comparison, $\mu(\mathrm{HCN}) = 2.98$ D. The *selection rules* for the electric dipole rotational transitions for diatomic molecules are $\Delta J = \pm 1$. Note that the probability of radiative deexcitation, expressed via A_{21} is *proportional to the mean electric dipole moment*. Consequently, molecules with large μ undergo rapid radiative (spontaneous) deexcitation. Also, because $A_{21} \propto \nu^3$, the probability of spontaneous emission increases with frequency.

The relation between the Einstein coefficients is given by

$$A_{21} = \frac{2h\nu^3}{c^2} B_{21} \tag{C.14}$$

and

$$g_1 B_{12} = g_2 B_{21}. \tag{C.15}$$

Assume that the medium is in local thermodynamic equilibrium (LTE) at temperature T. The populations of levels are determined by collisions and the Boltzmann equation (D.6) holds. From (C.9), (C.14) and (C.15):

$$\alpha_\nu = \frac{h\nu}{4\pi}\left[n_1\frac{g_2}{g_1}B_{21} - n_2\frac{c^2}{2h\nu^3}A_{21}\right]\phi_{21}(\nu) = \frac{h\nu}{4\pi}\left[n_1\frac{g_2}{g_1}\frac{c^2}{2h\nu^3}A_{21} - n_2\frac{c^2}{2h\nu^3}A_{21}\right]\phi_{21}(\nu), \quad \text{(C.16)}$$

hence

$$\alpha_\nu = \frac{c^2 n_1}{8\pi\nu^2}\frac{g_2}{g_1}A_{21}\left[1 - \frac{g_1 n_2}{g_2 n_1}\right]\phi_{21}(\nu). \quad \text{(C.17)}$$

Replacing Boltzmann's equation into (C.17) we find

$$\alpha_\nu = \frac{c^2 n_1}{8\pi\nu^2}\frac{g_2}{g_1}A_{21}\left[1 - \exp\left(-\frac{h\nu}{kT_{\rm ex}}\right)\right]\phi_{21}(\nu). \quad \text{(C.18)}$$

In the Rayleigh-Jeans approximation (hereafter RJ, see Appendix D),

$$\alpha_\nu = \frac{c^2 n_1}{8\pi\nu^2}\frac{g_2}{g_1}A_{21}\frac{h\nu}{kT_{\rm ex}}\phi_{21}(\nu). \quad \text{(C.19)}$$

Therefore, the optical depth in the RJ approximation is

$$\tau_\nu = \int \frac{c^2 n_1}{8\pi\nu^2}\frac{g_2}{g_1}A_{21}\frac{h\nu}{kT_{\rm ex}}\phi_{21}(\nu)\mathrm{d}s, \quad \text{(C.20)}$$

or

$$\tau_\nu = \frac{c^2}{8\pi\nu^2}\frac{g_2}{g_1}A_{21}\frac{h\nu}{kT_{\rm ex}}N_1\phi_{21}(\nu), \quad \text{(C.21)}$$

where $N_1 = \int n_1\, ds$ is the *column density* of level 1. If $\Delta\nu$ is the width of the line at half maximum, then

$$\phi_{21}\Delta\nu \approx 1 \quad \text{(C.22)}$$

and

$$\tau_\nu \approx \frac{c^2}{8\pi\nu}\frac{g_2}{g_1}A_{21}\frac{h}{kT_{\rm ex}}\frac{N_1}{\Delta\nu}. \quad \text{(C.23)}$$

Since the relation between frequency and velocity is

$$\frac{c}{\Delta v} = \frac{\nu}{\Delta\nu}, \quad \text{(C.24)}$$

the above equation be can written as

$$\tau_\nu \approx \frac{c^3}{8\pi\nu^2}\frac{g_2}{g_1}A_{21}\frac{h}{kT_{\rm ex}}\frac{N_1}{\Delta v}. \quad \text{(C.25)}$$

From equations (C.12) and (C.23),

$$\tau_\nu = \frac{c^2}{8\pi\nu}\frac{g_2}{g_1}\frac{64\pi^4}{3hc^3}\nu^3|\mu_{21}|^2\frac{h}{kT_{\rm ex}}\frac{N_1}{\Delta\nu} = \frac{8\pi^3\nu^2}{3kc}\frac{g_2}{g_1}|\mu_{21}|^2\frac{N_1}{T_{\rm ex}\Delta\nu}. \quad \text{(C.26)}$$

When there is no emission, we see from equation (C.1) that

$$I_\nu(s) = I_\nu(0)\mathrm{e}^{-\tau_\nu}. \quad \text{(C.27)}$$

Therefore, the probability of an average photon to leave the medium without being absorbed is simply $\mathrm{e}^{-\tau_\nu}$. Calculating the expectation value of optical depth,

$$\langle \tau_\nu \rangle \equiv \int_0^\infty \tau_\nu \mathrm{e}^{-\tau_\nu} \, \mathrm{d}\tau_\nu = 1, \tag{C.28}$$

tells us that the mean depth a photon travels is $\tau_\nu = 1$. From the definition of τ_ν, we can express the mean free path $\langle s \rangle$,

$$\langle \tau_\nu \rangle = \alpha_\nu \langle s \rangle = 1. \tag{C.29}$$

The mean free path is then

$$\langle s \rangle = \frac{1}{\alpha_\nu} = \frac{1}{n\sigma}, \tag{C.30}$$

where n is the number density and σ is the cross section of absorption.

Appendix D

Quantities in radio astronomy

D.1 Definitions

Astronomical measurements are often performed by comparing the power of received radiation from the source with that from a nearby emission-free region (background), and the result can be expressed as

$$\Delta I_\nu(s) = I_\nu(s) - I_\nu(0) = [S_\nu - I_\nu(0)]\left(1 - \mathrm{e}^{-\tau_\nu}\right). \tag{D.1}$$

At low frequencies ($h\nu/kT \ll 1$), the Planck law can be simplifed as the *Rayleigh-Jeans approximation* (RJ):

$$B_\nu^{\mathrm{RJ}}(T) \approx \frac{2h\nu^3}{c^2}\frac{1}{1+h\nu/kT-1} = \frac{2k\nu^2}{c^2}T. \tag{D.2}$$

For convenience, radio astronomers often express the radiation intensity in terms of temperature. From (D.2), the intensity is directly proportional to the *brightness temperature*, T_b,

$$I_\nu = \frac{2k\nu^2}{c^2}T_\mathrm{b}. \tag{D.3}$$

The brightness temperature becomes the kinetic temperature T when the medium is optically thick and emits radiation as a blackbody. In general, T_b is simply the temperature a source would have if its observed spectrum were generated by a blackbody. In situations when the RJ conditions are not met, such as at high frequencies (e.g., the 115-GHz CO(1-0) line emission from 10-K cold molecular clouds) or non-thermal emission, (D.3) can be used if the relevant "temperature" is understood to be different from the physical temperature T. This temperature is referred to as the *radiation temperature*, $J_\nu(T)$:

$$J_\nu(T) = \frac{c^2}{2k\nu^2}I_\nu = \frac{h\nu}{k}\frac{1}{\mathrm{e}^{h\nu/kT}-1}. \tag{D.4}$$

Substituting the quantities with their temperature equivalents in the RJ approximation in (D.1), we get an expression for the brightness temperature:

$$T_\mathrm{b} = [J_\nu(T_\mathrm{ex}) - J_\nu(T_\mathrm{bg})](1 - \mathrm{e}^{-\tau_\nu}). \tag{D.5}$$

The 2.73 K microwave background emission is taken to be $J_\nu(T_\mathrm{bg}) \to I_\nu(0)$, and emission $J_\nu(T_\mathrm{ex})$ arises from the source with the *excitation temperature* T_ex. The excitation temperature is defined by the *Boltzmann law*:

$$\frac{n_2}{n_1} = \frac{g_2}{g_1} \mathrm{e}^{-(E_2-E_1)/kT_{\mathrm{ex}}}, \tag{D.6}$$

where n_1 and n_2 are the densities of the energy levels E_1 and E_2 in a 2-level system, and g_1 and g_2 are the statistical weights (number of possible states within the same level).

The exication temperature is usually different from the kinetic temperature, T_{k}. The latter is defined for a system where particles have speeds given by the Maxwell-Boltzmann distribution function. It can be shown (see Wilson, Rohlfs & Hüttemeister 2010) that $T_{\mathrm{ex}} \to T_{\mathrm{b}}$ if radiation dominates in the system; if collisions dominate, then $T_{\mathrm{k}} \to T_{\mathrm{b}}$. In thermodynamic equilibrium, $T_{\mathrm{ex}} = T_{\mathrm{k}}$.

Radio telescopes measure a quantity which is referred to as the *antenna temperature*, T_{A}^*, corrected for atmospheric effects and losses in wire transmission. The fraction of the received power which is in the main beam of the telescope is the *main beam brightness temperature*:

$$T_{\mathrm{mb}} \equiv \frac{T_{\mathrm{A}}^*}{\eta_{\mathrm{mb}}}, \tag{D.7}$$

where η_{mb} is the main beam efficiency. If the size of the observed source is known, then it is possible to derive the brightness temperature

$$T_{\mathrm{b}} = \frac{T_{\mathrm{mb}}}{f_{\mathrm{b}}}, \tag{D.8}$$

where f_{b} is the beam filling factor. The beam filling factor is defined as

$$f_{\mathrm{b}} \equiv \frac{\Omega_{\mathrm{s}}}{\Omega_{\mathrm{s}} * \Omega_{\mathrm{b}}}, \tag{D.9}$$

where Ω_{s} is the solid angle defined by the source, and Ω_{b} is the beam size of the telescope. $*$ denotes convolution. If the source and the beam have the shape of a Gaussian function, then

$$f_{\mathrm{b}} = \frac{\theta_{\mathrm{s}}^2}{\theta_{\mathrm{s}}^2 + \theta_{\mathrm{b}}^2}, \tag{D.10}$$

because the covolution of two Gaussian functions is another Gaussian with the standard deviation of the product equal to $\sigma^2 = \sigma_{\mathrm{s}}^2 + \sigma_{\mathrm{b}}^2$. Here, θ_{s} is the angular diameter of the source, and θ_{b} that of the main beam of the telescope. When the source is much smaller than the beam, $f_{\mathrm{b}} = (\theta_{\mathrm{s}}/\theta_{\mathrm{b}})^2$. Finally, the radiation temperature above can be rewritten as the main beam temperature

$$T_{\mathrm{mb}} = f_{\mathrm{b}}[J_\nu(T_{\mathrm{ex}}) - J_\nu(T_{\mathrm{bg}})](1 - \mathrm{e}^{-\tau_\nu}). \tag{D.11}$$

D.2 Temperature-to-flux conversion

The conversion between the brightness temperature and the flux density S_ν[1] can be found from the definition of the flux density

$$S_\nu = \int_{\Omega_{\mathrm{s}}} \cos\theta \, I_\nu \mathrm{d}\Omega. \tag{D.12}$$

It can be written as

$$S_\nu = I_\nu \Omega_{\mathrm{s}} = \frac{2k\nu^2}{c^2} T_{\mathrm{b}} \Omega_{\mathrm{s}}. \tag{D.13}$$

[1]Note that the flux density and source function are written with the same letter S_ν throughout this work.

Combining (D.12) with (D.8) and (D.9) we find

$$S_\nu = \frac{2k\nu^2}{c^2} T_{\rm mb} \frac{\Omega_{\rm s} * \Omega_{\rm b}}{\Omega_{\rm s}} \Omega_{\rm s} = \frac{2k\nu^2}{c^2} T_{\rm mb} \left(\Omega_{\rm s} * \Omega_{\rm b}\right). \tag{D.14}$$

For a point source,

$$S_\nu = \frac{2k\nu^2}{c^2} T_{\rm mb} \Omega_{\rm b}. \tag{D.15}$$

For sources of known finite size, the "Jy-per-K" conversion factor is (D.13)

$$S_\nu / T_{\rm b} = \frac{2k\nu^2}{c^2} \Omega_{\rm s}. \tag{D.16}$$

D.3 Data cube, intensity and its moments

In observational astronomy, data obtained at a telescope contain spectral information in the form of a function of three variables - the intensity as a function of position (x, y) and the observed velocity (or frequency), usually corrected for the Doppler effect. A map (image) is created when the intensity is displayed on a 2-dimensional field, in conventional astronomical coordinates such as the equatorial (α, δ) or galactic (l, b) coordinates. Hence, each pixel of the map contains information on intensity as a function of velocity. An equivalent radio-astronomical quantity has been introduced elsewhere in this document as the *integrated intensity* (the $0^{\rm th}$ moment),

$$I \equiv \int T \, {\rm d}v \; [{\rm K \; km \; s^{-1}}]. \tag{D.17}$$

Frequently, we display the data as a velocity map to infer the line-of-sight component of the velocity of the source. One such quantity is the intensity-weighted *velocity field* (or the $1^{\rm st}$ moment of I), defined as

$$v_{\rm mom1} \equiv \frac{\int vT \, {\rm d}v}{\int T \, {\rm d}v} \; [{\rm km \; s^{-1}}]. \tag{D.18}$$

Additionally, we may define the $2^{\rm nd}$ moment, which simply gives a distribution of the Gaussian sigma (standard deviation), i.e., the intensity-weighted *velocity dispersion*, if the line profile is Gaussian. It is defined as

$$\sigma^2_{\rm mom2} \equiv \frac{\int T \left(v - v_{\rm mom1}\right)^2 {\rm d}v}{\int T \, {\rm d}v} \; [{\rm km \; s^{-1}}]. \tag{D.19}$$

Appendix E

CO as a tracer of molecular gas mass

Consider a uniform, spherical molecular cloud with radius R and mass $M(R)$. For a virialized cloud, i.e., one that is gravitationally bound, we may write that at a certain radius the centripetal force is equal to the gravitational force that holds the cloud particles together,

$$\langle v^2 \rangle = G\frac{M}{R}. \tag{E.1}$$

Define an observational quantity, the CO $(J = 1 \rightarrow 0)$ intensity, as the brightness temperature integrated over the line profile (velocity range Δv),

$$I_{\rm CO} \equiv \int T_{\rm b}\, {\rm d}v. \tag{E.2}$$

The CO luminosity is simply the integrated intensity over the solid angle extending over the source:

$$L_{\rm CO} \equiv D^2 \int I_{\rm CO}\, {\rm d}\Omega, \tag{E.3}$$

where D is the distance to the cloud. In the case of a spherical and uniform cloud,

$$L_{\rm CO} = \pi R^2 T_{\rm b} \Delta v. \tag{E.4}$$

Combining (E.1) and (E.4) we obtain

$$L_{\rm CO} = \pi R^2 T_{\rm b} \sqrt{\frac{GM}{R}} = \pi R^{3/2} T_{\rm b} \sqrt{GM}. \tag{E.5}$$

Assuming spherical shape, we can use $M = 4\rho R^3 \pi/3$ and

$$R^{3/2} = \sqrt{\frac{3M}{4\pi\rho}}. \tag{E.6}$$

Substituting (E.6) in (E.5) we find

$$L_{\rm CO} = \pi T_{\rm b} M \sqrt{\frac{3G}{4\pi\rho}}. \tag{E.7}$$

This can be rewritten as

$$M = \sqrt{\frac{4\pi\rho}{3G}} \frac{L_{\rm CO}}{\pi T_{\rm b}}. \tag{E.8}$$

Therefore, we conclude that

$$M \propto \frac{\sqrt{\rho}}{T_{\rm b}} L_{\rm CO}. \tag{E.9}$$

In words, the mass of the cloud is expected to be directly proportional to the CO luminosity. In the case of collisionally excited CO in LTE, as it is usually the case, the kinetic temperature $T_{\rm k} \rightarrow T_{\rm b}$. Apparently, if $\sqrt{\rho}/T_{\rm b}$ does not change from one cloud to another, there is a constant of proportionality which we call the *conversion factor*, $X_{\rm CO}$, between the CO luminosity and the H_2 mass (e.g., Bolatto et al. 2013a). In terms of measured quantities, it is usually expressed as

$$N({\rm H_2}) = X_{\rm CO} I_{\rm CO}. \tag{E.10}$$

Here, $N(H_2)$ is the column density of molecular hydrogen. Note that the conversion factor is often expressed in mass surface density units (the $\alpha_{\rm CO}$ factor). If the Galactic value is

$$X_{\rm CO} = 2 \times 10^{20}\ {\rm cm^{-2}}\ \left({\rm K\ km\ s^{-1}}\right)^{-1}, \tag{E.11}$$

it corresponds to

$$\alpha_{\rm CO} = 4.35\ M_\odot\ {\rm pc^{-2}}\ \left({\rm K\ km\ s^{-1}}\right)^{-1}. \tag{E.12}$$

Therefore, $X_{\rm CO}$ includes only H_2 mass, while $\alpha_{\rm CO}$ includes the *total mass of molecular gas* (H_2 + He, corrected for a factor 1.36). Now equation (E.10) becomes

$$\Sigma({\rm H_2}) = \alpha_{\rm CO} I_{\rm CO}, \tag{E.13}$$

where $\Sigma(H_2)$ is the total mass surface density of molecular gas.

Appendix F

Line width

The random velocity of a particle in an isothermal gas is

$$\langle v^2 \rangle = \langle v_x^2 \rangle + \langle v_y^2 \rangle + \langle v_z^2 \rangle = 3\langle v_x^2 \rangle. \tag{F.1}$$

The shape of molecular spectral lines is mostly dominated by thermal motion (i.e., collisions and Doppler effect) and turbulence. The former is well represented by a Gaussian function:

$$f(v_x) = A \exp\left(-\frac{v_x^2}{2\sigma^2}\right), \tag{F.2}$$

where σ is the standard deviation, and A is the maximum value of the function. The random velocity is related to σ by

$$\langle v_x^2 \rangle = \frac{\int_0^\infty v_x^2 \exp(v_x^2/2\sigma^2)\,\mathrm{d}v_x}{\int_0^\infty \exp(v_x^2/2\sigma^2)\,\mathrm{d}v_x} = \sigma^2. \tag{F.3}$$

This is obtained by solving the following integrals:

$$\int_0^\infty x^2 \mathrm{e}^{-ax^2}\,\mathrm{d}x = \frac{1}{4}\sqrt{\frac{\pi}{a^3}} \tag{F.4}$$

and

$$\int_0^\infty \mathrm{e}^{-ax^2}\,\mathrm{d}x = \frac{1}{2}\sqrt{\frac{\pi}{a}} \tag{F.5}$$

for $a > 0$.

The 1-dimensional *full-width at half-maximum* intensity of the line, FWHM $= 2\Delta v_x$, can be obtained from (F.2) as

$$\frac{1}{2} = \exp\left[-\frac{(\Delta v_x)^2}{2\sigma^2}\right] = \exp\left(-\frac{\mathrm{FWHM}^2}{8\sigma^2}\right). \tag{F.6}$$

It follows that

$$\mathrm{FWHM} = \sigma\sqrt{8\ln 2} = 2\sigma\sqrt{2\ln 2}. \tag{F.7}$$

From (F.1) and (F.3) we find

$$\mathrm{FWHM} = \sqrt{\frac{8\langle v^2 \rangle \ln 2}{3}} \tag{F.8}$$

and

$$\langle v^2 \rangle^{1/2} = \mathrm{FWHM} \sqrt{\frac{3}{8 \ln 2}} \tag{F.9}$$

is the 3-dimensional velocity.

Appendix G

Velocity frames and definitions

In observational astronomy, it is customary to define the velocity of the observed source relative to a reference frame. In extragalactic astronomy, where sources are significantly far from the Solar system, the redshift plays an important role. In addition, the motion of the Sun relative to the Galactic center must be taken into account. In the table below, we list the most commonly used velocity frames and definitions. The frames are barycentric, heliocentric, galactocentric, and those with respect to the local standard of rest (LSR), the Local Group, and the cosmic microwave background (CMB). For more details, see www.gb.nrao.edu/∼fghigo/gbtdoc/doppler.html and the references therein.

Table G.1: Velocity frames.

Frame	Reference position	Motion wrt barycenter (J2000.0)
Barycentric	barycenter of the Solar system	JPL Ephemeris DE403
Heliocentric	center of the Sun	JPL Ephemeris DE403
LSR (k)	kinematical local standard of rest	Solar motion 20.0 km s^{-1} towards $18^h03m50.24^s, +30^0 00' 16.8''$
LSR (d)	dynamical local standard of rest	Solar motion 16.55 km s^{-1} $(+9, +12, +7)$ km s^{-1} in (l, b) coordinates towards $17^h49^m58.66^s, +28^0 07' 03.92''$
Galactocentric	dynamical center of the Galaxy	dynamical LSR motion 254 km s^{-1} towards $l = 90^0, b = 0^0$ 266.2 km s^{-1} towards $20^h57^m32.57^s, +47^0 53' 46.0''$
Local Group	mean motion of the LG galaxies	Solar motion 306 km s^{-1} towards $l = 99^0, b = -4^0$ 306 km s^{-1} towards $22^h10^m24.03^s, +51^0 13' 54.19''$
CMB background	CMB dipole anisotropy (WMAP)	Solar motion 368.0 km s^{-1} towards $l = 263.85^0, b = 48.25^0$ 368.0 km s^{-1} towards $11^h11^m22.92^s, -06^0 52' 57.02''$

The relativistic relation between frequency and velocity is

$$\nu = \nu_0 \frac{\sqrt{1-\beta^2}}{1+\mathbf{V}\cdot\mathbf{v}_0/c}, \tag{G.1}$$

Table G.2: Velocity definitions.

Definition	Formula	Conversion to frequency
Radio	$V = c(\nu_0 - \nu)/\nu_0$	$\nu(V) = \nu_0(1-\beta)$
Optical	$V = c(\nu_0 - \nu)/\nu$	$\nu(V) = \nu_0(1+\beta)^{-1}$
Relativistic	$V = c(\nu_0^2 - \nu^2)/(\nu_0^2 + \nu^2)$	$\nu(V) = \nu_0(1-\beta^2)^{1/2}/(1+\beta)$
Redshift	$z = (\nu_0 - \nu)/\nu$	$\nu = \nu_0(1+z)^{-1}$

Notes: $\beta = V/c$

where $\beta \equiv V/c$, c is the speed of light, $\mathbf{v}_0$ the unit vector along the line of sight, $\mathbf{V}$ the velocity of the source moving with respect to the observer, and V its magnitude. In the case of radial motion, $\mathbf{V} \cdot \mathbf{v}_0 = V$, and this V is given in the table.

The non-relativistic radial velocity of a source is conventionally defined as:

$$V = cz, \tag{G.2}$$

where z is the redshift, which takes on positive values for receding sources and negative values for approaching sources.

Appendix H

MIRIAD (Multi-channel Image Reconstruction, Image Analysis and Display)

See spectrum of the central position of the image (BLC=0,0 and TRC=0,0)

imspec in=m82.map region="arcsec,box(0,0,0,0)" log=spectrum.txt options=noheader

With options=noheader we do not plot the header in the output text file.

Get statistics

imstat in=m82.map region="arcsec,box(0,0,0,0)"

Convolve to another resolution

convol map=m82.map out=m82.cnv fwhm=14 scale=4.5e-3 option=final

Warning: Not a good idea to apply convol to masked images.

Here, the scale factor makes sure that flux is conserved and given in Jy beam^{-1}. It is calculated from

$$f = 1/(1.13309(B/p)^2) \tag{H.1}$$

where B telescope beam, p pixel size.

With option=final fwhm= is the resolution *after* convolving.

Perform mathematical operations (add, subtract, multiply, or divide) on images

maths exp="m82.map1/m82.map2" out=map82.map12

This task is useful to make ratio maps of different data cubes.

Make a position-velocity map

velplot in=m82.map device=/xs log=data.log region="relpix,box(-70,-70,70,70)"

If region is omitted, then the entire image is plotted. Further details:
http://www.atnf.csiro.au/computing/software/miriad/userguide/node170.html

1. Example 1:

   Selection (type 1st character) :p

   >Enter cut number, position and angle (n,x,y,pa): 1,0,0,70

   One plot at (X,Y)=(0",0") and P.A.=70 deg.

2. Example 2:

   Selection (type 1st character) :p

   >Enter cut number, position and angle (n,x,y,pa): 1,-5,-5,70

   One plot at (X,Y)=(+5",-5") and P.A.=70 deg.

Set options (contours, units, scale, etc.) by:
Selection (type 1st character) :o

Make integrated intensity map with selected velocity range (channels)

Channel maps are useful to investigate emission within selected velocity range. In general, we use the command moment with region set to "kms" and two types of boxes: spatial and velocity. Below is an example.

moment in=map.mp out=mapch.mom0 mom=0 "region=kms,boxes(0,0,751,721)(124.48,184.44)" Here, the first box defines the bottom left corner and top right corner of the map, and the second box defines the velocity range in km s^{-1}. So the format is (x1,y1,x2,y2)(v1,v2).

Mask individual regions in maps

We can use the task cgcurs to make masks on arbitrary regions in maps. For example, by executing

cgcurs in=map.mp range=0,0.2 device=/xs options=region,3value nxy=1,1 a map will open in a new window where we can draw arbitrary polygons. For a data cube, it is possible to draw polygons in every channel individually. As a result, a new data set under the name "cgcurs.region" is created. To make a sub-image with the mask changes, execute

imsub in=map.mp out=map.mask region=@cgcurs.region The region option inputs the cgcurs data. Then, the data can be processed as before: for example, by using maths, and later moment and fits to export.

The cgcurs task is very useful in the cleaning process when the sidelobes are strong. By masking each channel in regions that resemble the telescope beam pattern, image fidelity can be improved significantly. That technique was implemented here in deriving maps in C+D CARMA configurations.

Make integrated intensity maps of regions masked using a box

moment in=map.mp out=map.region mom=0 "region=arcsec,boxes(-30,-15,30,15)"

Rotate data cube

regrid in=map.mp out=map.regrid rotate=15 The map is rotated to P.A. $= 75^0$.

Crop outside selected region

maths exp=map.mp out=map.crop "region=arcsec,box(-30,-15,30,15)" Crop outside the region with BLC=-30,-15 and TRC=+30,+15.

Make PV map of the total cube

reorder in=map.mp out=map.reorder mode="132" "132" is the order of axes. In this setup we make a PV map parallel to the major axis of the map.

Appendix I

Initial mass function

The initial mass function (IMF) of stellar populations was first derived by E. Salpeter (Salpeter 1955). It is defined as

$$\xi(\log m) = \frac{\mathrm{d}N}{\mathrm{d}\log m} = Cm^{-\Gamma}. \tag{I.1}$$

Equivalently,

$$\frac{\mathrm{d}N}{\mathrm{d}m} = C_m m^{-\alpha} \tag{I.2}$$

is the "mass spectrum" where $\alpha \equiv \Gamma + 1$ and C, C_m some constants. Salpeter proposed that the exponent was $\alpha = 2.35$ ($\Gamma = 1.35$):

$$\frac{\mathrm{d}N}{\mathrm{d}m} \propto m^{-2.35}. \tag{I.3}$$

This equation is very useful because it yields the total mass of stars. If m_{low} is the lowest stellar mass (low "cutoff" of the IMF) and m_{up} is the highest, the total stellar mass is simply

$$M_* = C_m \int_{m_{\mathrm{low}}}^{m_{\mathrm{up}}} m^{1-\alpha}\,\mathrm{d}m'. \tag{I.4}$$

This can be easily evaluated for $\alpha = 2.35$:

$$M_* = \frac{1}{0.35} C_m \left(m_{\mathrm{low}}^{-0.35} - m_{\mathrm{up}}^{-0.35} \right). \tag{I.5}$$

If we assume that luminosity and mass are related as

$$L = C_l m^3, \tag{I.6}$$

where C_l is a constant, then the total luminosity can be evaluated as

$$L_* = C_m C_l \int_{m_{\mathrm{low}}}^{m_{\mathrm{up}}} m^{3-\alpha}\mathrm{d}m'. \tag{I.7}$$

The result for $\alpha = 2.35$ is

$$L_* = \frac{1}{1.65} C_m C_l \left(m_{\mathrm{up}}^{1.65} - m_{\mathrm{low}}^{1.65} \right). \tag{I.8}$$

Note two main results: (1) the total stellar mass M_* is dominated by the low-mass stars, and (2) the total stellar luminosity L_* is dominated by the most massive stars. Usually one takes $m_{\rm up} = 100\,M_\odot$ and $m_{\rm low} = (0.1{-}1)\,M_\odot$.

Bibliography

Aalto, S., Booth, R. S., Black, J. H., Koribalski, B., & Wielebinski, R. 1994, A&A, 286, 365

Aalto, S., Booth, R. S., Black, J. H., & Johansson, L. E. B. 1995, A&A, 300, 369

Achtermann, J. M. & Lacy, J. H. 1995, ApJ, 439, 163

Aladro, R., Martín-Pintado, J., Martín, S., Mauersberger, R., & Bayet, E. 2011, A&A, 525, A89

Aladro, R., Martín, S., Martín-Pintado, J., Mauersberger, R., Henkel, C., Ocaña Flaquer, B., & Amo-Baladrón, M.A. 2011, A&A, 535, A84

Appleton, P. N., Davies, R. D., & Stephenson, R. J. 1981, MNRAS, 195, 327

Awaki, H., Ueno, S., Koyama, K., Tsuru, T., & Iwasawa, K. 1996, PASJ, 48, 409

Baan, W. A., Henkel, C., Loenen, A. F., Baudry, A., & Wiklind, T. 2008, A&A, 477, 747

Binney, J. & Tremaine, S., *Galactic dynamics*, 2008, Princeton University Press

Bolatto, A., Wolfire, M., & Leroy, A. 2013, ARA&A, 51, 207

Bolatto, A., et al. 2013, Nature, 499, 450

Bouwens, R. J., et al. 2011, Nature, 469, 504

Bransden, B. H. & Joachain, C. J., *Physics of atoms and molecules*, second edition, 2003, New York: Prentice Hall

Bregman, J. N., Schulman, E., & Tomisaka, K. 1995, ApJ, 439, 155

Bruzual, G. & Charlot, S. 2003, MNRAS, 344, 1000

Burbidge, E. M. & Burbidge, G. R. 1968, ApJ, 151, 99

Cappellari, M., et al. 2013, MNRAS, 432, 1862

Chevalier, R. A. & Clegg, A. W. 1985, Nature, 317, 44

Chynoweth, K. M., Langston, G. I., Yun, M. S., Lockman, F. J., Rubin, K. H. R., & Scoles, S.A. 2008, AJ, 135, 1983

Claude, S. M. X., Cunningham, C. T., Kerr, A. R., & Pan, S.-K. 2000, ALMA Memo 316

Coker, C. T., Thompson, T. A., & Martini, P. 2013, ApJ, 778, 79

Collison, P. M., Saikia, D. J., Pedlar, A., Axon, D. J., & Unger, S.W. 1994, MNRAS, 268, 203

Costagliola, F., et al. 2011, A&A, 528, A30

Cottrell, G. A. 1977, MNRAS, 178, 577

Creasey, P., Theuns, T., & Bower, R. G. 2013, MNRAS, 429, 1922

Dahlem, M., Aalto, S., Klein, U., Booth, R., Mebold, U., Wielebinski, R., & Lesch, H. 1990, A&A, 240, 237

Dame, T. M., Hartmann, D., & Thaddeus, P. 2001, ApJ, 547, 792

de Vaucouleurs, G., de Vaucouleurs, A., Corwin, H. G. Jr., Buta, R. J., Paturel, G., & Fouque, P. 1991, Third Reference Catalogue of Bright Galaxies, version 3.9 (New York: Springer-Verlag)

Di Mateo, T., Springel, V., & Hernquist, L. 2005, Nature, 433, 604

Doane, J.S. & Mathews, W. G. 1993, ApJ, 419, 573

Downes, D., & Solomon, P. M. 1998, ApJ, 507

Draine, B. T., *Physics of the interstellar and intergalactic medium*, 2011, Princeton University Press

Draine, B. T. & Bertoldi, F. 1996, ApJ, 468, 269

Efstathiou, G. 2000, MNRAS, 317, 697

Elmegreen, B. G. 1989, ApJ, 338, 178

Emerson, D. T., & Gräve, R. 1988, A&A, 190, 353

Engelbracht, C. W., et al. 2006, ApJ, 642, L127

Faber, S. M. & Jackson, R. E. 1976, ApJ, 204, 668

Fan, X. 2012, RAA, 12, 865

Ferrarese, L. & Merritt, D. 2000, ApJ, 539, L9

Federman, S. R., Lambert, D. L., Sheffer, Y., Cardelli, J.A., Andersson, B-G., van Dishoeck, E. F., & Zsargo, J. 2003, ApJ, 591, 986

Fenech, D., Beswick, R., Muxlow, T. W. B., Pedlar, A., & Argo, M.K. 2010, MNRAS, 408, 607

Forbes, D. A., Boisson, C., & Ward, M. J. 1992, MNRAS, 259, 293

Förster Schreiber, N. M., Genzel, R., & Lutz, D. 2003, ApJ, 599, 193

Fukui, Y. & Kawamura, A. 2010, ARA&A, 48, 547

Galliano, E., Alloin, D., Pantin, E., Lagage, P. O., & Marco, O. 2005, A&A, 438, 803

Gao, Y., & Solomon, P. M. 2004, 606, 271

García-Burillo, Martín-Pintado, J., & Fuente, A. 2001, ApJ, 563, L27

García-Burillo, S., Usero, A., Fuente, A., Martín-Pintado, Boone, F., Aalto, S., Krips, M., Neri, R., Schinnerer, E., & Tacconi, L.J. 2010, A&A, 519, A2

Gebhardt, K., et al. 2000, ApJ, 539, L13

von Glasow, W., Krause, M. G. H., Sommer-Larsen, J., & Burkert, A. 2013, MNRAS, 434, 1151

Goto, M., et al. 2003, ApJ, 598, 1038

Greve, A., Wills, K. A., Neininger, N., & Pedlar, A. 2002, A&A, 383, 56

Grimm, H.-J., Gilfanov, M., & Sunyaev, R. 2003, MNRAS, 339, 793

Harper-Clark, E. & Murray, N. 2009, ApJ, 693, 1696

Harrison, S., Faure, A., & Tennyson, J. 2013, MNRAS, 435, 3541

Heckman, T. M., Lee, A., & Miley, G. K. 1990, ApJS, 74, 833

Heike, K. & Awaki, H. 2007, PASJ, 59, 531

Henkel, C. & Mauersberger, R. 1993, A&A, 274, 730

Hoopes, C. G., et al. 2005, ApJ, 619, L99

Hopkins, P. F., Quataert, E., & Murray, N. 2012, MNRAS, 421, 3488

Ichikawa, T., Yanagisawa, K., Itoh, N., Tarusawa, K., van Driel, W., & Ueno, M. 1995, AJ, 109, 2038

Jansen, D. J., Spaans, M., Hogerheijde, M. R., & van Dishoeck, E. F. 1995, A&A, 303, 541

Jansen, D. J., van Dishoeck, E. F., Black, J. H., Spaans, M., & Sosin, C. 1995, A&A, 302, 223

Jiménez-Bailón, E., Santos-Lleó, M., Dahlem, M., Ehle, M., Mas-Hesse, J. M., Guainazzi, M., Heckman, T. M., & Weaver, K. A. 2005, A&A, 442, 861

Junkes, N., Zinnecker, H., Hensler, G., Dahlem, M., & Pietsch, W. 1995, A&A, 294, 8

Kaneda, H., Ishihara, D., Suzuki, T., Ikeda, N., Onaka, T., Yamagishi, M., Ohyama, Y., Wada, T., & Yasuda, A. 2010, A&A, 514, A14

Karachentsev, I. D., et al. 2002, A&A, 383, 125

Kerr, A. R., Pan, S.-K., & Effland, J.E. 2001, ALMA Memo 357

Kim, S., Martin, C. L., Stark, A. A., Lane, A. P. 2002, ApJ, 580, 896

Knapp, G. R. & Jura, M. 1976, ApJ, 209, 782

Koda, J., Sawada, T., Wright, M. C. H., et al. 2011, ApJSS, 193, 19

Kopp, M., Gerin, M., Roueff, E., & Le Bourlot, J. 1996, A&A, 305, 558

Koribalski, B., Dahlem, M., Mebold, U., & Brinks, E. 1993, A&A, 268, 14

Koribalski, B., Dettmar, R.-J., Mebold, U., & Wielebinski, R. 1996, A&A, 315, 71

Kotilainen, J., Forbes, D. A., Moorwood, A. F. M., van der Werf, P. P., & Ward, M. J. 1996, A&A, 313, 771

Kronberg, P. P., Biermann, P. P., & Schwab, F. R. 1985, ApJ, 291, 693

Krabbe, A., Sternberg, A., & Genzel, R. 1994, ApJ, 425, 72

Kroupa, P. 2001, MNRAS, 322, 231

Krumholz, M. R. & Thompson, T. A. 2013 MNRAS, 434, 2329

Lallement, R. 2004, A&A, 422, 391

Leitherer, C., Schraerer, D., Goldader, J. D., et al. 1999, ApJS, 123,3

Liszt, H. S. 1997, A&A, 322, 962

Liszt, H. S., Pety, J., & Lucas, R. 2010, A&A, 518, A45

Lo, K. Y., Cheung, K. W., Masson, C. R., Phillips, T. G., Scott, S. L., & Woody, D. P. 1987, ApJ, 312, 574

Lynds, C. R. & Sandage, A. R. 1963, AJ, 137, 1005

Maloney, P. 1990, *The Interstellar Medium in Galaxies*, eds. Thronson, H. A. & Shull, J. M., Kluwer. Dordrecht, p.493

Mangum, J. G., Wootten, A., & Plambeck, R. L. 1993, ApJ, 409, 282

Mangum, J. G., Emerson, D. T., & Greisen, E. W. 2000, ASP Conf. Ser. 217, 179

Mangum, J. G., Emerson, D. T., & Greisen, E. W. 2007, A&A, 474, 679

Mangum, J., Darling, J., Henkel, C., Menten, K. M., MacGregor, M., Svoboda, B. E., & Schinnerer, E. 2013, ApJ, 779, 33

Mao, R. Q., Henkel, C., Schulz, A., Zielinsky, M., Mauersberger, R., St$'$orzer, H., Wilson, T. L., & Gensheimer, P. 2000, A&A, 358, 433

Marcolini, A., Strickland, D. K., D'Ercole, A., Heckman, T. M., & Hoopes, C.G. 2005, MNRAS, 362, 626

Markova, N., Puls, J., Repolust, T., & Markov, H. 2004, A&A, 413, 693

Martin, C. 2005, ApJ, 621, 227

Matsushita, S., Kawabe, R., Matsumoto, H., Tsuru, T. G., Kohno, K., Morita, K., Okumura, S. K., & Vila-Vilaró, B. 2000, ApJ, 545, L107

McCrady, N. & Graham, J. R. 2007, ApJ, 663, 844

McKeith, C. D., Castles, J., Greve, A., & Downes, D. 1993, A&A, 272, 98

McKeith, C. D., Greve, A., Downes, D., & Prada, F. 1995, A&A, 293, 703

McKellar, A. 1940, PASP, 52, 187

McQuinn, K. B. W., Simon, R., Law, C. J., Jackson, J. M., Bania, T. M., & Clemens, D.P. 2002, ApJ, 576, 274

Meijerink, R. & Spaans, M. 2005, A&A, 436, 397

Meijerink, R., Spaans, M., & Israel, F. P. 2006, ApJ, 650, L103

Meijerink, R., Spaans, M., & Israel, F. P. 2007, A&A, 461, 793

Miller, G. E. & Scalo, J. M. 1978, PASP, 90, 506

Morgan, W. W. 1958, PASP, 70, 364

Muehle, S., Seaquist, E. R., & Henkel, C. 2007, ApJ, 671, 1579

Murray, N., Quataert, E., & Thompson, T. A. 2005, ApJ, 618, 569

Murray, N., & Rahman, M. 2010, ApJ, 709, 424

Murray, N., Quataert, E., & Thompson, T. A. 2010, ApJ, 709, 191

Murray, N., Ménard, B., & Thompson, T. A. 2011, ApJ, 735, 66

Mutchler, M., et al. 2007, PASP, 119, 1

Muxlow, T. W. B., Beswick, R. J., Garrington, S. T., Pedlar, A., Fenech, D. M., Argo, M. K., Van Eymeren, J., Ward, M., Zezas, A., & Brunthaler, A. 2010, MNRAS, 404, L109

Nakai, N., Hayashi, M., Handa, T., Sofue, Y., Hasegawa, T., & Sasaki, M. 1987, PASJ, 39, 685

Nakajima, T., Sakai, T., Kuno, N., & Ogawa, H. 2010, J. Infrared Milli Terahertz Waves, 31, 143

Nath, B. B. & Silk, J. 2009, MNRAS, 396, L90

Neininger, N., Guélin, M., Klein, U., García-Burillo, S., & Wielebinski, R. 1998, A&A, 339, 737

O'Connell, R. W. & Mangano, J. J. 1978, ApJ, 221, 62

O'Connell, R. W., Gallagher, J. S., III, Hunter, D. A., & Colley, W. N. 1995, ApJ, 446, L1

Ohyama, Y., et al. 2002, PASJ, 54, 891

Olofsson, H. & Rydbeck, G. 1984, A&A, 136, 17

Osterbrock, D. E. & Ferland, G. J., *Astrophysics of gaseous nebulae and active galactic nuclei*, 2006, University Science Books

Pan, K., Federman, S. R., Sheffer, Y., & Andersson, B-G. 2005, ApJ, 633, 986

Papadopoulos, P. P., van der Werf, P. P., Xilouris, E. M., Isaak, K. G., Yu Gao, & Muehle, S. 2012, MNRAS, 426, 2601

Phillips, A. C. 1993, AJ, 105, 486

Rieke, G., Lebofsky, M., Thompson, R., Low, F., & Tokunaga, A. 1980, ApJ, 238, 24

Rieke, G. H., Loken, K., Rieke, M. J., & Tamblyn, P. 1993, ApJ, 412, 99

Rodríguez-Fernández, N. J., Martín-Pintado, J., Fuente, A., & Wilson, T. L. 2004, A&A, 427, 217

Rodriguez-Rico, C. A., Viallefond, F., Zhao, J.-H., Goss, W. M., Anantharamaiah, K. R. 2004, ApJ, 616, 783

Roth, K. C. & Meyer, D. M. 1995, ApJ, 441, 129

Roussel, H., et al. 2010, A&A, 518, L66

Roy, A., Nath, B. B., Sharma, P., & Shchekinov, Y. 2013, MNRAS, 434, 3572

Rybicki, G. B. & Lightman, A. P., *Radiative processes in astrophysics*, 2004 (1979), Wiley-VCH

Saikia, D. J., Unger, S. W., Pedlar, A., Yates, G. J., Axon, D. J., Wolstencroft, R. D., Taylor, K., & Gyldenkerne, K. 1990, MNRAS, 245, 397

Saito, M., Sasaki, M., Kaneko, N., Nishimura, M., & Toyama, K. 1984, PASJ, 36, 305

Salak, D., Nakai, N., Miyamoto, Y., Yamauchi, A., & Tsuru, T. 2013, PASJ, 65, 66

Salpeter, E. E. 1955, ApJ, 121, 161

Sandage, A. & Bedke, J. The Carnegie Atlas of Galaxies, vol. II

Sanders, D. B., Mazzarella, J. M., Kim, D.-C., Surace, J. A., & Soifer, B.T. 2003, AJ, 126, 1607

Sandstrom, K. M., et al. 2013, ApJ, 777, 5

Sawada, T. et al. 2008, PASJ, 60, 445

Schilke, P., Groesbeck, T. D., Blake, G. A., & Phillips, T. G. 1997, ApJS, 108, 301

Schilke, P., Walmsley, C. M., Pineau des Forêts, G., & Flower, D. R. 1997, A&A, 321, 293

Schiano, A. V. R. 1985, ApJ, 299, 24

Seaquist, E. R., Frayer, D. T., & Bell, M. B. 1998, ApJ, 507, 745

Seaquist, E. R. & Clark, J. 2001, ApJ, 552, 133

Sérsic, J. L. & Pastoriza, M. 1965, PASP, 77, 287

Shapley, A. E., Steidel, C. C., Pettini, M., & Adelberger, K. L. 2003, ApJ, 588, 65

Sharma, M., Nath, B. B., & Shchekinov, Y. 2011, ApJL, 736, L27

Sharp, R. G. & Bland-Hawthorn, J. 2010, ApJ, 711, 818

Shen, J. & Lo, K. Y. 1995, ApJ, 445, L99

Shetty, R., Glover, S. C., Dullemond, C. P., & Klessen, R. S. 2011, MNRAS, 412, 1686

Shopbell, P. L. & Bland-Hawthorn, J. 1998, ApJ, 493, 129

Skatrud, D. D., de Lucia, F. C., Blake, G. A., & Sastry, K. V. L. N. 1983, Journal of Molecular Spectroscopy, 99, 35

Snow, T. P. & McCall, B.J. 2006, ARA&A, 44, 367

Sobolev, V. V. 1957, Soviet Astronomy, 1, 678

Sofue, Y. 1998, PASJ, 50, 227

Solomon, P. M., Rivolo, A. R., Barrett, J., & Yahil, A. 1987, ApJ, 319, 730

Solomon, P. M., Downes, D., Radford, S. J. E., & Barrett, J. W. 1997, ApJ, 478, 144

Stevens, I. R., Strickland, D. K., Wills, K. A. 1999, MNRAS, 308, L23

Stevens, I. R., Read, A. M., & Bravo-Guerrero, J. 2003, MNRAS, 343, L47

Strickland, D. K., Heckman, T. M., Colbert, E. J. M., Hoopes, C. G., & Weaver, K. A. 2004, ApJ, 606, 829

Strickland, D. K. & Heckman, T. M. 2009, ApJ, 697, 2030

Taylor, C. L., Walter, F., & Yun, M. S. 2001, ApJ, 562, L43

Telesco, C. M., Campins, H., Joy, M., Dietz, K., & Decher, R. 1991, ApJ, 369, 135

Thaddeus, R. & Clauser, J. F. 1966, Phys. Rev. Lett. 16, 819

Thompson, A. R., Moran, J. M., & Swenson, G. W. Jr. *Interferometry and synthesis in radio astronomy*, 2004, Second Edition, WILEY-VCH Verlag GmbH & Co. KGaA, Weinheim

Thornton, K., Gaudlitz, M., Janka, H.-T., & Steinmetz, M. 1998, ApJ, 500, 95

Townes, C. H. & Schawlow, A. L., *Microwave spectroscopy*, 2012 (1955), Dover Publications

Tremaine, S., et al. 2002, ApJ, 574, 740

Tsuru, T. G. et al. 2007, PASJ, 59, S269

Tully, R. B. 1988, Nearby Galaxies Catalog, vol.0, p.0

Ulich, B. L. & Haas, R. W. 1976, ApJ, 30, 247

Usero, A., García-Burillo, S., Martín-Pintado, J., Fuente, A., & Neri, R. 2006, A&A, 448, 457

van den Bergh, *Galaxy morphology and classification*, 1998, Cambridge University Press

van der Tak, F. F. S., Black, J. H., Sch´oier, F. L., Jansen, D. J., & van Dishoeck, E. F. 2007, A&A, 468, 627

van Dishoeck, E. F. & Black, J. H. 1986, ApJS, 62, 109

van Dishoeck, E. F. & Black, J. H. 1988, ApJ, 334, 771

Veilleux, S., Cecil, G., & Bland-Hawthorn, J. 2005, ARA&A, 43, 769

Veilleux, S., Rupke, D. S. N., & Swaters, R. 2009, ApJ, 700, L149

Veilleux, S., et al. 2013, ApJ, 776, 27

Veron-Cetty, M.-P. & Veron, P. 1985, A&A, 145, 425

Walter, F., Weiß, A., & Scoville, N. 2002, ApJ, 580, L21

Weinberg, S., *Cosmology*, 2008, Oxford University Press

Weiß, A., Walter, F., Neininger, N., & Klein, U. 1999, A&A, 345, L23

Weiß, A., Neininger, N., Henkel, C., Stutzki, J., & Klein, U. 2001a, ApJ, 554, L143

Weiß, A., Neininger, N., Hüttemeister, S., & Klein, U. 2001b, A&A, 365, 571

Weiß, A., Walter, F., & Scoville, N. 2005, A&A, 438, 533

Westmoquette, M., Smith, L. J., Gallagher III, J. S., O'Connell, R. W., Rosario, D. J., & de Grijs, R. 2007, ApJ, 671, 358

Wills, K. A., Redman, M. P., Muxlow, T. W. B., & Pedlar, A. 1999, MNRAS, 309, 395

Wills, K. A., Das, M., Pedlar, A., Muxlow, T. W. B., & Robinson, T.G. 2000, MNRAS, 316, 33

Wills, K. A., Pedlar, A., & Muxlow, T. W. B. 2002, MNRAS, 331, 313

Wilson, T. L., Rohlfs, K., & Hüttemeister, S., *Tools of radio astronomy*, 5th edition, 2009, Springer

Yamagishi, M., Kaneda, H., Ishihara, D., Kondo, T., Onaka, T., Suzuki, T., & Minh, Y. C. 2012, A&A, 541, A10

Young, J. S. & Sanders, D. B. 1986, ApJ, 302, 680

Young, J. S. & Scoville, N. Z. 1991, ARA&A, 29, 581

Yun, M. S., Ho, P. T. P., & Lo, K. Y. 1994, Nature, 372, 530

Zhang, D. & Thompson, T. A. 2012, MNRAS, 424, 1170